

Hydrology, water resources, and ecosystem sustainable development

Edited by

Wenlong Jing, Jay Lee, Pengyan Zhang
and Songshan Yue

Published in

Frontiers in Environmental Science
Frontiers in Ecology and Evolution
Frontiers in Earth Science



FRONTIERS EBOOK COPYRIGHT STATEMENT

The copyright in the text of individual articles in this ebook is the property of their respective authors or their respective institutions or funders. The copyright in graphics and images within each article may be subject to copyright of other parties. In both cases this is subject to a license granted to Frontiers.

The compilation of articles constituting this ebook is the property of Frontiers.

Each article within this ebook, and the ebook itself, are published under the most recent version of the Creative Commons CC-BY licence. The version current at the date of publication of this ebook is CC-BY 4.0. If the CC-BY licence is updated, the licence granted by Frontiers is automatically updated to the new version.

When exercising any right under the CC-BY licence, Frontiers must be attributed as the original publisher of the article or ebook, as applicable.

Authors have the responsibility of ensuring that any graphics or other materials which are the property of others may be included in the CC-BY licence, but this should be checked before relying on the CC-BY licence to reproduce those materials. Any copyright notices relating to those materials must be complied with.

Copyright and source acknowledgement notices may not be removed and must be displayed in any copy, derivative work or partial copy which includes the elements in question.

All copyright, and all rights therein, are protected by national and international copyright laws. The above represents a summary only. For further information please read Frontiers' Conditions for Website Use and Copyright Statement, and the applicable CC-BY licence.

ISSN 1664-8714
ISBN 978-2-8325-4114-2
DOI 10.3389/978-2-8325-4114-2

About Frontiers

Frontiers is more than just an open access publisher of scholarly articles: it is a pioneering approach to the world of academia, radically improving the way scholarly research is managed. The grand vision of Frontiers is a world where all people have an equal opportunity to seek, share and generate knowledge. Frontiers provides immediate and permanent online open access to all its publications, but this alone is not enough to realize our grand goals.

Frontiers journal series

The Frontiers journal series is a multi-tier and interdisciplinary set of open-access, online journals, promising a paradigm shift from the current review, selection and dissemination processes in academic publishing. All Frontiers journals are driven by researchers for researchers; therefore, they constitute a service to the scholarly community. At the same time, the *Frontiers journal series* operates on a revolutionary invention, the tiered publishing system, initially addressing specific communities of scholars, and gradually climbing up to broader public understanding, thus serving the interests of the lay society, too.

Dedication to quality

Each Frontiers article is a landmark of the highest quality, thanks to genuinely collaborative interactions between authors and review editors, who include some of the world's best academicians. Research must be certified by peers before entering a stream of knowledge that may eventually reach the public - and shape society; therefore, Frontiers only applies the most rigorous and unbiased reviews. Frontiers revolutionizes research publishing by freely delivering the most outstanding research, evaluated with no bias from both the academic and social point of view. By applying the most advanced information technologies, Frontiers is catapulting scholarly publishing into a new generation.

What are Frontiers Research Topics?

Frontiers Research Topics are very popular trademarks of the *Frontiers journals series*: they are collections of at least ten articles, all centered on a particular subject. With their unique mix of varied contributions from Original Research to Review Articles, Frontiers Research Topics unify the most influential researchers, the latest key findings and historical advances in a hot research area.

Find out more on how to host your own Frontiers Research Topic or contribute to one as an author by contacting the Frontiers editorial office: frontiersin.org/about/contact

Hydrology, water resources, and ecosystem sustainable development

Topic editors

Wenlong Jing – Guangzhou Institute of Geography, China

Jay Lee – Kent State University, United States

Pengyan Zhang – Henan University, China

Songshan Yue – Nanjing Normal University, China

Citation

Jing, W., Lee, J., Zhang, P., Yue, S., eds. (2023). *Hydrology, water resources, and ecosystem sustainable development*. Lausanne: Frontiers Media SA.

doi: 10.3389/978-2-8325-4114-2

Table of contents

- 04 **Multi-depth evolution characteristics of soil moisture over the Tibetan Plateau in the past 70 years using reanalysis products**
Yangxiaoyue Liu and Yaping Yang
- 23 **Satellite observations reveal decreasing soil erosion in Northeast Inner Mongolia, China, over the past four decades**
Wei Jiang, Zhiguo Pang, Juan Lv, Hongrun Ju, Lin Li and June Fu
- 31 **Local-neighborhood effects of environmental regulations on green technology innovation in manufacturing: Green credit-based regulation**
Ling Jiang, Yuqi Wang and Jian Zhang
- 44 **Heterogeneity and optimization of ecological security pattern on a mountain town: A case of Tianzhu County in the Hexi Corridor, China**
Zhijie Chen, Hong Chen, Minan Yang, Xi Wang, Yuefeng Jiang and Wei Zhang
- 55 **Assessing the contribution of vegetation variation to streamflow variation in the Lancang River Basin, China**
Yuan Liu, Weiqiang Chen, Ling Li, Junchang Huang, Xianglong Wang, Yulong Guo and Guangxing Ji
- 66 **The effect of animal husbandry on economic growth: Evidence from 13 provinces of North China**
Chu Wang, Jinbing Zhang and Wenneng Zhou
- 81 **Varying performance of eight evapotranspiration products with aridity and vegetation greenness across the globe**
Hongzhou Wang, Xiaodong Li, Cheng Tong, Yongkang Xu, Dongjun Lin, Jiazhi Wang, Fei Yao, Pengxuan Zhu and Guixia Yan
- 100 **Water quality parameters retrieval of coastal mariculture ponds based on UAV multispectral remote sensing**
Yumeng Zhang, Wenlong Jing, Yingbin Deng, Wenneng Zhou, Ji Yang, Yong Li, Yanpeng Cai, Yiqiang Hu, Xiaoyan Peng, Wenlu Lan, Mengwei Peng and Yimin Tang
- 112 **A prioritization protocol for coastal wetland restoration on Moloka'i, Hawai'i**
Judith Z. Drexler, Helen Raine, James D. Jacobi, Sally House, Pūlama Lima, William Haase, Arleone Dibben-Young and Bret Wolfe
- 131 **Changes in the water retention of mountainous landscapes since the 1820s in the Austrian Alps**
Gabriel Stecher, Severin Hohensinner and Mathew Herrnegger



OPEN ACCESS

EDITED BY

Wenlong Jing,
Guangzhou Institute of Geography,
China

REVIEWED BY

Yuyue Xu,
Nanjing University, China
Xin Lyu,
Beijing Normal University, China
Yongchang Ye,
South Dakota State University,
United States

*CORRESPONDENCE

Yangxiaoyue Liu,
lyxy@reis.ac.cn

SPECIALTY SECTION

This article was submitted to
Environmental Informatics and Remote
Sensing,
a section of the journal
Frontiers in Environmental Science

RECEIVED 28 June 2022

ACCEPTED 18 July 2022

PUBLISHED 22 August 2022

CITATION

Liu Y and Yang Y (2022), Multi-depth
evolution characteristics of soil
moisture over the Tibetan Plateau in the
past 70 years using reanalysis products.
Front. Environ. Sci. 10:979853.
doi: 10.3389/fenvs.2022.979853

COPYRIGHT

© 2022 Liu and Yang. This is an open-
access article distributed under the
terms of the [Creative Commons
Attribution License \(CC BY\)](https://creativecommons.org/licenses/by/4.0/). The use,
distribution or reproduction in other
forums is permitted, provided the
original author(s) and the copyright
owner(s) are credited and that the
original publication in this journal is
cited, in accordance with accepted
academic practice. No use, distribution
or reproduction is permitted which does
not comply with these terms.

Multi-depth evolution characteristics of soil moisture over the Tibetan Plateau in the past 70 years using reanalysis products

Yangxiaoyue Liu^{1,2*} and Yaping Yang^{1,2}

¹State Key Laboratory of Resources and Environmental Information Systems, Institute of Geographic Sciences and Natural Resources Research, Chinese Academy of Sciences, Beijing, China, ²Jiangsu Center for Collaborative Innovation in Geographical Information Resource Development and Application, Nanjing, China

Soil moisture (SM) is a crucial component of the hydrological cycle. Both the spatial–temporal distribution and the variation characteristics of SM are effective indicators of regional land surface water resource homogeneity and heterogeneity. With consideration of the crucial role of the Tibetan Plateau (TP) in the hydrological process in Asia, this study investigated the fluctuation of multi-depth soil moisture across the TP during 1950–2020 on a monthly scale against the background of global warming by using ERA5 reanalysis datasets. The correlation and potential causality between soil moisture and associated driving factors were explored. Our research revealed that the soil moisture across the TP shows a slight wetting trend at 0–100 cm depth for the past 70 years against the background of climate warming and increasing precipitation. Additionally, the wetting region (variation trend $\geq 0.005 \text{ m}^3/\text{m}^3$ per decade) had sufficient water supplementation from precipitation and a mild soil temperature increase. By comparison, there is a noteworthy warming tendency and falling precipitation in the sparsely distributed drying region (variation trend $\leq -0.005 \text{ m}^3/\text{m}^3$ per decade). In terms of vertical variation features, the temporal dynamic fluctuation of soil moisture and soil temperature evidently decreases as the depth increases, suggesting high sensitivity of the surface layer soil to atmospheric conditions. Precipitation and snowmelt preliminarily proved to be the dominant drivers causing spatial and temporal variations in soil moisture (occupying over 70% of the TP region), and bidirectional causality (ranging between 15.52% and 50.56%) was found between soil moisture and these two parameters. In summary, this study explored the spatial–temporal fluctuation in the evolutionary characteristics of SM, which is expected to advance our understanding of soil moisture dynamics under the conditions of climate change across the TP.

KEYWORDS

soil moisture, Tibetan Plateau, evolution characteristics, multi-depth, long time series

1 Introduction

Soil moisture is an important form of surface water storage and is widely recognized as an indispensable climate variable across the globe (Dorigo and De Jeu, 2016; Gruber et al., 2019; Deng et al., 2020a). The soil moisture layer is a pivotal area where atmospheric water, surface water, groundwater, and vegetation water are connected and exchanged (Koster et al., 2004; Swenson et al., 2008; Chen et al., 2014). Soil moisture is also a critical vehicle for storing and exchanging carbon, nitrogen, phosphorus, and other nutrients, which could have far-reaching effects on the growth of vegetation and microorganisms in ecosystems (Xu et al., 2004; Flanagan and Johnson, 2005). The spatial-temporal distribution of and variations in soil moisture directly affect geochemical, climatic, ecological, and hydrological processes and their interactions on the Earth's surface (Verrot and Destouni, 2016; Dorigo et al., 2017). Thus, it is important to investigate how soil moisture fluctuates both temporally and spatially across different depths and what the potential climate drivers could be.

Because it is essential to acquire sufficient soil moisture records before variation analysis, great efforts have been devoted to the monitoring of soil moisture since the 1930s (Robock et al., 2000). First, *in situ* measurements emerged as an effective and efficient method to detect and record accurate soil moisture levels at exact locations and depths (Dorigo et al., 2011). Nevertheless, as the requirements gradually changed from regional to large-scale observations, it was barely possible for point-scale-based measurements to provide a plausible spatial-continuous dataset. With the development of satellite technology, remotely sensed soil moisture observations have brought unprecedented opportunities for the availability of products with global coverage (Attema et al., 1998; Njoku et al., 2003; Bartalis et al., 2007; Spencer et al., 2010). Numerous satellite-retrieved soil moisture products have been utilized in various hydrological studies (Lakshmi et al., 2004; Seneviratne et al., 2010; Dorigo et al., 2017). However, owing to the limited penetration capacity of microwave signals and radio frequency interference, widespread gap regions exist in remotely sensed soil moisture retrievals, and microwave signals can merely depict the surface (> 5 cm) soil water content (Wang and Qu, 2009; Bradley et al., 2010). Comparatively speaking, the root-zone soil humidity conditions are certainly equally important in indicating agricultural drought levels, especially in analyzing the effects of water stress on the growth and yield of crops. Therefore, it is important to acquire multi-depth soil humidity information to gain a comprehensive understanding of the integral state of multi-depth soil moisture.

The accessibility of multi-depth soil moisture data is made possible by the emergence of data assimilation algorithms. The data assimilation approach integrates multi-source heterogeneous data to drive land surface models to retrieve long time-series surface parameter estimations. Moreover, it simultaneously overcomes the limitations of spatial

representation of *in situ* measurements, improves the restricted penetration depth of spaceborne microwave signals, and realizes the multi-depth spatial-temporal seamless coverage of soil moisture (Spennemann et al., 2015). Reanalysis data are derived by using a state-of-the-art data assimilation system to combine and optimally integrate various types of observation data with short-term weather forecast products (Hersbach et al., 2020). ERA5, the fifth generation of the European Centre for Medium-Range Weather Forecasts reanalysis, continuously provides soil moisture information for 0–289 cm depth and numerous climate variables across the globe since 1950 (Mahto and Mishra, 2019). Great attention has been paid to evaluation of the ERA5 soil moisture products since its inception. Li et al. (2020) validated soil moisture data originating from five reanalyses, namely the Japanese 55-year reanalysis (JRA-55) (Kobayashi et al., 2015), the National Centers for Environmental Prediction Climate Forecast System Reanalysis (CFSR) (Ek et al., 2003), the Modern-Era Retrospective analysis for Research and Applications version 2 (MERRA-2) (Gelaro et al., 2017), ERA-Interim (Dee et al., 2011), and ERA5. ERA5 showed better performance than the other four retrievals, as indicated by a high correlation coefficient and favorable annual cycles. Mahto and Mishra (2019) evaluated the quality of ERA5 soil moisture data in India, and they found that ERA5 can be either better than or comparable to other products retrieved from JRA-55, CFSR, MERRA-2, and ERA-Interim. Additionally, the applicability of ERA5 and ERA-Interim in describing soil moisture conditions across the Tibetan Plateau (TP) was acknowledged in previous studies (Zeng et al., 2015; Cheng et al., 2019). Many other climate variables of ERA5 (i.e., precipitation, temperature, evaporation) were also thoroughly assessed and found to be valuable for hydrological and climate change applications (Olason, 2018; Mahto and Mishra, 2019; Xin et al., 2021).

The TP, known as the “third pole” and the roof of the world, is the highest plateau in the world, with an average altitude of approximately 4,000–5,000 m (Yang et al., 2013). Given the climate particularity and ecological fragility caused by its unique terrain and location, the TP acts as an initiator and regulator of climate variation in the Northern Hemisphere. The climate evolution of the TP not only remarkably influences the corresponding climate change in Asia but also has a considerable impact on the Northern Hemisphere. Additionally, the TP can reveal notable sensitivity, advancement, and regulation of global climate change. Climate warming accelerates global hydrological circulation and strengthens the process of soil water evaporation (Li et al., 2022). Soil moisture, a critical component of the water cycle, is regarded as an effective indicator of climate change (Deng et al., 2020b). It is of great significance to systematically explore the evolutionary trend of soil moisture to promote the understanding of surface water circulation characteristics in the context of global warming. However, little is known about the

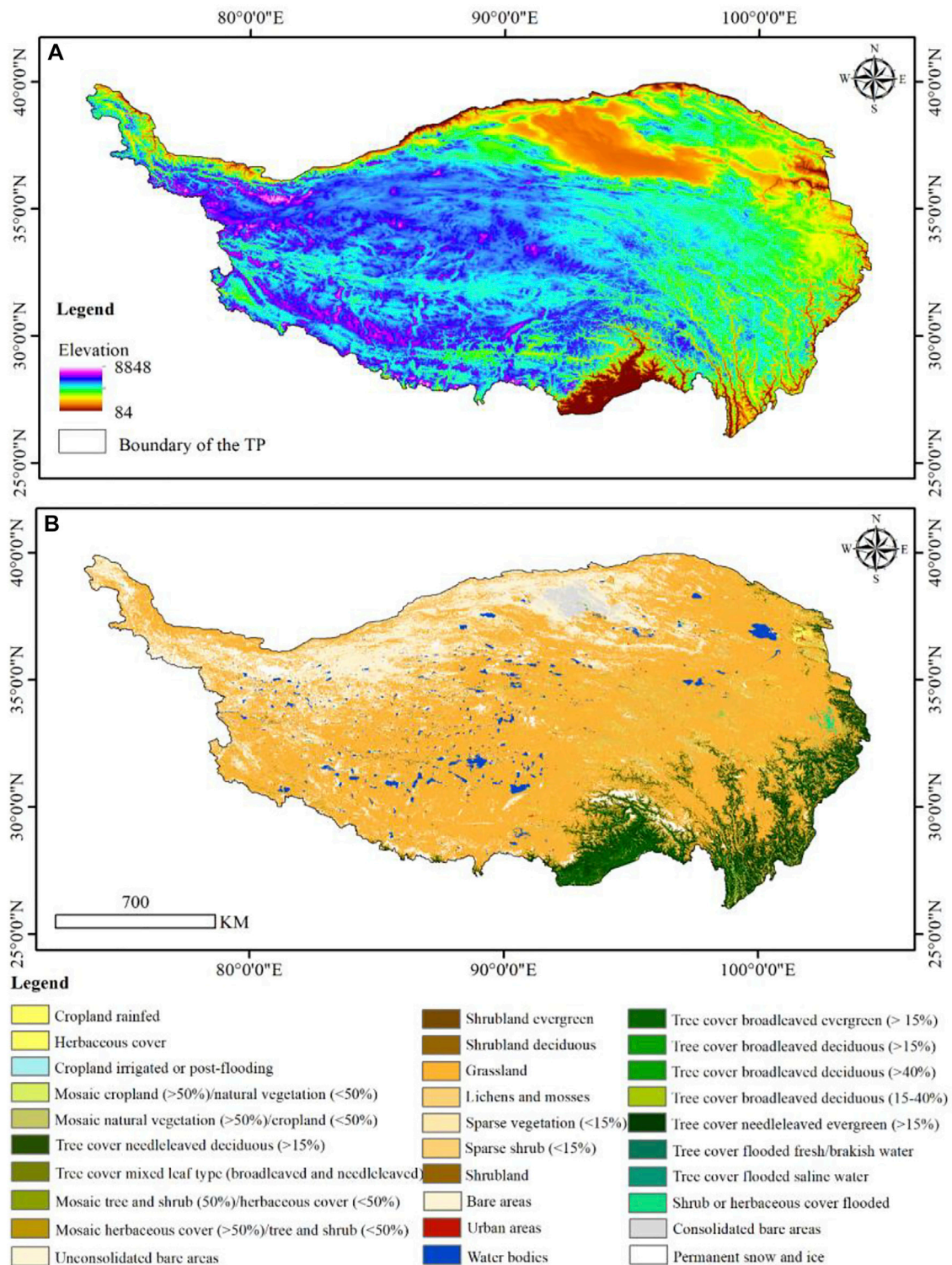
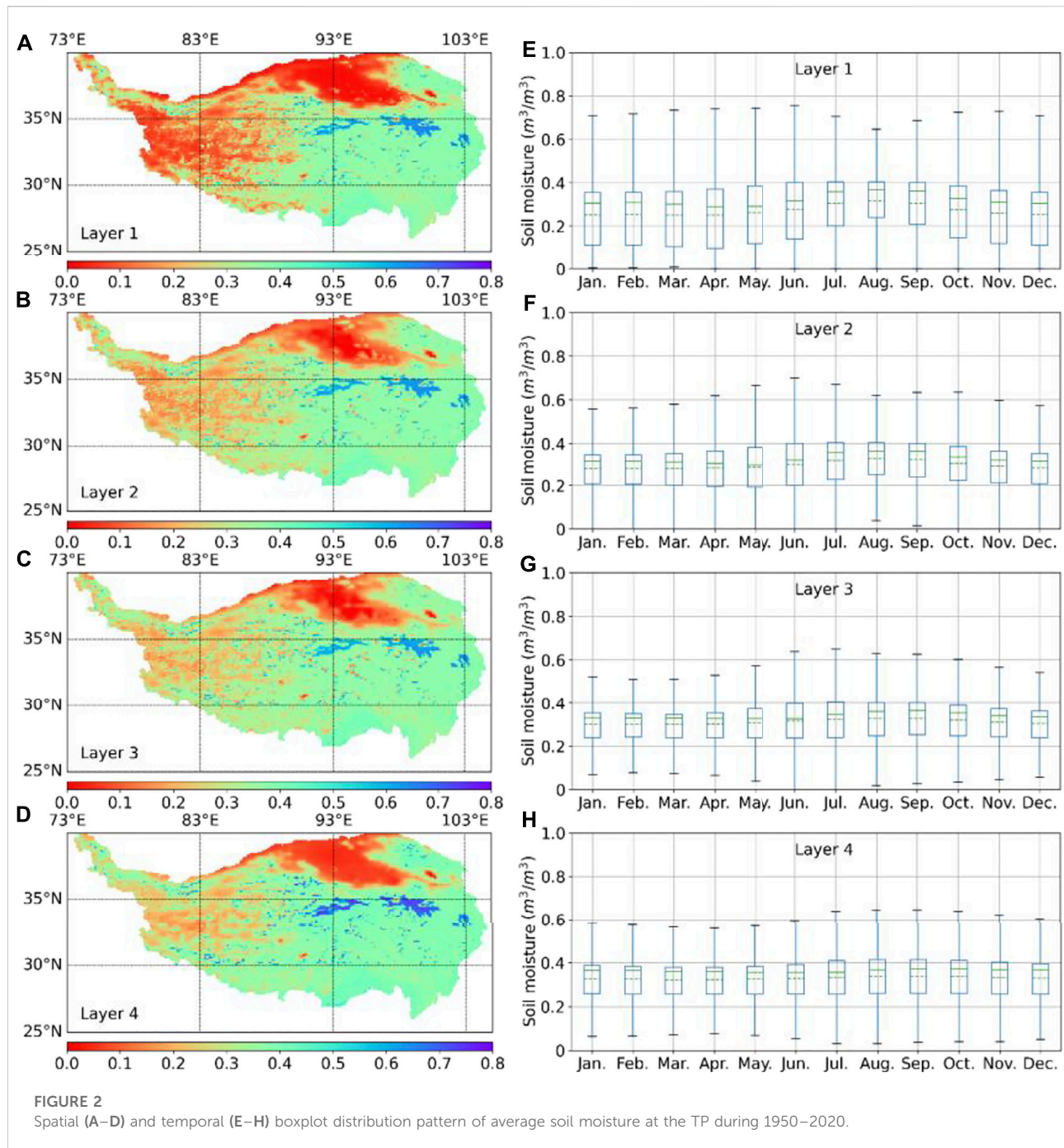


FIGURE 1

(A) Elevation distribution of the TP. This dataset is acquired from the Shuttle Radar Topography Mission (SRTM). For more details about the SRTM, readers are kindly referred to Farr et al. (2007). Moreover, the boundary of the TP is accessed from the National Tibetan Plateau Data Center, China (<http://data.tpdc.ac.cn/>). (B) Land cover types of the TP in 2017. The land cover data is retrieved from the European Space Agency Climate Change Initiatives Land Cover Project (<https://www.esa-landcover-cci.org/>). For more information about this dataset, readers are kindly referred to Bontemps et al. (2013).



trend of soil moisture across the TP, and previous studies have mainly focused on the accuracy evaluation of multi-source soil moisture products derived from *in situ* measurements (Bai et al., 2017; Chen et al., 2017; Xie et al., 2017; Li et al., 2018; Cheng et al., 2019; Xing et al., 2021).

In this study, the multi-depth soil moisture variation trend across the TP was disclosed by using ERA5 products with the

long-term perspective of 1950–2020. Closely related climate variables, including soil temperature, precipitation, snowmelt, and evaporation, were used to investigate potential causal links that may trigger variations in soil moisture. The main purpose of this study was to clarify the spatial and temporal fluctuation rules of multi-depth soil moisture and to investigate the dominant climatic factors that trigger the evolution of soil moisture. This

paper is organized as follows. **Section 2** introduces the basic properties of the TP, including location, terrain, climate, and land cover. The ERA5 soil moisture and ancillary climate variable datasets utilized in this study are also briefly introduced. In addition, the employed spatiotemporal trend analysis and causality investigation approaches are presented. **Section 3** describes the investigation results for temporal-spatial soil moisture and soil temperature variation trends across the TP, which reflect the evolutionary characteristics of the synthetic climate regime in the past 70 years. Moreover, the potential causal links between soil moisture and climatic parameters are investigated. In the final section, apart from the abovementioned climate variables, we discuss the other possible inherent mechanisms that may induce the fluctuations in soil moisture and explore the uncertain factors that may influence the results. Finally, conclusions are drawn from this study to summarize the findings and demonstrate future research directions.

2 Study region, data resources, and methodology

2.1 Study region

As shown in **Figure 1A**, the TP is the highest plateau in the world and is situated in Inner Asia (Gasse et al., 1991; Wang et al., 2021). Specifically, the TP, with a gross area of approximately $2.5 \times 10^6 \text{ km}^2$, is located between $26^{\circ}00' - 39^{\circ}47' \text{ N}$ (spanning 300–1,500 km from north to south) and $73^{\circ}19' - 104^{\circ}47' \text{ E}$ (spanning 2,800 km from east to west). The steep and complex terrain fluctuates greatly, ranging from 84 to 8,848 m. Generally, the terrain is relatively high in the west and low in the east. As presented in **Figure 2B**, the southeast margin is dominated by a tropical humid/semi-humid climate, and the remaining vast region contains semi-humid, semi-arid, and arid zones. Correspondingly, the southeastern margin is mainly covered by forests and humid soils. In comparison, alpine meadows, alpine scrubs, and desert meadows dominate the plateau climate region, along with relatively moderate soil moisture content. Moreover, there is a vast area of desert in the north of the TP, which is an important sensitive heat source in the Earth system, accompanied by high albedo, small soil heat capacity, and low water content.

2.2 Dataset

ERA5, the successor of ERA-Interim, provides a host of atmospheric, land, and oceanic climate variables (Hersbach et al., 2020). As a vital member of ERA5, ERA5-Land is focused on the consistent evolution of land variables from

1950 onwards (Muñoz-Sabater et al., 2021). It continually provides a description of past global climate features with high precision and favorable spatiotemporal integrity by utilizing the law of physics. These variables were designed and generated to depict the characteristics of hydrology and energy circulation quantifiably at the land surface from a long-term perspective.

In this study, we used ERA5-Land monthly averaged data to investigate the trend of soil moisture at the TP. As shown in **Table 1**, both soil moisture and ancillary climatic variable datasets were accessed from the Copernicus Climate Change Service Climate Data Store (<https://cds.climate.copernicus.eu/>) to systematically analyze the variation trends and possible driving forces. In addition to gravity, the land surface thermodynamic process originating from solar radiation can be the most crucial driver for the soil water cycle (Li et al., 2020); therefore, soil temperature estimation at a corresponding depth is selected as an essential supplement to understand soil moisture fluctuation tendencies. Precipitation is recognized as the dominant replenishment source of soil water at the TP, where there is barely any artificial interference, such as irrigation. Apart from the widely acknowledged promotion of precipitation to soil moisture content, non-negligible soil moisture-precipitation feedback has been observed. Soil moisture can promote or suppress precipitation based on different underlying surface properties (Hohenegger et al., 2009; Tuttle and Salvucci, 2016; Yang et al., 2018). Additionally, in the frozen season, precipitation in the form of snow hardly nourishes the soil. However, as the temperature rises, snowmelt is expected to significantly boost the soil water content. Therefore, it is assumed that using precipitation and snowmelt data together would be more beneficial for exploring soil moisture variation mechanisms than using only one of them. Evaporation records the accumulated amount of water evaporated from the Earth's surface, which is tightly linked to soil water deficits (Martens et al., 2017). Specifically, for the ERA5 evaporation product, negative values indicate evaporation, and positive values indicate condensation.

2.3 Methodology

2.3.1 Anomaly calculation

With the consideration that this study is mainly dedicated to investigating the long-term variation trend of soil moisture, anomalies in the employed datasets were calculated to simultaneously remove strong seasonality and explicitly magnify fluctuation regularity. Thus, the anomaly of each variable was calculated by deducting the multi-year average of a corresponding month, as in Xie et al. (2019). The specific equation is as follows:

$$\text{Anomaly}(i, j) = X(i, j) - \frac{1}{n} \sum_{i=1}^n X(i, j) \quad (1)$$

TABLE 1 Basic properties of the employed soil moisture and ancillary climatic variable datasets.

Variable	Unit	Depth	Temporal resolution	Spatial resolution	Time range
Soil moisture	m ³ /m ³	0–7 cm (layer 1) 7–28 cm (layer 2)	Monthly	0.1° × 0.1°	1950.01–2020.12
Soil temperature	°C	28–100 cm (layer 3) 100–289 cm (layer 4)			
Precipitation	mm	—			
Snowmelt	mm	—			
Evaporation	mm	—			

where $X(i, j)$ is the value of parameter X in month of i and the year of j , and n is the total number of years.

2.3.2 Rolling mean calculation

Several abnormal peak and valley values occasionally appeared in the anomaly results, which may be induced by unexpected extreme weather events during certain monthly scale periods. Because this study was focused on trend analysis over several decades rather than short-period extreme weather events, the rolling means of the soil moisture and the other variables were calculated to allow clear observation of temporal evolutionary tendencies. The rolling mean was obtained by subtracting the moving average of the anterior months (Zivot and Wang, 2003) as follows:

$$\text{Rolling mean}(t) = \overline{X(t - 11: t)} \quad (2)$$

where $\overline{X(t - 11: t)}$ is the moving average value of the variables utilized in the period from a time of $t - 121$ to t . In this case, time was calculated on a monthly basis.

2.3.3 Granger causality exploration

According to previous findings (Hohenegger et al., 2009; Martens et al., 2017; Li et al., 2020), soil moisture has tight bidirectional links to soil temperature, precipitation, snowmelt, and evaporation. Thus, in addition to exploring the soil moisture evolution law, it is crucial to demonstrate the causality between the soil moisture and these closely related variables, which could be beneficial for understanding the inherent driving mechanism of the evolution phenomenon. Moreover, it could be conducive to preliminarily determine the feedback of the soil moisture to these variables across the TP. The Granger causality, proposed by Nobel Economics Laureate Clive W. J. Granger in 1969, is a simple but effective statistical hypothesis test for determining whether the time series of a certain variable is useful in forecasting another one (Granger, 1969). Since its inception, Granger

causality analysis has been predominantly used in the field of economics (Hiemstra and Jones, 1994; Dutta, 2001; Kónya, 2006). Recently, Granger causality analysis has become increasingly popular in investigating the interactions of Earth system processes, resulting in stable and reliable findings (Jiang et al., 2015; Papagiannopoulou et al., 2017; Runge et al., 2019). The equations for the Granger causality test are as follows:

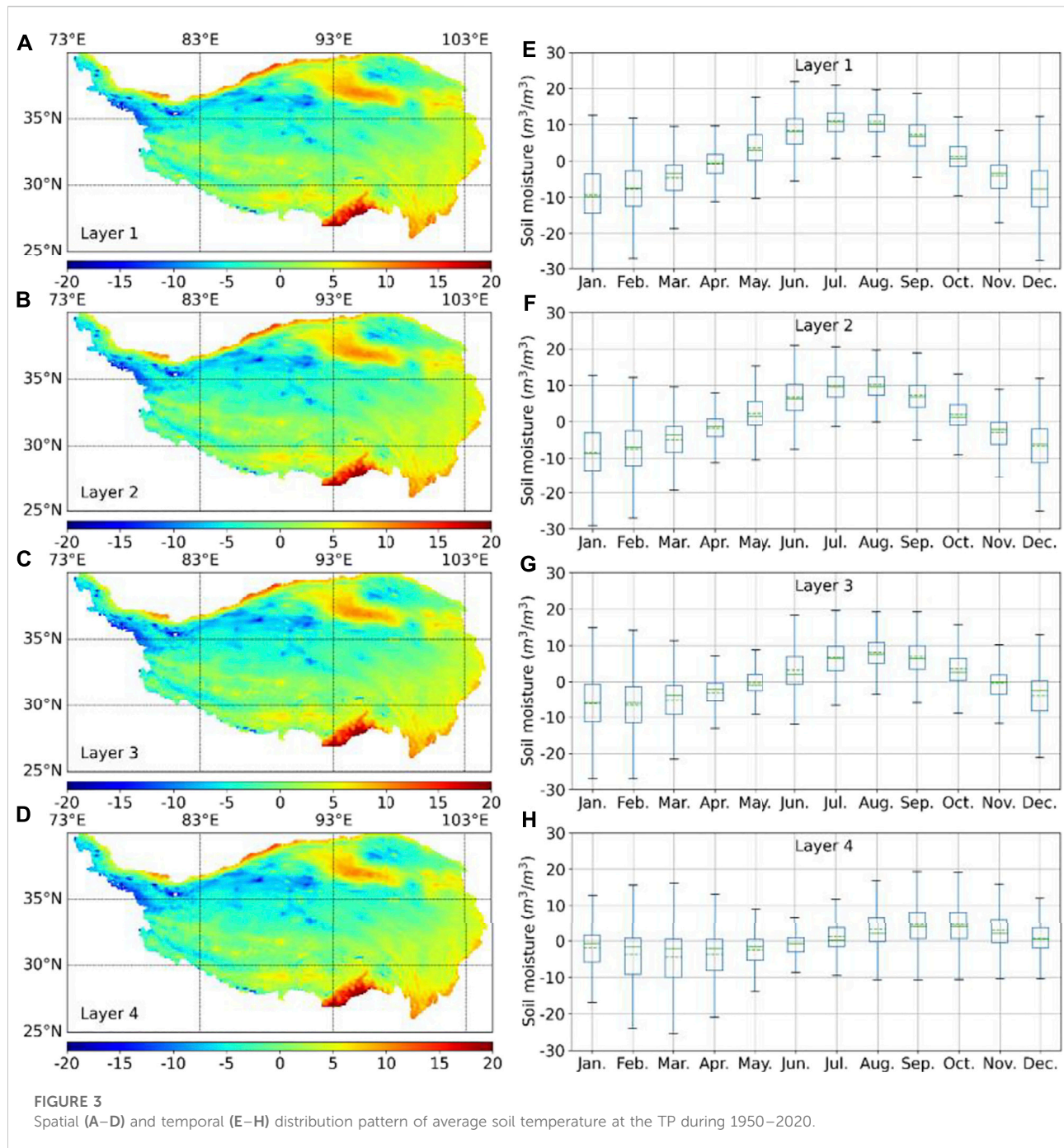
$$X_t = \sum_{i=1}^n a_i X_{t-i} + \sum_{i=1}^n b_i Y_{t-i} + \varepsilon_t \quad (3)$$

$$Y_t = \sum_{i=1}^n c_i Y_{t-i} + \sum_{i=1}^n d_i X_{t-i} + \eta_t \quad (4)$$

where X_t and Y_t are time series of two variables; n is the sample capacity; a_i , b_i , c_i , and d_i are regression coefficients; and ε_t and η_t are white noise. Both the time-series interrelationship and autocorrelation of the two target variables were tested by using Granger causality analysis. In addition, an F-test was used to check whether the Granger causality hypothesis was tenable (usually set $F \leq 0.05$ or 0.1). If the estimation of Y_t can be remarkably improved by taking X_t into consideration rather than merely using past Y_t values, it means that past values of X_t have a significant effect on the current value of Y_t , and vice versa.

2.3.4 Spatial–temporal perspective analysis

Soil moisture dynamics results from the combined non-linear effects of climate, soil properties, terrain, and vegetation. In addition, changing climate and artificial interference further exacerbate its uncertainty, randomness, and unpredictability. Consequently, soil moisture patterns exhibit a high degree of complexity. Therefore, it is necessary to comprehensively and systematically investigate the dynamics of soil moisture from the perspectives of time, depth, latitude, and longitude. It is thought that spatial–temporal perspective analysis could be helpful in gaining a clear and synthetic outlook of soil moisture



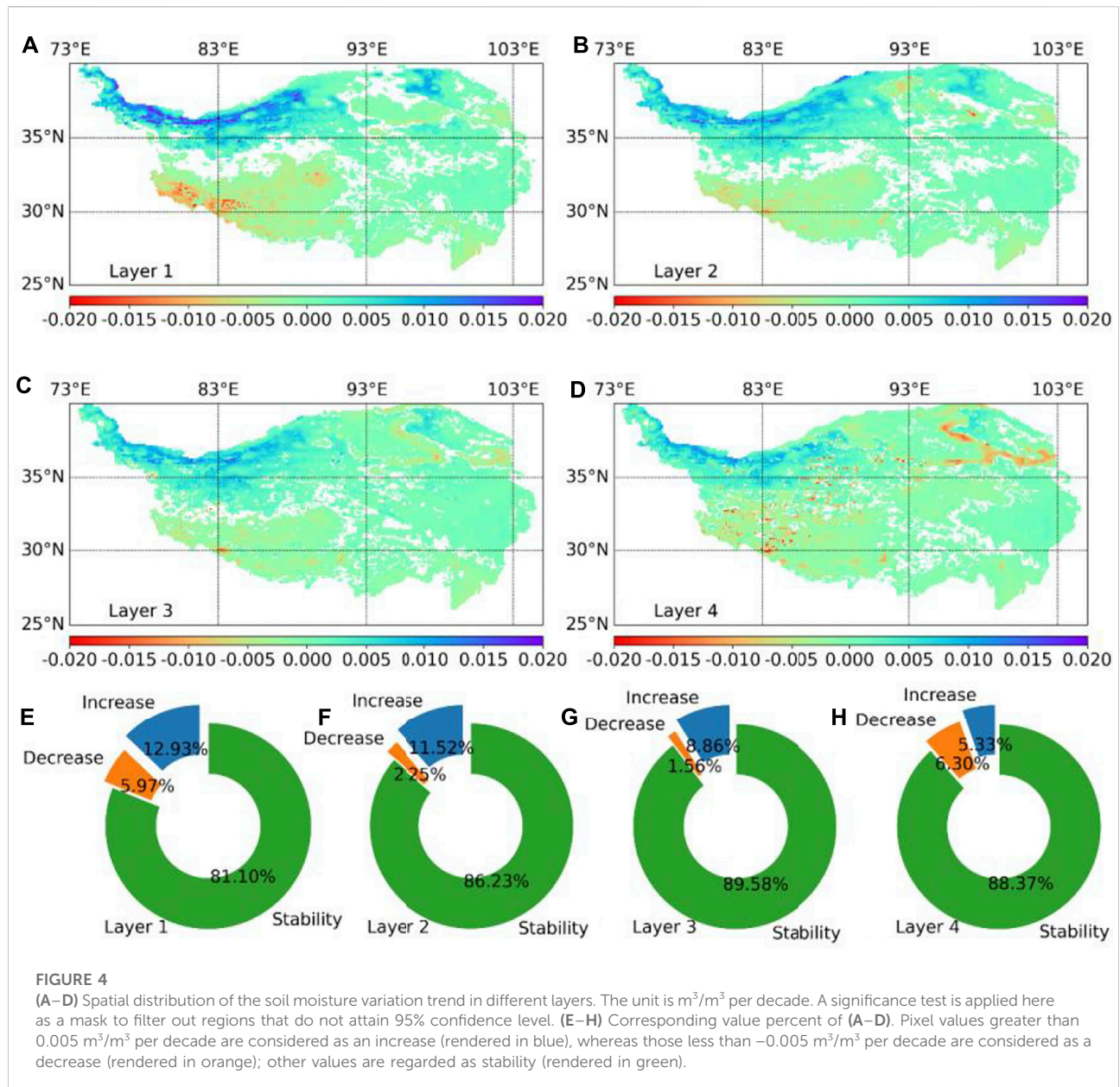
dynamic patterns across the TP (Zhang et al., 2015). The arithmetic mean of each pixel per month was calculated to express the average spatial/temporal distribution pattern of soil moisture. Similarly, the spatial/temporal variation trends were presented by calculating the pixel/month-scale rolling mean.

Additionally, a significance test with a 95% confidence level was used throughout the study to ensure the reliability and stability of our findings.

3 Results

3.1 Spatial–temporal perspective dynamic pattern analysis

As shown in Figure 2, the dry region is mainly distributed to the north and west of the TP. The northern drought area is located in the Qaidam Basin and is predominantly occupied by deserts. The western region is characterized by a severely



cold continental alpine climate and sparse precipitation. The soil moisture deficit was gradually alleviated when the depth increased. Comparatively, the southern and eastern parts of the TP remain relatively humid owing to the monsoon climate. In terms of the temporal sequence, as shown in the boxplot series (Mirzargar et al., 2014), soil moisture displays a mild seasonal rhythm cycle. Moreover, it is noteworthy that as the depth increases, the month for the maximum value emergence is delayed from June to August because it is not susceptible to surface atmospheric conditions. Similarly, the soil temperature also exhibited a delay. The corresponding soil temperature displayed evident evolution characteristics of a time series and favorably

matched the climate cycle (Figures 3E–H). The spatial distribution of soil temperature was in accordance with climatic features. In general, temperature is a critical indicator for characterizing the hydrothermal exchange intensity of the underlying surface. Nevertheless, it is difficult for temperature to play a decisive role in soil water content. For example, the average soil temperature in the north could reach $10\text{--}15^\circ\text{C}$ and in the western area could reach as low as -15 to -20°C , whereas the soil moisture showed similar drought levels despite the large temperature difference. In comparison, the soil maintains moderate humidity on the southern side of the TP, where the annual average temperature remains stable at $10\text{--}20^\circ\text{C}$.

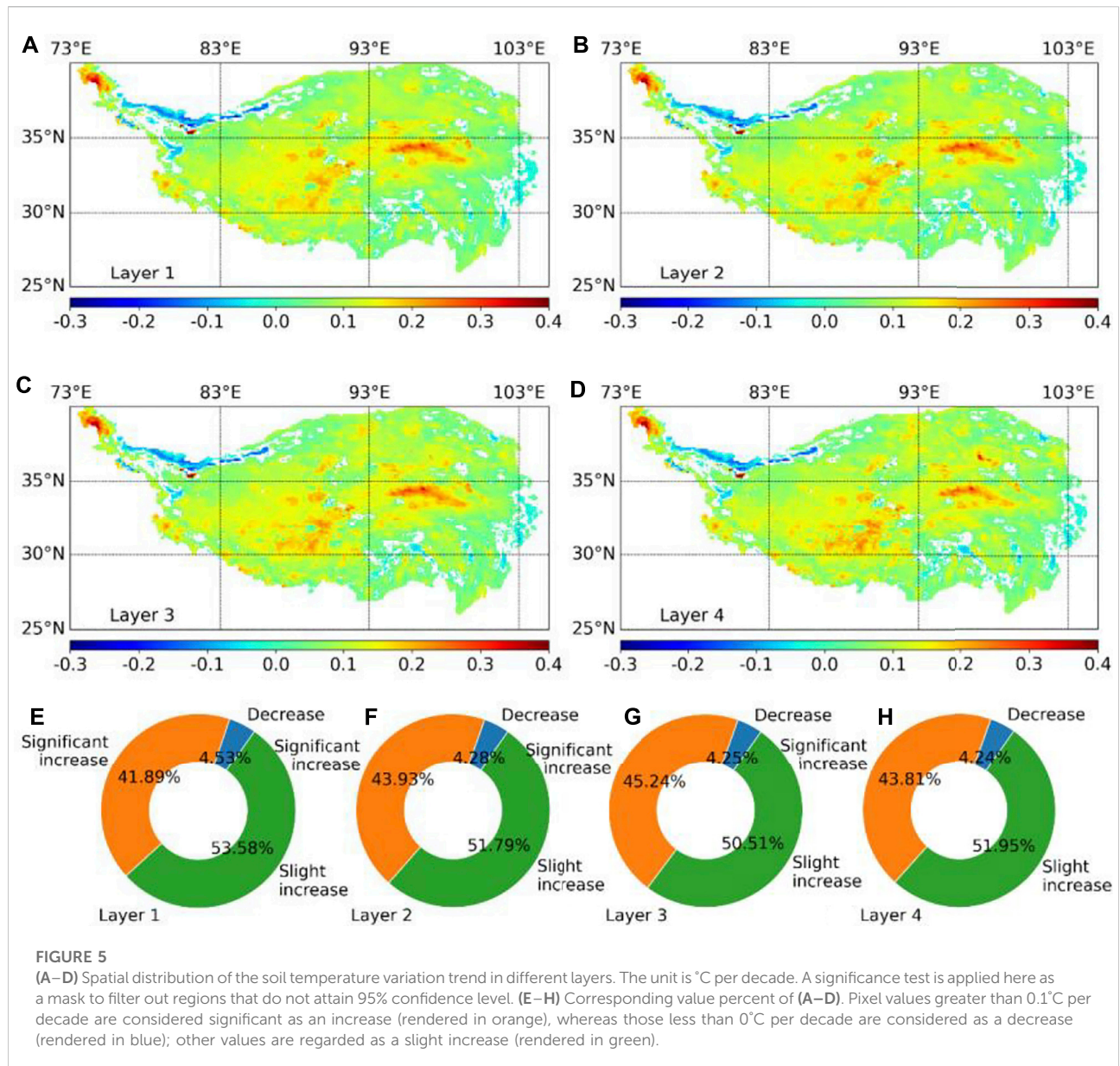


Figure 4 displays the spatial pattern of the soil moisture evolution trend at increasing depths from January 1950 to December 2020. Correspondingly, the evolution trend of the soil temperature was also examined (Figure 5) for attribution analysis. More than 80% of the TP shows stable soil moisture conditions, which are mainly distributed in the central and eastern regions. The proportion with a stable tendency was observed to rise slowly as depth increased, implying the insusceptibility of the deep soil layer. In addition, the fluctuation degree of the soil moisture series becomes notably mild from layers 1 to 4 (Figure 6), further illustrating the stability of the deep soil layer. The wetting area, accounting for 5.33%–12.93% as the soil depth decreases, is situated on the northwest

border, which belongs to the west side of the Kunlun Mountains, with an average altitude of above 5,500 m. This region, with glacier coverage exceeding 3,000 km², is one of the largest glacier areas in China (Yang et al., 1996). Glacial melt water is the source of several major rivers, including the Yangtze, Yellow, and Mekong Rivers. The drying region is sparsely distributed in the southwest, and the degree of drying is alleviated from layers 1 to 3. Overall, the soil moisture across the TP revealed a slight wetting trend from 0 to 100 cm depth during the past 70 years. However, the 100–289 cm depth soil showed an inapparent drying trend.

Under the background of global warming, the soil temperature generally rises throughout the TP at different

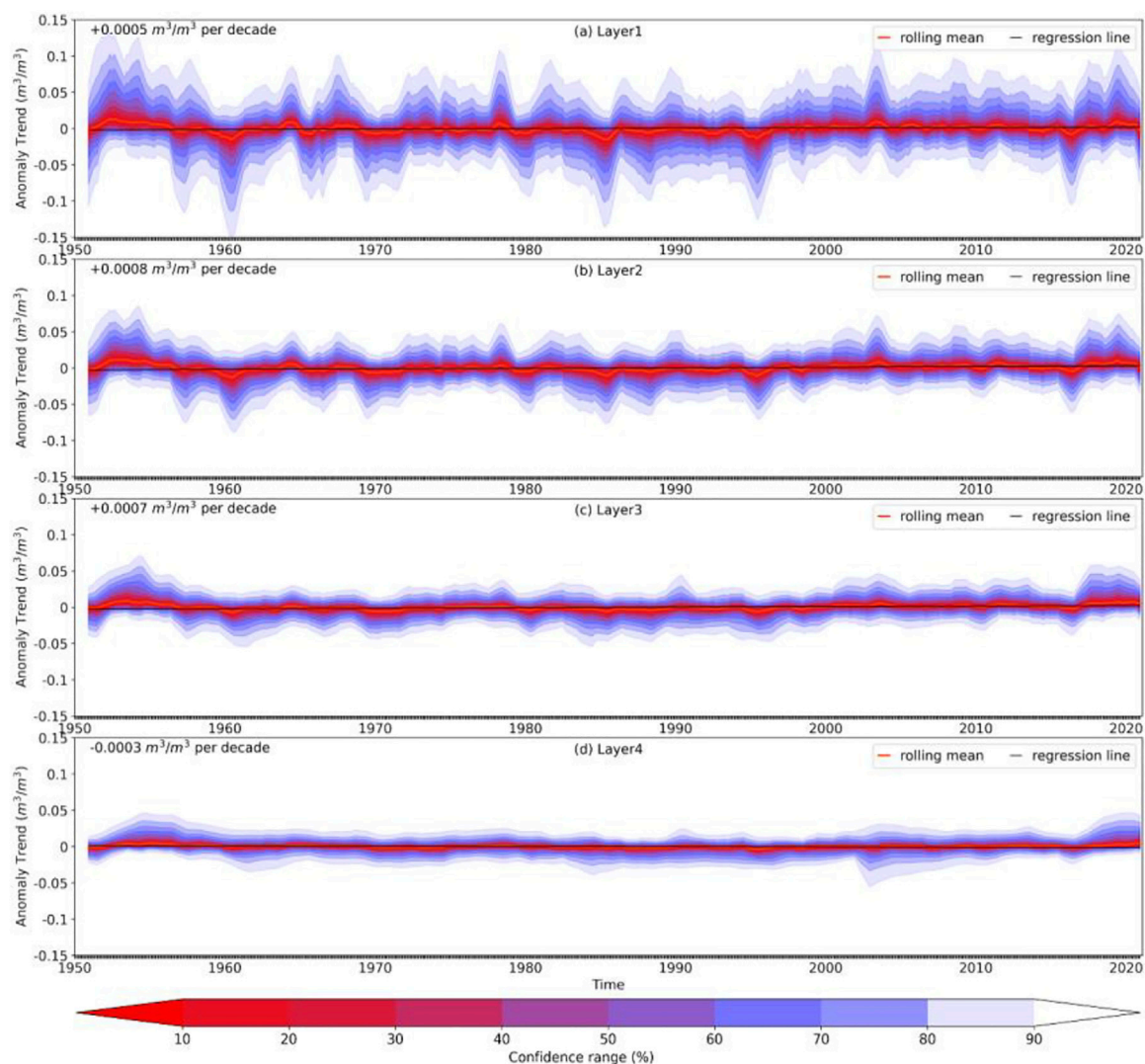


FIGURE 6

The temporal anomaly trend of soil moisture at increasing depth as presented by different layers (A–D) during 1950–2020 across the TP.

depths. The warming trend appears in more than 95% of the whole region, among which nearly half displays a significant increase of greater than 0.1°C per decade. The degree of fluctuation displayed a similar weakening trend with increasing soil depth (Figure 7). In particular, it is observed that the northwest border of the TP, namely the Karakoram, experiences a steady cooling process, which is probably induced by the declining average temperature in summer (Cogley, 2011; Gardelle et al., 2012; Azam et al., 2018). This unexpected phenomenon reflects the low sensitivity of the Karakoram to climate change. Because the overall soil moisture shows a stable or even wetting trend under warming conditions, there must be considerable water replenishment to effectively nourish soil layers. Therefore, it is meaningful that we go a step further

and learn the evolution characteristics of the soil-moisture-related climate parameters in the significantly drying and wetting regions, respectively.

3.2 Time-series analysis at wetting and drying regions

The features of temporal dynamics in regions with evident soil moisture increasing/decreasing tendencies were investigated to further advance our understanding of the variation mechanism. Water stress resulting from a soil moisture deficit directly affects vegetation growth and crop yield. However, excessive soil water can cause hypoxia, which can trigger root

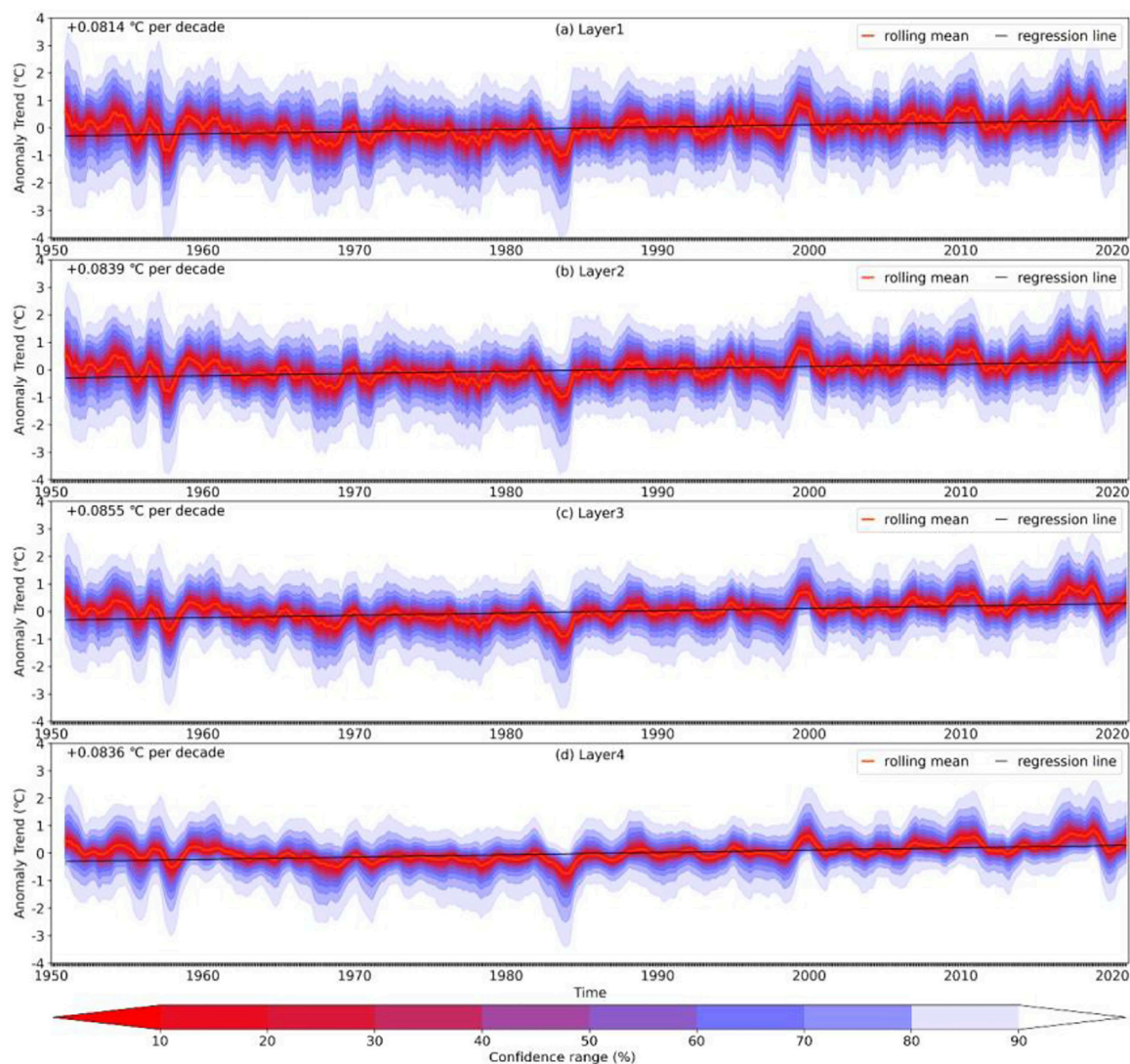


FIGURE 7

The temporal anomaly trend of soil temperature at increasing depth as presented by different layers (A–D) during 1950–2020 across the TP.

rot or even death. The wetting (pixel trend greater than $0.005 \text{ m}^3/\text{m}^3$ per decade) and drying (pixel trend less than $-0.005 \text{ m}^3/\text{m}^3$ per decade) regions were extracted and are plotted in Figures 8, 9, respectively, for analysis.

Similar to the overall pattern in the vertical dimension, both wetting and drying regions expressed gradually attenuated variation levels as the depth increased. However, in terms of soil temperature, the weakened variation trend in the vertical dimension was relatively imperceptible. It can be easily observed that the surface layer soil moisture (Figures 8A, 9A) and precipitation (Figures 8C, 9C) express homologous temporal dynamics, suggesting that the predominant driving force of precipitation is the variation in soil moisture. In comparison, snowmelt, although originating from frozen

precipitation, does not reveal dynamics analogous to precipitation.

It can be observed in Figure 8 that, accompanied by rising precipitation and snowmelt, the vertical soil moisture presents a decreasing wetting trend (from $0.0092 \text{ m}^3/\text{m}^3$ per decade to $0.004 \text{ m}^3/\text{m}^3$ per decade) as the depth increases. The decreasing wetting trend could provide indirect evidence to suggest that the supplied water is from the atmosphere and falls on the Earth's surface. It then migrates down through the soil pores layer by layer to recharge the water content of each soil layer under the combined effects of the soil molecular forces, gravity, and capillary forces with some conduction loss (Sokol et al., 2009). In terms of the drying region, as shown in Figure 9, there appears to be a significant heating up trend of

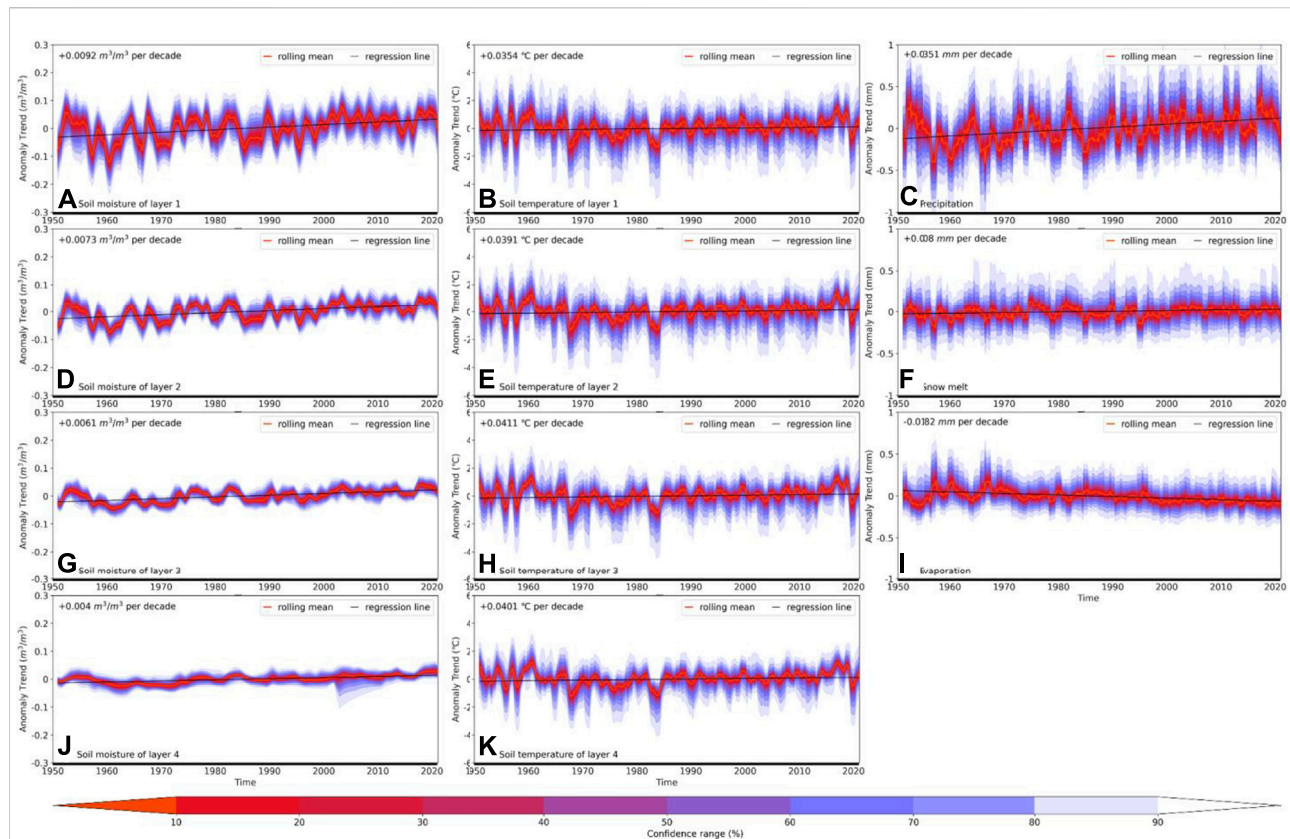


FIGURE 8

Time series of the evolutionary anomaly trends of soil moisture (A,D,G,J), soil temperature (B,E,H,K), precipitation (C), snowmelt (F), and evaporation (I) at the wetting region with confidence ranges and regression lines.

approximately 0.12°C per decade. Furthermore, precipitation and snowmelt displayed an almost identical declining trend of -0.017 mm per decade. Therefore, the soil becomes dry because of the deficiency in water nourishment and rising temperatures.

3.3 Causality investigation

Given the seemingly related temporal evolution series among soil moisture and climatic parameters across the TP, it is imperative to further explore the potential causality links, which would be of great significance in advancing our understanding of soil moisture variation mechanisms. First, density scatterplots were drawn to express the distribution correlation features across the TP in the past decades in a convenient way. As shown in Figure 10, regardless of increasing depth, the different layers of soil moisture responded consistently to climatic variables. Surprisingly, it appears that there is little correlation between temperature and soil moisture, implying that temperature could hardly be the immediate driving force in triggering soil moisture change. In

terms of water supplementation, both precipitation and snowmelt contributed remarkably to the promotion of soil moisture. Furthermore, according to the density distribution, there appears to be a threshold of approximately $0.35\text{--}0.40\text{ m}^3/\text{m}^3$, and the steadily increasing precipitation or snowmelt barely enriches the content of soil water when it attains this threshold. Moreover, although there is an obvious positive correlation between evaporation and soil moisture, the fluctuation in evaporation hardly has a material impact on soil moisture when the threshold is met. This threshold is called the saturated water content, which refers to the water content when both capillary and non-capillary pores are filled with water, and it represents the maximum water holding capacity of the soil (Vauclin et al., 1979; Schmugge et al., 1980). Additionally, the saturated moisture presents a visible vertical distribution characteristic of increasing trend from 0.35 to $0.40\text{ m}^3/\text{m}^3$ as the soil depth increases from 0 to 289 cm .

Apart from intuitive scatter correlation analysis, Granger analysis was employed to detect potential causality links between the soil moisture and climatic variables. As indicated in Figures 11A–D, there is an inconspicuous interaction between the soil moisture and temperature, as demonstrated by the extensively

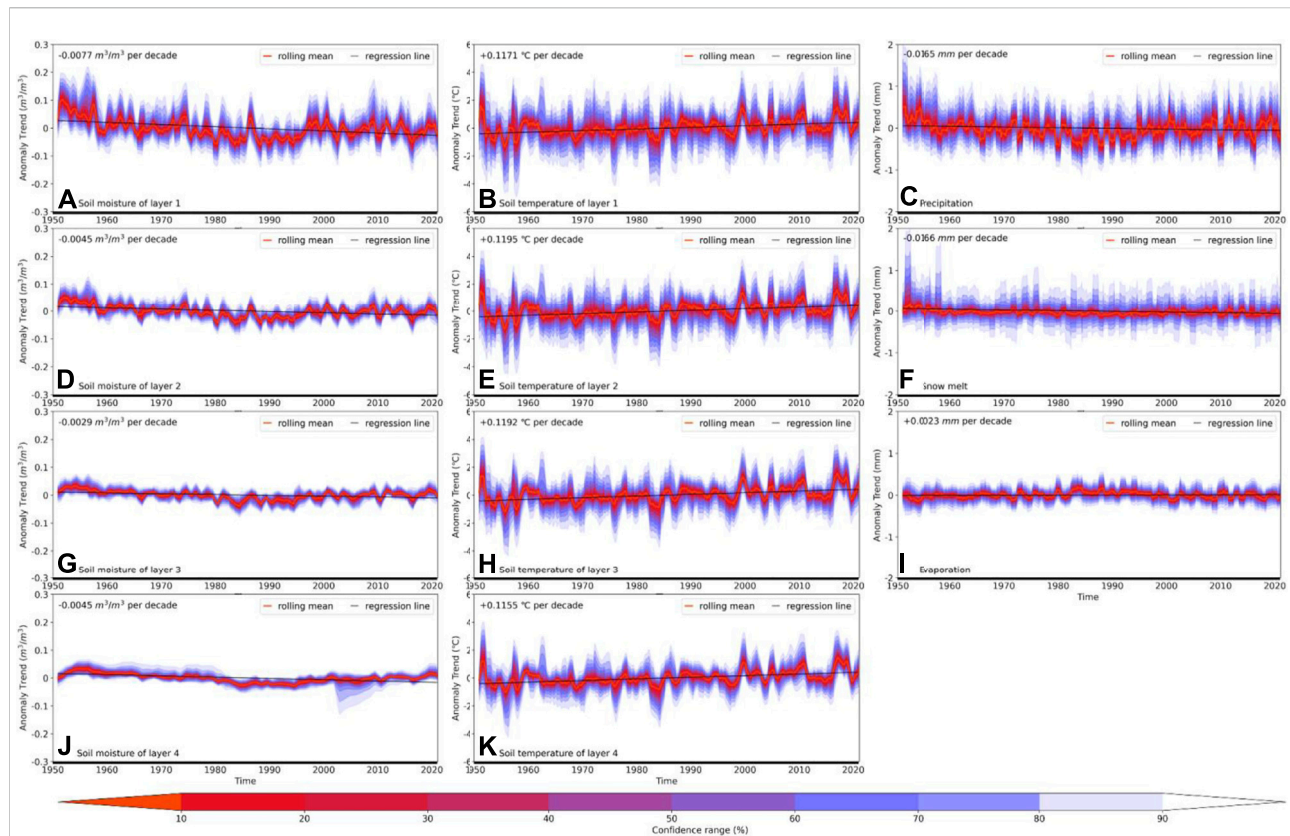


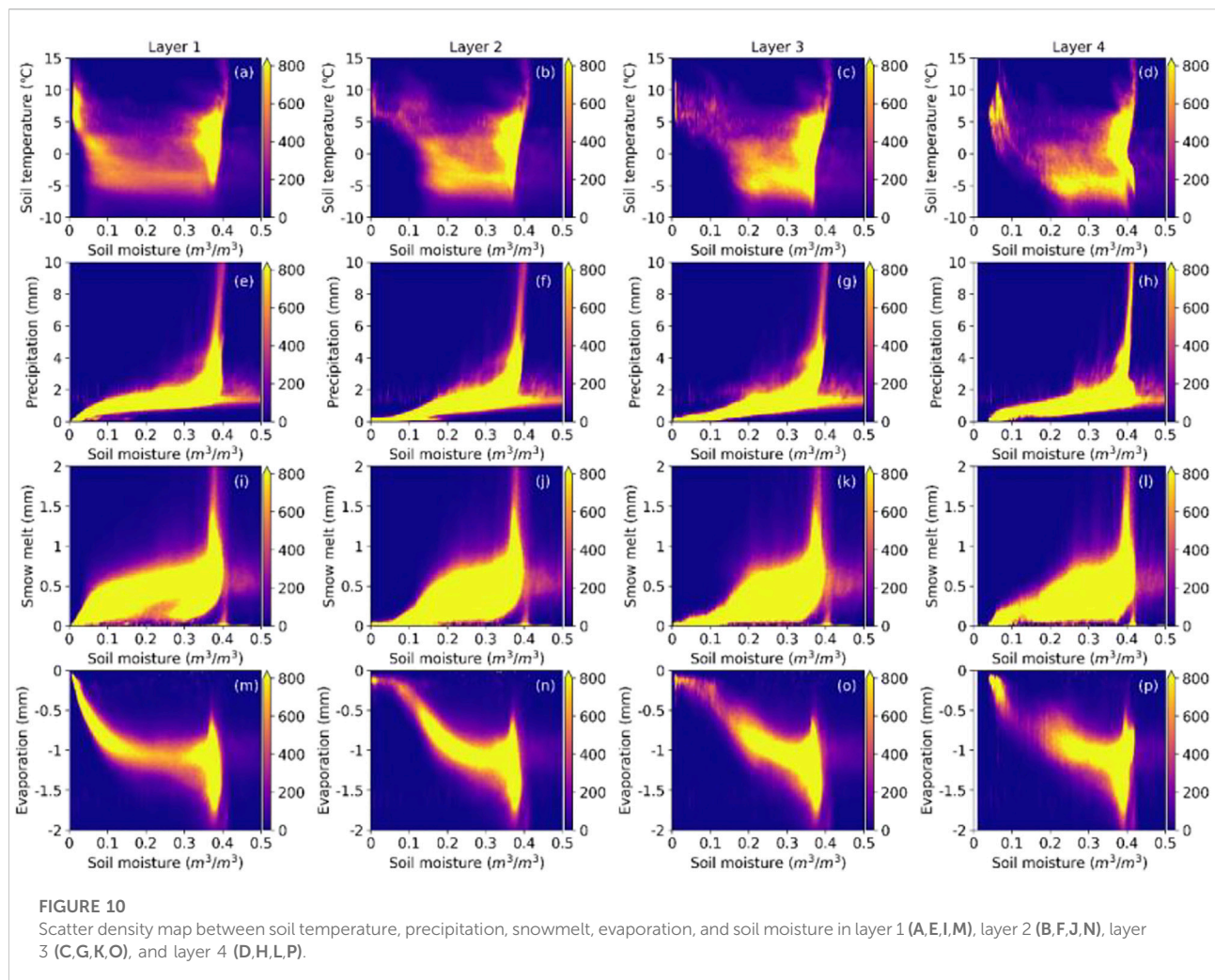
FIGURE 9

Time series of the anomaly evolutionary trends of soil moisture (A,D,G,J), soil temperature (B,E,H,K), precipitation (C), snowmelt (F), and evaporation (I) at the drying region with confidence ranges and regression lines.

distributed regions across the TP lacking a significant causal relationship. In addition, areas that are thought to have a causal link change unreasonably among different layers. However, it should be noted that the proportion of soil temperature recognized as the unidirectional cause of soil moisture experiences a noticeable increase from 15.68% to 44.80% as the depth gradually increases. This phenomenon signifies a more pronounced influence of temperature on the variation in soil moisture than on the relative surface moisture. Previous research has discovered the effectiveness of increasing the soil moisture in shrinking the soil temperature gap between daytime and nighttime, along with increasing heat storage capacity (Al-Kayssi et al., 1990). Nevertheless, it seems that the soil moisture had very limited effect on the soil temperature on a monthly scale, regardless of depth.

In terms of precipitation, as shown in Figures 11E–H, unidirectional causality relationships prevalently exist at the TP among all layers, proving the significant promotion effect of precipitation on soil moisture. Additionally, mutual correlations were observed across different layers despite a certain degree of fluctuation, providing substantial evidence for the feedback of soil moisture to precipitation on a

monthly scale. This feedback is mainly expressed by the 0–100 cm depth soil moisture and becomes weak for the fourth layer at 100–289 cm depth. Owing to the temperature features of the dominant plateau climate across the TP, there could be a lengthy freezing season throughout the year. Precipitation in the form of snow barely nourished the soil when the temperature remained below freezing point throughout the day. However, snow is a non-ignorable water supplement that has great potential for nourishing the soil. Few studies have systematically explored its positive effect on soil moisture; thus, preliminarily causality analysis is necessary for disclosing the probable correlation. Snowmelt, derived from the combined action of accumulated snow and the temperature climbing above freezing point, is thought to be effective in elevating soil moisture. Figures 11I–L explicitly show that snowmelt plays an increasingly vital role in nourishing the soil as the depth increases. Snowmelt is recognized to have a statistically significant effect on the current value of soil moisture and is thought to be the Granger cause of soil moisture. Accordingly, the significant proportion, including both the yellow and red regions, consistently increased from 70.02% to 84.80% as the soil depth increased. Evaporation, which is a



crucial method of soil water loss, is found to have bidirectional causality relationships with soil moisture across different layers, indicating tight mutual interaction, which is in accordance with previous studies (Krakauer et al., 2010; Vargas Zeppetello et al., 2019). The bidirectional causality gradually turns to unidirectional causality as the depth increases, signifying that evaporation is capable of affecting soil moisture regardless of depth, whereas the influence of soil moisture on evaporation decreases with the deepening of the soil layer from 0 to 289 cm.

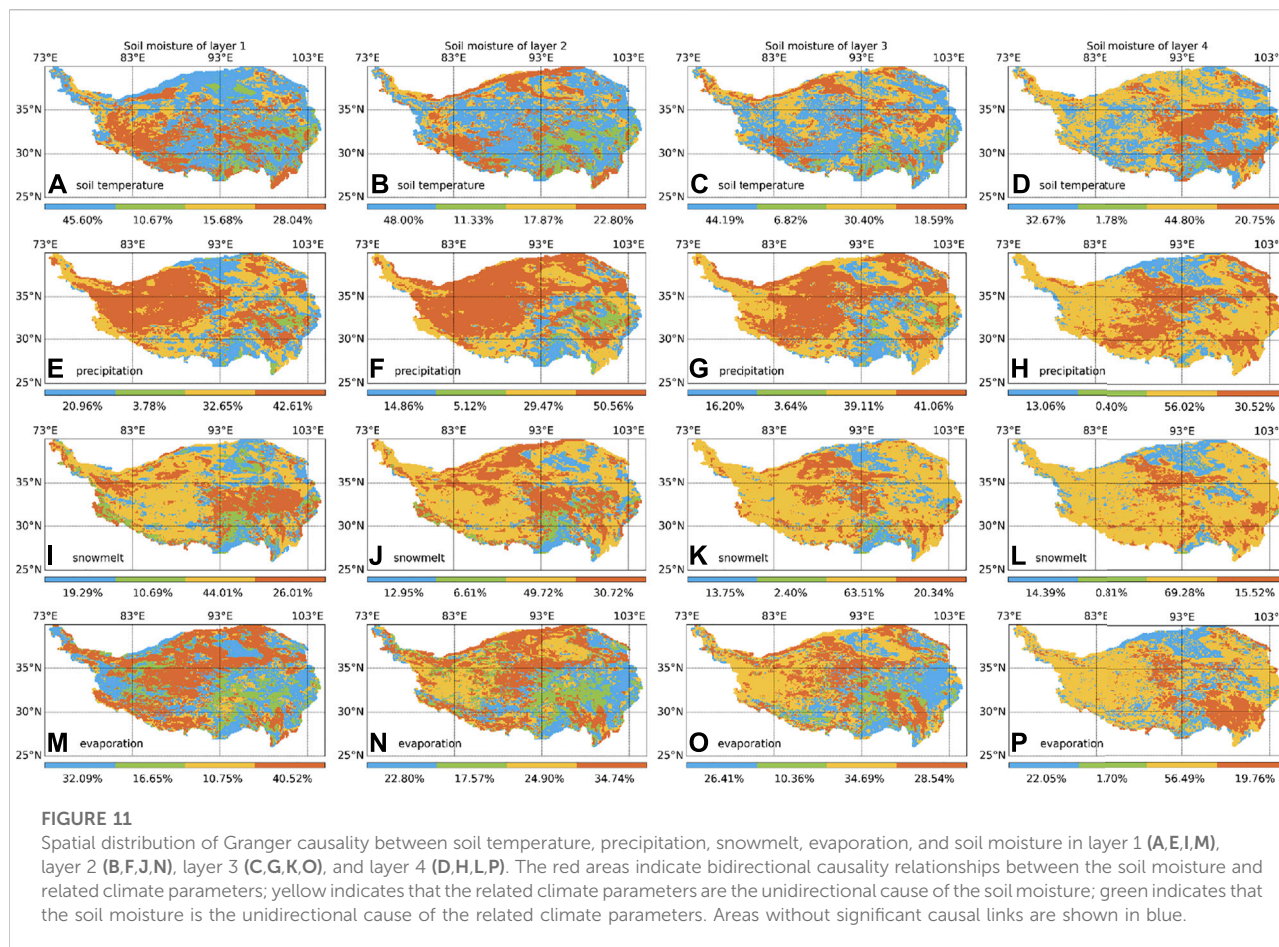
4 Discussion

Soil moisture, as a fundamental surface hydrological variable, is both an active participant and sensitive responder in various hydrological processes (Dobriyal et al., 2012; Peng et al., 2017; Deng et al., 2020a). The distribution and dynamics of soil moisture can be an effective indicator of regional climate evolution characteristics (Seneviratne et al., 2010; Zhang et al.,

2019; Deng et al., 2020b). The TP plays a crucial role in climate change in the Northern Hemisphere. Exploring the variability features of soil moisture across the TP is important to advancing our understanding of climate change. Thus, this study systematically and comprehensively investigated the variation trend of the soil moisture across the TP from a four-dimensional perspective (time, longitude, latitude, and depth) on a monthly scale during 1950–2020. The soil moisture and related climate variable information was retrieved from the ERA5-Land products, which have been widely evaluated and applied since inception (Hersbach et al., 2020; Muñoz-Sabater et al., 2021; Wu et al., 2021; Xu et al., 2022).

4.1 Driving mechanism of soil moisture variability

Our investigation revealed that the spatial–temporal series of the soil moisture remained roughly stable in the context of a prevalent



warming trend, implying sufficient water supplementation to consistently nourish the soil. Previous findings show a positive correlation between the trends of soil moisture and precipitation across the TP, which means that the wetting of the soil is mainly caused by increasing precipitation. Deng et al. (2020b) investigated the responses of soil moisture to regional climate change over three river source regions at the TP. They discovered a significant positive correlation between the soil moisture and precipitation in most case-study regions. Liu et al. (2013) analyzed the spatial distribution and dynamic variation of remotely sensed surface soil moisture across the TP and found a favorable correlation between the spatial-temporal evolution pattern of the soil moisture and precipitation. In addition, the fluctuation patterns of both moisture and temperature obviously declined as the soil depth increased, demonstrating the insensitivity of deep-layer soil to momentary atmospheric dynamics. Increased soil depth resulted in lower variability, which is in accordance with the findings of previous studies on the characteristics of surface and root-zone soil. Through a case study in France, Albergel et al. (2008) disclosed that the soil water indices derived from the surface layer agreed well with those from the root-zone layer. Paris Anguela et al. (2008) investigated the dynamics of surface and root-zone soil moisture

in France and shed light on the high variability of surface soil moisture resulting from atmospheric conditions and the stability of root-zone moisture. Meng et al. (2022) also discovered decreasing interannual fluctuations in deep-layer soil moisture by assessing the spatiotemporal variability of soil moisture across the Mongolian Plateau from 1982 to 2019.

Through spatial statistical distribution, it was observed that the significantly wetted region was mainly concentrated at the northwest border, whereas the drying region was sparsely distributed across the TP. It was observed that the wetting region was accompanied by a notable increase in precipitation, snowmelt, temperature, and evaporation. The drying region is characterized by evident warming, as well as slightly reduced precipitation, snowmelt, and evaporation. Moreover, we noticed that the wetting region belongs to the Karakoram, where the glacier experiences a slight mass gain and the temperature is steadily cooling (Cogley, 2011; Gardelle et al., 2012; Azam et al., 2018). According to Pascolini-Campbell et al. (2021), global land evapotranspiration increased by 10% during 2003–2019, mainly driven by increasing temperatures, and precipitation was increasingly partitioned into evapotranspiration rather than runoff. Jung et al. (2010) suggested that soil moisture limitation is the primary driver that restricts the rate of land

evapotranspiration. Deng et al. (2020a) analyzed the variation trend of global surface soil moisture from 1979 to 2017. Temperature and precipitation are the two predominant factors that lead to variation in the soil moisture across the TP. Additionally, a reasonably good agreement between the surface soil moisture and precipitation has been observed in tropical and temperate climate zones (Wagner et al., 2003). However, Dorigo et al. (2012) revealed that even though precipitation is the main driver of variations in soil moisture, its impact could be quite different owing to the combined influences of evaporation, soil type, irradiation, vegetation, and topography. In addition to land climate parameters, the sea can also transmit a far-reaching influence on soil moisture. Sheffield and Wood (2008) demonstrated that the leading modes of soil moisture variability are closely associated with sea surface temperatures.

The causality between multi-layer soil moisture and climate variables was investigated through correlation and Granger analysis. Instead of soil temperature, precipitation and snowmelt have been proven to be the main drivers in the variation trend of soil moisture, and the soil moisture also provides notable feedback to these supplements. Under the global warming scenario, precipitation across the TP continuously increases and is driven by the South Asian monsoon (Wang et al., 2021). A previous study illustrated the predominant positive feedback of the surface soil moisture to precipitation and the non-negligible negative feedback in wet and dry regions across the globe (Yang et al., 2018). According to an investigation of soil moisture–precipitation feedback across the United States, positive feedback generally appears in arid regions, whereas relatively humid regions tend to display negative feedback (Tuttle and Salvucci, 2016). In addition to the significant differences resulting from different case-study areas, feedback also varies in terms of different resolutions. The 25-km grid Consortium for Small-Scale Modeling Model in Climate Mode (CCLM) simulations basically maintain strong positive soil moisture–precipitation feedback, whereas the 2.2-km resolution expresses dominantly negative feedback over the alpine regions (Hohenegger et al., 2009). In general, the specific feedback of soil moisture to precipitation varies unpredictably based on hydrothermal conditions, regions, and scales. Additionally, through Granger analysis, we found that, although the feedback of soil moisture to evaporation gradually decreased, the impact of evaporation on soil moisture continuously increased as the depth increased. The soil moisture interacts with the atmosphere primarily through dynamic surface water and energy balances (Delworth and Manabe, 1988). It is widely acknowledged that evaporation is limited by the available soil moisture in dry regions and the temperature in humid regions (Vargas Zeppetello et al., 2019). The mutual feedback mechanism between evaporation and multi-layer soil moisture has been used to estimate global land evaporation and root-zone soil moisture (Martens et al., 2017).

4.2 Uncertainty factors

Apart from the abovementioned factors, surface hydrological evolution phenomena such as glacier melt, permafrost thaw, and lake expansion, induced by a warming climate, could all boost the increase in soil water content. Many other factors (i.e., soil texture, groundwater depth, and vegetation) could also affect the spatial and temporal distribution patterns of the soil moisture. This study is expected to advance the understanding of the effect of climate change across the TP during 1950–2020 from the perspective of soil moisture. Although we obtained some significant discoveries through the investigation, it is necessary to discuss the possible existence of uncertainty in order to maintain rigor.

Notably, human activities could play a non-negligible role in triggering variations in soil moisture. The ever-increasing human water withdrawal significantly causes stress on the sustainable water resource supply, which potentially affects the pattern of soil moisture. The population density of the TP is quite low because the plateau climate is not suitable for human living. However, it is still critical to quantitatively explore the influence of human water consumption on the soil moisture variability across the TP in future studies.

The analysis results were mainly derived by using ERA5-Land products, which could inevitably have both spatially and temporally varied biases in terms of the complex land surface properties. Numerous studies have evaluated the accuracy of ERA5-Land products and demonstrated their good performance in fitting the dynamics of ground observations (Li et al., 2020; Muñoz-Sabater et al., 2021; Xu et al., 2022). However, errors occasionally occur in plateau mountain climate zones. Additionally, because the multi-depth soil moisture and climatic parameters used in this study are all from ERA5-Land products, inherent uniformity inevitably exists among these datasets. Future work with diverse data sources that are independent of each other is needed to investigate the correlation between soil moisture and climatic factors with more objectivity.

As a classical measurement method, the Granger causality test has been widely accepted and used in Earth system science studies. However, this method may not be sufficiently rigorous to define a temporally related phenomenon as a causality. Therefore, this study merely conducted a causality analysis to attempt to explain the reason for the variations in soil moisture.

5 Conclusion

In summary, this study systematically and comprehensively investigated the evolutionary characteristics of soil moisture from a four-dimensional (time, longitude, latitude, and depth) perspective across the TP during 1950–2020. It was found that, based on the interaction of climate warming and increasing precipitation, soil moisture across the TP had a slight wetting trend at a depth of

0–100 cm over the past 70 years. Moreover, there is sufficient water supply from precipitation and a mild soil temperature increase in the wetting region (variation trend greater than $0.005 \text{ m}^3/\text{m}^3$ per decade). In comparison, the drying region (variation trend of less than $-0.005 \text{ m}^3/\text{m}^3$ per decade) is accompanied by a noteworthy warming tendency and falling precipitation. In terms of vertical variation features, the temporal dynamic fluctuation of the soil moisture evidently decreases as the depth increases, suggesting high sensitivity of near-surface-layer soil moisture to atmospheric conditions. Through correlation and Granger causality analysis, precipitation and snowmelt were preliminarily proved to be the dominant drivers causing the spatial and temporal variations in the soil moisture. Bidirectional causality relationships were found between soil moisture and these two parameters. Evaporation changes then occurred owing to the joint efforts of rising temperature and water supplementation. This study explored the spatial-temporal fluctuation of the evolutionary characteristics of soil moisture, which is expected to boost our understanding of soil moisture dynamics under the conditions of climate change across the TP. With consideration of the intrinsic inhomogeneity of soil moisture, more work is needed to further clarify the mechanism underlying soil moisture variations.

Data availability statement

The original contributions presented in the study are included in the article/supplementary material; further inquiries can be directed to the corresponding author.

Author contributions

Conceptualization, methodology, writing—original draft preparation, YL; Writing—review and editing, supervision, funding acquisition, YY.

References

- Al-Kayssi, A. W., Al-Karaghoul, A., Hasson, A., and Beker, S. (1990). Influence of soil moisture content on soil temperature and heat storage under greenhouse conditions. *J. Agric. Eng. Res.* 45, 241–252. doi:10.1016/s0021-8634(05)80152-0
- Albergel, C., Rudiger, C., Pellarin, T., Calvet, J. C., Fritz, N., Froissard, F., et al. (2008). From near-surface to root-zone soil moisture using an exponential filter: an assessment of the method based on *in-situ* observations and model simulations. *Hydrol. Earth Syst. Sci.* 5 (3), 1323–1337. doi:10.5194/hess-12-1323-2008
- Attema, E. P. W., Duchossois, G., and Kohlhammer, G. (1998). “ERS-1/2 SAR land applications: overview and main results,” in *IEEE international geoscience & Remote sensing symposium*. Seattle, WA: IEEE.
- Azam, M. F., Wagnon, P., Berthier, E., Vincent, C., Fujita, K., and Kargel, J. S. (2018). Review of the status and mass changes of himalayan-karakoram glaciers. *J. Glaciol.* 64 (243), 61–74. doi:10.1017/jog.2017.86
- Bai, X., He, B., Li, X., Zeng, J., Wang, X., Wang, Z., et al. (2017). First assessment of Sentinel-1A data for surface soil moisture estimations using a coupled water cloud model and advanced integral equation model over the tibetan plateau. *Remote Sens.* 9 (7), 714. doi:10.3390/rs9070714
- Bartalis, Z., Wagner, W., Naeimi, V., Hasenauer, S., Scipal, K., Bonekamp, H., et al. (2007). Initial soil moisture retrievals from the METOP-A advanced scatterometer (ASCAT). *Geophys. Res. Lett.* 34 (20), L20401. doi:10.1029/2007gl031088
- Bontemps, S., Defourny, P., Radoux, J., Van Bogaert, E., Lamarche, C., Achard, F., et al. (2013). “Consistent global land cover maps for climate modelling communities: Current achievements of the ESA’s land cover CCI,” in *Proceedings of the ESA living planet symposium* (Edinburgh).
- Bradley, D., Brambora, C., Wong, M. E., Miles, L., Durachka, D., Farmer, B., et al. (2010). “Radio-frequency interference (RFI) mitigation for the soil moisture active/passive (SMAP) radiometer,” in *Geoscience and Remote sensing symposium*. Honolulu, Hawaii: IEEE.
- Chen, T., de Jeu, R., Liu, Y., van der Werf, G., and Dolman, A. (2014). Using satellite based soil moisture to quantify the water driven variability in ndvi: a case

Funding

This work was supported in part by the Special Program of Network Security and Informatization of the Chinese Academy of Sciences (CAS-WX2021SF-0106-03), in part by the Second Tibetan Plateau Scientific Expedition and Research Program (2019QZKK09), in part by the National Natural Science Foundation of China under Grant 42101475, in part by the Geographic Resources and Ecology Knowledge Service System of the China Knowledge Center for Engineering Sciences and Technology under Grant CKCEST-2015-1-4, in part by the National Earth System Science Data Center (<http://www.geodata.cn/>), and in part by the Guangzhou Science and Technology Plan Program (202102020676).

Acknowledgments

We thank the reviewers for their very insightful comments on this article.

Conflict of interest

The authors declare that the research was conducted in the absence of any commercial or financial relationships that could be construed as a potential conflict of interest.

Publisher’s note

All claims expressed in this article are solely those of the authors and do not necessarily represent those of their affiliated organizations, or those of the publisher, the editors, and the reviewers. Any product that may be evaluated in this article, or claim that may be made by its manufacturer, is not guaranteed or endorsed by the publisher.

- study over mainland australia. *Remote Sens. Environ.* 140 (140), 330–338. doi:10.1016/j.rse.2013.08.022
- Chen, Y., Yang, K., Qin, J., Cui, Q., Lu, H., La, Z., et al. (2017). Evaluation of SMAP, SMOS, and AMSR2 soil moisture retrievals against observations from two networks on the tibetan plateau. *J. Geophys. Res. Atmos.* 122 (11), 5780–5792. doi:10.1002/2016jd026388
- Cheng, M., Zhong, L., Ma, Y., Zou, M., Ge, N., Wang, X., et al. (2019). A study on the assessment of multi-source satellite soil moisture products and reanalysis data for the Tibetan Plateau. *Remote Sens. (Basel)*. 11 (10), 1196. doi:10.3390/rs11101196
- Cogley, J. G. (2011). Present and future states of himalaya and karakoram glaciers. *Ann. Glaciol.* 52 (59), 69–73. doi:10.3189/172756411799096277
- Dee, D. P., Uppala, S. M., Simmons, A. J., Berrisford, P., Poli, P., Kobayashi, S., et al. (2011). The ERA-Interim reanalysis: configuration and performance of the data assimilation system. *Q. J. R. Meteorological Soc.* 137 (656), 553–597.
- Delworth, T. L., and Manabe, S. (1988). The influence of potential evaporation on the variabilities of simulated soil wetness and climate. *J. Clim.* 1 (5), 523–547. doi:10.1175/1520-0442(1988)001<0523:tiopeo>2.0.co;2
- Deng, M., Meng, X., Li, Z., Lyv, Y., Lei, H., Zhao, L., et al. (2020). Responses of soil moisture to regional climate change over the three rivers source region on the tibetan plateau. *Int. J. Climatol.* 40 (4), 2403–2417. doi:10.1002/joc.6341
- Deng, Y., Wang, S., Bai, X., Luo, G., Wu, L., Cao, Y., et al. (2020). Variation trend of global soil moisture and its cause analysis. *Ecol. Indic.* 110, 105939. doi:10.1016/j.ecolind.2019.105939
- Dobriyal, P., Qureshi, A., Badola, R., and Hussain, S. A. (2012). A review of the methods available for estimating soil moisture and its implications for water resource management. *J. Hydrology* 458–459, 110–117. doi:10.1016/j.jhydrol.2012.06.021
- Dorigo, W. A., Wagner, W., Hohensinn, R., Hahn, S., Paulik, C., Xaver, A., et al. (2011). The international soil moisture Network: a data hosting facility for global *in situ* soil moisture measurements. *Hydrol. Earth Syst. Sci.* 15 (5), 1675–1698. doi:10.5194/hess-15-1675-2011
- Dorigo, W., de Jeu, R., Chung, D., Parinussa, R., Liu, Y., Wagner, W., et al. (2012). Evaluating global trends (1988–2010) in harmonized multi-satellite surface soil moisture. *Geophys. Res. Lett.* 39 (18). doi:10.1029/2012gl052988
- Dorigo, W., and De Jeu, R. (2016). Satellite soil moisture for advancing our understanding of earth system processes and climate change. *Int. J. Appl. Earth Observation Geoinformation* 48, 1–4. doi:10.1016/j.jag.2016.02.007
- Dorigo, W., Wagner, W., Albergel, C., Albrecht, F., Balsamo, G., Brocca, L., et al. (2017). ESA CCI soil moisture for improved earth system understanding: state-of-the-art and future directions. *Remote Sens. Environ.* 203, 185–215. doi:10.1016/j.rse.2017.07.001
- Dutta, A. (2001). Telecommunications and economic activity: an analysis of granger causality. *J. Manag. Inf. Syst.* 17 (4), 71–95.
- Ek, M., Mitchell, K. E., Lin, Y., Rogers, E., Grunmann, P., Koren, V., et al. (2003). Implementation of Noah land surface model advances in the national centers for environmental prediction operational mesoscale Eta model. *J. Geophys. Res.* 108 (D22), 2002JD003296. doi:10.1029/2002jd003296
- Farr, T. G., Rosen, P. A., Caro, E., Crippen, R., Duren, R., Hensley, S., et al. (2003). *The shuttle radar topography mission*. 45. doi:10.1029/2005RG000183
- Flanagan, L. B., and Johnson, B. G. (2005). Interacting effects of temperature, soil moisture and plant biomass production on ecosystem respiration in a northern temperate grassland. *Agric. For. Meteorology* 130 (3–4), 237–253. doi:10.1016/j.agrformet.2005.04.002
- Gardelle, J., Berthier, E., and Arnaud, Y. (2012). Slight mass gain of karakoram glaciers in the early twenty-first century. *Nat. Geosci.* 5 (5), 322–325. doi:10.1038/ngeo1450
- Gasse, F., Arnold, M., Fontes, J. C., Fort, M., Gibert, E., Huc, A., et al. (1991). A 13,000-year climate record from western tibet. *Nature* 353 (6346), 742–745. doi:10.1038/353742a0
- Gelaro, R., McCarty, W., Suarez, M. J., Todling, R., Molod, A., Takacs, L., et al. (2017). The modern-era retrospective analysis for research and applications, version 2 (MERRA-2). *J. Clim.* 30 (14), 5419–5454. doi:10.1175/jcli-d-16-0758.1
- Granger, C. W. (1969). Investigating causal relations by econometric models and cross-spectral methods. *Econometrica* 37, 424–438. doi:10.2307/1912791
- Gruber, A., Scanlon, T., van der Schalie, R., Wagner, W., and Dorigo, W. (2019). Evolution of the ESA CCI Soil Moisture climate data records and their underlying merging methodology. *Earth Syst. Sci. Data* 11 (2), 717–739. doi:10.5194/essd-11-717-2019
- Hersbach, H., Bell, B., Berrisford, P., Hirahara, S., Horanyi, A., Munoz-Sabater, J., et al. (2020). The ERA5 global reanalysis. *Q. J. R. Meteorol. Soc.* 146 (730), 1999–2049. doi:10.1002/qj.3803
- Hiemstra, C., and Jones, J. D. J. T. J. o. F. (1994). Testing for linear and nonlinear granger causality in the stock price-volume relation. *J. Finance* 49 (5), 1639–1664. doi:10.1111/j.1540-6261.1994.tb04776.x
- Hohenegger, C., Brockhaus, P., Bretherton, C. S., and Schar, C. (2009). The soil moisture–precipitation feedback in simulations with explicit and parameterized convection. *J. Clim.* 22 (19), 5003–5020. doi:10.1175/2009jcli2604.1
- Jiang, B., Liang, S., and Yuan, W. (2015). Observational evidence for impacts of vegetation change on local surface climate over northern china using the granger causality test. *J. Geophys. Res. Biogeosci.* 120 (1), 1–12. doi:10.1002/2014jg002741
- Jung, M., Reichstein, M., Ciais, P., Seneviratne, S. I., Sheffield, J., Goulden, M. L., et al. (2010). Recent decline in the global land evapotranspiration trend due to limited moisture supply. *Nature* 467 (7318), 951–954. doi:10.1038/nature09396
- Kobayashi, S., Ota, Y., Harada, Y., Ebata, A., Mori, M., Onoda, H., et al. (2015). The JRA-55 reanalysis: general specifications and basic characteristics. *J. Meteorological Soc. Jpn.* 93 (1), 5–48. doi:10.2151/jmsj.2015-001
- Kónya, L. (2006). Exports and growth: granger causality analysis on OECD countries with a panel data approach. *Econ. Model.* 23 (6), 978–992. doi:10.1016/j.econmod.2006.04.008
- Koster, R. D., Dirmeyer, P. A., Guo, Z., Bonan, G., Chan, E., Cox, P., et al. (2004). Regions of strong coupling between soil moisture and precipitation. *Science* 305 (5687), 1138–1140. doi:10.1126/science.1100217
- Krakauer, N., Cook, B., and Puma, M. (2010). Contribution of soil moisture feedback to hydroclimatic variability. *Hydrol. Earth Syst. Sci.* 14 (3), 505–520. doi:10.5194/hess-14-505-2010
- Lakshmi, V., Piechota, T., Narayan, U., and Tang, C. (2004). Soil moisture as an indicator of weather extremes. *Geophys. Res. Lett.* 31 (11), 1–4. doi:10.1029/2004gl019930
- Li, C., Lu, H., Yang, K., Han, M., Wright, J., Chen, Y., et al. (2018). The evaluation of SMAP enhanced soil moisture products using high-resolution model simulations and *in-situ* observations on the Tibetan plateau. *Remote Sens.* 10 (4), 535. doi:10.3390/rs10040535
- Li, M., Wu, P., and Ma, Z. (2020). A comprehensive evaluation of soil moisture and soil temperature from third-generation atmospheric and land reanalysis data sets. *Int. J. Climatol.* 40 (13), 5744–5766. doi:10.1002/joc.6549
- Li, M., Wu, P., Ma, Z., Pan, Z., Lv, M., Yang, Q., et al. (2022). The increasing role of vegetation transpiration in soil moisture loss across China under global warming. *J. Hydrometeorol.* 23 (2), 253–274. doi:10.1175/jhm-d-21-0132.1
- Liu, Q., Du, J., Shi, J., and Jiang, L. (2013). Analysis of spatial distribution and multi-year trend of the remotely sensed soil moisture on the tibetan plateau. *Sci. China Earth Sci.* 56 (12), 2173–2185. doi:10.1007/s11430-013-4700-8
- Mahto, S. S., and Mishra, V. (2019). Does ERA-5 outperform other reanalysis products for hydrologic applications in India? *J. Geophys. Res. Atmos.* 124 (16), 9423–9441. doi:10.1029/2019jd031155
- Martens, B., Miralles, D. G., Lievens, H., van der Schalie, R., de Jeu, R. A. M., Fernandez-Prieto, D., et al. (2017). GLEAM v3: satellite-based land evaporation and root-zone soil moisture. *Geosci. Model Dev.* 10 (5), 1903–1925. doi:10.5194/gmd-10-1903-2017
- Meng, F., Luo, M., Sa, C., Wang, M., and Bao, Y. (2022). Quantitative assessment of the effects of climate, vegetation, soil and groundwater on soil moisture spatiotemporal variability in the mongolian plateau. *Sci. Total Environ.* 809, 152198. doi:10.1016/j.scitotenv.2021.152198
- Mirzargar, M., Whitaker, R. T., and Kirby, R. M. (2014). Curve boxplot: generalization of boxplot for ensembles of curves. *IEEE Trans. Vis. Comput. Graph.* 20 (12), 2654–2663. doi:10.1109/tvcg.2014.2346455
- Muñoz-Sabater, J., Dutra, E., Agustí-Panareda, A., Albergel, C., Arduini, G., Balsamo, G., et al. (2021). ERA5-Land: a state-of-the-art global reanalysis dataset for land applications. *Earth Syst. Sci. Data* 13 (9), 4349–4383. doi:10.5194/essd-13-4349-2021
- Njoku, E. G., Jackson, T., Lakshmi, V., Chan, T., and Nghiem, S. (2003). Soil moisture retrieval from AMSR-E. *IEEE Trans. Geosci. Remote Sens.* 41 (2), 215–229. doi:10.1109/tgrs.2002.808243
- Olauson, J. J. R. e. (2018). ERA5: The new champion of wind power modelling. 126, 322. doi:10.1016/j.renene.2018.03.056
- Papagiannopoulou, C., Miralles, D. G., Decubber, S., Demuzere, M., Verhoest, N. E. C., Dorigo, W. A., et al. (2017). A non-linear Granger-causality framework to investigate climate–vegetation dynamics. *Geosci. Model Dev.* 10 (5), 1945–1960. doi:10.5194/gmd-10-1945-2017
- Paris Anguela, T., Zribi, M., Hasenauer, S., Habets, F., and Loumagne, C. (2008). Analysis of surface and root-zone soil moisture dynamics with ERS scatterometer and the hydrometeorological model SAFRAN-ISBA-MODCOU at grand morin watershed (France). *Hydrol. Earth Syst. Sci.* 12 (6), 1415–1424. doi:10.5194/hess-12-1415-2008

- Pascolini-Campbell, M., Reager, J. T., Chandanpurkar, H. A., and Rodell, M. (2021). Retracted article: A 10 per cent increase in global land evapotranspiration from 2003 to 2019. *Nature* 593 (7860), 543–547. doi:10.1038/s41586-021-03503-5
- Peng, J., Loew, A., Merlin, O., and Verhoest, N. E. C. (2017). A review of spatial downscaling of satellite remotely sensed soil moisture. *Rev. Geophys.* 55 (2), 341–366. doi:10.1002/2016rg000543
- Robock, A., Vinnikov, K. Y., Srinivasan, G., Entin, J. K., Hollinger, S. E., Speranskaya, N. A., et al. (2000). The global soil moisture data bank. *Bull. Am. Meteorol. Soc.* 81 (6), 1281–1299. doi:10.1175/1520-0477(2000)081<1281:tgsmdb>2.3.co;2
- Runge, J., Bathiany, S., Bollt, E., Camps-Valls, G., Coumou, D., Deyle, E., et al. (2019). Inferring causation from time series in earth system sciences. *Nat. Commun.* 10 (1), 2553–2613. doi:10.1038/s41467-019-10105-3
- Schmugge, T., Jackson, T., and McKim, H. (1980). Survey of methods for soil moisture determination. *Water Resour. Res.* 16 (6), 961–979. doi:10.1029/wr016i006p00961
- Seneviratne, S. I., Corti, T., Davin, E. L., Hirschi, M., Jaeger, E. B., Lehner, I., et al. (2010). Investigating soil moisture–climate interactions in a changing climate: a review. *Earth-Science Rev.* 99 (3–4), 125–161. doi:10.1016/j.earscirev.2010.02.004
- Sheffield, J., and Wood, E. F. J. J. O. C. (2008). Global trends and variability in soil moisture and drought characteristics, 1950–2000, from observation-driven simulations of the terrestrial hydrologic cycle. *J. Clim.* 21 (3), 432–458. doi:10.1175/2007jcli1822.1
- Sokol, Z., Blizňová, V., and Michaelides, S. (2009). Areal distribution and precipitation-altitude relationship of heavy short-term precipitation in the Czech Republic in the warm part of the year. *Atmos. Res.* 94 (4), 652–662. doi:10.1016/j.atmosres.2009.03.001
- Spencer, M., Wheeler, K., White, C., West, R., Piepmeier, J., Hudson, D., et al. (2010). “The Soil Moisture Active Passive (SMAP) mission L-Band radar/radiometer instrument,” in *Geoscience and Remote sensing symposium (IGARSS)* (Honolulu, Hawaii: IEEE International), 3240
- Spennemann, P. C., Rivera, J. A., Saulo, A. C., and Penalba, O. C. (2015). A comparison of GLDAS soil moisture anomalies against standardized precipitation index and multisatellite estimations over south america. *J. Hydrometeorol.* 16 (1), 158–171. doi:10.1175/jhm-d-13-0190.1
- Swenson, S., Famiglietti, J., Basara, J., and Wahr, J. (2008). Estimating profile soil moisture and groundwater variations using GRACE and Oklahoma mesonet soil moisture data. *Water Resour. Res.* 44 (1). doi:10.1029/2007wr006057
- Tuttle, S., and Salvucci, G. D. (2016). Empirical evidence of contrasting soil moisture–precipitation feedbacks across the united states. *Science* 352 (6287), 825–828. doi:10.1126/science.aaa7185
- Vargas Zeppetello, L. R., Battisti, D. S., and Baker, M. B. (2019). The origin of soil moisture evaporation “regimes”. *J. Clim.* 32 (20), 6939–6960. doi:10.1175/jcli-d-19-0209.1
- Vauclin, M., Khanji, D., and Vachaud, G. (1979). Experimental and numerical study of a transient, two-dimensional unsaturated-saturated water table recharge problem. *Water Resour. Res.* 15 (5), 1089–1101. doi:10.1029/wr015i005p01089
- Verrot, L., and Destouni, G. (2016). Worldwide soil moisture changes driven by future hydro-climatic change scenarios. *Hydrol. Earth Syst. Sci. Discuss.*, 1. doi:10.5194/hess-2016-165
- Wagner, W., Scipal, K., Pathe, C., Gerten, D., Lucht, W., Rudolf, B., et al. (2003). Evaluation of the agreement between the first global remotely sensed soil moisture data with model and precipitation data. *J. Geophys. Res.* 108 (D19), 4611. doi:10.1029/2003jd003663
- Wang, L., and Qu, J. J. (2009). Satellite remote sensing applications for surface soil moisture monitoring: a review. *Front. Earth Sci. China* 3 (2), 237–247. doi:10.1007/s11707-009-0023-7
- Wang, T., Zhao, Y., Xu, C., Ciais, P., Liu, D., Yang, H., et al. (2021). Atmospheric dynamic constraints on tibetan plateau freshwater under paris climate targets. *Nat. Clim. Chang.* 11 (3), 219–225. doi:10.1038/s41558-020-00974-8
- Wu, Z., Feng, H., He, H., Zhou, J., and Zhang, Y. (2021). Evaluation of soil moisture climatology and anomaly components derived from ERA5-land and GLDAS-2.1 in China. *Water Resour. Manage.* 35 (2), 629–643. doi:10.1007/s11269-020-02743-w
- Xie, X., He, B., Guo, L., Miao, C., and Zhang, Y. (2019). Detecting hotspots of interactions between vegetation greenness and terrestrial water storage using satellite observations. *Remote Sens. Environ.* 231, 111259. doi:10.1016/j.rse.2019.111259
- Xie, Z., Hu, Z., Gu, L., Sun, G., Du, Y., and Yan, X. (2017). Meteorological forcing datasets for blowing snow modeling on the tibetan plateau: evaluation and intercomparison. *J. Hydrometeorol.* 18 (10), 2761–2780. doi:10.1175/jhm-d-17-0075.1
- Xin, Y., Lu, N., Jiang, H., Liu, Y., and Yao, L. (2021). Performance of ERA5 reanalysis precipitation products in the guangdong-hong kong-macao greater bay area, China. *J. Hydrology* 602, 126791. doi:10.1016/j.jhydrol.2021.126791
- Xing, Z., Fan, L., Zhao, L., De Lannoy, G., Frappart, F., Peng, J., et al. (2021). A first assessment of satellite and reanalysis estimates of surface and root-zone soil moisture over the permafrost region of Qinghai-Tibet Plateau. *Remote Sens. Environ.* 265, 112666. doi:10.1016/j.rse.2021.112666
- Xu, J., Ma, Z., Yan, S., and Peng, J. (2022). Do ERA5 and ERA5-land precipitation estimates outperform satellite-based precipitation products? a comprehensive comparison between state-of-the-art model-based and satellite-based precipitation products over mainland China. *J. Hydrol. X.* 605, 127353. doi:10.1016/j.jhydrol.2021.127353
- Xu, L., Baldocchi, D. D., and Tang, J. (2004). How soil moisture, rain pulses, and growth alter the response of ecosystem respiration to temperature. *Glob. Biogeochem. Cycles* 18 (4). doi:10.1029/2004gb002281
- Yang, J.-S., Robinson, P., Jiang, C. F., and Xu, Z. Q. (1996). Ophiolites of the kunlun mountains, china and their tectonic implications. *Tectonophysics* 258 (1–4), 215–231. doi:10.1016/0040-1951(95)00199-9
- Yang, K., Qin, J., Zhao, L., Chen, Y., Tang, W., Han, M., et al. (2013). A multi-scale soil moisture and freeze-thaw monitoring network on the third Pole. *Bull. Am. Meteorol. Soc.* 94 (12), 1907–1916. doi:10.1175/bams-d-12-00203.1
- Yang, L., Sun, G., Zhi, L., and Zhao, J. (2018). Negative soil moisture-precipitation feedback in dry and wet regions. *Sci. Rep.* 8 (1), 4026. doi:10.1038/s41598-018-22394-7
- Zeng, J., Li, Z., Chen, Q., Bi, H., Qiu, J., and Zou, P. (2015). Evaluation of remotely sensed and reanalysis soil moisture products over the tibetan plateau using *in-situ* observations. *Remote Sens. Environ.* 163, 91–110. doi:10.1016/j.rse.2015.03.008
- Zhang, M., Huang, X., Chuai, X., Yang, H., Lai, L., and Tan, J. (2015). Impact of land use type conversion on carbon storage in terrestrial ecosystems of china: a spatial-temporal perspective. *Sci. Rep.* 5 (1), 10233–10313. doi:10.1038/srep10233
- Zhang, Q., Fan, K., Singh, V. P., Song, C., Xu, C. Y., and Sun, P. (2019). Is himalayan-tibetan plateau “drying”? historical estimations and future trends of surface soil moisture. *Sci. Total Environ.* 658, 374–384. doi:10.1016/j.scitotenv.2018.12.209
- Zivot, E., and Wang, J. (2003). “Rolling analysis of time series,” in *Modeling financial time series with S-Plus®* (New York, NY: Springer), 299.



OPEN ACCESS

EDITED BY

Wenlong Jing,
Guangzhou Institute of Geography,
China

REVIEWED BY

Min Zhao,
Beijing Normal University, China
Zuoqi Chen,
Fuzhou University, China
Ce Zhang,
University of Lancaster, United Kingdom

*CORRESPONDENCE

Wei Jiang,
jiangwei@iwhr.com
Zhiguo Pang,
pangzg@iwhr.com

SPECIALTY SECTION

This article was submitted to
Environmental Informatics and Remote
Sensing,
a section of the journal
Frontiers in Earth Science

RECEIVED 07 July 2022

ACCEPTED 29 July 2022

PUBLISHED 25 August 2022

CITATION

Jiang W, Pang Z, Lv J, Ju H, Li L and Fu J
(2022), Satellite observations reveal
decreasing soil erosion in Northeast
Inner Mongolia, China, over the past
four decades.
Front. Earth Sci. 10:988521.
doi: 10.3389/feart.2022.988521

COPYRIGHT

© 2022 Jiang, Pang, Lv, Ju, Li and Fu.
This is an open-access article
distributed under the terms of the
[Creative Commons Attribution License](#)
(CC BY). The use, distribution or
reproduction in other forums is
permitted, provided the original
author(s) and the copyright owner(s) are
credited and that the original
publication in this journal is cited, in
accordance with accepted academic
practice. No use, distribution or
reproduction is permitted which does
not comply with these terms.

Satellite observations reveal decreasing soil erosion in Northeast Inner Mongolia, China, over the past four decades

Wei Jiang^{1,2*}, Zhiguo Pang^{1,2*}, Juan Lv^{1,2}, Hongrun Ju³, Lin Li^{1,2}
and June Fu^{1,2}

¹State Key Laboratory of Simulation and Regulation of Water Cycle in River Basin, China Institute of Water Resources and Hydropower Research, Beijing, China, ²Remote Sensing Technology Application Center, Research Center of Flood and Drought Disaster Reduction of the Ministry of Water Resources, Beijing, China, ³School of Tourism and Geography Science, Qingdao University, Qingdao, China

Knowledge regarding the soil erosion change patterns in Northeast Inner Mongolia (NIM) is essential for ecological security and sustainable development. Multisource satellite remote sensing with auxiliary data, including meteorology, land use, vegetation coverage, and digital elevation, was collected to establish a distributed soil erosion model to quantify the soil erosion intensity in Northeast Inner Mongolia. The results showed that soil erosion in Northeast Inner Mongolia, China, decreased by 100,654 km² from 1978 to 2018. The area change rates of the mild, moderate, strong, intensive and severe soil erosion intensities were -48.91%, -41.41%, 32.63%, -91.15%, and -91.14%, respectively. The decrease in soil erosion was mainly located in the Hulunbuir and Tongliao regions. Our findings from satellite observations provide information about the soil erosion intensity and spatial distribution required for policy-making and the management of soil erosion prevention in Northeast Inner Mongolia.

KEYWORDS

soil erosion, long time series, remote sensing, change pattern, northeast inner Mongolia

Introduction

Soil erosion leads to land degradation, sedimentation and ecological deterioration, which inevitably threaten ecological security and food production (Borrelli et al., 2021; Lyu et al., 2021). With the impact of climate change and human activities, soil erosion has become a widespread environmental problem (Li et al., 2013; Liu et al., 2020). Long-term series soil erosion investigations are helpful for improving our scientific understanding of the evolution pattern of soil erosion, objectively evaluating the control effects of soil and water conservation measures and promoting the sustainable development of the natural-economic-environment (Duan et al., 2012; Jiang et al., 2016; Lyu et al., 2021; Xie et al., 2022).

Currently, remote sensing technology is a unique means used to investigate long time series dynamic changes in soil erosion at the regional scale (Zhou et al., 2016; Alexakis et al., 2019; Long et al., 2019; Wang and Zhao, 2020). Various soil erosion parameters, including digital elevation models, vegetation cover and land use, can be extracted from multisource satellite imagery to calculate the soil erosion intensity using a soil erosion model (Jiang et al., 2016; Xiao et al., 2021; Lin and Zhao, 2022). (Liu et al., 2020) completed the national soil erosion survey of China in 2011 and employed a multistage, unequal probability, systematic area sampling method. Based on a geographic information system and remote sensing approach, (Jiang et al., 2016), applied the revised wind erosion equation (RWEQ) model to simulate the wind erosion intensity of Inner Mongolia between 2001 and 2010. (Zhou et al., 2016) further investigated the dynamic monitoring of soil wind erosion in Inner Mongolia, China, during 1985–2011 at a 1-km scale. Since the Landsat series satellites can be extended from 1972 to the present day, the information required for soil erosion models, such as land cover and vegetation cover, can be obtained from Landsat images (El Jazouli et al., 2019).

The soil erosion in Northeast Inner Mongolia (NIM), an important grain production base with black soil in China, was very severe in the last century and has been effectively curbed through ecological restoration by afforestation (Lyu et al., 2021). However, comprehensive exploration based on longer time series soil erosion change patterns in Northeast Inner Mongolia at a 30-m spatial resolution is still lacking. The motivation of this study

was to determine the soil erosion dynamic change patterns in Northeast Inner Mongolia over the past four decades. To achieve this goal, two issues were addressed through the following actions: 1) multisource satellite imageries at five key time nodes (1978, 1985, 1995, 2005, and 2018) with the distributed model of soil erosion were employed to calculate the soil erosion intensity; 2) the dynamic patterns of soil erosion intensity were determined, and the driving factors of the changing patterns were explored. The main contribution of this paper is that it presents new knowledge regarding soil erosion change in Northeast Inner Mongolia, China.

Study area

Northeast Inner Mongolia is situated in Northeast China and includes 30 banners (counties, cities, districts) in four leagues (cities) of Hulunbuir, Hinggan League, Tongliao and Chifeng, with a total land area of 387,488 km². The location of the study area is shown in Figure 1A, and it is one of the three largest black soil belts in the world, namely, the northeast black soil area. The study area involves the Erguna River, the Nenjiang River and the Liaohe River, which belong to the cold temperate zone and the mid-temperate zone continental climate zone, with an annual precipitation of 242.5–566.9 mm. The soil erosion type is mainly wind erosion with intermittent water erosion and freeze-thaw erosion in the north.

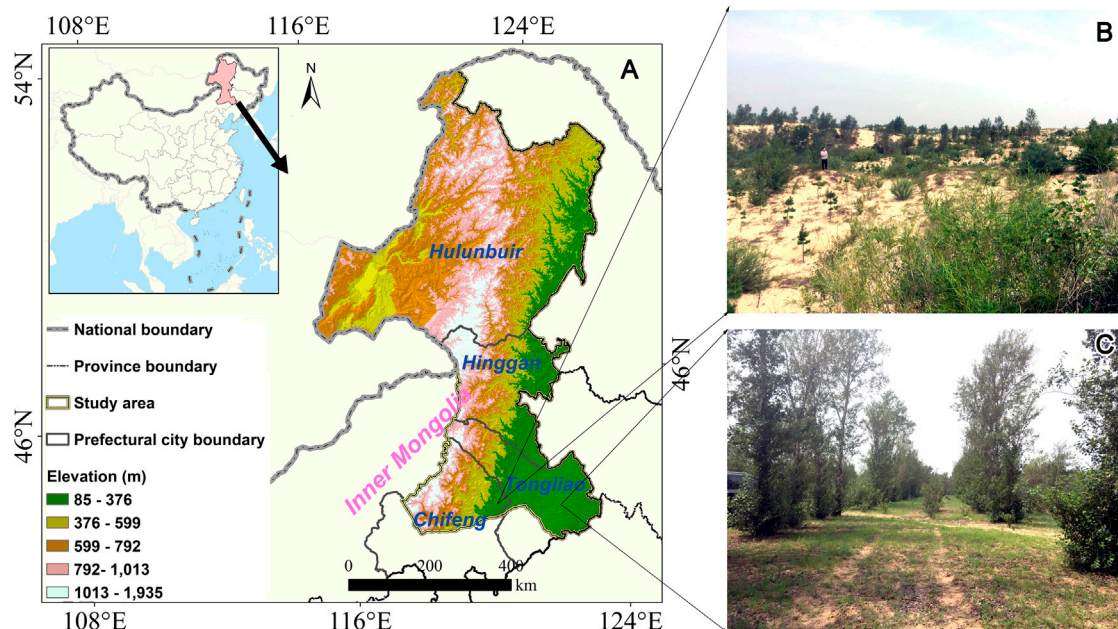


FIGURE 1
The location of the study area. (A) The boundary of Northeast Inner Mongolia. (B,C) Field survey photos after soil erosion control.

Due to the coupling of its unique climate and soil conditions with highly intensive human activities, soil erosion, especially wind erosion, has become a major threat to food security and healthy living. Over the past decades, afforestation has had an important effect on the control of soil erosion in Northeast Inner Mongolia, and vegetation cover has been successfully restored in desert (Figure 1B) and grassland areas (Figure 1C). Therefore, the use of various satellite remote sensing can better explain the evolution of soil erosion in Northeast Inner Mongolia.

Methods

According to the Regional Soil Erosion Dynamic Monitoring Technology Regulation (RSEDMTR), the technical flow of the soil erosion model was revised (Supplementary Figure S1). Considering the lack of long time series freeze–thaw observations in the study area, the soil erosion types were defined as wind erosion and water erosion. The soil erosion intensity was calculated and analyzed using the following three steps:

In the first step, to overcome the challenge of the spatial and temporal inconsistencies of multisource remote sensing and monitoring station data, the land use and land cover (LULC), vegetation coverage (VC), meteorological data and topographical data were collected from existing remote sensing products and station data, which are summarized in Supplementary Table S1. The LULC data were acquired from China's Land-Use/Cover Datasets (CLUDs) (Liu et al., 2002; Liu et al., 2014). The CLUD dataset is a national-scale multiperiod land use/land cover thematic database constructed by manual visual interpretation using Landsat remote sensing imagery from the 1970s to 2020. The data were classified into six classes and 25 subclasses of land use with a mapping accuracy over 91%. Moderate Resolution Imaging Spectroradiometer (MODIS) normalized difference vegetation index (NDVI) products were from 2000 to 2018 with 250 m, and Global Inventory Monitoring and Modeling System (GIMMS) NDVI products are from 1981 to 2018 with 8 km. To generate the long time series vegetation coverage (VC) data, the spatiotemporal fusion algorithm was used to produce the normalized difference vegetation index (NDVI) from 1981 to 2018 with 250 m based MODIS NDVI and GIMMS NDVI (Guo et al., 2020). The slope and slope length of the terrain were obtained from digital elevation model (DEM) data with 30 m, which were acquired from the United States Geological Survey (USGS). The rainfall and wind speed of site observations acquired from the China Meteorological Administration (CMA) were converted into raster data by Kriging interpolation. The LULC, VC, meteorological data and topographical data were preprocessed at a 30 m spatial resolution.

In the second step, based on the Regional Soil Erosion Dynamic Monitoring Technology Regulation (RSEDMTR), the

slope, slope length, vegetation coverage and rainfall were used to calculate the water erosion modulus by referring to the Chinese Soil Loss Equation (CSLE) (Liu et al., 2020; Liu and Liu, 2020). The land use, wind speed and vegetation coverage were employed to calculate the wind erosion modulus. According to the soil erosion classification and grading standards (Supplementary Tables S2, S3), the water and wind erosion moduli were reclassified into six intensities (slight, mild, moderate, strong, intensive and severe). The soil erosion intensity (S) for each pixel was calculated using the following formula:

$$S = \text{Max}(S_{\text{water}}, S_{\text{wind}})$$

where S_{water} represents the intensity of water erosion and S_{wind} represents the intensity of wind erosion. If $S_{\text{water}} = S_{\text{wind}}$, then the erosion type of the pixel is wind erosion.

In the third step, based on the soil erosion intensity, the spatial, temporal and intensity change patterns in Northeast Inner Mongolia from 1978 to 2018 were analyzed, and the driving factors of the change patterns were discussed.

Results

Spatial patterns of soil erosion dynamic change

Based on the flow of soil erosion dynamic monitoring, the results of the intensity distribution of water soil erosion and wind soil erosion in Northeast Inner Mongolia from 1978 to 2018 are shown in Figure 2. In terms of the distribution pattern of soil erosion in Northeast Inner Mongolia, the dominant soil erosion type in the study area was wind erosion, and soil erosion was located in western Hulunbuir, southern Hinggan League, Tongliao, and Chifeng. The east-central region of Hulunbuir is Greater Khingan, an important forestry base in China, with high altitudes and high forest cover. Thus, the intensity of soil erosion calculated by our method is slight in Greater Khingan. Over the past 4 decades, the wind erosion area showed a remarkable decline in the Hulunbuir and Tongliao regions, while the water erosion area remained stable. From the change area of soil erosion decline, it can be seen that wind erosion declined sharply from 2005 to 2018, which was related to afforestation ecological restoration. The intensity of soil erosion in Northeast Inner Mongolia has changed significantly over the past 40 years. The remarkable intensity change in soil erosion over the past four decades occurred in the shift from mild soil erosion to slight erosion; the area of high-intensity soil erosion has decreased significantly, especially in the farmland areas of Chifeng and Tongliao, which suggests that windbreak forests constructed around farmland

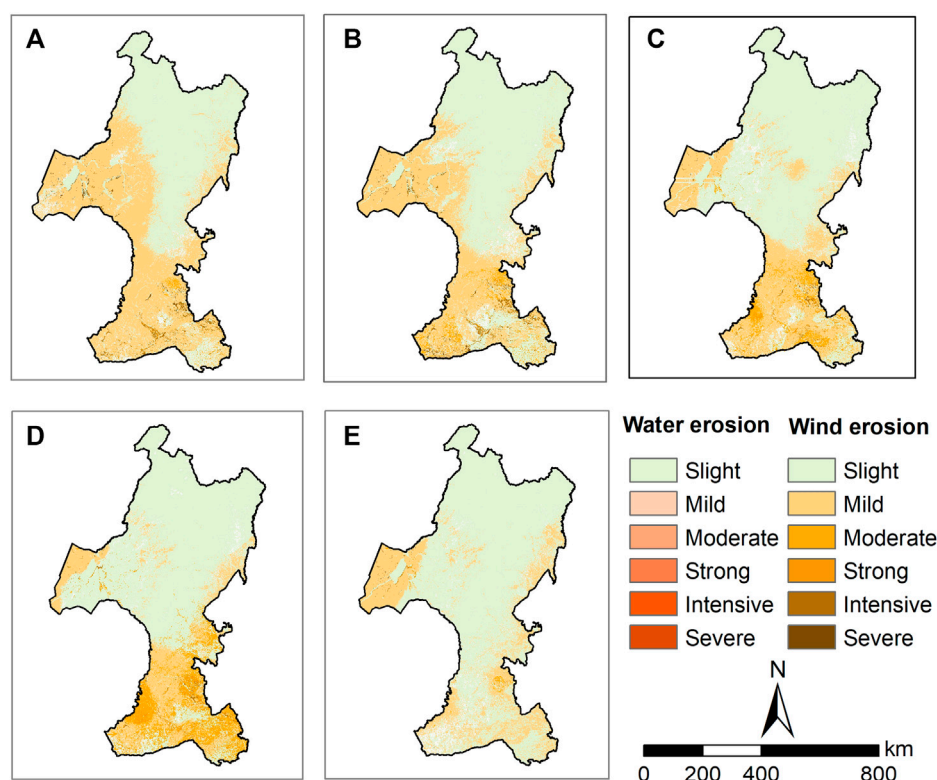


FIGURE 2

Soil erosion spatial pattern dynamic change in Northeast Inner Mongolia. (A) 1978, (B) 1985, (C) 1995, (D) 2005, (E) 2018.

effectively curb the migration of farmland soil due to wind erosion.

Temporal patterns of soil erosion dynamic monitoring

The area changes in soil erosion in Northeast Inner Mongolia from 1978 to 2018 are shown in Figure 3. The soil erosion in Northeast Inner Mongolia has decreased remarkably over the past four decades. In 1978, the area of soil erosion was 203,538 km², while in 2018, the area of soil erosion was 102,884 km², a decrease of 100,654 km² over the four decades. In the process of decreasing the soil erosion area, the wind erosion area decreased most significantly, with an area of 100,517 km².

According to the Inner Mongolia soil erosion census, the areas of soil erosion in 1995 and 2018 were 143,620 km² and 104,564 km², respectively. Compared with the area calculated in this study, the relative errors were −3.52 and 1.63%, respectively, which indicates that the results calculated by this method are more credible.

Based on the soil erosion classification and grading standards, the mild, moderate, strong, intensive and severe intensities were categorized as soil erosion. The intensity area and change in soil erosion in different periods are summarized in Supplementary Table S3. From 1978 to 2018, mild soil erosion accounted for the largest proportion in each period, and the change rate of mild soil erosion was −48.91%. Moreover, the area of intensive and severe soil erosion decreased by more than 91%, followed by the area of mild and moderate soil erosion, while the area of strong soil erosion increased by 268 km². The results showed that the rate of decrease of high-intensity soil erosion was sharp, and the decrease in the area of low-intensity soil erosion was large, which suggested that the high-intensity soil erosion had been converted to low-intensity soil erosion. Thus, soil and water conservation measures, such as restoring vegetation, controlling slope (channel) erosion and preventing grassland degradation, have performed well over the past four decades.

Furthermore, the area changes in water erosion intensity and wind erosion intensity over the past four decades are shown in Figure 4. Mild and moderate erosion were the main types of water erosion, with the area of mild erosion increasing by 28.47% and the area of moderate erosion decreasing by 32.57%. Regarding wind

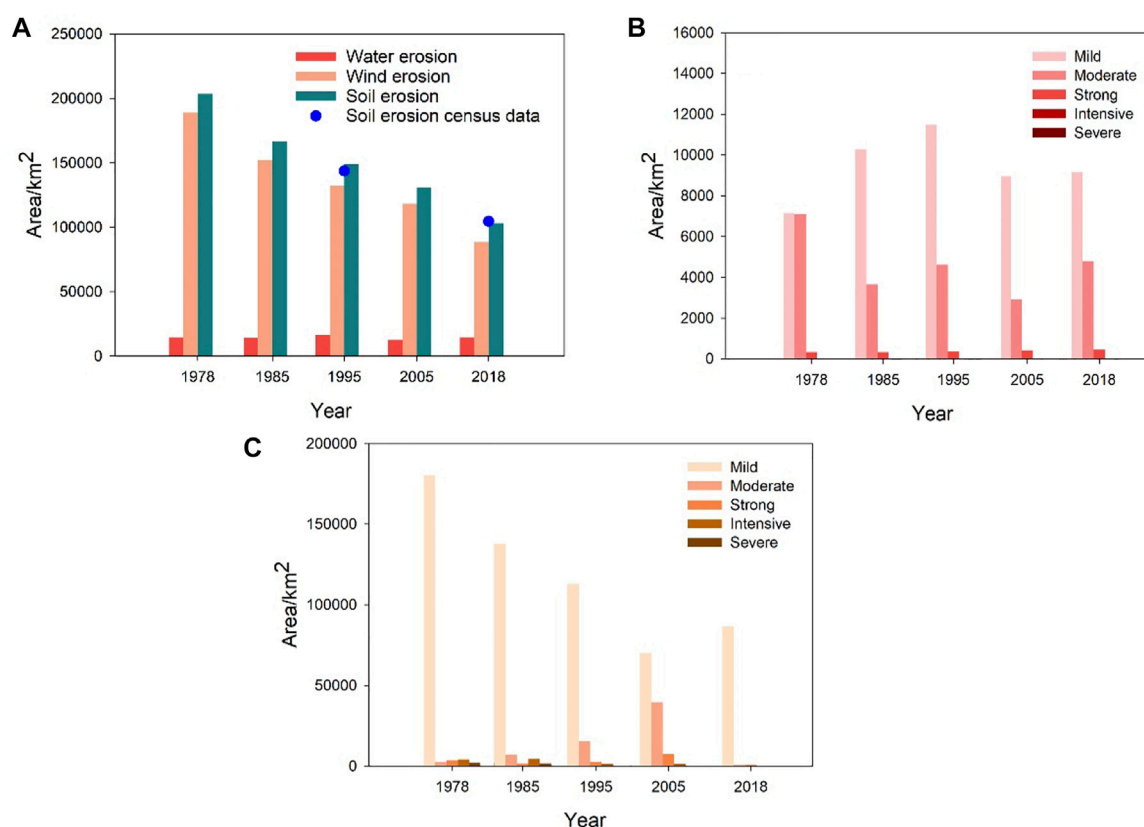


FIGURE 3

(A) Soil erosion area and validation in Northeast Inner Mongolia from 1978 to 2018. The area change of water erosion (B) and wind erosion (C) in Northeast Inner Mongolia from 1978 to 2018.

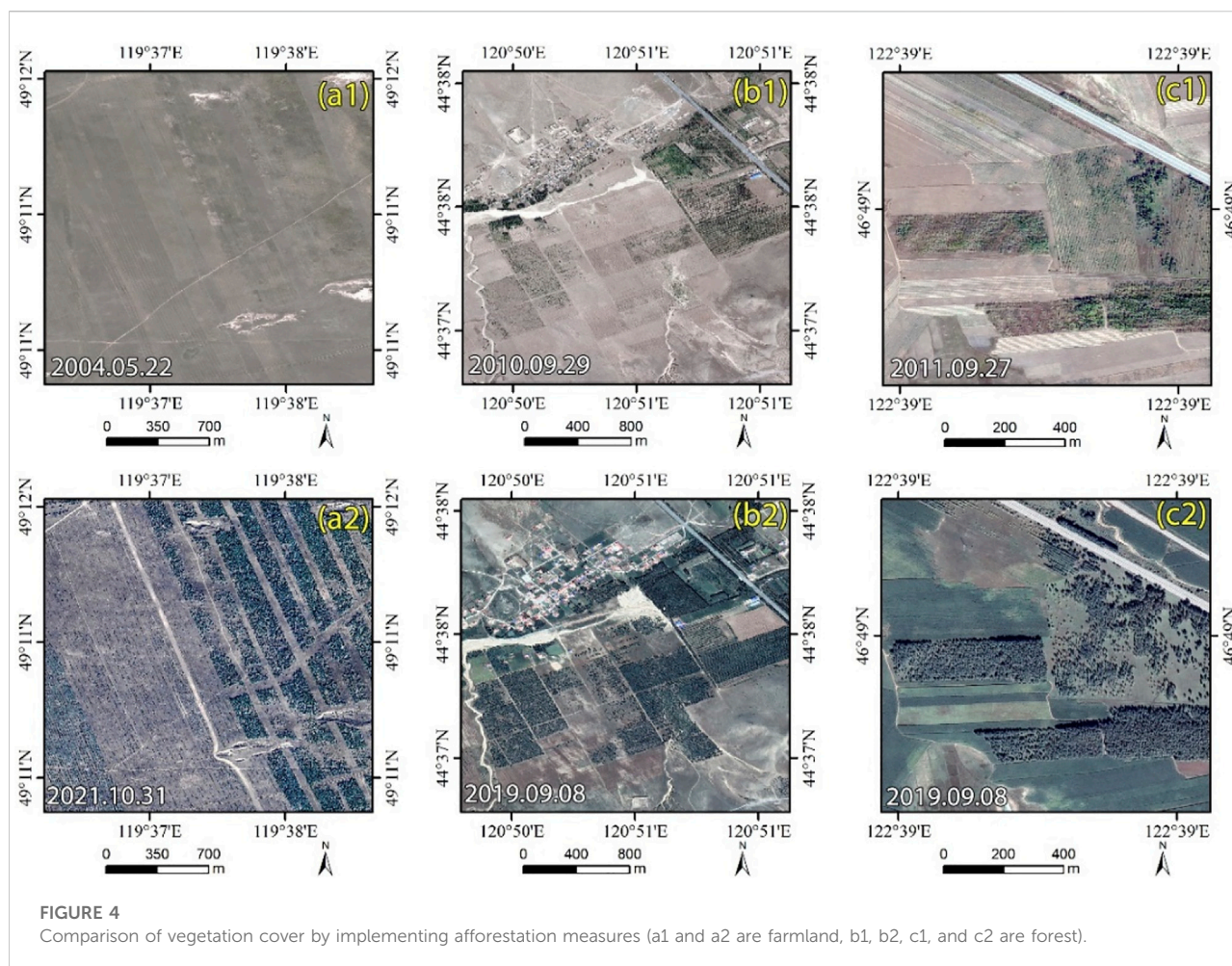
erosion, mild erosion accounted for the most intensity, and the area of decreasing mild erosion was 93,704 km². Moreover, the areas of moderate, intensive and severe wind erosion decreased by 68.07, 91.73 and 91.22%, respectively. Thus, the decline in low-intensity wind erosion contributed to regional soil erosion improvement.

Discussion

Long time series of soil erosion survey data are important for the assessment of the effectiveness of soil erosion management (Liu et al., 2020). Although long time series and high-resolution remote sensing data provide new opportunities to conduct soil erosion assessments, there are also some challenges, such as remote sensing data consistency and seasonal differences, which can lead to uncertainty in soil erosion assessments at the regional scale. Compared with previous studies (Wang et al., 2018; Zhang et al., 2018), this study collected various satellite

remote sensing data and products and adopted data processing methods, such as vegetation coverage data generated using a spatiotemporal fusion algorithm, LULC data with a consistent classification system, and the soil erosion calculations referring to the Regional Soil Erosion Dynamic Monitoring Technology Regulation (RSEDMTR), to reduce the uncertainty of the data on the results. Compared to the Inner Mongolia soil erosion census, the relative error in the area of soil erosion calculated was -3.52 and 1.63% in 1995 and 2018, respectively, which indicates that the results of the soil erosion calculations are scientifically reliable. Moreover, recent studies have shown that wind erosion in Inner Mongolia has declined significantly, which is generally consistent with the findings of this study (Zhang et al., 2018).

Land use, meteorological factors, and vegetation cover are the key drivers of soil erosion pattern change (Zhu et al., 2021). In the past four decades, the slower wind speeds (Fang et al., 2022) and increased vegetation cover (Zhang et al., 2018) have collectively led to a decrease in wind erosion area. Although agricultural



development may pose a risk of soil erosion, the intensity of soil erosion can be effectively reduced by planting trees around agricultural land, as shown in Figure 4 (a2). Moreover, the afforestation measures implemented in China have had a significant effect on increasing the vegetation cover in the desert area (Li et al., 2018; Wang et al., 2020). The comparison of vegetation cover is shown in Figure 4 (b1), (b2), (c1), and (c2), indicating that vegetation cover change is the main driving factor for the decline in soil erosion intensity (Yin et al., 2018).

Conclusion

Long-term series soil erosion investigations with remote sensing data are helpful for improving our scientific understanding of soil and water conservation management effectiveness assessments and planning. This study introduced multisource remote sensing technology and station data to explore the soil erosion change patterns in Northeast Inner

Mongolia from 1978 to 2018. The results showed that the dominant soil erosion type was wind erosion, and the area of soil erosion decreased by 100,654 km². The wind erosion area showed a remarkable decline in the Hulunbuir and Tongliao regions, while the water erosion area remained stable. The remarkable intensity change in soil erosion over the past four decades occurred in the shift from mild soil erosion to slight erosion; the area of high-intensity soil erosion has decreased significantly. The area change rates of the mild, moderate, strong, intensive and severe soil erosion intensities were -48.91%, -41.41%, 32.63%, -91.15%, and -91.14%, respectively. The slower wind speeds and increased vegetation cover have collectively led to a decrease in wind erosion area, and the vegetation cover change derived by afforestation measures is the main driving factor for the decline in soil erosion intensity. The present study objectively reveals the changes in soil erosion in Northeast Inner Mongolia under the joint action of human activity and the natural environment and can provide support for safeguarding food security and ecologically sustainable development.

Data availability statement

The original contributions presented in the study are included in the article/Supplementary Material, further inquiries can be directed to the corresponding authors.

Author contributions

WJ conceived and designed the framework, performed the experiments, and wrote the paper. ZP and JL contributed to data preparation and analysis. HJ, LL, and JF performed the experiments. All authors discussed the results and contributed to the final manuscript.

Funding

This research was funded by the Water Conservancy Technology Demonstration Project (SF-202001), and Innovation Talent Project of the Research Center of Flood and Drought Disaster Reduction of the Ministry of Water Resources (202110) and National Natural Science Foundation of China (51779269).

Acknowledgments

We give thanks to the research team at the China's Land-Use/Cover Datasets (CLUDs), United States Geological Survey and

China Meteorological Administration for providing the multisource data. The authors thank editors and three reviewers for their valuable comments to improve our manuscript.

Conflict of interest

The authors declare that the research was conducted in the absence of any commercial or financial relationships that could be construed as a potential conflict of interest.

Publisher's note

All claims expressed in this article are solely those of the authors and do not necessarily represent those of their affiliated organizations, or those of the publisher, the editors and the reviewers. Any product that may be evaluated in this article, or claim that may be made by its manufacturer, is not guaranteed or endorsed by the publisher.

Supplementary material

The Supplementary Material for this article can be found online at: <https://www.frontiersin.org/articles/10.3389/feart.2022.988521/full#supplementary-material>

References

- Alexakis, D. D., Tapoglou, E., Vozinaki, A.-E. K., and Tsanis, I. K. (2019). Integrated use of satellite remote sensing, artificial neural networks, field spectroscopy, and GIS in estimating crucial soil parameters in terms of soil erosion. *Remote Sens.* 11 (9), 1106. doi:10.3390/rs11091106
- Borrelli, P., Alewell, C., Alvarez, P., Anache, J. A. A., Baartman, J., Ballabio, C., et al. (2021). Soil erosion modelling: A global review and statistical analysis. *Sci. total Environ.* 780, 146494. doi:10.1016/j.scitotenv.2021.146494
- Duan, X., Xie, Y., Liu, B., Liu, G., Feng, Y., and Gao, X. (2012). Soil loss tolerance in the black soil region of Northeast China. *J. Geogr. Sci.* 22 (4), 737–751. doi:10.1007/s11442-012-0959-5
- Fang, K., Bai, M., Azorin-Molina, C., Dong, Z., Camarero, J. J., Zhang, P., et al. (2022). Wind speed reconstruction from a tree-ring difference index in northeastern Inner Mongolia. *Dendrochronologia* 72, 125938. doi:10.1016/j.dendro.2022.125938
- Guo, Y., Wang, C., Lei, S., Yang, J., and Zhao, Y. (2020). A framework of spatio-temporal fusion algorithm selection for Landsat NDVI time series construction. *ISPRS Int. J. Geo-Information* 9 (11), 665. doi:10.3390/ijgi9110665
- Jazouli, A., Barakat, A., Khellouk, R., Rais, J., and Baghdadi, M. (2019). Remote sensing and GIS techniques for prediction of land use land cover change effects on soil erosion in the high basin of the Oum Er Rbia River (Morocco). *Remote Sens. Appl. Soc. Environ.* 13, 361–374. doi:10.1016/j.rsase.2018.12.004
- Jiang, L., Xiao, Y., Zheng, H., and Ouyang, Z. (2016). Spatio-temporal variation of wind erosion in Inner Mongolia of China between 2001 and 2010. *Chin. Geogr. Sci.* 26 (2), 155–164. doi:10.1007/s11769-016-0797-y
- Li, D., Xu, D., Wang, Z., You, X., Zhang, X., and Song, A. (2018). The dynamics of sand-stabilization services in Inner Mongolia, China from 1981 to 2010 and its relationship with climate change and human activities. *Ecol. Indic.* 88, 351–360. doi:10.1016/j.ecolind.2018.01.018
- Li, X., Wu, B., and Zhang, L. (2013). Dynamic monitoring of soil erosion for upper stream of Miyun Reservoir in the last 30 years. *J. Mt. Sci.* 10 (5), 801–811. doi:10.1007/s11629-013-2559-y
- Lin, H., and Zhao, Y. (2022). Soil erosion assessment of alpine grassland in the source park of the yellow river on the qinghai-Tibetan plateau, China. *Front. Ecol. Evol.* 9, 771439. doi:10.3389/fevo.2021.771439
- Liu, J., Liu, M., Deng, X., Zhang, Z., and Luo, D. (2002). The land use and land cover change database and its relative studies in China. *J. Geogr. Sci.* 12 (3), 275–282. doi:10.1007/s11769-002-0033-9
- Liu, J., Kuang, W., Zhang, Z., Xu, X., Qin, Y., Ning, J., et al. (2014). Spatiotemporal characteristics, patterns, and causes of land-use changes in China since the late 1980s. *J. Geogr. Sci.* 24 (2), 195–210. doi:10.1007/s11442-014-1082-6
- Liu, B., Xie, Y., Li, Z., Liang, Y., Zhang, W., Fu, S., et al. (2020). The assessment of soil loss by water erosion in China. *Int. Soil Water Conservation Res.* 8 (4), 430–439. doi:10.1016/j.iswcr.2020.07.002
- Liu, J., and Liu, H. (2020). Soil erosion changes during the last 30 years and contributions of gully erosion to sediment yield in a small catchment, southern China. *Geomorphology* 368, 107357. doi:10.1016/j.geomorph.2020.107357
- Long, T., Zhang, Z., He, G., Jiao, W., Tang, C., Wu, B., et al. (2019). 30 m resolution global annual burned area mapping based on Landsat images and google earth engine. *Remote Sens.* 11 (5), 489. doi:10.3390/rs11050489
- Lyu, X., Li, X., Wang, H., Gong, J., Li, S., Dou, H., et al. (2021). Soil wind erosion evaluation and sustainable management of typical steppe in Inner Mongolia, China. *J. Environ. Manag.* 277, 111488. doi:10.1016/j.jenvman.2020.111488

- Wang, H., and Zhao, H. (2020). Dynamic changes of soil erosion in the taohe river basin using the RUSLE model and Google Earth engine. *Water* 12 (5), 1293. doi:10.3390/w12051293
- Wang, L.-Y., Xiao, Y., Rao, E.-M., Jiang, L., Xiao, Y., and Ouyang, Z.-Y. (2018). An assessment of the impact of urbanization on soil erosion in Inner Mongolia. *Int. J. Environ. Res. public health* 15 (3), 550. doi:10.3390/ijerph15030550
- Wang, Z., Peng, D., Xu, D., Zhang, X., and Zhang, Y. (2020). Assessing the water footprint of afforestation in Inner Mongolia, China. *J. Arid Environ.* 182, 104257. doi:10.1016/j.jaridenv.2020.104257
- Xiao, Y., Yang, B., Guo, Y., Lu, R., Zhang, D., Zhang, D., et al. (2021). Spatial-temporal evolution patterns of soil erosion in the yellow river basin from 1990 to 2015: Impacts of natural factors and land use change. *Geomatics, Nat. Hazards Risk* 12 (1), 103–122. doi:10.1080/19475705.2020.1861112
- Xie, Y., Wang, L., An, R., Luo, X., Lu, Y., Liu, Y., et al. (2022). The effect of sloping land conversion program on soil erosion in shaanxi province, China: A spatial panel approach. *Front. Environ. Sci.* 10, 913712. doi:10.3389/feart.2022.913712
- Yin, H., Pflugmacher, D., Li, A., Li, Z., and Hostert, P. (2018). Land use and land cover change in Inner Mongolia - understanding the effects of China's re-vegetation programs. *Remote Sens. Environ.* 204, 918–930. doi:10.1016/j.rse.2017.08.030
- Zhang, H., Fan, J., Cao, W., Harris, W., Li, Y., Chi, W., et al. (2018). Response of wind erosion dynamics to climate change and human activity in Inner Mongolia, China during 1990 to 2015. *Sci. Total Environ.* 639, 1038–1050. doi:10.1016/j.scitotenv.2018.05.082
- Zhou, Y., Guo, B., Wang, S., Tao, H., Liu, W., Yang, G., et al. (2016). Dynamic monitoring of soil wind erosion in Inner Mongolia of China during 1985–2011 based on geographic information system and remote sensing. *Nat. Hazards* 83 (1), 1–17. doi:10.1007/s11069-015-1763-1
- Zhu, B., Zhou, Z., and Li, Z. (2021). Soil erosion and controls in the slope-gully system of the loess plateau of China: A review. *Front. Environ. Sci.* 9, 657030. doi:10.3389/feart.2021.657030



OPEN ACCESS

EDITED BY

Jay Lee,
Kent State University, United States

REVIEWED BY

Chengpeng Lu,
Lanzhou University, China
Zhimin Liu,
East China Normal University, China

*CORRESPONDENCE

Jian Zhang,
zjcufe@cufe.edu.cn

SPECIALTY SECTION

This article was submitted to
Environmental Informatics and Remote
Sensing, a section of the journal
Frontiers in Environmental Science

RECEIVED 17 October 2022

ACCEPTED 08 November 2022

PUBLISHED 28 November 2022

CITATION

Jiang L, Wang Y and Zhang J (2022),
Local-neighborhood effects of
environmental regulations on green
technology innovation in
manufacturing: Green credit-
based regulation.
Front. Environ. Sci. 10:1072180.
doi: 10.3389/fenvs.2022.1072180

COPYRIGHT

© 2022 Jiang, Wang and Zhang. This is
an open-access article distributed
under the terms of the [Creative
Commons Attribution License \(CC BY\)](#).
The use, distribution or reproduction in
other forums is permitted, provided the
original author(s) and the copyright
owner(s) are credited and that the
original publication in this journal is
cited, in accordance with accepted
academic practice. No use, distribution
or reproduction is permitted which does
not comply with these terms.

Local-neighborhood effects of environmental regulations on green technology innovation in manufacturing: Green credit-based regulation

Ling Jiang¹, Yuqi Wang² and Jian Zhang^{1*}

¹School of Government, Central University of Finance and Economics, Beijing, China, ²School of Public Administration and Policy, Renmin University of China, Beijing, China

With the deterioration of environmental pollution, resource security and climate crisis, transforming the mode of economic development and developing a green economy have turned into an international consensus. However, environmental regulations (ERs) can help facilitate technological innovation. As an important financial support for the green innovation transformation of China's manufacturing industry, it is crucial to exploit the policy synergy between green credit (GC) and ERs at the regional level to stimulate technological innovation effects. GC, as a financial instrument, can play a unique role in ERs; therefore, the relationship between ERs and the level of green technology innovation (GTI) based on the GC perspective deserves an in-depth study. Using a spatial Durbin model (SDM) for the panel data of 30 Chinese provinces from 2006 to 2016, this paper explores the spatial effects of ERs and GC on GTI in manufacturing and the moderating effects of GC policies on ERs affecting GTI. The research finds that ERs exert a negative impact on local manufacturing GTIs and undermine the innovation effect in neighboring locations through spatial spillover effects. The development of GC helps stimulate the transformation of GTI in local manufacturing industries with further attention on the effects of policy instruments and their combinations. The moderating effect of GC suggests that its development can weaken the inhibiting effect of ERs on GTI in local and neighboring areas and is particularly significant in coastal areas. Our study provides a theoretical basis and policy insights for coordinating government external intervention and market operation laws at the regional level to bring into play the incentive effect of technological innovation.

KEYWORDS

green credit, environmental regulation, green technology innovation, regulatory effect, spatial effect

1 Introduction

China's industrial supply capacity has grown to the point of being able to support economic development (Bressanelli et al., 2019; Bressanelli et al., 2022). However, the development model at the expense of the ecological environment at the expense of the ills of increasingly prominent institutional barriers, technical factor shortcomings, and phase conversion resistance is still accumulating and has become a real obstacle to the process of green and sustainable development (Geng et al., 2022; Jayachandran, 2022). The new situation of a tight time window for achieving carbon peaking and carbon neutrality presents high requirements for China's industrial low-carbon transformation and green development, and realizing the coordinated development of industrial transformation and ecological civilization has become a major strategic issue (Kolkiş et al., 2020; Zhao et al., 2021; Zhao et al., 2022). The 19th National Congress report of the Communist Party of China proposed the building of a market-oriented green technology innovation (GTI) system, focusing on the change from factor inputs to green system change and technology innovation-driven, from the scale advantage to innovation development advantage of the development path, has become an important support to achieve industrial green transformation (de Oliveira et al., 2018; Li and Gao, 2022). It can be observed that green technology progress has become the optimal means to achieve a "win-win" for environmental pollution control and regional economic growth.

As the core driving force and important support for green development transformation, GTI combines the concepts of "green" and "innovation," updating product processes and market services through technological innovation to reduce pollution emissions, improve resource utilization efficiency (Lv et al., 2021; Suki et al., 2022), and directly optimize the green industrial structure to promote regional green development transformation (Behera and Sethi, 2022). Environmental regulation (ERs) policy is a common way to stimulate enterprises to engage in GTI, and it plays a significant role in the pollution treatment cost expenditure of the front-end support of enterprises and the pollution emission of the end-end regulation of enterprises (Hassan et al., 2022). Green credit (GC) is an important instrument of green finance and a market-based instrument included in the broad ERs. GC accounts for over 90% of the existing green financial instruments in China and effectively promotes GTI by enterprises (Zhang et al., 2022).

Compared with traditional non-clean technology areas, the profit advantage of GTI is relatively weak (Shen et al., 2021); relying on only market forces is insufficient to support the transformation of China's industrial economy into green technology-oriented innovation (Wei et al., 2020). There is an urgent need for the government to effectively implement ecological, green, and scientific environmental economic

policies and regulatory instruments. According to the "Porter hypothesis", the role of ERs in promoting innovation is constrained by the financial status of the enterprises (Liu et al., 2021). The micro-subjects of regional green technology innovation are enterprises, and enterprises require continuous and stable financial support to conduct GTI. If ERs are strong in a certain region, it leads to an increase in the demand for funds for pollution control and innovation investment, which may cause polluting enterprises to adopt the avoidance strategy of relocating nearby. This leads to a significant difference in the technological innovation effect of ERs between local and neighboring regions (Mbanyele and Wang, 2022), resulting in the phenomenon of "ERs failure" at the regional level (Zhong and Peng, 2022). Therefore, green financial support is the key for the government to fully play its role in ERs.

ERs are implemented by the state and targeted at individual or organizational enterprises. It has been widely used as a traditional tool for environmental protection and is a key external driver of GTI, but its incentive effect on micro-individual technology innovation remains controversial (Böcher, 2012; Karmaker et al., 2021; Zhao et al., 2022).

Relevant studies have shown that green finance, with economic and environmental benefits, has become an emerging environmental governance tool for achieving market-oriented GTI (Liu et al., 2017; Irfan et al., 2022; Sharif et al., 2022). However, under the constraints of ERs, the potential for green finance to provide financial support for enterprises to engage in GTI activities to alleviate the contradiction between environmental protection and economic development requires in-depth exploration. First, the relationship between ERs and technological innovation exhibits an inverted "U" curve; when the intensity of ERs is weak, it promotes technological innovation activities. When the intensity of ERs exceeds a certain threshold, ERs restrict technological innovation, i.e., it is difficult for innovation compensation to cover the cost of compliance (Zhang and Wei, 2014). The interregional gradient in the intensity of the enforcement of ERs in China has led to regions with more lenient environmental policies, thereby providing opportunities for neighboring firms to circumvent the high-cost business practices of pollution abatement and technological innovation (Zhang et al., 2022). Second, as a new environmental economic policy, the essence of GC policy is that commercial banks provide differentiated loan pricing and credit lines for energy-saving, clean production, and environmental enterprises with high energy consumption and high pollution (Soundarrajan and Vivek, 2016; Su et al., 2022; Wang et al., 2022), which can effectively alleviate the financial dilemma of GTI in regional manufacturing industries (Nabeeh et al., 2021). On the one hand, green credit compresses the financing space of highly polluting enterprises and increases the financing cost, forcing enterprises to carry out methods of technological innovation and transformation of production. On the other hand, green credit provides a wider range of

external financing channels for polluting enterprises to achieve green innovation and transformation, which can effectively relieve the financial difficulties of green technology innovation in regional manufacturing industries. However, it is difficult to rationally allocate the limited credit funds among different regions based on the principle of parity. This results in a large difference in the level of GC development on the impact of GTI in local and neighboring regions. Third, in the field of environmental policy, government mechanisms have long dominated ecological and environmental governance, while the constraints of financial scarcity and government failure have hindered government mechanisms from matching the demand for ecological and environmental improvement. However, as the ecological environment is a quasi-public good, green finance, as a new market-based instrument for ecological governance, can exert a multiplier effect in a more effective, equitable, and sustainable manner when coordinated with the traditional environmental regulatory system (Falcone, 2020). Finally, geographically, there are differences between coastal and inland regions in terms of economic development level, government control, regional ecological environment, and financial market development, which leads to interregional differences in ERs and GC for GTI in manufacturing. On the one hand, it lies in the fact that ERs instruments in coastal areas are more effective in generating “innovation compensation” than those in inland areas (Ren et al., 2018; Nie et al., 2022). On the other hand, the incentive-matching effect of GC and ERs is more pronounced in coastal areas than that in inland areas, which exerts a positive moderating effect on GTI (He and Yan, 2020).

There is spatial variability in the impact of ERs intensity on GC. When ERs are weak, the implementation of GC can effectively guide enterprises to develop GTI by limiting financing to “three high” enterprises. When ERs are strong, i.e., when the cost of green technology research and development and the difficulty of financing seriously hinders the green transformation of enterprises, more capital supply in GC is used to solve part of the financing loan problem, thereby effectively promoting the GTI of enterprises. However, existing studies on GTI are mostly from a single perspective of ERs and GC, and fail to analyze their synergistic effects and spatial spillover effects. To fill this gap, this paper expands the spatial analysis framework of GTI by verifying the synergistic effect of GC and ERs on GTI and its regional differences. In terms of research content, this paper explores the synergies between green credit as a new environmental governance tool and traditional environmental regulation instruments on GTI in manufacturing. In terms of study dimensions, heterogeneity analysis is enriched by grouping by region.

Based on this, the key questions that our study addresses are: 1) Is there a local effect or spatial spillover effect of GC on the GTI of enterprises? 2) In terms of interregional equity, is there a crowding-out effect on GTI in neighboring regions due to a

shortage of financial resources and competition from local governments? 3) As a new type of environmental governance tool, how will the integration of GC into an integrated framework of ERs and GTI create synergies with traditional ERs instruments? Therefore, our study examined 30 provinces (including municipalities and autonomous regions) in China (excluding Hong Kong, Macao, Taiwan, and the Tibet Autonomous Region) as the research sample, employed a spatial econometric model to explore the effects of ERs and GC on the role of GTI in manufacturing, and used a moderating effect model to test the role of GC in the process of ERs affecting manufacturing technology innovation (Figure 1). Based on the aforementioned theoretical analysis, this paper proposes the following hypotheses:

Hypothesis 1: A nonlinear relationship exists between ERs and regional manufacturing green technology innovation, and this effect is characterized by “spatial spillover.”

Hypothesis 2: Green credit has a positive promotion effect on green technology innovation in the local manufacturing industry, but there is a resource crowding-out effect on neighboring areas.

Hypothesis 3: An incentive-matching effect exists between local GC and ERs on GTI in manufacturing. When green credit is invested at a certain level, it is conducive to alleviating the crowding-out of funds for technological innovation by ERs and stimulating the “innovation compensation effect” of ERs for green technological innovation.

Hypothesis 4: Heterogeneity exists between coastal and inland regions in terms of the impact of green credit and ERs on green technology innovation in manufacturing.

2 Materials and methods

2.1 Methods

2.1.1 Spatial econometric model setting

To investigate the spatial spillover effects of ERs and GC, we employed spatial econometric empirical analysis. The spatial Durbin model (SDM) based on panel data can effectively solve the possible endogeneity problem of interregional ERs variables. Drawing on the existing scholarly works (Ni et al., 2020), the model is constructed as shown in Model (1).

$$GTI_{it} = \alpha + \rho WGTI_{it} + \beta_1 ER_{it} + \beta_2 GC_{it} + \theta_1 WERS_{it} + \theta_2 WGC_{it} + \partial X_{it} + \varepsilon_{it} \quad (1)$$

To test the moderating effect of GC on ERs and GTI in manufacturing in Hypothesis 3, we constructed spatial econometric models with moderating effects for the extended analysis in this paper. The model is constructed as shown in Model (2).

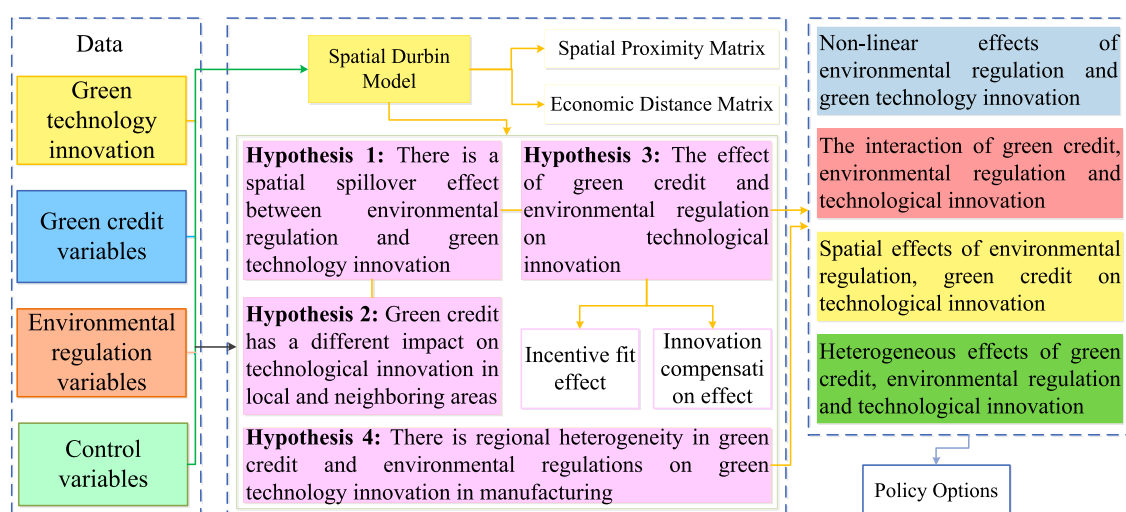


FIGURE 1
Framework flow chart.

$$GTI_{it} = \alpha + \rho WGTI_{it} + \beta_1 ERS_{it} + \beta_2 GC_{it} + \beta_3 ERS_{it} * GC_{it} + \theta_1 WERS_{it} + \theta_2 WGC_{it} + \theta_3 WERS_{it} * GC_{it} + \partial X_{it} + \varepsilon_{it} \quad (2)$$

where i is a province ($i = 1, 2, \dots, 30$); t is the year ($t = 2006, 2007, \dots, 2016$); GTI_{it} is the GTI intensity; ERS_{it} is the ERs intensity; GC_{it} is GC; $ERS_{it} * GC_{it}$ is the cross term of GC and ERs; X_{it} is a control variable, including urbanization level (URB), innovation human resource input (HRI), and fiscal decentralization (FE); and ε_{it} is an unpredictable error term.

2.1.2 Spatial weight matrix setting

The spatial econometric model reflects the spatial relationship between economic variables by setting a spatial weight matrix, and different spatial weight matrices represent different forms of spatial distances between variables, reflecting the different ways of influencing regional spatial effects (Zhang et al., 2020). Here, we selected the spatial adjacency matrix and the economic distance spatial weight matrix.

1) Spatial adjacency matrix. The most commonly used spatial weight matrix is the spatial adjacency matrix. According to Anselin and Griffith (Anselin and Griffith, 2010), a 0–1 weight matrix was constructed for the spatial adjacency of 30 provinces (autonomous regions and municipalities directly under the central government) in China as follows, where the matrix was assigned the value of one when two regions are adjacent and 0 when two regions were not adjacent. The calculation formula is shown in Model (3).

$$\omega_{ij} = \begin{cases} 1 & i \neq j \text{ and when two regions are adjacent} \\ 0 & i = j \text{ or when two regions are not adjacent} \end{cases} \quad (3)$$

2) Economic distance matrix. In addition to considering the influence of geographical distance on economic variables, economic distance is an important factor in portraying regional economic differences. The weight calculation formula is shown below. GDP_i and GDP_j represent the economic development level of two regions, expressed as the gross domestic production (GDP) per capita. Usually, the smaller the income gap between regions, the greater the weight, and the larger the gap, the smaller the weight. Here, we chose the inverse of the absolute value of the difference in economic distance to represent. The economic distance matrix reflects the economic gap between two regions and is an important factor that affects regional economic differences. Drawing on the existing scholarly works (Shao et al., 2016), the formula shown in Model 4) is set to express the economic distance between provinces (autonomous regions and municipalities directly under the central government) in terms of the economic distance matrix.

$$\omega_{ij} = \frac{1}{|GDP_i - GDP_j|} \quad (4)$$

where $\overline{GDP}_i = \frac{1}{T} \sum_{t=1}^T GDP_{it}$ denotes the average GDP value in region i at time T .

2.2 Variable selection and data sources

The sample interval was 2006–2016, and the paper covered 30 provinces (including municipalities directly under the Central Government and autonomous regions) (excluding data from

TABLE 1 Variable settings.

Variables	Definition	Description	Data sources
Explained variables	Green technology innovation (GTI)	Number of green invention patent applications (GIPA)	The website of the State Intellectual Property Office (According to the International Patent Classification launched by the WIPO in 2010)
Explanatory variables	Environmental regulations (ERs)	Expenditure indicators	Total investment in industrial pollution control/Total industrial output (ERSM)
		Regulatory indicators	Total emission fee revenue/Emission fee paying units number of units (ERRI)
	Green credit (GC)		Interest expense ratio of non-six high-energy-consuming industries
Control variables	Urbanization level (URB)	Urban population/Resident population	China Industrial Statistics Yearbook, China Environment Yearbook
	Human resource inputs (HRI)	The proportion of personnel engaged in scientific and technological activities in enterprises above the scale	China Environment Yearbook
	Fiscal decentralization (FE)	Local government budgetary expenditure as a percentage of GDP	China Industrial Statistics Yearbook

Hong Kong, Macao, Taiwan, and Tibet Autonomous Region). Definition of Main Variables and their data sources were related to the statistical yearbooks of previous years (Table 1).

(1)GTI. Since the number of green invention patent applications (GIPA) can be time-sensitive to directly examine green technology innovation activities of enterprises, GIPA was adopted as the main characterization indicator of GTI (Bai et al., 2019). Specifically, according to the “Green List of International Patent Classifications” launched in 2010, we used patent classification numbers to search for GIPAs and calculate the total number of green patent applications per year by region.

(2)GC. Considering that interest expense can reflect the size of credit, the interest expense ratio of non-six energy-consuming industries was chosen to indirectly measure the degree of GC development according to the research method of Guo et al. (2019) and Jiang et al. (2020), where the amount of green credit is the interest expenses of industrial industries in each province total interest expenditure minus the six major energy-consuming industries interest expenditure.

(3)ERs. Most previous studies measured the intensity of ERs from two perspectives: environmental inputs (pollution control investment, government environmental fiscal expenditure, and abatement costs) and environmental performance (sewage charges, sewage taxes, and disposal rates of pollutants). Considering that economic ERs are more likely to internalize external environmental costs, our study focused on economic ERs and measured the intensity of

ERs using a composite index of expenditure and regulatory indicators (Michael, 2012; Chen et al., 2022).

- ①Expenditure indicators focus on governance inputs, using the ratio of industrial investment in pollution control to industrial value added to measure.
- ②Regulatory indicators are based on the regulatory strength of governmental departments in implementing ERs system policies. Based on the previous research method (Yang et al., 2008; Guo et al., 2017; Huang et al., 2020), the amount of unit emission fee revenue was used as a regulatory-type index.

Drawing from the research of Peng and Yuan (2018), this study employed the min-max standardization method to calculate the composite index of ERs and set Model 5) for calculation.

$$ERs_{ij} = \frac{ERSM_{ij} - \min(ERSM_i)}{\max(ERSM_i) - \min(ERSM_i)} + \frac{ERRI_{ij} - \min(ERRI_i)}{\max(ERRI_i) - \min(ERRI_i)}, i = 1, 2, \dots, 11; j = 1, 2, \dots, 3 \quad (5)$$

where ERs_{ij} is the composite index of ERs in the j th province in year i ; $ERSM_{ij}$ and $ERRI_{ij}$ are the proportion of ERs investment amount and the average income of ERs in the j th province in year i , respectively. $\max(ERSM_i)$ and $\min(ERSM_i)$ denote the maximum and minimum values of the proportion of ERs investment amount in each province of the country in year i , respectively; $\max(ERRI_i)$ and $\min(ERRI_i)$ denote the maximum and minimum values of the average ERs income of each province in the country in year i , respectively.

TABLE 2 Baseline regression results.

Variables	(1)		(2)		(3)	
	Explanatory variables	Spatial lag term	Explanatory variables	Spatial lag term	Explanatory variables	Spatial lag term
ERs	−52.6977*** (18.1920)	517.1359*** (177.0373)	−49.8707*** (18.2888)	776.212*** (218.1744)	−193.1733** (79.49742)	742.2429*** (141.7734)
GC			0.4108 (0.7356)	−9.4125** (4.2752)	2.985739** (1.223334)	−0.6212095 (1.881881)
ERs*GC					−5.780011*** (1.940179)	−20.44289*** (3.667265)
URB	−3.7699*** (0.8756)	−21.1647*** (3.3705)	−3.6609*** (0.8931)	−20.7201*** (3.3723)	2.918633*** (0.9607014)	8.830221*** (2.161529)
FE	−1.2693 (0.8126)	93.2869*** (10.0703)	−0.9218 (1.0184)	108.4958*** (12.0243)	−1.032939 (1.252515)	−12.95635*** (2.453519)
HRI	349.1797*** (46.358)	595.2315 (385.2307)	340.8392*** (46.1967)	707.2458* (388.6115)	135.8331** (56.50001)	−303.9127*** (109.2929)
ρ	−0.5631*** (0.0773)		−0.5337*** (0.0815)		−0.5894*** (0.0666)	
sigma2_e	12895.7*** (1011.242)		12700.25*** (992.5672)		17866.64*** (1472.002)	
N	330		330		330	
R ²	0.7646		0.7653		0.7313	
Time fixed effects	Yes		Yes		Yes	
Regional fixed effects	No		No		No	

Note: Standard errors are in parentheses; *, **, and *** indicate significance at 10%, 5%, and 1% significance levels, respectively.

3 Results

3.1 Nonlinear effects of ERs and GTI

Here, the SDM is selected as the optimal choice by combining the Lagrange Multiplier (LM) and Wald tests, and the results of the Hausman test are used to select the fixed effects estimation results and set the time fixed model. As shown in Table 2, Models (1)–(3) are the results of the maximum likelihood estimation of the SDM with the inclusion of the cross terms of GC, ERs, and GC in turn.

As can be seen from Table 2, ERs hinder GTI in China's manufacturing industry. The analysis of the coefficient estimates for the explanatory variables shows that the regression coefficient of ERs is significantly negative under the three models, indicating that there is a significant negative relationship between the intensity of ERs and GTI in manufacturing in the region. This implies that all provinces in the country are in the primary stage of cost saving, with weak innovation support, such as technological improvement and optimization of management models. Innovation compensation can hardly compensate for the high

production costs caused by ERs, and supporting funds and policies also lead to the effect of industrial GTI transformation being difficult to show. Thus, it is difficult to offset the negative impact of ERs on the crowding-out effect of innovation input.

Second, Table 2 shows that GC policy could play the “Porter effect” and positively promote GTI in China's manufacturing industry. From the estimated coefficients of the variables in Model (2), the incentive effect of GC for technological innovation can be effectively brought into play in the policy context of green finance booming. The reason may be that, by the type of enterprise, high energy-consuming enterprises such as “two high and one leftover” face financing constraints, which need to be eliminated, or they are prompted to improve the efficiency of GTI and adjust their industrial structure to reduce undesirable output (Hsu et al., 2014). Simultaneously, enterprises in the clean industry or promoting green projects are the first to develop environmentally friendly technologies and products with the financial support of GC and achieve value-added business benefits with the “first-mover advantage” achieved in market competition, thereby generating an “innovation compensation effect.”

TABLE 3 Results of spatial effect decomposition.

Variables	Local effects	Neighborhood effects	Total effect
ERs	360.7769*** (104.9865)	1881.845*** (470.0905)	2242.622*** (549.2083)
GC	3.9215*** (1.0305)	−0.9533* (0.4980)	2.9681*** (0.9923)
ERs*GC	−10.3576*** (2.5218)	−52.0130*** (11.8762)	−62.3707*** (13.7590)
URB	5.1159*** (1.1665)	23.8607*** (6.7586)	28.9766*** (7.5480)
FE	−3.7377*** (1.3863)	−30.3266*** (7.1541)	−34.0643*** (7.8939)
HRI	86.0695*** (15.2457)	−513.1767* (277.3744)	322.5305*** (45.3532)

Note: “*, **, and ***” indicate significance at the 10%, 5%, and 1% significance levels, respectively.

3.2 Interaction of GC, ERs, and GTI

We have verified the role of ERs and GC for GTI in manufacturing based on independent perspectives. Next, this paper explores the role of the combination of GC and ERs on GTI from the perspective of coordination and cooperation. Table 2 shows the regression results of ERs and GC. Among them, model 3) contains the regression results of the interaction term with the inclusion of GC and ERs. The main effect and spatial lag coefficients of the interaction term, ERs*GC, are negative, indicating that the combination of GC development and ERs inhibits GTI behavior in manufacturing. These results suggest the negative GC effect as a new type of environmental governance instrument in combination with traditional ERs instruments in terms of driving effects on technological innovation. The reason may be that, after a certain level of ERs intensity, the combination of GC and ERs exerts a greater negative effect on GTI. High-intensity ERs contributed to a rapid increase in production costs for companies in a short time, leading to great social and economic pressure on these companies and hindering the development of GTI. Although GC provides financial support to green enterprises and projects, the interaction term between GC and ERs is negative because GTI is characterized by high risks and long-term lags, and the economic benefits to enterprises are highly uncertain. Therefore, GC does not significantly moderate this negative effect.

3.3 Spatial effect decomposition of ERs and GC on GTI

The previous section outlines the verification of the applicability of the empirical analysis using time-fixed effects

SDM, but we consider possible errors in the spillover effects using point estimation tests, and this section highlights our use of partial differential methods to estimate the direct, indirect, and total effects of ERs and GC on technological innovation (Table 3). First, from the spatial decomposition term, the effect of ERs on local and neighboring GTI is significantly positive, and the technology innovation due to the strengthening of ERs may have had the same promotion effect on other regions (Qu, 2018).

As can be seen from Table 3, there is a positive spillover effect of ERs on GTI in manufacturing in surrounding areas. First, according to the “pollution refuge hypothesis”, if the intensity of ERs in the region increases, polluters will choose to move out of the region because of the rising cost. However, for other regions, the relaxed regulatory policies afford the region a comparative cost advantage, and polluting industries move in. Under the effect of the transfer of polluting industries, the industrial structure of the transferred areas gradually tends toward a lower level. Under the “race to the bottom” effect of local governments, there are ERs policy games and GDP competition in each region. When a certain location implements a more stringent environmental access policy, other regional governments adopt the “race to the bottom” strategy of ERs to achieve GDP growth and attract the inflow of resources by not raising or lowering environmental standards, thereby inhibiting industrial restructuring (Wheeler, 2001). In addition, certain studies have pointed out that in the context of high-quality economic development, the central environmental protection inspectors require the upgrading of ERs policies in each region, and the current competition model between governments is more of a “race to the top” model, where there is a demonstration learning effect when a certain location upgrades their ERs intensity (Holzinger and Sommerer, 2011). However, recently, the central government

TABLE 4 Regression results for coastal areas.

Variables	(1)		(2)		(3)	
	Explanatory variables	Spatial lag term	Explanatory variables	Spatial lag term	Explanatory variables	Spatial lag term
ERs	−242.0669** (114.5396)	−68.4763 (139.5423)	−279.2151** (114.9229)	−210.6165 (190.6699)	−1608.857*** (540.879)	−2179.927* (841.2198)
GC			4.3889* (2.5289)	0.2689 (3.1312)	−2.3887 (3.9406)	−11.5965** (6.1234)
ERs*GC					24.3053** (10.1908)	42.3713** (18.1917)
URB	7.5687*** (2.6582)	−14.7501*** (3.2878)	8.3830*** (2.6901)	−14.0579*** (4.1655)	4.9414* (2.7597)	−5.9774 (6.0476)
FE	−7.6293 (4.7230)	9.9746 (7.7643)	−6.4774 (4.7546)	9.2361 (7.7973)	−0.9915 (4.8866)	14.1393* (7.7702)
HRI	−9.9422 (137.1479)	1571.359*** (191.6342)	−96.3301 (146.0242)	1610.91*** (197.4466)	44.1174 (145.311)	1546.101*** (211.1206)
rho	−0.3244*** (0.1101)		−0.3051*** (0.1158)		−0.3205*** (0.1162)	
sigma2_e	35693.2*** (4764.796)		34680.27*** (4619.154)		31585.64*** (5225.005)	
N	121		121		121	
R ²	0.6973		0.6926		0.7691	
Time fixed effects	Yes		Yes		Yes	
Spatial fixed effects	No		No		No	

has abandoned the past “GDP-only” performance appraisal system and fully incorporated green development indicators, which, to an extent, has promoted the GTI process.

Recently, driven by policies such as ecological civilization construction and high-quality urban development, intergovernmental competition in pursuit of mobility elements has gradually weakened, and the concept of green development has increasingly become an important part of the assessment. Technology-intensive industries have become the driving force of regional development and exert a pivotal impact on economic development, government financial growth, the attraction of investment, raising the share of green innovation inputs, and evolving the industrial structure toward cleanliness to an extent. Our model results may provide theoretical implications for designing effective environmental regulatory policies and avoiding inefficiency losses from government intervention.

Second, Table 3 shows that GC exerted significant positive direct effects and negative spillover effects on manufacturing technology innovation. GC development improves the mismatch between the cost and benefit of GTI through the transmission mechanisms of the “financial support effect,” “capital allocation effect,” and “risk diversification effect” and promotes the transformation of the local manufacturing industry into green

and clean innovation by achieving technological progress. A significant negative spillover relationship exists between GC and GTI in neighboring regions, mainly because the scarcity property of GC, as a financial resource, leads to an increase in credit funds in the region accompanied by a decrease in credit funds in other regions, which reinforces the status quo of interregional competition for resource elements.

3.4 Spatial heterogeneity analysis of GC, ERs, and GTI

China is a vast country, and there are significant differences in resource endowments, economic development levels, and historical and cultural factors between coastal and inland regions. To further investigate regional ERs, GC, and their heterogeneous effects on technological innovation, we divide the sample into the two aforementioned regions and conduct an empirical analysis based on the geographical adjacency matrix (Tables 4, and 5).

The study shows that the local and spatial spillover effects of ERs on GTI in coastal areas are significantly negative, which in turn undermines the GTI process in neighboring areas. If there is no reasonable environmental compensation mechanism among

TABLE 5 Regression results for inland areas.

Variables	(1)		(2)		(3)	
	Explanatory variables	Spatial lag term	Explanatory variables	Spatial lag term	Explanatory variables	Spatial lag term
ERs	−16.6524*** (3.8199)	1.2836 (8.4041)	−5.3412 (4.3867)	22.1422*** (9.4931)	−8.1045 (14.2953)	−15.9790 (31.7198)
GC			0.9492*** (0.2025)	1.3644*** (0.5099)	1.0068*** (0.2387)	1.0165* (0.5742)
ERs*GC					0.0695 (0.3713)	1.0406 (0.8335)
URB	−2.2397*** (0.3749)	−2.5611** (1.2228)	−2.2343*** (0.3546)	−2.2807* (1.2046)	−2.2550*** (0.3538)	−2.5038** (1.2135)
FE	−0.3863** (0.1806)	−0.9990*** (0.2766)	0.1217 (0.2102)	−0.4840 (0.3970)	0.1448 (0.2235)	−0.3505 (0.4125)
HRI	213.1057*** (23.9985)	122.4469** (49.7956)	211.819*** (22.8401)	163.2779*** (47.9725)	208.8026*** (23.0490)	164.8343*** (48.0144)
rho	−0.3728*** (0.1002)		−0.4740*** (0.1013)		−0.4632*** (0.1016)	
sigma2_e	371.9718*** (36.9780)		33.2568*** (33.1742)		328.1741*** (32.9261)	
N	209		209		209	
R ²	0.7377		0.7996		0.7998	
Time fixed effects	Yes		Yes		Yes	
Spatial fixed effects	No		No		No	

local governments, it is difficult to bridge the benefit gap caused by the governance costs and opportunity costs paid by each region for green transformation, which in turn restricts the equity of regional manufacturing innovation development. The impact of ERs in inland areas on GTI is significantly negative, and the impact on GTI in surrounding areas is insignificant, which is mainly constrained by resource endowment, industrial structure, and institutional culture, thereby hindering the stimulation of the dynamics of regional GTI activities.

GC in coastal areas exerts a positive effect on green technologies in the region and a negative effect on GTI in neighboring regions. At the firm level, this can be explained by the fact that the strict credit granting policy of GC, by setting environmental access thresholds, induces heavily polluting firms to focus on investment in production factors at the end of pollution reduction, which in turn inhibits local GTI activities. As GC resources become the focus of competition between regions, the abundance of local GC resources further exacerbates the innovation financing dilemma of neighboring regions, thereby inhibiting the GTI level in neighboring regions (Zhou et al., 2021). The local effect of GC on GTI in inland regions is significantly positive, while the spatial spillover effect

does not pass the significance test, indicating that the competition for GC resources in inland regions does not intensify. The reason for this phenomenon is that coastal regions have advantages in terms of economic conditions, market system formations, and technological innovation resource reserves. In particular, the pace of economic green transformation has always been at the forefront for China, with more complete ERs policy measures and mature pollution control experience. Therefore, GC can be combined with traditional ERs instruments to create a gaining effect of regional technological innovation activities. However, the impact of the cross-sectional term of ERs and GC on local technological innovation in inland regions is insignificant, indicating that GC policies and traditional ERs instruments in inland regions have not yet produced incentive-matching effects.

3.5 Robustness tests

To better verify the mechanism of action between ERs, GC, and GTI, we use the following methods to test the robustness of the empirical results and the results are reported in Table 6.

TABLE 6 Results of the robustness test.

Variables	Change variables		Matrix replacement	
	Explanatory variables	Spatial lag term	Explanatory variables	Spatial lag term
ERs	−0.0002247* (0.0000586)	0.0021512*** (0.0006652)	215.6618*** (63.9564)	1049.1520* (801.2933)
GC	−0.0000447*** (0.0000118)	−0.000613*** (0.0000195)	3.4224*** (1.0000)	−8.2127* (4.3694)
ERs*GC	9.26e-06* (1.95e-06)	−0.0000719*** (0.0000191)	−6.6493*** (1.5378)	−6.5004 (16.0011)
URB	0.0001161*** (0.0000114)	0.0001309*** (0.0000261)	−3.4978*** (0.8891)	−20.1427*** (3.3156)
FE	−0.0000403*** (0.0000149)	−0.0001596*** (0.000026)	−1.6417* 1.0126)	105.0759*** (12.7486)
HRI	−0.0031841*** (0.0006714)	−0.0026401** (0.0013354)	306.9133*** (36.0654)	617.9172* (384.3012)
rho	0.1502739*** (0.0024763)		−0.4982*** (0.1116)	
sigma2_e	2.58e-06*** (2.00e-07)		12151.94*** (962.5566)	
N	330		330	
R ²	0.5306		0.7930	
Time fixed effects	Yes		Yes	
Spatial fixed effects	No		No	

- (1) Considering the interaction of ERs strategies and the spillover effects of GTI levels occurring in neighboring regions, as well as multiple factors, geographical and cognitive proximity also exert an impact. Therefore, here, the economic spatial weight matrix is used instead of the 0–1 geographical neighborhood weight matrix, and the results of the study do not show a significant change in the sign and significance of the regression coefficients of the core variables, confirming that our findings are extremely robust.
- (2) The combined index of GIPAs and green utility patent applications is chosen as the measure of GTI, based on which GTI was calculated. Through the model analysis, we observe that the regression results are very robust for the green innovation variables and the replacement of the weight matrix, which further validates the scientific nature of our findings.

4 Conclusion and policy implications

4.1 Conclusion and discussion

By incorporating both environmental regulation and green credit policies into the analytical framework of GTI, this paper empirically tests the joint effect of GC and ERs on GTI. Based on

inter-regional interaction strategies and differences, this paper also explores the local effects and spatial spillover effects of environmental regulation and green credit at the regional level, and empirically examines the uneven locational characteristics of the technological innovation effects of ERs and GC. The main findings of this paper include the following: 1) the local impact and spatial spillover effect of ERs on GTI in manufacturing industries at the national level is mainly reflected in the inhibitory effect. The negative effect of “following cost” is greater than the “compensation effect” of technological innovation; that is, environmental regulation policies that raise firms’ production costs and lack economic incentives are ineffective in promoting innovation. GC policies can stimulate the transformational development of GTI in local manufacturing industries, but the scarcity of resources weakens the innovation level of green technology in manufacturing industries in neighboring provinces through spatial spillover effects. 2) The combination of GC development and ERs can produce synergistic and complementary incentive-coordinated technology innovation driving effects. The complementary effects of GC fund supply and product, process, and emission reduction are significant, making the economic performance of ERs for technology innovation prominent. Considering the ecological environment has quasi-public goods characteristics, GTI is a complex systemic project, and green finance, as a new

market-based instrument for ecological and environmental governance, can play a complementary role with traditional environmental regulatory systems in a more effective, equitable and sustainable manner. However, it is difficult to promote green innovation transformation by purely relying on the regulation means of GC. The traditional ERs means are fundamental in stimulating technology innovation despite the hard constraint of commercial banks and emission enterprises (Feng and Liang, 2022). 3) The eastern coastal regions with strong innovation vitality and endogenous dynamics. For inland regions with little experience in environmental governance and a weak innovation base, a “circular-coordination” mechanism for GC resources should be constructed. By region, there are regional differences in the technological innovation effects of ERs and GC. The local effect of ERs on GTI in coastal areas is significantly positive; that is, strong innovation vitality and endogenous dynamics of coastal regions enable environmental regulation measures and green financial development produces incentive-matching effects. Although environmental regulation measures for inland areas with little experience in environmental governance and a weak innovation base are significantly negative for local GTI and insignificant for neighboring GTI, GC effectively stimulates the dynamic role of local GTI activities and exerts a significant marginal effect on the financial dilemma of local manufacturing investment in research and development (R&D) green technology.

The following shortcomings exist for this study: 1) It is appropriate to use prefecture-level city data to explore the spatial effects of ERs, GC, and GTI in manufacturing based on regional scales. Given the availability of GC-related data, provincial panel data, and the large error in measuring GC variables by indirect methods, there are limitations in the generalizability of the study findings. 2) The “Porter hypothesis” and the regulatory role of GC are closely related to the type of ERs, which include formal ERs instruments (command and control and market incentives) and informal ERs instruments (information disclosure, public participation, and voluntary regulation) (Zhou et al., 2022). However, the influence factors considered in this study are relatively single, and different types of ERs tools can be included in the same model in future studies to examine their differential impacts on GTI in manufacturing. 3) Considering that the spatial spillover effect follows the law of distance decay, there is a certain bias in the empirical test based on the entire domain only, and the local spatial matrix of different distance ranges should be set in the future to explore the GTI effect.

4.2 Policy implications

Based on the empirical findings of our study, the following policy implications about the integration of ERs and green finance policies are proposed accordingly.

First, based on the spatial dependence of interprovincial manufacturing GTI, local governments should establish a good competitive relationship with each other, strengthen strategic interoperability and positive interaction with neighboring regions, and stimulate local green development with the implementation of green innovation and transformation strategies by regional industries holistically.

Second, the central government should abandon the traditional approach in the design of policies, systems, and processes for environmental and social risk management, and coordinate a regionally differentiated GC system instead. GC policies should be made on a “person-by-person” basis; that is the eastern coastal should leverage the role of commercial banks and other financial sectors in promoting the supply of GC funds to meet the financial needs of high-level technological innovation. It is necessary to improve the green policy system, such as the environmental information disclosure of enterprises, information sharing between environmental protection departments and banks, and strengthen the prescreening and post-supervision mechanism to weaken the influence of information asymmetry. For inland regions, local governments can create an innovative atmosphere through financial support, construction of innovative subjects, and strengthening intellectual property protection, so as to construct a cooperative mechanism and innovation-supportive for interregional credit policies (Liu and Nie, 2022) in the place of the interregional competition for resources with a cooperative mechanism for interregional credit resources to support GTI (Liu and Nie, 2022).

Third, as GTI is a complex systemic project, it is difficult to promote green innovation transformation by purely relying on the regulation means of GC. The traditional ERs means are fundamental in stimulating technology innovation despite the hard constraint of commercial banks and emission enterprises (Feng and Liang, 2022). The ERs system can be planned in a unified manner by establishing a coordinating management institution for GTI, GC, and ERs to coordinate green development data, such as scientific and technological innovation, capital loans, and pollution emissions, and make joint efforts from the market investment and financing and government supervision levels (Chen et al., 2022).

Fourth, considering that GTI activities are characterized by high risks, economies of scale, and innovation spillovers (Wicki and Hansen, 2019), the institutional environment for technology innovation is the key to the “Porter effect.” Local governments can create an innovative atmosphere through financial support, construction of innovative subjects, strengthening intellectual property protection, and other basic systems, which in turn attract the gathering of high-end production factors, such as capital, talents, and knowledge. Concomitantly, the GC policy can also be dovetailed with the science and technology policy, incorporate the green R&D investment and performance of enterprises into the environmental policy assessment, and make joint efforts from the market investment and financing and government supervision levels (Chen et al., 2022).

Data availability statement

The original contributions presented in the study are included in the article/supplementary material, further inquiries can be directed to the corresponding author.

Author contributions

Conceptualization, LJ, JZ, and YW; methodology, JZ and YW.; software, YW; writing—original draft preparation, LJ; writing—review and editing, LJ and JZ; project administration, LJ; funding acquisition, LJ. All authors have read and agreed to the published version of the manuscript.

Funding

This research was funded by the National Natural Science Foundation of China, grant number 72074238, 72074239; the Fundamental Research Funds for the Central University of

Finance and Economics; and the Double First-class Discipline Construction Project of Central University of Finance and Economics.

Conflict of interest

The authors declare that the research was conducted in the absence of any commercial or financial relationships that could be construed as a potential conflict of interest.

Publisher's note

All claims expressed in this article are solely those of the authors and do not necessarily represent those of their affiliated organizations, or those of the publisher, the editors and the reviewers. Any product that may be evaluated in this article, or claim that may be made by its manufacturer, is not guaranteed or endorsed by the publisher.

References

- Anselin, L., and Griffith, D. A. (2010). Do spatial effects really matter in regression analysis? *Pap. Reg. Sci.* 65, 11–34. doi:10.1111/J.1435-5597.1988.TB01155.X
- Bai, Y., Song, S. Y., Jiao, J. L., and Yang, R. R. (2019). The impacts of government R&D subsidies on green innovation: Evidence from Chinese energy-intensive firms. *J. Clean. Prod.* 233 (1), 819–829. doi:10.1016/j.jclepro.2019.06.107
- Behera, P., and Sethi, N. (2022). Nexus between environment regulation, FDI, and green technology innovation in OECD countries. *Environ. Sci. Pollut. Res.* 29, 52940–52953. doi:10.1007/s11356-022-19458-7
- Böcher, M. (2012). A theoretical framework for explaining the choice of instruments in environmental policy. *For. Policy Econ.* 16, 14–22. doi:10.1016/j.forpol.2011.03.012
- Bressanelli, G., Perona, M., and Sacconi, N. (2019). Challenges in supply chain redesign for the circular economy: A literature review and a multiple case study. *Int. J. Prod. Res.* 57 (23), 7395–7422. doi:10.1080/00207543.2018.1542176
- Bressanelli, G., Visintin, F., and Sacconi, N. (2022). Circular economy and the evolution of industrial districts: A supply chain perspective. *Int. J. Prod. Econ.* 243, 108348. doi:10.1016/j.ijspe.2021.108348
- Chen, L., Wang, N., Li, Q. Y., and Zhou, W. J. (2022). Environmental regulation, foreign direct investment and China's economic development under the new normal: Restrain or promote? *Environ. Dev. Sustain.*, 1–22. doi:10.1007/s10668-022-02239-0
- Chen, Z. G., Zhang, Y. Q., Wang, H. S., Ouyang, X., and Xie, Y. X. (2022). Can green credit policy promote low-carbon technology innovation? *J. Clean. Prod.* 359, 132061. doi:10.1016/j.jclepro.2022.132061
- de Oliveira, U. R., Espindola, L. S., da Silva, I. R., da Silva, L. N., and Rocha, H. M. (2018). A systematic literature review on green supply chain management: Research implications and future perspectives. *J. Clean. Prod.* 187, 537–561. doi:10.1016/j.jclepro.2018.03.083
- Falcone, P. M. (2020). Environmental regulation and green investments: The role of green finance. *Int. J. Green. Econ.* 14 (2), 159–173. doi:10.1504/IJGE.2020.109735
- Feng, Y. C., and Liang, Z. (2022). How does green credit policy affect total factor productivity of the manufacturing firms in China? The mediating role of debt financing and the moderating role of environmental regulation. *Environ. Sci. Pollut. Res.* 29, 31235–31251. doi:10.1007/s11356-021-17984-4
- Geng, W. L., Li, Y. Y., Zhang, P. Y., Yang, D., Jing, W. L., and Rong, T. Q. (2022). Analyzing spatio-temporal changes and trade-offs/synergies among ecosystem services in the Yellow River Basin China. *Ecol. Indic.* 138, 108825. doi:10.1016/j.ecolind.2022.108825
- Guo, L. L., Qu, Y., and Tseng, M. L. (2017). The interaction effects of environmental regulation and technological innovation on regional green growth performance. *J. Clean. Prod.* 162, 894–902. doi:10.1016/j.jclepro.2017.05.210
- Guo, Q., Zhou, M., Liu, N. N., and Wang, Y. Y. (2019). Spatial effects of environmental regulation and green credits on green technology innovation under low-carbon economy background conditions. *Int. J. Environ. Res. Public Health* 16 (17), 3027. doi:10.3390/ijerph16173027
- Hassan, T., Khan, Y., He, C. L., Chen, J., Alsagr, N., Song, H. M., et al. (2022). Environmental regulations, political risk and consumption-based carbon emissions: Evidence from OECD economies. *J. Environ. Manage.* 320, 115893. doi:10.1016/j.jenvman.2022.115893
- He, C., and Yan, G. J. (2020). Path selections for sustainable development of green finance in developed coastal areas of China. *J. Coast. Res.* 104 (1), 77–81. doi:10.2112/JCR-SI104-014.1
- Holzinger, K., and Sommerer, T. (2011). 'Race to the bottom' or 'race to brussels'? Environmental competition in europe. *J. Common Mark. S.* 49 (2), 315–339. doi:10.1111/j.1468-5965.2010.02135.x
- Hsu, P. H., Tian, X., and Xu, Y. (2014). Financial development and innovation: Cross-country evidence. *J. Financ. Econ.* 112 (1), 116–135. doi:10.1016/j.jfineco.2013.12.002
- Huang, L. X., Liu, S. L., Han, Y. H., and Peng, K. M. (2020). The nature of state-owned enterprises and collection of pollutant discharge fees: A study based on Chinese industrial enterprises. *J. Clean. Prod.* 271, 122420. doi:10.1016/j.jclepro.2020.122420
- Irfan, M., Razzaq, A., Sharif, A., and Yang, X. D. (2022). Influence mechanism between green finance and green innovation: Exploring regional policy intervention effects in China. *Technol. Forecast. Soc. Change* 182, 121882. doi:10.1016/j.techfore.2022.121882
- Jayachandran, S. (2022). How economic development influences the environment. *Annu. Rev. Econ.* 14, 229–252. doi:10.1146/annurev-economics-082321-123803
- Jiang, H. L., Wang, W. D., Wang, L., and Wu, J. H. (2020). The effects of the carbon emission reduction of China's green finance: An analysis based on green credit and green venture investment. *Fin. Forum.* 25 (11), 39–48. doi:10.16529/j.cnki.11-4613/f.2020.11.006
- Karmaker, S. C., Hosan, S., Chapman, A. J., and Saha, B. B. (2021). The role of environmental taxes on technological innovation. *Energy* 232, 121052. doi:10.1016/j.energy.2021.121052

- Kolkiş, S., Krajacic, G., Duic, N., Rosen, M. A., and Al-Nimr, M. A. (2020). Advances in integration of energy, water and environment systems towards climate neutrality for sustainable development. *Energy Convers. Manag.* 225, 113410. doi:10.1016/j.enconman.2020.113410
- Li, M. Y., and Gao, X. (2022). Implementation of enterprises' green technology innovation under market-based environmental regulation: An evolutionary game approach. *J. Environ. Manage.* 308, 114570. doi:10.1016/j.jenvman.2022.114570
- Liu, J. Y., Xia, Y., Fan, Y., Lin, S. M., and Wu, J. (2017). Assessment of a green credit policy aimed at energy-intensive industries in China based on a financial CGE model. *J. Clean. Prod.* 163, 293–302. doi:10.1016/j.jclepro.2015.10.111
- Liu, S., Xu, R. X., and Chen, X. Y. (2021). Does green credit affect the green innovation performance of high-polluting and energy-intensive enterprises? Evidence from a quasi-natural experiment. *Environ. Sci. Pollut. Res.* 28, 65265–65277. doi:10.1007/s11356-021-15217-2
- Liu, X. M., and Nie, W. D. (2022). Study on the coupling coordination mechanism of green technology innovation, environmental regulation, and green finance. *Environ. Sci. Pollut. Res.* 29, 71796–71809. doi:10.1007/s11356-022-20905-8
- Lv, C. C., Shao, C. H., and Lee, C. C. (2021). Green technology innovation and financial development: Do environmental regulation and innovation output matter? *Energy Econ.* 98, 105237. doi:10.1016/j.eneco.2021.105237
- Mbanyele, W., and Wang, F. R. (2022). Environmental regulation and technological innovation: Evidence from China. *Environ. Sci. Pollut. Res.* 29, 12890–12910. doi:10.1007/s11356-021-14975-3
- Nabeeh, N. A., Abdel-Basset, M., and Soliman, G. (2021). A model for evaluating green credit rating and its impact on sustainability performance. *J. Clean. Prod.* 280, 124299. doi:10.1016/j.jclepro.2020.124299
- Ni, Y., Chen, B. Y., and Wang, Y. W. (2020). Financial development, environmental regulation and green total factor productivity—an empirical analysis based on spatial Durbin model[J]. *J. Guizhou Univ. Fin. Econ.* (03), 12–21. doi:10.3969/j.issn.1003-6636.2020.03.002
- Nie, G. Q., Zhu, Y. F., Wu, W. P., Xie, W. H., and Wu, K. X. (2022). Impact of voluntary environmental regulation on green technological innovation: Evidence from Chinese manufacturing enterprises. *Front. Energy Res.* 10, 889037. doi:10.3389/fenrg.2022.889037
- Peng, C., and Yuan, P. (2018). Environmental regulation intensity and provincial economic growth in China—a reconstruction based on the intensity of environmental regulation[J]. *J. Yunnan Univ. Fin. Econ.* 34 (10), 37–51. doi:10.16537/j.cnki.jynufe.000353
- Qu, W. B. (2018). Environmental regulation, spatial spillover and regional ecological efficiency: An empirical analysis of Douban Panel Model based on space. *J. Beijing Inst. Tech. Soc. Sci. Ed.* 20 (6), 27–33. doi:10.15918/j.jbitss1009-3370.2018.5179
- Ren, S. G., Li, X. L., Yuan, B. L., Li, D. Y., and Chen, X. H. (2018). The effects of three types of environmental regulation on eco-efficiency: A cross-region analysis in China. *J. Clean. Prod.* 173, 245–255. doi:10.1016/j.jclepro.2016.08.113
- Shao, S., Li, X., Cao, J. H., and Yang, L. L. (2016). Economic policy options for haze pollution management in China—a perspective based on spatial spillover effects. *Econ. Res.* 51 (09), 73–88.
- Sharif, A., Saqib, N., Dong, K. Y., and Khan, S. A. R. (2022). Nexus between green technology innovation, green financing, and CO₂ emissions in the G7 countries: The moderating role of social globalisation. *Sustain. Dev.* 1–13. doi:10.1002/sd.2360
- Shen, F., Liu, B., Luo, F., Wu, C. C., Chen, H., and Wei, W. D. (2021). The effect of economic growth target constraints on green technology innovation. *J. Environ. Manage.* 292, 112765. doi:10.1016/j.jenvman.2021.112765
- Soundararajan, P., and Vivek, N. (2016). Green finance for sustainable green economic growth in India. *Agric. Econ.* 62, 35–44. doi:10.17221/174/2014-AGRICECON
- Su, C. W., Li, W. H., Umar, M., and Lobont, O. R. (2022). Can green credit reduce the emissions of pollutants? *Econ. Anal. Policy* 74, 205–219. doi:10.1016/j.eap.2022.01.016
- Suki, N. M., Suki, N. M., Afshan, S., Sharif, A., Kasim, M. A., and Mohd Hanafi, S. R. (2022). How does green technology innovation affect green growth in ASEAN-6 countries? Evidence from advance panel estimations. *Gondwana Res.* 111, 165–173. doi:10.1016/j.gr.2022.06.019
- Wang, H. T., Qi, S. Z., Zhou, C. B., Zhou, J. J., and Huang, X. Y. (2022). Green credit policy, government behavior and green innovation quality of enterprises. *J. Clean. Prod.* 331, 129834. doi:10.1016/j.jclepro.2021.129834
- Wei, W. D., Cai, W. Q., Guo, Y., Bai, C. Q., and Yang, L. Z. (2020). Decoupling relationship between energy consumption and economic growth in China's provinces from the perspective of resource security. *Resour. Policy* 68, 101693. doi:10.1016/j.resourpol.2020.101693
- Wheeler, D. (2001). Racing to the bottom? Foreign investment and air pollution in developing countries. *J. Environ. Dev.* 10 (3), 225–245. doi:10.1596/1813-9450-2524
- Wicki, S., and Hansen, E. G. (2019). Green technology innovation: Anatomy of exploration processes from a learning perspective. *Bus. Strategy Environ.* 28 (6), 970–988. doi:10.1002/bse.2295
- Yang, H. S., Chen, S. L., and Zhou, Y. Z. (2008). Local government competition and environmental policy-empirical evidence from province's governments in China. *South China J. Econ.* (6), 15–30. doi:10.3969/j.issn.1000-6249.2008.06.002
- Zhang, H., Liu, Z., and Zhang, Y. J. (2022). Assessing the economic and environmental effects of environmental regulation in China: The dynamic and spatial perspectives. *J. Clean. Prod.* 334, 130256. doi:10.1016/j.jclepro.2021.130256
- Zhang, H., and Wei, X. P. (2014). Green paradox or forced emission-reduction: Dual effect of environmental regulation on carbon emissions. *China Pop. Res. Environ.* 24 (9), 21–29. doi:10.3969/j.issn.1002-2104.2014.09.004
- Zhang, P. Y., Yang, D., Qin, M. Z., and Jing, W. L. (2020). Spatial heterogeneity analysis and driving forces exploring of built-up land development intensity in Chinese prefecture-level cities and implications for future urban land intensive use. *Land Use Policy* 99, 104958. doi:10.1016/j.landusepol.2020.104958
- Zhang, S. L., Wu, Z. H., He, Y. N., and Hao, Y. (2022). How does the green credit policy affect the technological innovation of enterprises? Evidence from China. *Energy Econ.* 113, 106236. doi:10.1016/j.eneco.2022.106236
- Zhao, A. W., Wang, J. Y., Sun, Z. Z., and Guan, H. J. (2022). Environmental taxes, technology innovation quality and firm performance in China—a test of effects based on the porter hypothesis. *Econ. Anal. Policy* 74, 309–325. doi:10.1016/j.eap.2022.02.009
- Zhao, X., Ma, X. W., Chen, B. Y., Shang, Y. P., and Song, M. L. (2021). Challenges toward carbon neutrality in China: Strategies and countermeasures. *Resour. Conserv. Recycl.* 176, 105959. doi:10.1016/j.resconrec.2021.105959
- Zhong, Z. Q., and Peng, B. H. (2022). Can environmental regulation promote green innovation in heavily polluting enterprises? Empirical evidence from a quasi-natural experiment in China. *Sustain. Prod. Consum.* 30, 815–828. doi:10.1016/j.spc.2022.01.017
- Zhou, G. Y., Liu, C., and Luo, S. M. (2021). Resource allocation effect of green credit policy: Based on DID model. *Math. (Basel)* 9 (2), 159. doi:10.3390/math9020159
- Zhou, Z. Q., Feng, H. H., Wang, H. L., and Wang, K. X. (2022). Influence of heterogeneous environmental regulation policies on the strategy of pollutant discharge for enterprise: An evolutionary game approach. *Environ. Res. Commun.* 4 (9), 095002. doi:10.1088/2515-7620/ac8971



OPEN ACCESS

EDITED BY
Pengyan Zhang,
Henan University, China

REVIEWED BY
Wei Wei,
Northwest Normal University, China
Wei Zhou,
Southwest University, China

*CORRESPONDENCE
Hong Chen,
✉ chenplan@126.com

SPECIALTY SECTION
This article was submitted to
Environmental Informatics
and Remote Sensing,
a section of the journal
Frontiers in Environmental Science

RECEIVED 23 November 2022
ACCEPTED 19 December 2022
PUBLISHED 10 January 2023

CITATION
Chen Z, Chen H, Yang M, Wang X, Jiang Y
and Zhang W (2023), Heterogeneity and
optimization of ecological security pattern
on a mountain town: A case of Tianzhu
County in the Hexi Corridor, China.
Front. Environ. Sci. 10:1106379.
doi: 10.3389/fenvs.2022.1106379

COPYRIGHT
© 2023 Chen, Chen, Yang, Wang, Jiang
and Zhang. This is an open-access article
distributed under the terms of the [Creative
Commons Attribution License \(CC BY\)](#).
The use, distribution or reproduction in
other forums is permitted, provided the
original author(s) and the copyright
owner(s) are credited and that the original
publication in this journal is cited, in
accordance with accepted academic
practice. No use, distribution or
reproduction is permitted which does not
comply with these terms.

Heterogeneity and optimization of ecological security pattern on a mountain town: A case of Tianzhu County in the Hexi Corridor, China

Zhijie Chen¹, Hong Chen^{2,3*}, Minan Yang¹, Xi Wang¹,
Yuefeng Jiang^{2,3} and Wei Zhang¹

¹School of Architecture and Urban Planning, Lanzhou Jiaotong University, Lanzhou, China, ²Faculty of Geomatics, Lanzhou Jiaotong University, Lanzhou, China, ³National-Local Joint Engineering Research Center of Technologies and Applications for National Geographic State Monitoring, Lanzhou, China

As a primary concern in the ecosystem, understanding the impact of spatial heterogeneity of ecological networks on the development of environmental sustainability has overarching significance. The Tibetan Plateau's edge is a vital contribution to the study of the plateau's ecological network. However, there are few studies and explorations on the county-level ecological network in the arid region. This study aimed to evaluate ecological network spatial patterns in Tianzhu County and establish an ecological security evaluation index system. We used the minimum cumulative resistance (MCR) model and built an ecological resistance surface model from the exploratory spatial data analysis (ESDA) method. Then, by identifying ecological corridors and ecological nodes from the gravity model, we analyzed the ecological security pattern and proposed specific plans for optimizing the situation. The results showed that 1) county ecological security overall has been lower, and its values showed spatial heterogeneity in each direction, and 2) the Z-Score of the ecological security evaluation index was 70.1893, which shows ecological vulnerability in the arid region has significant spatial autocorrelation. The study identified 156 ecological corridors and 112 ecological nodes, which formed an ecological spatial pattern of "one belt and three zones." Our analytical framework offers a valuable tool for constructing ecological security patterns in Tianzhu County and selecting "sources" at the regional scale, which can be applied to landscapes and geographical contexts for sustainable development in arid regions.

KEYWORDS

land use, ecological security, spatial pattern, MCR, arid region

1 Introduction

The ecosystem is an essential basis for human survival and development, which is also a support system of human life. It is the primary part of the regional ecological pattern, which connects isolated landscape patches by ecological corridors (Jiao et al., 2021; Peng et al., 2022). This system combines with point, line, and surface to improve the self-discipline of the landscape and maintain regional ecological surrounding stability (Fan and Myint, 2014; Liang et al., 2022). However, the ecological network is a special and complex network of landscape ecology, which is a complex network that is composed of three pattern elements—ecological sources, ecological corridors, and ecological nodes (Luo et al., 2022). Therefore, the structure, function, and interrelationship of the ecological network have been important research points in network and science and landscape ecology research (Jiang et al., 2022; Shen et al., 2022). The

integrity of the ecological network structure and its advantages and disadvantages will determine whether the ecological network's function can work properly.

According to integrated landscape ecology and land planning theory, in recent years, scholars built ecological networks, including Nature 2000 Network, Emerald Network, Dutch National Ecological Network, and European Ecological Network (Möckel, 2017). Aiming at different objects, the research of ecological network construction mainly focuses on the forest ecological network, wetland ecological network, urban green space ecological network, and desert ecological network protection (Raji et al., 2022). Ecological network construction had been formed on the basis of a research paradigm, including ecological source identification and ecological corridor identification. It mainly identifies ecological sources by assessing the suitability of ecological habitats and the importance of ecological connectivity (Wan et al., 2019; Streib et al., 2020). Among them, the importance of environmental assessment is the most used method. The method of identifying ecological corridors by constructing resistance surfaces is usually based on the value distribution of land cover. The lowest cost path analysis is usually used to extract ecological corridors. However, this study considers the obstacles of landscape heterogeneity to ecological flow, although they ignore the mutual attraction of ecological resources and do not consider the interaction of ecological resources (Fan et al., 2017; Cunha and Magalhães, 2019). The application of the gravity model in space interaction provides a way to study the interaction between ecological sources. The gravity model was first used to study the inter-city spatial structure and later widely used in regional economic research, urban group interaction, and inter-city trade research. At present, gravity models have been widely used in the study of regional economic connections or spatial interactions. Based on the interaction force theory, using the improved MCR model and gravity model, the ecological network of the study area is extracted by comparing the minimum cumulative ecological resistance and the maximum ecological gravity between different ecological sources (Hu et al., 2019; Dai et al., 2021). In China, the types of Tianzhu landforms are more special, including alpine mountains on the Qinghai-Tibet Plateau, an oasis in arid areas, and monsoon valleys. Complex climatic types and terrain and geomorphology together affect the formation of ecological networks with great ecological value and vulnerability (Huang et al., 2022; Wang et al., 2022). To this purpose, ecological networks are even more needed to connect broken habitats through ecological corridors and ecological nodes to form a complete landscape network to ensure regional ecological security (Yang et al., 2022a; Dai et al., 2022). This abstracts the actual regional ecological network into an ecological topology network.

The stability and balance of the ecosystem will determine human life directly. However, the utilization and development scale of land has increased dramatically over the past century. Especially in northwestern China, this tendency, therefore, caused serious damage to the structure and function of the ecosystem and produced a series of problems, such as a sharp decline in biodiversity, degeneration of grassland, and soil erosion and desertification (Zhou et al., 2020; Geng et al., 2022). This phenomenon is more obvious in Tibet and China. In addition, the major climate type of Tianzhu is alpine on the Tibetan Plateau and the

climate of the local area is arid desert and monsoon type (Gu et al., 2018; Zhang et al., 2020). So, the diversity and complexity of climate are especially prominent here, which have a significant impact on the ecosystem. The security of the ecosystem and sustainable development in this region have been the focus of research in our study for a long time (Wang and Pan, 2019; Wen and Hou, 2021). We used the gravity model and minimum cumulative resistance model to extract the ecological network. Through the ecosystem, importance assessment identifies ecological sources. The improved ecological resistance model will be used to calculate the minimum cumulative ecological resistance between ecological sources, and the improved ecological gravity model will be used to calculate the ecological gravity between ecological sources. According to the interaction force theory, the ecological corridor is determined by comparing the combined forces between different ecological sources. Finally, it provides new methods and new research perspectives for regional ecological planning and also provides reference and guidance for the formulation of environmental protection and sustainable development policies in the alpine mountainous regions of the arid region.

2 Data sources and methods

2.1 Study area

Tianzhu is situated in the arid region of Northwest China. It is situated at the intersection of the Qinghai-Tibet plateau, the loess plateau, the Inner Mongolia plateau, and the northeast edge of the Qinghai-Tibet plateau (Figure 1A). Its altitude is between 2,040 m and 4,874 m, with an average altitude of 3,075.86 m. The landform is a priority in the mountainous area, mountain range crisscross, ravine crisscross, and more mountains. Situated in the middle of the county, whistling lies between east and west. It is the throat of the ancient Silk Road and the gateway of the Hexi Corridor (Figure 1B). Furthermore, it is the watershed between the inland river and the outflow river. Rivers are widely disseminated, rich in water resources, and divided into two major water systems: the Shiyang river system and the Yellow River system (Figure 1C). The annual runoff of surface water is 1.024 billion m³, and the recharge of groundwater is 420 million m³. With whistling as the boundary, the south of Wushaoling has a continental plateau monsoon climate, while the north has a temperate continental semi-arid climate, with an average yearly temperature of -8°C to 4°C. The vertical distribution of the climatic zone is very obvious, and the weather in small regions is complex and changeable, with droughts, hail, floods, frost, snow, and other natural disasters. Tianzhu has jurisdiction over 17 townships.

2.2 Data sources

In this study, land use data were obtained from the GlobeLand30 (GLC30) dataset (<https://www.globallandcover.com/>) for the year 2020. The study area covers seven types of land use: cropland, forest, grassland, shrubland, wetland, water, impervious surface (IS), and bare land. The average overall accuracy of the data is 84.61%, and the average Kappa coefficient is .80 (Bouslihimi et al., 2022). The DEM datasets with 30 m spatial resolution were obtained from the

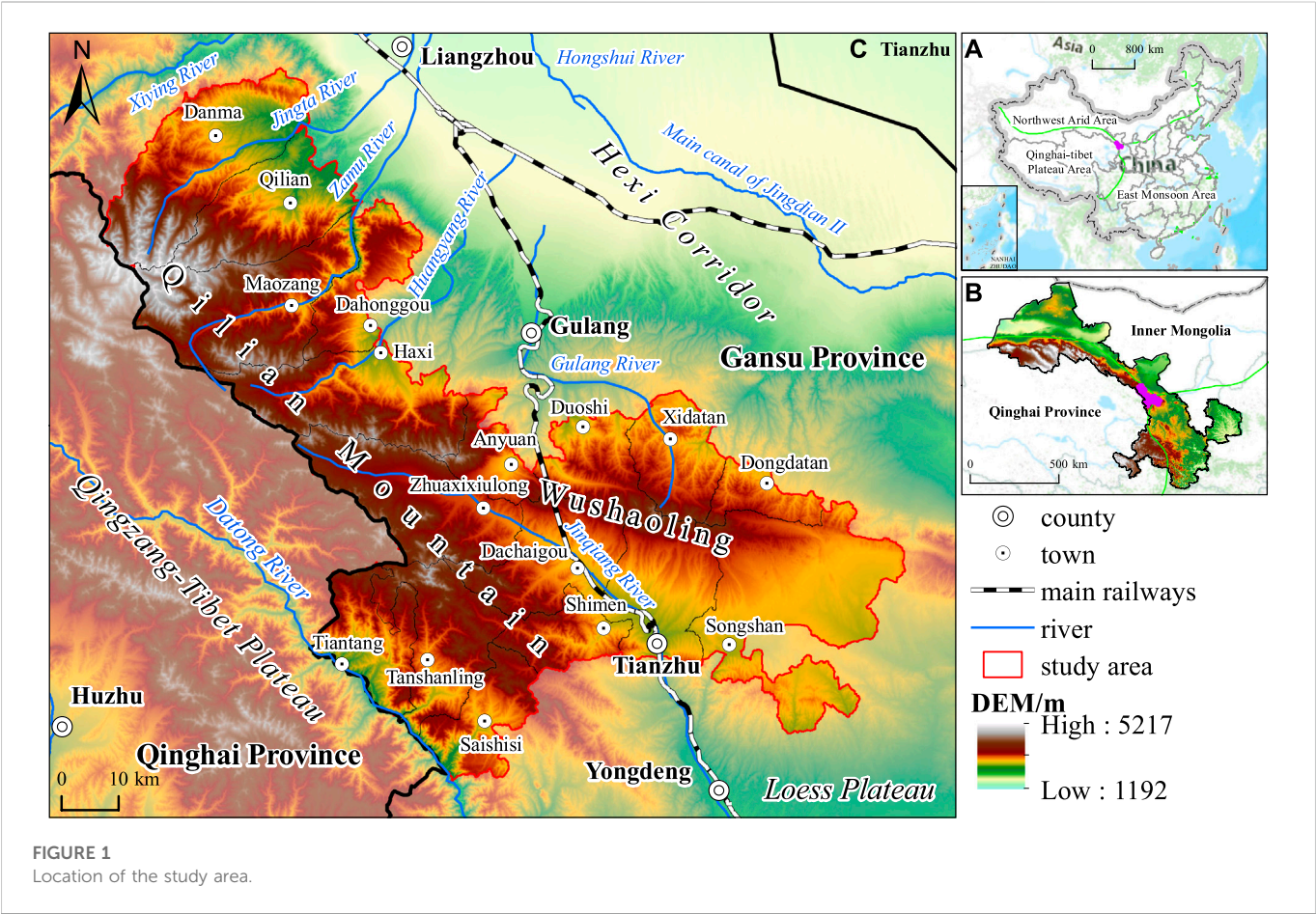


TABLE 1 List of the in this study.

Category	Data	Year	Spatial resolution
Land use	Land use	2020	30 m
Terrain factors	DEM/slope	2010	30 m
Basic data	Boundaries/rivers	2017	Vector
Ecological factors	NDVI	2019	1 km
	Soil erosion	2010	1 km
Road networks	Distance to main roads	2020	30 m
	Distance to railways	2020	30 m

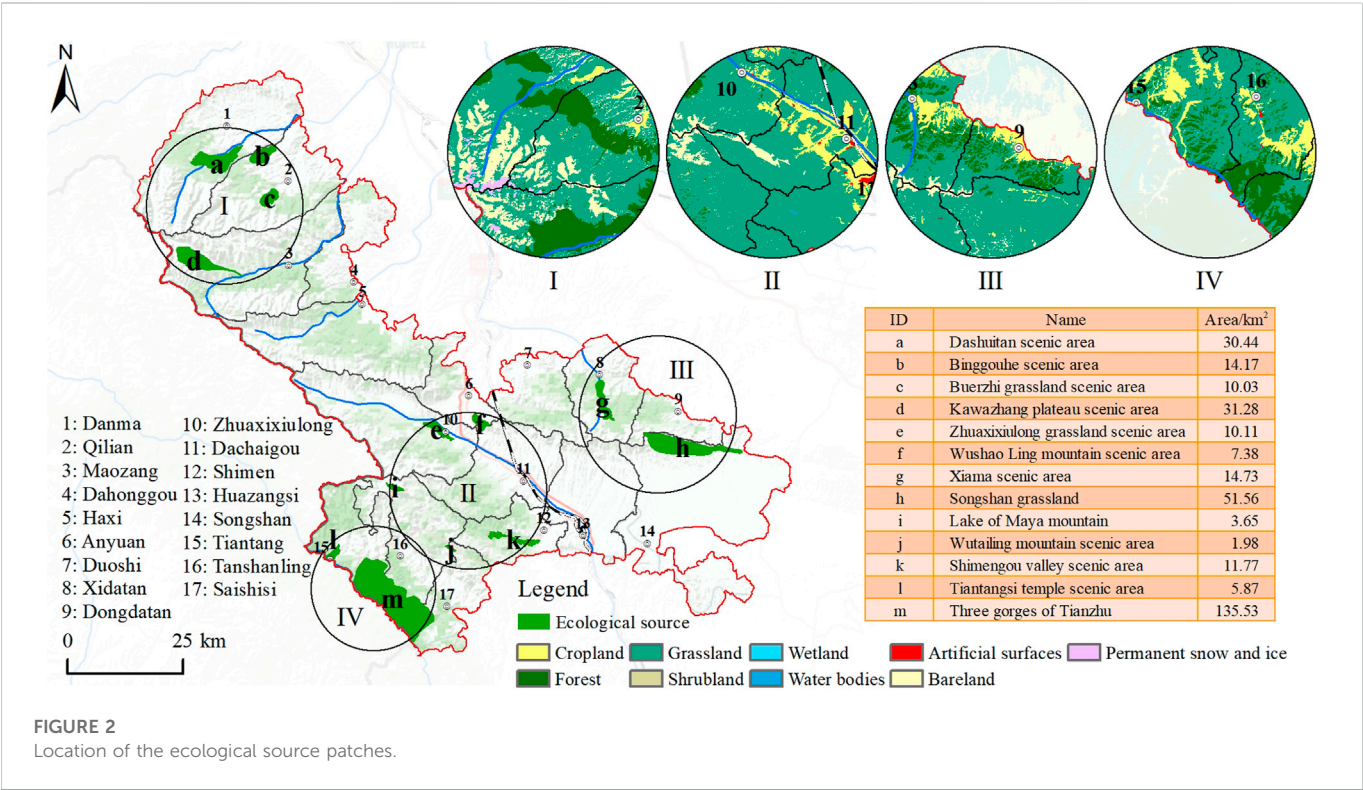
Shuttle Radar Topography Mission (SRTM). The slope was derived from the SRTM DEM dataset. The basic geographic data, NDVI, and soil erosion datasets were obtained from the Resource and Environment Science Data Centre of the Chinese Academy of Sciences (<https://www.resdc.cn>). ArcMap10.4 was mainly used for data processing and calculation. Distance analysis, reclassification, and raster calculation of raw data are shown in Table 1. Ecological security assessment uses zonal tools for statistical analysis. In the analysis of spatial heterogeneity, a 1 km × 1 km grid was created based on the fishnet tool, and hot spot analysis (Geti's-Ord Gi*) was used in spatial statistics tools to evaluate the cold and hot spot patterns of ecological

resistance values, and then cluster and outlier analysis (Anselin Local Moran's I) was used to compute local spatial autocorrelation features. The ecological network construction process uses the cost distance tool in the spatial analyst tools to obtain the ecological security spatial distribution map and uses the cost path to extract the “ridgeline” on the surface of the ecological security pattern. These processes will be specifically introduced in the research methodology.

Ecological source patches mainly select objects with good habitat quality and high value of ecological services as targets, such as ecological wetland parks, forest reserves, nature reserves, scenic spots, and other green patches (Zhang et al., 2022). Elevation and slope affect the spatial distribution and utilization of land resources (Wang et al., 2019; Tang et al., 2022). Land use type will affect the material energy and information exchange within and between ecological source nodes. Vegetation coverage can improve local microclimate and play a positive role in the effective recovery and protection of biodiversity. Rivers can purify harmful substances and improve the ecological function of the environment. The closer the river is, the better the expansion of the ecological source. On the contrary, the influence of traffic roads and other indicators on the surrounding land use, the change of production land use structure, and landscape patterns are mainly considered. Generally speaking, if the distance from the road is closed, the gravitation of urban construction expansion will be greater, which is more unfavorable to the spatial expansion of ecological sources. The level of ecological security is divided into one to four levels from

TABLE 2 Value system for ecological resistance factors.

Ecological land expansion resistance	1	2	3	4
Elevation (m)	<2600	2600–2800	2800–3000	>3000
Slope (°)	<7	7–15	15–25	>25
Landscape type	Forest grass	Water	Cultivated	Construction
NDVI	>75%	75%–50%	50%–30%	<30%
Soil erosion (t·km ⁻² ·a ⁻¹)	<1000	1000–2500	2500–5000	>5000
Distance from tourist attractions (m)	<1000	—	1000–5000	>5000
Distance from industrial land (m)	>1500	1000–1500	500–1000	<500
Distance from water bodies (m)	<100	100–500	500–1000	>1000
Distance from roads (m)	>2000	1000–2000	500–1000	<500
Distance from settlements (m)	>1500	1000–1500	500–1000	<500



high to low (Table 2), and the corresponding weight is assigned to each ecological evaluation resistance factor.

2.3 Methods

2.3.1 Minimum cumulative resistance model

The least cumulative resistance model can calculate the resistance of spatial dimensions in heterogeneous space to obstacles to biological migration and species diffusion. The channel with the least cumulative resistance is the channel with the lowest cost of consumption and the highest possibility of expansion (Wang et al., 2021). The formula is given as follows:

$$V_{MCR} = f_{\min} \sum_{j=n}^{i=m} D_{ij} R_i, \tag{1}$$

where V_{MCR} is the value of the minimum cumulative resistance surface; f is a function of the positive correlation that reflects the relation of the least resistance for any point in space to the distance from any point to any source and the characteristics of the landscape base surface; \min denotes the minimum value of cumulative resistance produced in different processes of landscape unit i transforming into a different source unit j ; D_{ij} is the spatial distance between landscape unit i and source unit j ; and R_i denotes the resistance coefficient that exists in transition from landscape unit i to source unit j .

The ecological source patches in the model in this study mainly choose objects with good habitat quality and high ecological service

value as targets, such as ecological wetland parks, forest reserves, nature reserves, scenic spots, and other green space patches. The determination of the drag factor is a key step in the establishment of the drag surface model. Based on the combination of natural factors and socioeconomic factors and following the principles of accessibility and easy quantification, the study selected 13 indicators of natural factors and socioeconomic factors as resistance evaluation factors in the resistance surface model to form the ecological security evaluation index system (Figure 2). The resistance factor is divided into four levels, and the resistance coefficient is expressed as 1, 2, 3, and 4 (Table 2). The larger the value is, the greater the resistance is and the higher the cost is. ArcGIS 10.4 was used to establish the ecological security resistance surface model, and the cost-distance module was used to calculate the cumulative cost resistance surface of ecological sources. Based on MCR, the cost-path tool is used to identify the minimum cumulative cost path between ecological sources as the basis for potential ecological corridors.

2.3.2 Gravity method

The intensity of interactions between the source and the target can be used to characterize the effectiveness of the potential ecological corridor and the importance of connection plaques. When the cost distance between plaques is larger, the interaction is smaller, and the importance ecological corridors connecting become strong (Su et al., 2019). Based on the gravity model to quantify the ecological source of the MCR model to extract the potential between the importance of ecological corridors and calculate the interaction between the ecological source matrix, quantitative evaluation is used to select the intensity of the interaction between source plaques, judging from the strength size of the corridor in the area of relative important degree, to identify potentially important ecological corridor, and form an ecological security network. The effectiveness of potential ecological corridors and the importance of connecting ecological patches are mainly expressed by the strength of the interaction between the source and the target. The calculation formula of the gravity model is given as follows:

$$G_{ab} = \frac{N_a \cdot N_b}{D_{ab}^2} = \frac{\left(\frac{1}{P_a} \times \ln S_a\right) \left(\frac{1}{P_b} \times \ln S_b\right)}{\left(\frac{L_{ab}}{L_{max}}\right)} = \frac{L_{max}^2 \ln(S_a S_b)}{L_{ab}^2 P_a P_b}, \quad (2)$$

where G_{ab} is the interaction force between patches a and b of ecological origin. N_a and N_b are the weights of patches a and b , respectively. D_{ab} is the standardized value of the potential ecological corridor resistance between patches a and b of the ecological origin. p is the resistance value of patches. S is the area of patches. L_{ab} is the cumulative resistance value of the ecological corridor between patches a and b . L_{max} is the maximum value of the ecological corridor resistance value in the study area. The landscape resistance of potential ecological corridors will affect species migration. A small resistance is conducive to the migration and dispersal of species, and *vice versa*, it hinders the connection between species.

2.3.3 Exploratory spatial data analysis

Exploratory spatial data analysis explores the distribution characteristics of spatial objects based on the correlation and degree analysis of sample values in the space. Global spatial autocorrelation reflects the overall trend of spatial correlation of observed variables in the whole research area (Rong et al., 2022). At a given significance level, if Moran's I is significantly positive, it

means that the area with high (or low) ecological security resistance has a significant spatial agglomeration. The closer the value is to 1, the smaller the overall spatial difference is. On the contrary, when Moran's I is significantly negative, it indicates that there is a significant spatial difference in the level of economic development between the region and the surrounding areas. The closer the value is to -1, the larger the overall spatial difference is. When Moran's I is 0, the space is irrelevant (Liu et al., 2022). The formulas are as follows:

$$I = \frac{N}{S_0} \cdot \frac{\sum_{i=1}^N \sum_{j=1}^N w_{ij} (X_i - \bar{X})(X_j - \bar{X})}{\sum_{i=1}^N \sum_{j=1}^N (X_i - \bar{X})^2}, \quad (3)$$

$$S_0 = \sum_{i=1}^N \sum_{j=1}^N w_{ij}, \quad (4)$$

where $i \neq j$; N is the number of research objects; X is the observed value; \bar{X} is the mean value of X ; w_{ij} is the space weight matrix between i and j of the research object; the value of space adjacent is 1 and that of non-adjacent is 0. Moran's I results were statistically tested by the Z-test.

$$Z(I) = (I - E(I)) / \sqrt{\text{Var}(I)}, \quad (5)$$

where $Z(I)$ is the mathematical expectation, with a value of $-1/(n-1)$. $\text{Var}(I)$ is the variance of I . If the Z value of the positive statistic of Moran's I is larger than the function of normal distribution, the critical value of 1.96 is at the level of .05. This shows that there is a significant positive correlation in spatial distribution. Although global spatial autocorrelation analysis can reveal the dependence of things as a whole, it ignores the possibility of local instability. We need to introduce the local spatial autocorrelation (LISA) method to reveal the autocorrelation of local regional units in adjacent space. We used Local Moran's I index to measure the heterogeneity of spatial elements between regional units i and j , and the calculation formula is given as follows:

$$I_i = Z_i \sum_{j=1}^n w_{ij} Z_j, \quad (6)$$

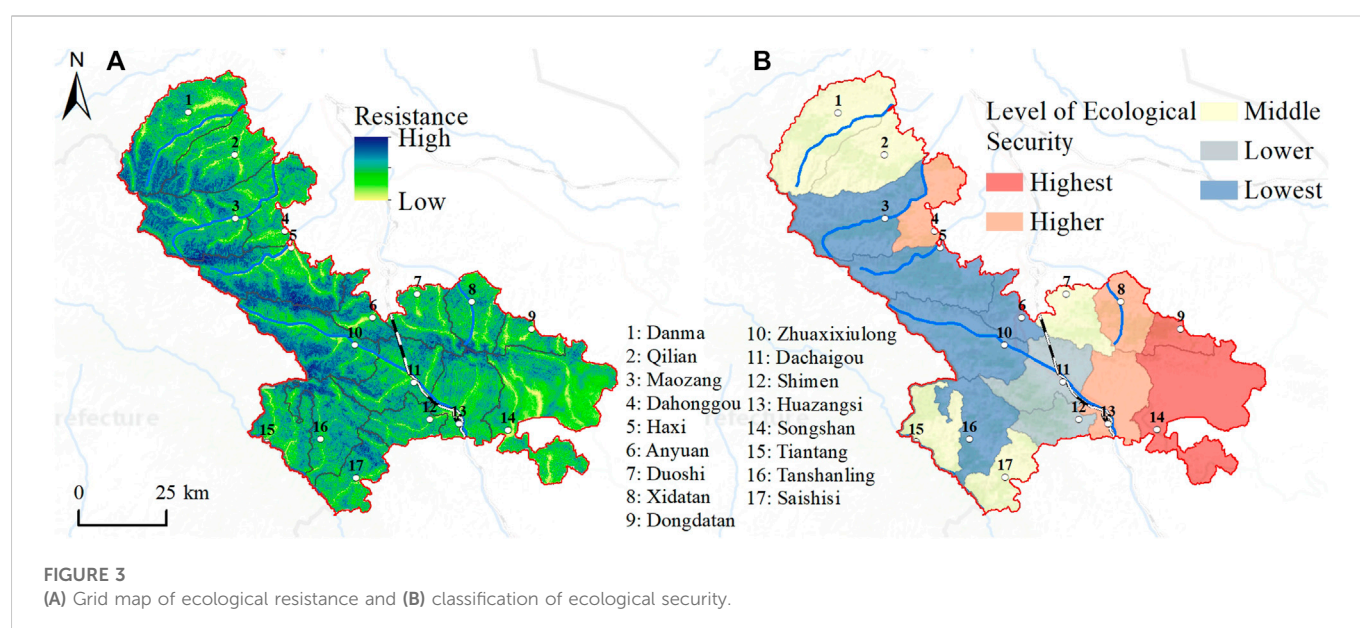
where Z is the standardized result of observed values on space elements i and j ; w_{ij} is the space weight matrix. Getis-Ord G_i^* can further measure the characteristics of the local spatial autocorrelation. It is used to identify high-value clusters and low-value clusters in different spatial regions, that is, the spatial distribution of hot spots and cold spots. The calculation formula is given as follows:

$$G_i^*(d) = \sum_{j=1}^n w_{ij}(d) X_j / \sum_{j=1}^n X_j. \quad (7)$$

To facilitate comparison and analysis, $G_i^*(d)$ is standardized in this study.

$$Z(G_i^*) = (G_i^* - E(G_i^*)) / \sqrt{\text{Var}(G_i^*)}, \quad (8)$$

where $E(G_i^*)$ and $\text{Var}(G_i^*)$ are, respectively, the mathematical expectation and coefficient of variation of G_i^* and $W_{ij}(d)$ is the spatial weight. If $Z(G_i^*)$ is positive and significant, it indicates that the value around position i is relatively high (above the mean), which belongs to a high-value spatial cluster (hot spot). On the contrary, if it is negative and significant, it means that the value around position i is lower than the mean and it belongs to the low-value spatial clustering (cold spot area). In this study, a grid is created using ArcGIS 10.4, and zonal statistics are performed on the ecological resistance surface with a grid width of 1000 m \times 1000 m. Then, the generated point data were



extracted to associate with the grid. The ecologically safe global Moran's I index calculation is performed in GeoDa 1.14 software. Hot spot analysis was used in ArcGIS 10.4 to analyze the hot and cold features of the ecological security pattern and its significance (Nie et al., 2021). Eventually, cluster and outlier analysis was used to obtain the spatial clustering results of the ecological security pattern.

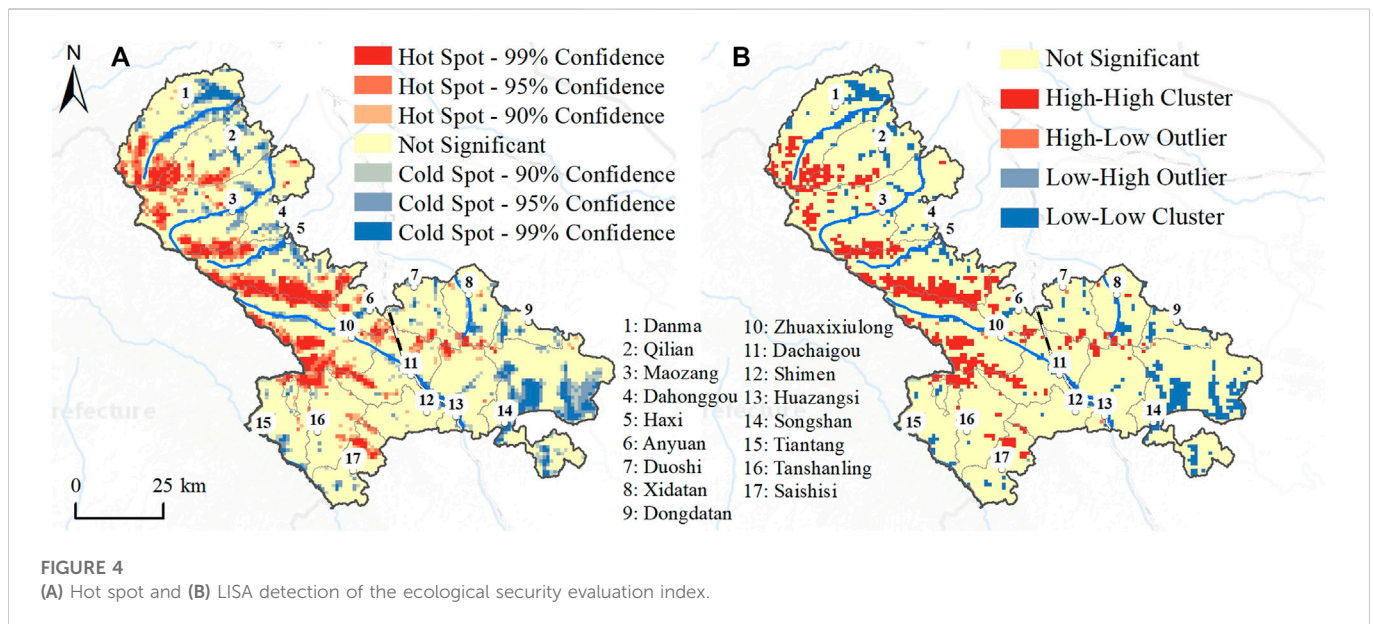
3 Results

3.1 Ecological security assessment

According to the current situation of the county's tourism resources and the background of the ecological and tourism industries as poverty alleviation projects, large landscape patches with good habitat conditions and natural reserves are selected as ecological source nodes, and 13 large habitat patches are selected as regional organisms. The total area of diverse source patches was 328.49 km². These patches are the main activity range and important habitat of biological species in the study area and provide important guarantees for the survival and reproduction of species. They have extremely important ecosystem functions and ecological values. According to the combination of natural factors and socioeconomic factors, and following the principles of accessibility and quantification, 10 indicators of natural factors and socioeconomic factors were selected as the resistance evaluation factors in the resistance surface model. The ecological resistance surface was established. According to the ecological resistance value factors in Table 3, we used the grid data processing method to establish the comprehensive resistance surface of ecological factors and obtained the spatial distribution map of the ecological security evaluation level (Lin et al., 2022; Wei et al., 2022). The spatial distribution of the ecological resistance comprehensive resistance surface shows that the minimum ecological resistance is 1.0150, the maximum ecological resistance is 3.6150, and the average ecological resistance is

2.5489. To make the classification of the ecological security pattern at the township level more reasonable, first, we use the average value of ecological resistance as a limit and binarize the ecological security resistance surface. Then, we used the zonal tool of ArcGIS 10.4 to make statistics on the grid surface of ecological security resistance (Figure 3A). In this process, we classified the ecological security resistance values of 17 towns based on the ratio of the ecological resistance values "grid area below average" and "grid area above average." Finally, we used the Natural Breaks (Jenks) method to compare the values for classification. The ratio of the ecological security classification is .4834–2.5616. Among them, the lowest security level is .4834–.5647, the lower security level is .5648–.7716, the medium-security level is .7717–1.0076, the higher-security level is 1.0077–1.3577, and the highest security level is 1.3578–2.5616.

In the spatial characteristics of ecological security, Figure 3B shows that the ecological security pattern of the county is characterized by high east and low west. The highest security level area mainly includes Songshan and Dongdatan, and their area accounts for 14.76% of the total area. The higher-security level areas are Huazangsi, Xidatan, and Dahonggou, and their area accounts for 14.20% of the total area. The medium-security level area is distributed in Qilian, Danma, Tiantang, Duoshi, and Saishisi, and their area accounts for 28.37% of the total area. The lower-security level area is mainly distributed in Shimen and Dachaigou, and their area accounts for 9.01% of the total area. The lowest security level areas are mainly distributed in Haxi, Maozang, Anyuan, Tanshanling, and Zhuaxixiulong, and their area accounts for 33.66% of the total area. The ecological security evaluation results show that the ratio of the area of the highest security level and the higher-security level to the total area is 28.96%. The area of the lower-security level and the lowest security level accounted for 42.67%. It shows that the ecological security level of Tianzhu is generally low. At the same time, areas above the medium-security level are mainly closely related to the distribution of river systems. The terrain in these areas is relatively flat. The lower-security level areas are mainly



mountainous areas with high altitudes and large slopes. These areas are vulnerable to ecological conditions due to natural conditions and human activities.

3.2 Spatial heterogeneity analysis of ecological security

Analysis of the spatial distribution and agglomeration spatial heterogeneity of the ecological security level in Tianzhu was carried out. The results show that the global Moran's I index for ecological security is .4469. This indicates that there is a spatial autocorrelation in the ecological security resistance value. Moran's I generally uses the Z method for significance testing. The significance of Moran's I index and Z -Score test is that when Moran's $I > 0$, $Z\text{-Score} > 1.96$ ($p\text{-value} < .05$), Moran's I value can indicate the significance of its spatial positive correlation. The $Z\text{-Score}$ of the ecological security evaluation index is equal to 70.1893 ($p\text{-value} = .0000$), which is much greater than 1.96, indicating that the spatial distribution of ecological security levels of a county shows a strong positive spatial correlation. Figure 4A shows that hot spots and cold spots have significant spatial differences. The cold spot is mainly distributed in the east. The hot spot is mainly distributed in the west. Hot spots and cold spots have a larger proportion of 99% and 95% confidence intervals. In addition, not significant grid cells are regions where the ecological security resistance index is not highly spatial. The value of the local autocorrelation Moran's I index divides The geographic space is divided into four parts based on the value of the local autocorrelation Moran's I index: "high-high (HH), low-low (LL), high-low (HL), and low-high (LH)." Among them, the high-high cluster indicates that the central area with a high ecological security resistance index has a high ecological security resistance index in the surrounding area, and it is reflected in the spatial correlation as a diffusion effect (Peng et al., 2018). The low-low cluster indicates that the ecological security resistance indexes of the central area and

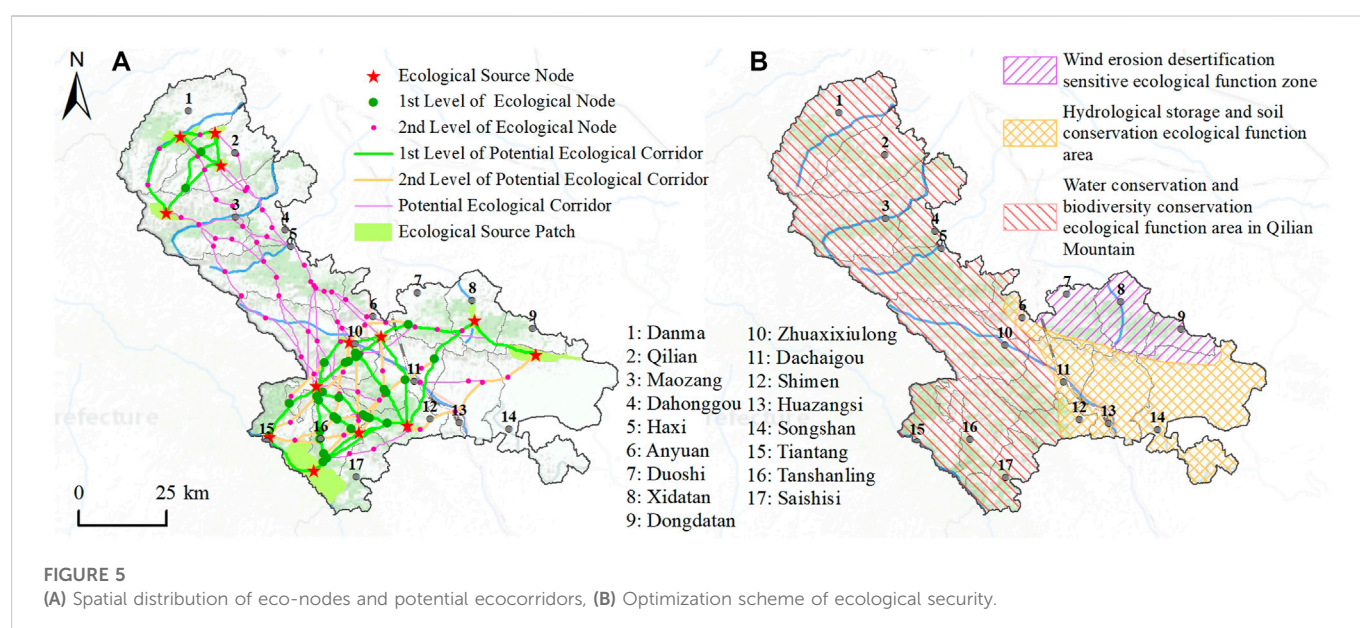
adjacent areas are low, and they belong to a low level of ecological security.

At the same time, there is a significant positive spatial correlation between the high-high and low-low ecological security resistance indexes in the geographic space. High-low indicates that the high-adjacent value of the ecological security resistance index in the central area is low, and it exhibits a polarization effect in spatial correlation. Low-high indicates that the resistance index of ecological security in the central area is low and that of the adjacent is high. It belongs to the transition zone in spatial correlation. According to Figure 4B, the ecological security resistance index of the county is mainly based on two types of high-high and low-low agglomerations, which have obvious spatial distribution characteristics of flakes, while the high-low and low-high types in space. The effect of aggregation is not obvious. For the high-high distribution area, its ecosystem is relatively fragile, and geological hazards and soil erosion are highly sensitive (Kang et al., 2021; Liu et al., 2022). Biodiversity protection should be strengthened, and biological measures and engineering should be combined to control soil erosion, moderately develop ecological tourism, and develop tourism agriculture. For the low-low area, under the guidance of land space planning and ecological planning, stricter use controls should be implemented to ensure the rational use of land, coordinate the orderly expansion of urban land use, and strengthen the protection of cultivated land and ecological conservation.

3.3 Ecological corridor identification and optimization

3.3.1 Identification of potential ecological corridors

Construction of the Tianzhu ecological security network based on the MCR model. The results show that the lowest resistance value of the ecological cumulative consumption resistance surface is 0, and the highest value is 108,564.9. High resistance values are



mainly distributed in the southeast and northwest regions. The southeast region is mainly densely distributed in towns and villages. The northwest direction is concentrated on the snow-covered mountains above 4,000 m. The area of the low resistance value is widely distributed. It is mainly in the periphery of the northwest alpine region of the county, and it is an area with high habitat quality. Then, we calculated the minimum cumulative consumption path between each ecological source patch and other ecological source patches. The potential ecological corridors are established, and the cumulative resistance value of each potential ecological corridor is calculated (Figure 5A). The results showed that a total of 156 potential ecological corridors were generated in the study area. We calculated and identified 33 important corridors through the gravity model. Among them, there are 12 secondary potential corridors with an importance value between 50 and 100. There are 21 first-level potential corridors with importance values greater than 100. There are 123 general corridors with importance values less than 50. It can be known from the table of ecological gravitation between ecological source nodes that the importance values of the interaction intensity between the ecological patches selected in the study area are significantly different. The minimum value is 7.8182, which indicates that the interaction between ecological source patches 3 and 13 is the weakest, and the landscape resistance between ecological source patches is very large. The maximum value is 1090.7625, which indicates that the interaction between ecological source patches 3 and 7 is the strongest. The ecological resistance between the ecological corridors is relatively small, and the quality of habitat conditions is high. As ecological corridors play an important role in the richness, migration, and diffusion of biological species, it is necessary to strictly control and protect important ecological corridors during the construction of an ecological security network (Padró et al., 2020; Liu et al., 2021). At the same time, the ecological pattern of general corridors should also be improved and optimized in planning such as green space

system planning to improve the habitat suitability of this type of ecological corridor.

3.4 Optimization of the spatial layout of the ecological network

Ecological nodes are generally located at the weakest point of the ecological function in ecological corridors. They are mainly composed of the intersections of the smallest path and the largest path or the intersection of the smallest path. It is beneficial to reduce the cost of ecological corridors and improve the ecological service function of the regional ecological network (Huang et al., 2021; Nie et al., 2021). Therefore, according to the ecological source areas, corridors, and ecological nodes, ecological planning and layout are carried out to build a “point–line–surface” ecological service function network system that blends. It is of great significance to strengthen functional health and service sustainability. In the end, we extracted 156 potential ecological corridors in the county, with a total length of about 1248.00 km², of which the length of the first and second corridors accounted for 53.50% of the total length. In addition, based on the generated potential ecological corridors and the minimum cumulative resistance surface, the spatial analysis function of ArcGIS was used to extract 112 ecological nodes between the potential ecological corridors in the study area. We refer to the actual spatial distribution of ecological source patches, important potential ecological corridors, and ecological nodes in the county and “Tianzhu Urban and Rural Overall Planning (2018–2035)” issued by the local government. In the end, we proposed the ecological network framework layout model of the “One Belt and Three Zones” (Figure 5B). Among them, the “Belt” is mainly the Jinjiang river urban agglomeration and development zone. The “Three zones” refer to the ecological function areas sensitive to wind erosion and sand, the ecological function areas for hydrological storage and soil conservation, and the ecological function areas for water conservation and biodiversity maintenance in the Qilian

Mountains. Among them, the hydrological storage and soil conservation ecological function areas are based on the Jinqiang river, connecting Huazangsi, Shimen, Dachaigou, Anyuan, and Zhuaxiulong. The ecological function areas of water conservation and biodiversity maintenance of the Qilian Mountains include Tanshanling, Saishisi, Tiantang, Haxi, Danma, Qilian, Maozang, and Dahonggou. Wind erosion and desertification-sensitive ecological functional areas cover Songshan, Duoshi, Xidatan, and Dongdatan.

4 Discussions

We aimed at the layout pattern of the ecological network framework and protected the integrity of important ecological source patches such as various types of scenic areas and nature reserves in the region through land space planning and related ecological function zone planning. We increased the patch area through green space planning, improved the habitat quality of ecological source patches in the ecological network framework, enhanced the habitat suitability of biological species to patches, and strengthened the protection and construction of ecological source sites in the ecological network framework. We combined existing tourism routes and green space networks to rationally plan corridors such as roads, river systems, and shelterbelts in the area and further improve the ecological network structure (Su et al., 2016; Yang et al., 2022b). Since outward traffic roads mainly radiate outward from the center of Huazangsi Town, we should strengthen the protection of ecologically sensitive points where ecological corridors and roads intersect and strengthen the coupling analysis of regional ecological sensitivity and socioeconomic and industrial layout (Galli et al., 2020). We must closely integrate ecological security construction with the development of regional environmental governance projects, ecological industries, and tourism poverty alleviation projects, which will help us carry out the overall layout and planning of the ecological compensation mechanism. The research methods and results also have certain theoretical and practical significance for future research on ecological security construction in the alpine region of the Qinghai–Tibet Plateau.

Meanwhile, China's natural zone transition zone is an important regional ecological system. At different spatial scales and geographic locations, there are obvious transitional characteristics of the terrain, climate, hydrology, soil, vegetation, and other factors (He et al., 2019). Wind erosion and desertification-sensitive ecological function areas are generated based on the environmental characteristics of the arid regions in the northwest. The Qilian Mountains' water conservation and biodiversity conservation ecological function zones are determined based on the climatic characteristics and topographic features of the Qinghai–Tibet Alpine Region (Zhou et al., 2021). The hydrological storage and soil conservation ecological function zones are formed by the unique environmental characteristics of the eastern monsoon region in the northwest, where the Loess Plateau, Inner Mongolia Plateau, and Qinghai–Tibet Plateau meet. The Yellow River and its tributaries form a spatial distribution pattern. As well as the layout of regional transportation arteries. These three typical characteristics have important impacts on regional ecosystem security.

The ecological security pattern method based on the MCR model is widely used in the research of urban planning, land use, and ecological evaluation. It has certain advantages in the expression of

ecological processes and spatial visualization of influencing factors. This study mainly uses raster data based on the minimum cumulative resistance model method to evaluate ecological security, extract ecological corridors, and construct an ecological network framework for Tianzhu (Guo et al., 2020). Overall, the research results are more in line with the actual situation of the county. In the currently implemented "Tianzhu Urban and Rural Overall Planning (2018–2035)" and "The 14th Five-Year Plan for Economic and Social Development and Long-Range Objectives through the Year 2035 of Tianzhu County", the importance of ecological network construction in ecological security construction was emphasized. This study uses the quantitative method based on the MCR model. The layers of potential ecological corridors extracted at different levels are richer, and the spatial positioning of the corridors is clearer. The study of ecological security patterns is a long-term and complex process, and the research focus of this study does not consider the supporting effect of the study area on the Hexi Corridor and the Qilian Mountain area. Therefore, the research on the influence of the ecological security pattern of the small-scale study area on the larger spatial scale still needs to be further strengthened. In addition, the ecological corridor in this study is a linear element, which lacks the exploration of the width of the ecological corridor and radiation channel. Corridors with different widths can directly affect the function of the regional ecosystem, and the utilization and demand width of corridors are different for various biological species. How to determine the optimal width of the ecological corridor in the study area? Making it produce the maximum ecological benefits is a key direction for subsequent research.

5 Conclusion

This study takes Tianzhu as the research area, establishes the ecological resistance surface according to the ecological resistance factor index, analyzes the spatial distribution characteristics of ecological security level, selects large scenic areas and nature reserves as ecological source nodes, and constructs ecological source nodes of ecological accumulation and resistance surface. Finally, the MCR model and gravity model are used to extract potential ecological corridors and identify important potential ecological corridors. The main conclusions are as follows. 1) The level of ecological security is relatively low. Ecological security presents the spatial characteristics of low north and high south. It has higher ecological security and high-level areas occupying 32.79% of the total county area, while lower and low-level areas account for 51.89%. The ESDA analysis of the spatial distribution of ecological security shows that the global Moran's I index is .4469, and the results of the hot spot analysis show that the ecological security level of the county is mainly high–high (HH) and low–low (LL). It has obvious flake-shaped agglomeration and distribution characteristics. 2) Based on the ecological network pattern characteristics of Tianzhu, we proposed a layout model of the "One Belt, Three Zones" ecological network framework for the construction and protection of ecological economic development and tourism economic development. This model can serve as an important supplement to the spatial layout of the ecological industry and provide a decision-making basis for ecological security planning.

Data availability statement

The original contributions presented in the study are included in the article/Supplementary Material; further inquiries can be directed to the corresponding author.

Author contributions

ZC and HC contributed to the conception of this study. ZC and MY carried out the design and production of some diagrams. ZC and WZ contributed significantly to the analysis and manuscript preparation. ZC and YJ performed the data analyses and wrote the manuscript. WZ and XW helped perform the analysis with constructive discussions. All authors contributed to the article and approved the submitted version.

Funding

This research was supported by the Young Scholars Science Foundation Project of Gansu Province (No.21JR7RA343), the Foundation of Key Projects of Natural Science of Gansu Province (Grant Nos. 21JR7RA278 and 21JR7RA28121), the Young Scholars Science Foundation of Lanzhou Jiaotong University (Grant number

2021019), and the Foundation of Key Talent Projects of Gansu Province (No. 2021RCXM073).

Acknowledgments

This is a short text to acknowledge the contributions of specific colleagues, institutions, or agencies 455 that aided the efforts of the authors

Conflict of interest

The authors declare that the research was conducted in the absence of any commercial or financial relationships that could be construed as a potential conflict of interest.

Publisher's note

All claims expressed in this article are solely those of the authors and do not necessarily represent those of their affiliated organizations, or those of the publisher, the editors, and the reviewers. Any product that may be evaluated in this article, or claim that may be made by its manufacturer, is not guaranteed or endorsed by the publisher.

References

- Bouslim, Y., Kharrou, M. H., Miftah, A., Attou, T., Bouchaou, L., and Chehbouni, A. (2022). Comparing pan-sharpened landsat-9 and sentinel-2 for land-use classification using machine learning classifiers. *J. Geovisualization Spatial Analysis* 6 (2), 35–17. doi:10.1007/S41651-022-00130-0
- Cunha, N. S., and Magalhães, M. R. (2019). Methodology for mapping the national ecological network to mainland Portugal: A planning tool towards a green infrastructure. *Ecol. Indic.* 104, 802–818. doi:10.1016/j.ecolind.2019.04.050
- Dai, L., Liu, Y., and Luo, X. (2021). Integrating the MCR and DOI models to construct an ecological security network for the urban agglomeration around Poyang Lake, China. *Sci. Total Environ.* 754, 141868. doi:10.1016/j.scitotenv.2020.141868
- Dai, Y., Diao, Y., Dai, C., Li, Y., Sun, G., Zahoor, B., et al. (2022). Spatial-temporal dynamics and evolution of ecological security in a rapid urbanization city, Southwest China. *Front. Ecol. Evol.* 10, 866. doi:10.3389/fenvs.2022.914567
- Fan, C., and Myint, S. (2014). A comparison of spatial autocorrelation indices and landscape metrics in measuring urban landscape fragmentation. *Landscape Urban Plan.* 121, 117–128. doi:10.1016/j.landurbplan.2013.10.002
- Fan, Y., Qiao, Q., and Fang, L. (2017). Network analysis of industrial metabolism in industrial park – a case study of Huai'an economic and technological development area. *J. Clean. Prod.* 142, 1552–1561. doi:10.1016/j.jclepro.2016.11.149
- Galli, A., Iha, K., Moreno Pires, S., Mancini, M. S., Alves, A., Zokai, G., et al. (2020). Assessing the Ecological Footprint and biocapacity of Portuguese cities: Critical results for environmental awareness and local management. *Cities* 96, 102442. doi:10.1016/j.cities.2019.102442
- Geng, W., Li, Y., Zhang, P., Yang, D., Jing, W., and Rong, T. (2022). Analyzing spatio-temporal changes and trade-offs/synergies among ecosystem services in the Yellow River Basin, China. *Ecol. Indic.* 138, 108825. doi:10.1016/j.ecolind.2022.108825
- Gu, Q., Wei, J., Luo, S., Ma, M., and Tang, X. (2018). Potential and environmental control of carbon sequestration in major ecosystems across arid and semi-arid regions in China. *Sci. Total Environ.* 645, 796–805. doi:10.1016/j.scitotenv.2018.07.139
- Guo, J., Wei, Z., Ren, J., Luo, Z., and Zhou, H. (2020). Early-warning measures for ecological security in the Qinghai alpine agricultural area. *Int. J. Environ. Res. Public Health* 17 (24), 9292–9329. doi:10.3390/ijerph17249292
- He, Y., Jiang, X., Wang, N., Zhang, S., Ning, T., Zhao, Y., et al. (2019). Changes in mountainous runoff in three inland river basins in the arid Hexi Corridor, China, and its influencing factors. *Sustain. Cities Soc.* 50, 101703. doi:10.1016/j.scs.2019.101703
- Hu, M., Li, Z., Yuan, M., Fan, C., and Xia, B. (2019). Spatial differentiation of ecological security and differentiated management of ecological conservation in the Pearl River Delta, China. *Ecol. Indic.* 104, 439–448. doi:10.1016/j.ecolind.2019.04.081
- Huang, K., Peng, L., Wang, X., and Chen, T. (2022). Integrating landscape connectivity and natural-anthropogenic interaction to understand karst vegetation restoration: A case study of guizhou Province, China. *Front. Ecol. Evol.* 10, 844437. doi:10.3389/fenvs.2022.844437
- Huang, X., Wang, H., Shan, L., and Xiao, F. (2021). Constructing and optimizing urban ecological network in the context of rapid urbanization for improving landscape connectivity. *Ecol. Indic.* 132, 108319. doi:10.1016/j.ecolind.2021.108319
- Jiang, H., Peng, J., Zhao, Y., Xu, D., and Dong, J. (2022). Zoning for ecosystem restoration based on ecological network in mountainous region. *Ecol. Indic.* 142, 109138. doi:10.1016/j.ecolind.2022.109138
- Jiao, M., Wang, Y., Hu, M., and Xia, B. (2021). Spatial deconstruction and differentiation analysis of early warning for ecological security in the Pearl River Delta, China. *Sustain. Cities Soc.* 64, 102557. doi:10.1016/j.scs.2020.102557
- Kang, J., Zhang, X., Zhu, X., and Zhang, B. (2021). Ecological security pattern: A new idea for balancing regional development and ecological protection. A case study of the jiaodong peninsula, China. *Glob. Ecol. Conservation* 26, e01472. doi:10.1016/j.gecco.2021.e01472
- Liang, C., Zeng, J., Zhang, R. C., and Wang, Q. W. (2022). Connecting urban area with rural hinterland: A stepwise ecological security network construction approach in the urban–rural fringe. *Ecol. Indic.* 138, 108794. doi:10.1016/j.ecolind.2022.108794
- Lin, L., Hao, Z., Post, C. J., and Mikhailova, E. A. (2022). Monitoring ecological changes on a rapidly urbanizing island using a Remote sensing-based ecological index produced time series. *Remote Sens.* 14 (22), 5773. doi:10.3390/rs14225773
- Liu, C., Wang, C., Li, Y., and Wang, Y. (2022a). Spatiotemporal differentiation and geographic detection mechanism of ecological security in Chongqing, China. *Glob. Ecol. Conservation* 35, e02072. doi:10.1016/j.gecco.2022.e02072
- Liu, J., Cao, X., Zhao, L., Dong, G., and Jia, K. (2022b). Spatiotemporal differentiation of land ecological security and its influencing factors: A case study in jinan, shandong Province, China. *Front. Environ. Sci.* 10, 8. doi:10.3389/fenvs.2022.824254
- Liu, Y., Zhao, C., Liu, X., Chang, Y., Wang, H., Yang, J., et al. (2021). The multi-dimensional perspective of ecological security evaluation and drive mechanism for Baishuijiang National Nature Reserve, China. *Ecol. Indic.* 132, 108295. doi:10.1016/j.ecolind.2021.108295
- Luo, Y., Zhu, Z., Wu, J., Zhang, Y., Li, X., Zhao, W., et al. (2022). Exploring habitat patch clusters based on network community detection to identify restored priority areas of

- ecological networks in urban areas. *Urban For. Urban Green.* 78, 127771. doi:10.1016/j.ufug.2022.127771
- Möckel, S. (2017). The European ecological network “Natura 2000” and the appropriate assessment for projects and plans under Article 6(3) of the Habitats Directive. *Nat. Conserv.* 23, 1–29. doi:10.3897/natureconservation.23.13599
- Nie, W., Shi, Y., Siaw, M. J., Yang, F., Wu, R., Wu, X., et al. (2021). Constructing and optimizing ecological network at county and town Scale: The case of Anji County, China. *Ecol. Indic.* 132, 108294. doi:10.1016/j.ecolind.2021.108294
- Padró, R., La Rota-Aguilera, M. J., Giocoli, A., Cirera, J., Coll, F., Pons, M., et al. (2020). Assessing the sustainability of contrasting land use scenarios through the Socioecological Integrated Analysis (SIA) of the metropolitan green infrastructure in Barcelona. *Landsc. Urban Plan.* 203, 103905. doi:10.1016/j.landurbplan.2020.103905
- Peng, J., Pan, Y., Liu, Y., Zhao, H., and Wang, Y. (2018). Linking ecological degradation risk to identify ecological security patterns in a rapidly urbanizing landscape. *Habitat Int.* 71, 110–124. doi:10.1016/j.habitatint.2017.11.010
- Peng, W., Zhang, Z., He, G., Liu, X., Wang, W., Cai, Y., et al. (2022). Integrating potential land use conflict into ecological security pattern in response to land use/cover changes at a county scale in yangtze river delta, China. *Front. Earth Sci.* 10, 535. doi:10.3389/feart.2022.875433
- Raji, S. A., Odunuga, S., and Fasona, M. (2022). Spatially explicit scenario analysis of habitat quality in a tropical semi-arid zone: Case study of the sokoto–rima basin. *J. Geovisualization Spatial Analysis* 6 (1), 11. doi:10.1007/s41651-022-00106-0
- Rong, T., Zhang, P., Zhu, H., Jiang, L., Li, Y., and Liu, Z. (2022). Spatial correlation evolution and prediction scenario of land use carbon emissions in China. *Ecol. Inf.* 71, 101802. doi:10.1016/j.ecoinf.2022.101802
- Shen, Z., Wu, W., Chen, S., Tian, S., Wang, J., and Li, L. (2022). A static and dynamic coupling approach for maintaining ecological networks connectivity in rapid urbanization contexts. *J. Clean. Prod.* 369, 133375. doi:10.1016/j.jclepro.2022.133375
- Streib, L., Kattwinkel, M., Heer, H., Ruzika, S., and Schäfer, R. B. (2020). How does habitat connectivity influence the colonization success of a hemimetabolous aquatic insect? - a modeling approach. *Ecol. Model.* 416, 108909. doi:10.1016/j.ecolmodel.2019.108909
- Su, K., Yu, Q., Yue, D., Zhang, Q., Yang, L., Liu, Z., et al. (2019). Simulation of a forest-grass ecological network in a typical desert oasis based on multiple scenes. *Ecol. Model.* 413, 108834. doi:10.1016/j.ecolmodel.2019.108834
- Su, Y., Chen, X., Liao, J., Zhang, H., Wang, C., Ye, Y., et al. (2016). Modeling the optimal ecological security pattern for guiding the urban constructed land expansions. *Urban For. Urban Green.* 19, 35–46. doi:10.1016/j.ufug.2016.06.013
- Tang, Y., Tang, J., Yu, X., Qiu, L., Wang, J., Hou, X., et al. (2022). Land ecological protection policies improve ecosystem services: A case study of lishui, China. *Front. Environ. Sci.* 10, 1661. doi:10.3389/fenvs.2022.973524
- Wan, H. Y., Cushman, S. A., and Ganey, J. L. (2019). Improving habitat and connectivity model predictions with multi-scale resource selection functions from two geographic areas. *Landsc. Ecol.* 34 (3), 503–519. doi:10.1007/S10980-019-00788-W
- Wang, S., Zhang, X., Wu, T., and Yang, Y. (2019). The evolution of landscape ecological security in Beijing under the influence of different policies in recent decades. *Sci. Total Environ.* 646, 49–57. doi:10.1016/j.scitotenv.2018.07.146
- Wang, T., Li, H., and Huang, Y. (2021). The complex ecological network’s resilience of the Wuhan metropolitan area. *Ecol. Indic.* 130, 108101. doi:10.1016/j.ecolind.2021.108101
- Wang, Y., Liao, J., He, Y., and Chen, P. (2022). Evolution and ecological implications of land development and conservation patterns on the Qinghai-Tibet Plateau. *Land* 11 (10), 1797. doi:10.3390/land11101797
- Wang, Y., and Pan, J. (2019). Building ecological security patterns based on ecosystem services value reconstruction in an arid inland basin: A case study in ganzhou district, NW China. *J. Clean. Prod.* 241, 118337. doi:10.1016/j.jclepro.2019.118337
- Wei, L., Zhou, L., Sun, D., Yuan, B., and Hu, F. (2022). Evaluating the impact of urban expansion on the habitat quality and constructing ecological security patterns: A case study of jiziwan in the Yellow River basin, China. *Ecol. Indic.* 145, 109544. doi:10.1016/j.ecolind.2022.109544
- Wen, J., and Hou, K. (2021). Research on the progress of regional ecological security evaluation and optimization of its common limitations. *Ecol. Indic.* 127, 107797. doi:10.1016/j.ecolind.2021.107797
- Yang, D., Lou, Y., Zhang, P., and Jiang, L. (2022a). Spillover effects of built-up land expansion under ecological security constraint at multiple spatial scales. *Front. Ecol. Evol.* 10, 460. doi:10.3389/fevo.2022.907691
- Yang, D., Zhang, P., Jiang, L., Zhang, Y., Liu, Z., and Rong, T. (2022b). Spatial change and scale dependence of built-up land expansion and landscape pattern evolution—case study of affected area of the lower Yellow River. *Ecol. Indic.* 141, 109123. doi:10.1016/j.ecolind.2022.109123
- Zhang, J., Zhu, H., Zhang, P., Song, Y., Zhang, Y., Li, Y., et al. (2022). Construction of gi network based on mspa and plus model in the main urban area of zhengzhou: A case study. *Front. Environ. Sci.* 10, 402. doi:10.3389/fenvs.2022.878656
- Zhang, P., Yang, D., Qin, M., and Jing, W. (2020). Spatial heterogeneity analysis and driving forces exploring of built-up land development intensity in Chinese prefecture-level cities and implications for future Urban Land intensive use. *Land Use Policy* 99, 104958. doi:10.1016/j.landusepol.2020.104958
- Zhou, L., Dang, X., Mu, H., Wang, B., and Wang, S. (2021). Cities are going uphill: Slope gradient analysis of urban expansion and its driving factors in China. *Sci. Total Environ.* 775, 145836. doi:10.1016/j.scitotenv.2021.145836
- Zhou, L., Zhou, C., Che, L., and Wang, B. (2020). Spatio-temporal evolution and influencing factors of urban green development efficiency in China. *J. Geogr. Sci.* 30 (5), 724–742. doi:10.1007/s11442-020-1752-5



OPEN ACCESS

EDITED BY

Wenlong Jing,
Guangzhou Institute of
Geography, China

REVIEWED BY

Jiabo Yin,
Wuhan University, China
Yangxiaoyue Liu,
Institute of Geographic Sciences and
Natural Resources Research
(CAS), China
He Jin,
University of South Florida,
United States

*CORRESPONDENCE

Guangxing Ji
✉ guangxingji@henau.edu.cn

SPECIALTY SECTION

This article was submitted to
Environmental Informatics and
Remote Sensing,
a section of the journal
Frontiers in Ecology and Evolution

RECEIVED 30 September 2022

ACCEPTED 13 December 2022

PUBLISHED 10 January 2023

CITATION

Liu Y, Chen W, Li L, Huang J, Wang X,
Guo Y and Ji G (2023) Assessing the
contribution of vegetation variation to
streamflow variation in the Lancang
River Basin, China.
Front. Ecol. Evol. 10:1058055.
doi: 10.3389/fevo.2022.1058055

COPYRIGHT

© 2023 Liu, Chen, Li, Huang, Wang,
Guo and Ji. This is an open-access
article distributed under the terms of
the [Creative Commons Attribution
License \(CC BY\)](#). The use, distribution
or reproduction in other forums is
permitted, provided the original
author(s) and the copyright owner(s)
are credited and that the original
publication in this journal is cited, in
accordance with accepted academic
practice. No use, distribution or
reproduction is permitted which does
not comply with these terms.

Assessing the contribution of vegetation variation to streamflow variation in the Lancang River Basin, China

Yuan Liu, Weiqiang Chen, Ling Li, Junchang Huang,
Xianglong Wang, Yulong Guo and Guangxing Ji*

College of Resources and Environmental Sciences, Henan Agricultural University, Zhengzhou, China

The Lancang River Basin (LCRB) is the largest international river in Southeast Asia, and any change in its streamflow, i.e., due to the ecological environment and runoff, may lead to disputes between countries to a certain extent. However, the impact of vegetation change on streamflow in the LCRB needs to be clarified. To assess the impact of vegetation change on streamflow in the LCRB, the functional relationship between Budyko parameter (ω) and Normalized Difference Vegetation Index (NDVI) was first computed for constructing a modified Budyko formula. Finally, we quantitatively estimated the influence of different factors on streamflow variation in the LCRB using the modified Budyko formula and the elastic coefficient method. The conclusions were as follows: (1) A sudden change in streamflow at the Yunjinghong hydrological station appeared in 2005; (2) Budyko parameter (ω) has a good linear functional relationship with NDVI in the LCRB ($p < 0.01$); (3) ND vegetation variation played the largest driving force behind streamflow variation in the LCRB, accounting for 34.47%. The contribution rates of precipitation, potential evaporation, and anthropogenic activities on streamflow variation from 1982 to 2015 were 16.83, 17.61, and 31.09%, respectively.

KEYWORDS

streamflow variation, vegetation variation, attribution analysis, adjusted Budyko equation, Lancang River

1. Introduction

Since the Industrial Revolution, the global temperature rise has been confirmed by a large number of climate observation data (Allen et al., 2009; Yin et al., 2021). The rise in global temperature affects the changes in different events such as precipitation, terrestrial water storage, runoff, and vegetation (Zhu et al., 2016; Chen et al., 2019; Jing et al., 2020a,b; Yin et al., 2022a), leading to frequent occurrences of extreme meteorological and hydrological disasters (Yin et al., 2018, 2022b; Gu et al., 2022; Ji et al., 2022a), which in turn have a series of huge and far-reaching impacts on human health, industrial and agricultural production, and social economy (Moore and Diaz, 2015). Climate warming has also become a major global social problem of common

concern to all mankind (Tilley, 2015). In recent decades, many vegetation restoration projects have been undertaken across China, and the vegetation coverage has increased rapidly (Wei et al., 2008; Lü et al., 2015). Vegetation plays a vital role in terrestrial ecosystems and is involved in the process of radiation balance and hydrological cycle, which effectively regulates the ecological environment (Ji et al., 2021a). Vegetation change affects the streamflow to a large extent by changing hydrological processes (vegetation transpiration and interception) and then affects the availability of water resources in the river basin (Bi et al., 2020; Ji et al., 2022b). Runoff is a vital part of the hydrological cycle. Streamflow variation directly affects human activity and life, and its sustainable development in the river basin. Previous studies found that, under the comprehensive influence of various factors, the streamflow of many rivers in the world shows a significantly decreasing trend (Vörösmarty, 2000; Ji et al., 2021b). Therefore, calculation of the impact of vegetation changes on streamflow quantitatively helps to evaluate the hydrological effects of ecological restoration measures and provide scientific guidance for water resource management and ecological environmental protection in the river basin.

To assess the impact of vegetation change on the water cycle, many scholars carried out relevant research works. Liang et al. (2015) found that Budyko parameter was positively correlated with the area of ecological restoration in most river basins of the Loess Plateau and ecological restoration measures are the leading factor for the decline in runoff in most watersheds. Li S. et al. (2016) found that the Normalized Difference Vegetation Index (NDVI) in the Kuye River basin showed a significant increase in the trends after 2000, while the runoff coefficient showed a significant decline in the trends, mainly because the vegetation change led to a reduction in surface albedo and a significant increase in vegetation evapotranspiration eventually led to a decline in runoff. Li Y. et al. (2016) analyzed the impact of climate change and human activities on the runoff in the middle and the lower reaches of the Yellow River using the Budyko formula and the elastic coefficient method. They arrived at the conclusion that the change in the underlying surface caused by the conversion-of-farmland-to-forest project has been the main factor for causing this decline in runoff in the Kuye River basin since 2000. Wang et al. (2020) discovered that a 1% increase of vegetation coverage would increase by 3~4 mm evapotranspiration, while ecological restoration plays an important role in the decline in runoff in the middle reaches of the Yellow River. Most of the studies calculated the contribution of underlying surface change to runoff through the change in Budyko parameter, but the functional relationship between vegetation change and Budyko parameter was not clearly given because of which we cannot directly quantify the contribution of vegetation change to runoff.

The Lancang River Basin (LCRB) is the largest international river in Southeast Asia (Jing et al., 2020c). For transboundary

watersheds, changes in its streamflow, i.e., the ecological environment and runoff, may lead to disputes between countries to a certain extent. In recent years, due to the combined action of human activities and climate change, the vegetation and streamflow of the LCRB have undergone significant changes. Therefore, many scholars have analyzed the characteristics and influencing factors of vegetation changes and streamflow changes in the LCRB. Li and Liu (2012) investigated the change characteristics of vegetation coverage in the LCRB and its relationship with climate factors. Their results illustrated that the vegetation coverage in the LCRB had a fluctuating and increasing tendency during the period from 2000 to 2009 and that each year's average annual NDVI was >0.45 , indicating that its ecological environment showed a trend in improvement. Fan et al. (2012) analyzed the dynamic changes in vegetation coverage in the LCRB from 2001 to 2010, and the results showed that, from 2001 to 2010, the vegetation coverage in the LCRB showed an upward trend as a whole. There were regional differences in the change rate of NDVI, and most of the regions showed an increasing trend in the change rate of NDVI. Tang et al. (2014) found that the impact of human activities on streamflow variation in the LCRB is slightly greater than that of climate change (54.6 and 45.4%, respectively). Han et al. (2019) assessed the impact of climate factors and human activities on streamflow variation in the Lancang River Basin. Compared to the base period (1980–1986), the contribution rates of human activities to streamflow variation were 43 (1987–2007) and 95% (2008–2014), respectively. Liu et al. (2020) found that the annual average precipitation (P_r) of the LCRB did not decrease significantly, the annual potential evaporation (ET_0) increased significantly, and the runoff depth (R) decreased significantly. Compared with the base period (1961–2004), the reduction in P_r is the main reason for the decline in runoff depth during the 2005–2015 period, with a contribution rate of 45.64%. The contribution rates of ET_0 and human activities to streamflow variation were 13.91 and 40.45%, respectively. However, a few studies have computed the quantitative contribution of vegetation variation to streamflow variation in the LCRB.

Therefore, this study assesses the impact of vegetation variation on the streamflow variation in the Lancang River Basin (LCRB) by the following three steps: (1) Analyzing the change characteristics of meteorological and hydrological elements; (2) calculating the functional relationship between the underlying surface parameters (ω) and NDVI, and constructing a modified Budyko formula; and (3) estimating quantitatively the influence of human activities, climate factors, and vegetation on streamflow variation in the Lancang River Basin using the modified Budyko formula. This study is conducive to understanding the impact of ecological restoration project on water cycle and is beneficial to the management and rational utilization of water resources in the LCRB.

2. Study region

The Lancang River Basin (LCRB) originates from Jifu Mountain in the Qinghai Province and flows through Qinghai, Tibet, and Yunnan provinces, between $94.39^{\circ}\sim 103.66^{\circ}\text{E}$ and $20.87^{\circ}\sim 33.36^{\circ}\text{N}$ (Figure 1). After flowing out of China, the river is called the Mekong River. The terrain in the LCRB is high and fluctuates greatly. Therefore, the climate in the river basin varies greatly. The temperature and precipitation increase from the north to the south. The higher the altitude, the lower the temperature and the lesser the precipitation. The runoff of the river basin mainly comes from precipitation, groundwater, and snowmelt. Dry and wet seasons in the LRCB are distinct. The wet season lasts from May to October, and the dry season lasts from November to April. The precipitation in the wet season accounts for $\sim 85\%$, and heavy rains are mostly concentrated during the period from June to August. Few torrential rains are witnessed in the upper reaches, while main torrential rain areas are witnessed in the middle reaches of the basin. Due to the changeable climate type and geographical environment, the vegetation distribution in the river basin shows latitude zonality and vertical zonality. The vegetation types include alpine vegetation, meadow, shrub, coniferous forest, mixed coniferous and broad-leaved forest, and broad-leaved forest. The NDVI value of the river basin rises from northwest to southeast with strong spatial heterogeneity. The low NDVI values are mostly distributed in the Naqu, Yushu, the west of Chengdu, and the north of Diqing, with an altitude above 4,000 m. The vegetation types are mainly alpine, alpine meadow, and shrub. The high NDVI values are mainly distributed in Pu'er and Xishuangbanna with rich vegetation types, mainly subtropical and tropical vegetation (Zhang et al., 2020).

3. Data and methods

3.1. Data

The NDVI data from 1982 to 2015 were obtained from NOAA Climate Data Record Advanced Very High Resolution Radiometer (NOAA CDR AVHRR) data (<https://www.ncei.noaa.gov/products/climate-data-records/normalized-difference-vegetation-index>). First, data format conversion and projection conversion were carried out on the NDVI data. Then, the average value composite method eliminated the influence of some random factors and was applied for calculating the average of the grid. Finally, the NDVI data set of the Lancang River Basin was obtained.

The data of meteorological stations in and around the Lancang River Basin from 1982 to 2015 were gathered from China Meteorological Data Service Center's science data sharing service network (<https://www.cma.gov.cn/>), mainly including precipitation, temperature, wind speed, and relative humidity.

The runoff data of the Yunjinghong hydrological station from 1982 to 2015 were obtained from the Hydrological Yearbook and the National Earth System Science Data Center (<http://www.geodata.cn/>).

3.2. Methods

3.2.1. Bernaola-Galvan segmentation algorithm

The Bernaola-Galvan segmentation algorithm (BG segmentation algorithm) is a heuristic mutation detection method for non-stationary time series data (Bernaola-Galvan and Ch Ivanov, 2001). BG segmentation algorithm divides non-stationary sequence data into multiple stationary sequences. Each subsequence datum has different average values and represents different physical backgrounds. After decomposition, each subsequence datum has the variability of average periodic scale. Therefore, BG segmentation algorithm is a new method to effectively detect mutation years. Its calculation steps are as follows (Feng et al., 2005; Wang et al., 2018):

- (1) Taking the i th point as the dividing point, calculate the average value and standard deviation of the left and right segments around the i th point, which are recorded as $\mu_L(i)$, $\mu_R(i)$, $S_L(i)$, and $S_R(i)$ ($I = 1, 2, 3, \dots, N - 1$), respectively.
- (2) Use the t -test to measure the significance of the difference between U_L and U_R and is rescored as $T(i)$:

$$T(i) = |\mu_L(i) - \mu_R(i)|/S_D \quad (1)$$

$$S_D = [(S_L^2(i) + S_R^2(i))/N_L + N_R - 2]^{1/2} \times (1/N_L + 1/N_R)^{1/2} \quad (2)$$

S_D is the joint variance; N_L and N_R are the numbers of samples in the left and right segments around the i th point, respectively.

- (3) Calculate the significance probability $P(T_{max})$ corresponding to the maximum value (T_m) of t -test statistics by the Monte Carlo simulation.

$$P(T_{max}) = \text{Prob}(T \leq T_m) \quad (3)$$

$$P(T_{max}) \approx \left[\left(1 - I_{\nu/(v+T_m^2)}(\delta\nu, \delta) \right) \right]^\gamma \quad (4)$$

$\gamma = 4.19 \ln N - 11.54$, $\delta = 0.40$, N is the sample of the time series $x(t)$, $\nu = N - 2$, $I_X(a, b)$ is the incomplete β function. P_0 is a threshold set in this study, and its value range is $[0.5, 0.95]$. If $P(T_{max}) \geq P_0$, $X(t)$ is divided into two sequences; otherwise, it is not divided.

- (4) Repeating Steps (1)–(3), respectively, for the two newly sequences to detect all mutation points. In addition, to ensure the effectiveness of statistics, if the length of the subsequence is $\leq l_0$, the subsequence will not be segmented. Furthermore, $l_0 \geq 25$.

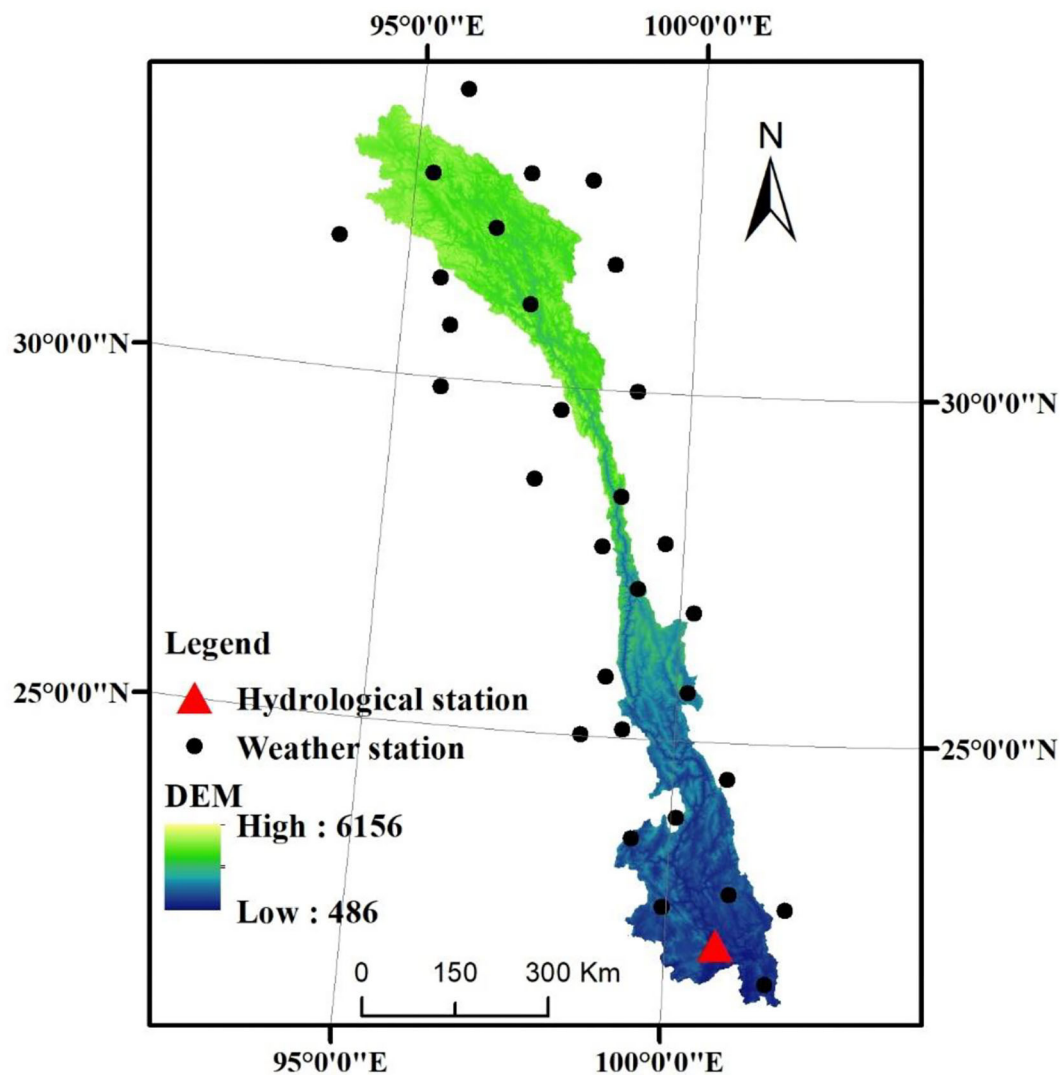


FIGURE 1
The location of hydro-meteorological stations in and around the study region.

3.2.2. Budyko hypothesis

The Budyko hypothesis represents the fact that actual evapotranspiration is limited by water supply conditions (mainly precipitation) and energy supply conditions (mainly potential evaporation). It is an effective method to decompose quantitatively the impact of different factors on streamflow variation, which has been used widely (Wu et al., 2017; Ji et al., 2021c).

The water balance equation in a basin is given as follows:

$$R = Pr - ET \quad (5)$$

In the formula, R is the runoff depth, Pr is the precipitation, and ET is the actual evaporation, which can be calculated

according to the Choudhury-Yang formula (Choudhury, 1999; Yang et al., 2008).

$$ET = \frac{Pr \times ET_0}{(Pr^\omega + ET_0^\omega)^{1/\omega}} \quad (6)$$

ω is the characteristic parameter of the underlying surface, and its value reflects the change of human activity intensity. Human activities can affect runoff variation in the Lancang River Basin from many aspects, including vegetation restoration projects, construction of water conservancy engineering facilities, urban residents' domestic water, and agricultural irrigation water. ET_0 represents the potential evaporation (mm), which can be calculated by the

Penman-Monteith formula.

$$ET_0 = \frac{0.408 \Delta (R_n - G) + \gamma \frac{900}{T+273} U_2 (e_a - e_d)}{\Delta + \gamma (1 + 0.34 U_2)} \quad (7)$$

Combining Equations 5 and 6, we converted the water balance equation to the following equation:

$$R = Pr - \frac{Pr \times ET_0}{(Pr^\omega + ET_0^\omega)^{1/\omega}} \quad (8)$$

Li et al. (2013) studied the relationship between NDVI and Budyko parameter (ω) in 26 rivers and found that there is a good univariate linear function relationship between them.

$$\omega = a \times NDVI + b \quad (9)$$

$$R = Pr - \frac{Pr \times ET_0}{(Pr^{a \times NDVI + b} + ET_0^{a \times NDVI + b})^{1/(a \times NDVI + b)}} \quad (10)$$

3.2.3. Elastic coefficient method

The elasticity coefficient is equal to the ratio of the dependent variable change rate to the independent variable change rate, which analyzes the sensitivity of dependent variable to independent variable (Liu et al., 2012). The greater the absolute value of elasticity coefficient, the stronger the sensitivity of streamflow to various influencing factors. The elasticity coefficient of streamflow to other factors can be expressed as follows:

$$\varepsilon_x = \frac{\alpha R}{\alpha x} \times \frac{x}{R} \quad (11)$$

ε_x is the elastic coefficient; R is the runoff depth (mm); and x refers to specific factors, such as precipitation, potential evaporation, and vegetation. If $\varepsilon_x > 0$, it indicates that runoff increases with the increase in variable x and vice versa. The greater the absolute value of ε_x , the stronger the sensitivity of runoff to variable x .

The elastic coefficients of runoff on precipitation (ε_{Pr}), potential evaporation (ε_{ET_0}), underlying surface characteristic parameters (ε_ω), and NDVI (ε_{NDVI}) can be calculated by Equations 12–15

(Xu et al., 2014; Ji et al., 2022b).

$$\varepsilon_{Pr} = \frac{\left(1 + \left(\frac{ET_0}{Pr}\right)^\omega\right)^{1/\omega+1} - \left(\frac{ET_0}{Pr}\right)^{\omega+1}}{\left(1 + \left(\frac{ET_0}{Pr}\right)^\omega\right) \left[\left(1 + \left(\frac{ET_0}{Pr}\right)^\omega\right)^{1/\omega} - \left(\frac{ET_0}{Pr}\right)\right]} \quad (12)$$

$$\varepsilon_{ET_0} = \frac{1}{\left(1 + \left(\frac{ET_0}{Pr}\right)^\omega\right) \left[1 - \left(1 + \left(\frac{ET_0}{Pr}\right)^{-\omega}\right)^{1/\omega}\right]} \quad (13)$$

$$\varepsilon_\omega = \frac{\ln \left(1 + \left(\frac{ET_0}{Pr}\right)^\omega\right) + \left(\frac{ET_0}{Pr}\right)^\omega \ln \left(1 + \left(\frac{ET_0}{Pr}\right)^{-\omega}\right)}{\omega \left(1 + \left(\frac{ET_0}{Pr}\right)^\omega\right) \left[1 - \left(1 + \left(\frac{ET_0}{Pr}\right)^{-\omega}\right)^{1/\omega}\right]} \quad (14)$$

$$\varepsilon_{NDVI} = \varepsilon_w \frac{a \times NDVI}{a \times NDVI + b} \quad (15)$$

The runoff time series data are divided into two periods: the base period (T_1) and the change period (T_2). The average annual precipitation rates in the T_1 and T_2 periods are marked as Pr_1 and Pr_2 . The change in annual precipitation (ΔPr) from T_1 to T_2 period is expressed as follows:

$$\Delta Pr = Pr_2 - Pr_1 \quad (16)$$

Similarly, the change in potential evaporation (ΔET_0), characteristic parameters of underlying surface ($\Delta \omega$) and NDVI ($\Delta NDVI$) from T_1 to T_2 all are calculated.

$$\Delta ET_0 = ET_{02} - ET_{01} \quad (17)$$

$$\Delta \omega = \omega_2 - \omega_1 \quad (18)$$

$$\Delta NDVI = NDVI_2 - NDVI_1 \quad (19)$$

ΔR_{Pr} , ΔR_{E0} , ΔR_w , ΔR_{NDVI} , and ΔR_H , respectively, represent the runoff depth change values caused by the change in precipitation, potential evaporation, underlying surface feature parameters, NDVI, and anthropogenic factors from the T_1 to T_2 period.

$$\Delta R_{Pr} = \varepsilon_{Pr} \frac{R}{Pr} \times \Delta Pr \quad (20)$$

$$\Delta R_{ET_0} = \varepsilon_{ET_0} \frac{R}{ET_0} \times \Delta ET_0 \quad (21)$$

$$\Delta R_\omega = \varepsilon_\omega \frac{R}{\omega} \times \Delta \omega \quad (22)$$

$$\Delta R_{NDVI} = \varepsilon_{NDVI} \frac{R}{NDVI} \times \Delta NDVI \quad (23)$$

$$\Delta R_H = \Delta R_\omega - \Delta R_{NDVI} \quad (24)$$

$$\Delta R = \Delta R_{Pr} + \Delta R_{E0} + \Delta R_{NDVI} + \Delta R_H \quad (25)$$

$$\eta_{R_{Pr}} = \Delta R_{Pr} / \Delta R \times 100\% \quad (26)$$

$$\eta_{R_{E0}} = \Delta R_{E0} / \Delta R \times 100\% \quad (27)$$

$$\eta_{R_{NDVI}} = \Delta R_{NDVI} / \Delta R \times 100\% \quad (28)$$

$$\eta_{R_H} = \Delta R_H / \Delta R \times 100\% \quad (29)$$

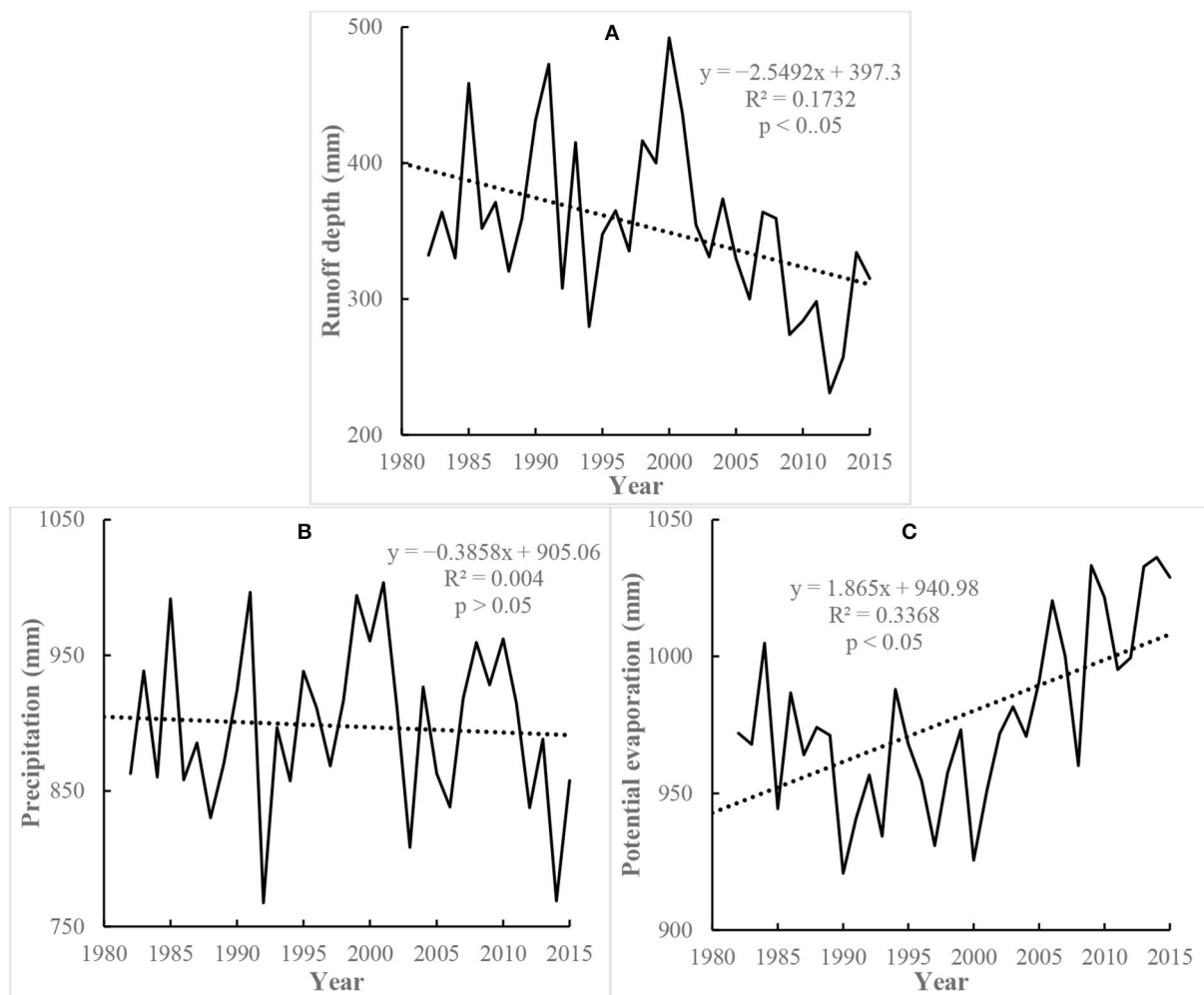


FIGURE 2 Interannual variation of runoff depth (A), precipitation (B), and potential evaporation (C) in the Lancang River Basin (LCRB) from 1982 to 2015.

$\eta_{R_{Pr}}$, $\eta_{R_{ET_0}}$, $\eta_{R_{NDVI}}$, and η_{R_H} , respectively, represent the contribution rates of precipitation, potential evaporation, NDVI, and human factors on runoff variation.

4. Results and analysis

4.1. Trend analysis of meteorological and hydrological data

The linear regression method was used to analyze the change trends of runoff depth, precipitation, and potential evaporation in the LCRB from 1982 to 2015, and the results are shown in Figure 2.

From 1982 to 2015, the runoff depth of the LCRB showed a fluctuation and significant reduction

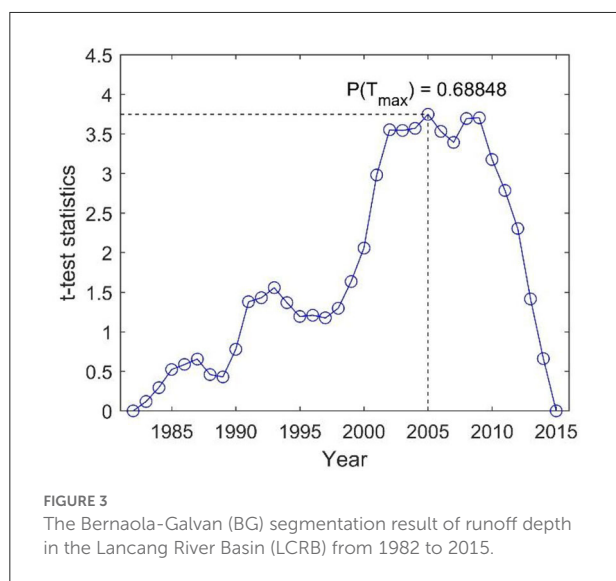
trend ($p < 0.05$), with a slope of -2.5492 mm/a (Figure 2A). During the period of 1982–2015, the runoff depth of the river basin in 2000 was the maximum (492.05 mm), and the runoff depth in 2012 was the lowest (230.91 mm).

During the period of 1982–2015, the precipitation showed a non-significant decreasing trend ($p > 0.05$), with a slope of -0.3858 mm/a (Figure 2B). From 1982 to 2015, the precipitation in 2001 was the maximum (1,003.63 mm) and that in 1992 was the lowest (767.51 mm).

There was a significant fluctuating growth trend in potential evaporation ($p < 0.05$), with a slope of 1.865 mm/a (Figure 2C). During the period of 1982–2015, the potential evaporation was the maximum in 2014 (1,036.25 mm) and was the minimum in 1991 (920.77 mm).

4.2. BG segmentation result of runoff depth

In this study, the BG segmentation algorithm is used to distinguish the abrupt years of the annual runoff data from 1982 to 2015 in the LCRB (Figure 3). P_0 is set to 0.68 and l_0 is set to 25. From Figure 3, we found that t -test statistics takes the largest value in 2005 and it is ~ 3.75 , which showed that the annual runoff of the Yunjinghong hydrological station changed dramatically in 2005 and its mutation year may be fixed as 2005. According to formula (4), we calculated the significance probability $P(T_{max})$, corresponding to the maximum value

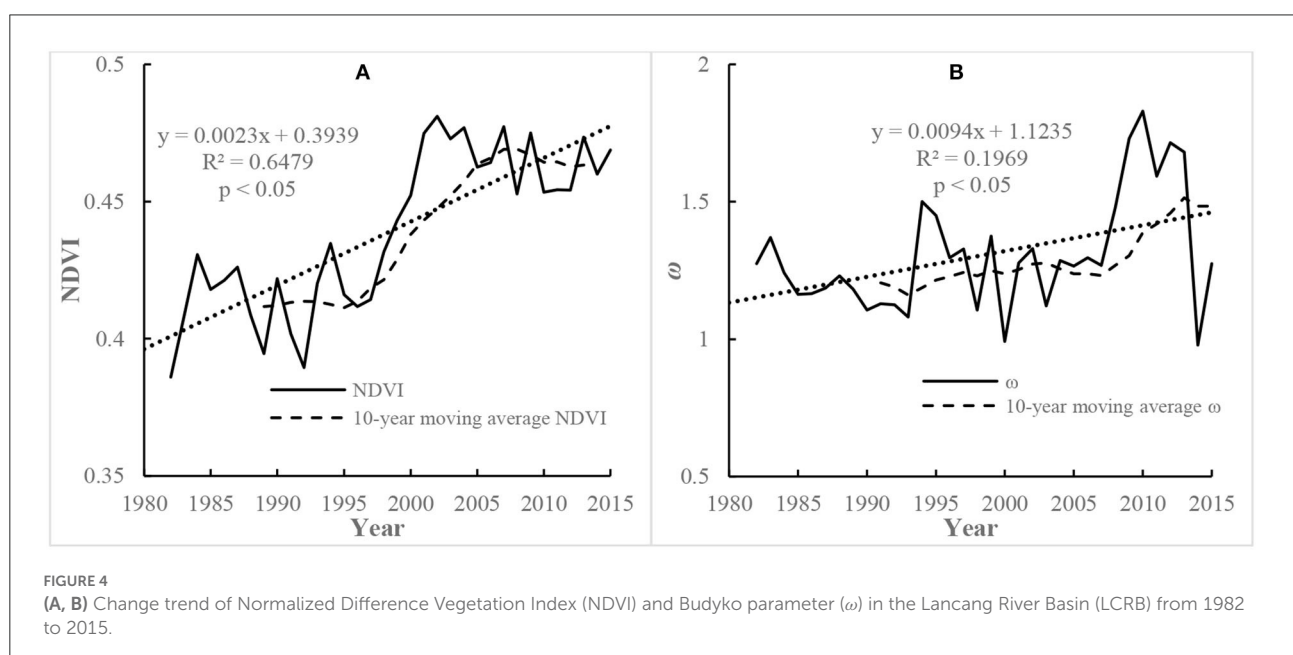


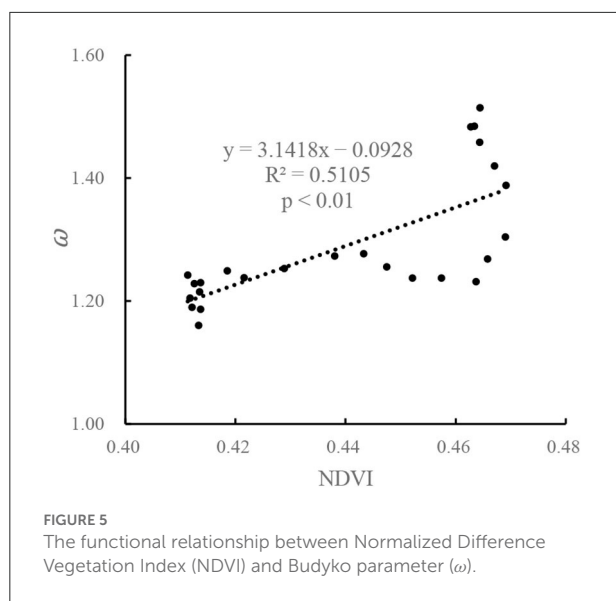
(T_m) of t -test statistics, by the Monte Carlo simulation. If $P(T_{max}) > P_0$, we believe that the sudden change in runoff is significant. The result showed that the significance probability $P(T_{max})$, corresponding to the maximum value (T_m) of t -test statistics (2005), is $0.688 > 0.68$. This result further proves the reliability of the result that the annual runoff series data of the Yunjinghong hydrological station mutated in 2005.

4.3. Attribution analysis of streamflow variation

For the Choudhury-Yang formula, if the values of precipitation and potential evaporation in each year during the period of 1982–2015 can be obtained, we calculated the Budyko parameter (ω) in each year. The changing trend of NDVI and Budyko parameter (ω) in the LCRB is shown in Figure 4. From 1982 to 2015, the NDVI of the Lancang River Basin displayed a significant fluctuation increasing trend ($p < 0.05$), and its average annual growth rate was $0.0023/a$ (Figure 4A). The Budyko parameter (ω) displayed a significant growth trend ($p < 0.05$), with a slope of $0.094/10a$ (Figure 4B).

In the Budyko formula, precipitation (Pr), potential evaporation (ET_0), and underlying surface parameters (ω) are the three driving factors affecting streamflow change. ω denotes the characteristic parameters of the underlying surface and is applied to characterize the influence of human factors. Previous studies showed that vegetation changes have a significant impact on Budyko parameter (ω) (Zeng and Cai, 2016; Zhang et al., 2016; Abatzoglou and Ficklin, 2017). Li et al. (2013) studied the relationship between NDVI and Budyko parameter (ω) in 26





ivers and found that there is a good univariate linear function relationship between them.

To reveal the quantitative relationship between vegetation and Budyko parameters and identify the impact of vegetation change on streamflow, this study established a linear functional equation between NDVI and Budyko parameter (ω) by the following two steps: (1) calculating the 10-year moving average value of NDVI and ω , respectively, and (2) calculating the coefficients (a and b) of the univariate linear regression equation by the least square method. Finally, a linear regression equation was obtained (Figure 5), $a = 3.1418$, $b = -0.0928$, and its R^2 is 0.5105 and adjusted R^2 is 0.4892 ($p < 0.01$).

According to the BG segmentation result of runoff data from 1982 to 2015, we divided the entire study period into two phases: T_1 (1982–2004) and T_2 (2005–2015). Table 1 displays the values of different variables in T_1 (1982–2004) and T_2 (2005–2015) periods. The average runoff depths in the T_1 (1982–2004) period were ~ 375.905 and 304.147 mm in the T_2 (2005–2015) period. The average annual runoff depth decreased by 71.758 mm from T_1 to T_2 , and the relative change rate was -19.09% . The precipitation decreased by 18.336 mm from 903.475 mm in the T_1 period to 885.139 mm in the T_2 period, with a relative change rate of -2.03% . The potential evaporation, Budyko parameter (ω), and NDVI all increased from the T_1 period to the T_2 period, and their relative change rates were 5.15 , 17.39 , and 8.18% , respectively.

In this study, Budyko equation and the elastic coefficient method were used to calculate the influence of various factors on the streamflow variation in the LCRB (Table 2). The elastic coefficient of runoff on precipitation (ε_{Pr}) is 1.73 , indicating that a 10% increase in precipitation causes a 17.3% increase of streamflow. The elastic coefficients of potential evaporation

(ε_{ET_0}), underlying surface characteristic parameters (ε_{ω}) and NDVI (ε_{NDVI}), are -0.73 , -0.83 , and -0.89 , respectively. These values indicated that a 10% increase of potential evaporation, ω , and NDVI decreases by 7.3 , 8.3 , and 8.9% of streamflow. Overall, the streamflow change in the LCRB is the most sensitive to precipitation and the least sensitive to potential evaporation.

Compared to the period during 1982–2004, the contribution rate of climatic factors to runoff depth variation during the period from 1982 to 2015 is 34.47% . Among them, precipitation and potential evaporation contributed 16.83 and 17.61% , respectively. Moreover, the contribution rates of vegetation variation and anthropogenic activities to runoff depth variation during the period from 1982 to 2015 are 34.47 and 31.09% , respectively. Overall, vegetation variation played the largest driving force for streamflow variation in the LCRB.

The change in river runoff is caused by many factors, such as human activities, climate change, and vegetation change. The ecological and hydrological effects of vegetation change serves as the research focus of hydrology and ecology. Many studies assumed that the increase in afforestation or vegetation reduces the runoff (Zhang et al., 2021; Ji et al., 2022b), and the results of this study are consistent with the conclusion (Table 2). With further restoration of vegetation, the NDVI increases significantly. Although the precipitation in this period increased by 2.03% and the potential evapotranspiration increased by 5.15% , the runoff decreased by 19.19% , indicating that vegetation gradually became the dominant factor in controlling the runoff changes (Tables 1, 2). Vegetation changes can affect runoff changes in many ways as per the following points: (1) the increase in vegetation leaf area increases evapotranspiration from plant leaves, leading to a decrease in soil water content, which in turn affects the surface runoff and (2) the increase in vegetation coverage effectively increases the interception capacity of rainfall, thus influencing the variability of runoff. However, vegetation restoration cannot lead to an unlimited increase of NDVI; therefore, with the vegetation restoration and stabilization, the vegetation change will not have a great impact on the runoff change.

5. Conclusions and discussions

5.1. Discussions

The implementation of a series of water and soil conservation and ecological restoration measures in the LCRB has significantly changed the underlying surface parameters (ω). The value of ω in the Budyko equation is closely related to soil, terrain, and vegetation coverage types. The soil and terrain do not change in a short time, while vegetation factors become the main factors affecting ω . NDVI and ω showed a strong synergistic trend (Figure 5).

TABLE 1 The eigenvalues of climate, hydrology, and Normalized Difference Vegetation Index (NDVI) variables in the Lancang River Basin (LCRB).

Periods	R/mm	Pr/mm	ET_0/mm	ω	NDVI
T_1	375.905	903.475	961.336	1.219	0.428
T_2	304.147	885.139	1,010.832	1.431	0.463
Δ	-71.758	-18.336	49.496	0.212	0.035

TABLE 2 Attribution analysis of streamflow variation in the Lancang River Basin (LCRB).

ε_{Pr}	ε_{ET_0}	ε_{ω}	ε_{NDVI}	ΔR_{Pr}	ΔR_{ET_0}	ΔR_{NDVI}	ΔR_H	$\eta_{R_{Pr}}$	$\eta_{R_{ET_0}}$	$\eta_{R_{NDVI}}$	η_{R_H}
1.73	-0.73	-0.83	-0.89	-12.47	-13.04	-25.54	-23.04	16.83%	17.61%	34.47%	31.09%

The contribution analysis of vegetation restoration to runoff changes verifies further the fact that the increase in vegetation coverage causes the attenuation of runoff in the LCRB (Table 2).

The situation that improper vegetation reconstruction reduces water resources should be highly concerning. The government should reasonably plan vegetation restoration according to the actual conditions prevalent at the river basin. Yang et al. (2019) analyzed the impact of different vertical structures on water yield conducting a simulated rainfall experiment in the field, and recorded that the vertical structure of vegetation is an important factor influencing water yield. Therefore, according to the vegetation coverage conditions, the area can be divided into two: vegetation restoration period and key protected areas. The key protection areas can be optimized and the vegetation structure adjusted to increase the runoff as much as possible while keeping the ecological environment less changed. Moreover, the vegetation restoration area should be based on artificial vegetation restoration, and the restoration structure of vegetation should be planned scientifically in the restoration process to control the reduction of runoff flow as much as possible, and, these works need to be studied further.

Although this study has analyzed in depth the sensitivity of streamflow variation in vegetation variation in the LCRB, there are still some indefiniteness as given in the following points: (1) There are a few meteorological stations in the study area. To increase the number of meteorological stations, some meteorological station data outside the study area are added to the study, but there are only 29 meteorological stations. Obtaining the mean value of meteorological elements' data in the LCRB through the Kriging interpolation method would lead to some indefiniteness. (2) The attribution analysis of streamflow variation assumes that the precipitation, potential evaporation, and underlying surface parameter are independent. However, in fact, the three variables are interrelated. Climate change affects the growth of vegetation (Liu et al., 2016). The underlying surface change also provides feedback on atmospheric movement and affects regional and even global

climate change. (3) The water conservancy project built by humans directly affects the temporal and spatial changes of monthly and annual runoff. However, this study considers only the impact of ecological restoration on runoff, neglecting the impact of water and soil conservation engineering measures on runoff leads to some indefiniteness.

In the follow-up study, the water heat coupling model (Leuning et al., 2008; Zhang et al., 2018) reflecting the information on vegetation change should be used for accurately simulating the hydrological process of streamflow variation affected by climate factors, vegetation variation, and reservoir operation. In addition, most of the studies ignored the influence of climate change on the vegetation in the river basin and did not distinguish the contribution rate of human activities and climate factors to vegetation change. Subsequently, we will calculate the contribution of vegetation restoration caused by climate change to runoff change.

5.2. Conclusions

Based on the meteorological, hydrological, and NDVI data of the Lancang River Basin from 1982 to 2015, this study analyzed first the change characteristics of meteorological and hydrological elements. Then, the functional relationship between Budyko parameter (ω) and NDVI was calculated for constructing a modified Budyko formula. Finally, we estimated quantitatively the influence of vegetation variation on streamflow variation in the LCRB using the modified Budyko formula and the elastic coefficient method.

The conclusions showed that (1) the sudden change in streamflow at the Yunjinghong hydrological station appeared in 2005, (2) Budyko parameter (ω) has a good linear functional relation with NDVI in the LCRB ($p < 0.01$), and (3) vegetation variation played the largest driving force for streamflow variation in the LCRB, accounting for 34.47%. The contribution rates of precipitation, potential evaporation, and anthropogenic activities on streamflow variation from 1982 to 2015 are 16.83, 17.61, and 31.09%, respectively.

Data availability statement

Publicly available datasets were analyzed in this study. The names of the repository/repositories and accession number(s) can be found in the article/supplementary material.

Author contributions

Conceptualization: GJ. Data curation: YL, JH, XW, and YG. Methodology and writing—original draft: YL and GJ. Funding acquisition: WC, LL, and JH. Project administration: WC and LL. Writing—review and editing: WC, LL, and GJ. All authors contributed to the article and approved the submitted version.

Funding

This research work was funded by the National Key R&D Program of China (2021YFD1700900), the National Natural Science Foundation of China (42077004), the Research Project

of Henan Science and Technology Think Tank (HNKJZK-2022-04C), and the Special Fund for Top Talents in Henan Agricultural University (30501031).

Conflict of interest

The authors declare that the research was conducted in the absence of any commercial or financial relationships that could be construed as a potential conflict of interest.

Publisher's note

All claims expressed in this article are solely those of the authors and do not necessarily represent those of their affiliated organizations, or those of the publisher, the editors and the reviewers. Any product that may be evaluated in this article, or claim that may be made by its manufacturer, is not guaranteed or endorsed by the publisher.

References

- Abatzoglou, J., and Ficklin, D. (2017). Climatic and physiographic controls of spatial variability in surface water balance over the contiguous United States using the Budyko relationship. *Water Resour. Res.* 53, 7630–7643. doi: 10.1002/2017WR020843
- Allen, M. R., Frame, D. J., Huntingford, C., Jones, C. D., Lowe, J. A., Meinshausen, M., et al. (2009). Warming caused by cumulative carbon emissions towards the trillionth tonne. *Nature* 458, 1163–1166. doi: 10.1038/nature08019
- Bernaola-Galvan, P., and Ch Ivanov, P. (2001). Nunes Amaral. Scale Invariance in the nonstationarity of human heart rate. *nPhys* 87, 1–4. doi: 10.1103/PhysRevLett.87.168105
- Bi, Z., Li, Y., Lin, Y., Bu, T., and Huang, H. (2020). Quantitative assessment on the effects of vegetation changes on runoff based on Budyko theory in the Kuyehe River Basin of northern China. *J. Beijing For. Univ.* 42, 61–71.
- Chen, C., Park, T., Wang, X., Piao, S., Xu, B., Chaturvedi, R. K., et al. (2019). China and India lead in greening of the world through land-use management. *Nat. Sustain.* 2, 122–129. doi: 10.1038/s41893-019-0220-7
- Choudhury, B. J. (1999). Evaluation of an empirical equation for annual evaporation using field observations and results from a biophysical model. *J. Hydrol.* 216, 99–110.
- Fan, N., Xie, G. D., Zhang, C. S., Chen, L., Li, W. H., and Cheng, S. K. (2012). Spatial-temporal dynamic changes of vegetation cover in Lancang River Basin during 2001–2010. *Resour. Sci.* 34, 1222–1231.
- Feng, G. L., Gong, Z. Q., Dong, W. J., and Li, J. P. (2005). Abrupt climate change detection based on heuristic segmentation algorithm. *Acta Phys. Sin.* 54, 5494–5499. doi: 10.7498/aps.54.5494
- Gu, L., Chen, J., Yin, J., Slater, L. J., Wang, H. M., Guo, Q., et al. (2022). Global increases in compound flood-hot extreme hazards under climate warming. *Geophys. Res. Lett.* 49, e2022GL097726. doi: 10.1029/2022GL097726
- Han, Z., Long, D., Fang, Y., Hou, A., and Hong, Y. (2019). Impacts of climate change and human activities on the flow regime of the dammed Lancang River in Southwest China. *J. Hydrol.* 570, 96–105. doi: 10.1016/j.jhydrol.2018.12.048
- Ji, G., Huang, J., Guo, Y., and Yan, D. (2022b). Quantitatively calculating the contribution of vegetation variation to runoff in the middle reaches of Yellow River Using an Adjusted Budyko Formula. *Land* 11, 535. doi: 10.3390/land11040535
- Ji, G., Lai, Z., Xia, H., Liu, H., and Wang, Z. (2021b). Future runoff variation and flood disaster prediction of the Yellow River basin based on CA-Markov and SWAT. *Land* 10, 421. doi: 10.3390/land10040421
- Ji, G., Lai, Z., Yan, D., Wu, L., and Wang, Z. (2022a). Spatiotemporal patterns of future meteorological drought in the Yellow River Basin based on SPEI under RCP scenarios. *Int. J. Clim. Change Strat. Manag.* 14, 39–53. doi: 10.1108/IJCCSM-01-2021-0004
- Ji, G., Song, H., Wei, H., and Wu, L. (2021a). Attribution analysis of climate and anthropic factors on runoff and vegetation changes in the source area of the Yangtze River from 1982 to 2016. *Land* 10, 612. doi: 10.3390/land10060612
- Ji, G., Wu, L., Wang, L., Yan, D., and Lai, Z. (2021c). Attribution analysis of seasonal runoff in the source region of the Yellow River using seasonal Budyko Hypothesis. *Land* 10, 542. doi: 10.3390/land10050542
- Jing, W., Di, L., Zhao, X., Yao, L., Xia, X., Liu, Y., et al. (2020b). A data-driven approach to generate past GRACE-like terrestrial water storage solution by calibrating the land surface model simulations. *Adv. Water Resour.* 143, 103683. doi: 10.1016/j.advwatres.2020.103683
- Jing, W., Zhang, P., Zhao, X., Yang, Y., Jiang, H., Xu, J., et al. (2020a). Extending GRACE terrestrial water storage anomalies by combining the random forest regression and a spatially moving window structure. *J. Hydrol.* 590, 125239. doi: 10.1016/j.jhydrol.2020.125239
- Jing, W., Zhao, X., Yao, L., Jiang, H., Xu, J., Yang, J., et al. (2020c). Variations in terrestrial water storage in the Lancang-Mekong river basin from GRACE solutions and land surface model. *J. Hydrol.* 580, 124258. doi: 10.1016/j.jhydrol.2019.124258
- Leuning, R., Zhang, Y. Q., Rajaud, A., Cleugh, H., and Tu, K. (2008). A simple surface conductance model to estimate regional evaporation using MODIS leaf area index and the Penman-Monteith equation. *Water Resour. Res.* 44, 1–17. doi: 10.1029/2007WR006562
- Li, D., Pan, M., Cong, Z., and Wood, E. (2013). Vegetation control on water and energy balance within the Budyko framework. *Water Resour. Res.* 49, 969–976. doi: 10.1002/wrcr.20107
- Li, S., Liang, W., Fu, B., Lü, Y., Fu, S., Wang, S., et al. (2016). Vegetation changes in recent large scale ecological restoration projects and subsequent impact on water resources in China's Loess Plateau. *Sci. Total Environ.* 569, 1032–1039. doi: 10.1016/j.scitotenv.2016.06.141

- Li, Y., Liu, C., Zhang, D., Liang, K., Li, X., and Dong, G. (2016). Reduced runoff due to anthropogenic intervention in the Loess Plateau, China. *Water* 8, 458. doi: 10.3390/w8100458
- Li, Y., and Liu, G. (2012). Characteristics of vegetation cover changes in Lancang Basin based on MODIS vegetation index products (MOD13). *Resour. Sci.* 34, 1214–1221.
- Liang, W., Bai, D., Wang, F., Fu, B., Yan, J., Wang, S., et al. (2015). Quantifying the impacts of climate change and ecological restoration on streamflow changes based on a Budyko hydrological model in China's Loess Plateau. *Water Resour. Res.* 51, 6500–6519. doi: 10.1002/2014WR016589
- Liu, C., Li, Y., Liu, X., Bai, P., and Liang, K. (2016). Impact of vegetation change on water transformation in the Middle Yellow River. *Yellow River* 38, 7–12.
- Liu, H., Wang, Z., Ji, G., and Yue, Y. (2020). Quantifying the impacts of climate change and human activities on runoff in the Lancang River basin based on the Budyko Hypothesis. *Water* 12, 3501. doi: 10.3390/w12123501
- Liu, X., Liu, C., Luo, Y., Zhang, M., and Xia, J. (2012). Dramatic decrease in streamflow from the headwater source in the central route of China's water diversion project: climatic variation or human influence? *J. Geophys. Res. Atmosp.* 117, 1–10. doi: 10.1029/2011JD016879
- Lü, Y., Zhang, L., Feng, X., Zeng, Y., Fu, B., Yao, X., et al. (2015). Recent ecological transitions in China: greening, browning, and influential factors. *Sci. Rep.* 5, 8732. doi: 10.1038/srep08732
- Moore, F. C., and Diaz, D. B. (2015). Temperature impacts on economic growth warrant stringent mitigation policy. *Nat. Clim. Change* 5, 127–131. doi: 10.1038/nclimate2481
- Tang, J., Yin, X., Yang, P., and Zhang, Z. (2014). Assessment of contributions of climatic variation and human activities to streamflow changes in the Lancang River, China. *Water Resour. Manag.* 28, 2953–2966. doi: 10.1007/s11269-014-0648-5
- Tilley, H. (2015). The global governance of climate change. *Revista Portuguesa De Pneumologia* 16SA, S83–S88.
- Vörösmarty, C. J. (2000). Global water resources: vulnerability from climate change and population growth. *Science* 289, 284–288. doi: 10.1126/science.289.5477.284
- Wang, F., Wang, Z. M., Yang, H. B., and Zhao, Y. (2018). Study of the temporal and spatial patterns of drought in the Yellow River basin based on SPEI. *Sci. China Earth Sci.* 61, 1098–1111. doi: 10.1007/s11430-017-9198-2
- Wang, X., Yang, D., Fang, X., Cheng, C., Zhou, C., Zhang, X., et al. (2020). Impacts of ecological restoration on water resources in middle reaches of Yellow River. *Bull. Soil Water Conserv.* 40, 205–212.
- Wei, X., Sun, G., Liu, S., Jiang, H., Zhou, G., and Dai, L. (2008). The forest-streamflow relationship in China: a 40-year retrospect. *J. Am. Water Resour. Assoc.* 44, 1076–1085. doi: 10.1111/j.1752-1688.2008.00237.x
- Wu, J., Miao, C., Wang, Y., Duan, Q., and Zhang, X. (2017). Contribution analysis of the long-term changes in seasonal runoff on the Loess Plateau, China, using eight Budyko-based methods. *J. Hydrol.* 545, 263–275. doi: 10.1016/j.jhydrol.2016.12.050
- Xu, X., Yang, D., Yang, H., and Lei, H. (2014). Attribution analysis based on the Budyko hypothesis for detecting the dominant cause of runoff decline in Haihe basin. *J. Hydrol.* 510, 530–540. doi: 10.1016/j.jhydrol.2013.12.052
- Yang, C., Yao, W., Xiao, P., and Qin, D. (2019). Effects of vegetation cover structure on runoff and sediment yield and its regulation mechanism. *J. Hydraul. Eng.* 50, 1078–1085.
- Yang, H., Yang, D., Lei, Z., and Sun, F. (2008). New analytical derivation of the mean annual water-energy balance equation. *Water Resour. Res.* 44, W03410. doi: 10.1029/2007WR006135
- Yin, J., Gentile, P., Zhou, S., Sullivan, S. C., Wang, R., Zhang, Y., et al. (2018). Large increase in global storm runoff extremes driven by climate and anthropogenic changes. *Nat. Commun.* 9, 4389. doi: 10.1038/s41467-018-06765-2
- Yin, J., Guo, S., Gentile, P., Sullivan, S. C., Gu, L., He, S., et al. (2021). Does the hook structure constrain future flood intensification under anthropogenic climate warming? *Water Resour. Res.* 57, e2020WR028491. doi: 10.1029/2020WR028491
- Yin, J., Guo, S., Wang, J., Chen, J., Zhang, Q., Gu, L., et al. (2022a). Thermodynamic driving mechanisms for the formation of global precipitation extremes and ecohydrological effects. *Sci. China Earth Sci.* 65, 1–19. doi: 10.1007/s11430-022-9987-0
- Yin, J., Slater, L., Gu, L., Liao, Z., Guo, S., and Gentile, P. (2022b). Global increases in lethal compound heat stress-hydrological drought hazards under climate change. *Geophys. Res. Lett.* 49, e2022GL100880. doi: 10.1029/2022GL100880
- Zeng, R., and Cai, X. (2016). Climatic and terrestrial storage control on evapotranspiration temporal variability: analysis of river basins around the world. *Geophys. Res. Lett.* 43, 185–195. doi: 10.1002/2015GL066470
- Zhang, D., Liu, X., Zhang, Q., Liang, K., and Liu, C. (2016). Investigation of factors affecting intra-annual variability of evapotranspiration and streamflow under different climate conditions. *J. Hydrol.* 543, 759–769. doi: 10.1016/j.jhydrol.2016.10.047
- Zhang, D., Liu, X. M., and Bai, P. (2018). Different influences of vegetation greening on regional water-energy balance under different climatic conditions. *Forests* 9, 412. doi: 10.3390/f9070412
- Zhang, J., Zhang, C., Bao, Z., Li, M., Wang, G., Guan, X., et al. (2021). Effects of vegetation cover change on runoff in Huang-Huai-Hai River Basin. *Adv. Water Sci.* 32, 813–823.
- Zhang, T., Yi, G., and Zhang, T. (2020). Spatial-temporal variation in NDVI and its response to climate in the Lancang River Basin from 2000 to 2017. *Geomat. Spatial Inform. Technol.* 43, 49–53.
- Zhu, Z., Piao, S., Myneni, R. B., Huang, M., Zeng, Z., Canadell, J. G., et al. (2016). Greening of the earth and its drivers. *Nat. Clim. Change* 6, 791–795. doi: 10.1038/nclimate3004



OPEN ACCESS

EDITED BY

Wenlong Jing,
Guangzhou Institute of Geography,
China

REVIEWED BY

Xin Lyu,
Beijing Normal University, China
Laing Zhou,
Lanzhou Jiaotong University, China

*CORRESPONDENCE

Wenneng Zhou,
✉ zhouwn@gdut.edu.cn

SPECIALTY SECTION

This article was submitted to
Environmental Informatics and Remote
Sensing,
a section of the journal
Frontiers in Environmental Science

RECEIVED 31 October 2022

ACCEPTED 01 December 2022

PUBLISHED 20 January 2023

CITATION

Wang C, Zhang J and Zhou W (2023),
The effect of animal husbandry on
economic growth: Evidence from
13 provinces of North China.
Front. Environ. Sci. 10:1085219.
doi: 10.3389/fenvs.2022.1085219

COPYRIGHT

© 2023 Wang, Zhang and Zhou. This is
an open-access article distributed
under the terms of the [Creative
Commons Attribution License \(CC BY\)](#).
The use, distribution or reproduction in
other forums is permitted, provided the
original author(s) and the copyright
owner(s) are credited and that the
original publication in this journal is
cited, in accordance with accepted
academic practice. No use, distribution
or reproduction is permitted which does
not comply with these terms.

The effect of animal husbandry on economic growth: Evidence from 13 provinces of North China

Chu Wang¹, Jinbing Zhang² and Wenneng Zhou^{3*}

¹Business School, The University of Queensland, Brisbane, QLD, Australia, ²College of Geography and Environmental Science, Henan University, Kaifeng, China, ³Guangdong Provincial Key Laboratory of Water Quality Improvement and Ecological Restoration for Watersheds, School of Ecology, Environment and Resources, Guangdong University of Technology, Guangzhou, China

Promoting animal husbandry industry is important to help strengthen the agricultural sector. This study starts from both socio-economic and natural factors perspectives. Based on an exploratory spatial analysis, spatial econometric model, and geographically weighted regression (GWR) model, selecting the 13 Provinces of North China as the study area, this study analyzes the spatio-temporal differences and the driving factors. This study found: 1) Between 2006 and 2017, the spatial and temporal differences of GDP in the 13 provinces were statistically significant, with increased total production values and a slowed growth of the industry. In addition, the study area showed an east-west dichotomy in husbandry industry. 2) GDP had shown obvious spatial agglomeration, of which areas with the high production value were in east of Beijing, and areas with low production value were in western Inner Mongolia, Xinjiang and Gansu. 3) Population, animal husbandry output values, numbers of large livestock, and cultivated areas had greatly influenced the GDP of 13 provinces in north China. 4) The three influencing factors on GDP in the 13 provinces were found to be population, animal husbandry output values, and the sizes of cultivated areas. We should synthesize these influencing factors, supplemented with public policy concessions and compensatory measures to develop policies for improving the level of local economic development. Based on this, this study aims to provide a reference for decision making to promote the coordinated development of livestock husbandry and economic growth in China, and even provide a scientific reference for the management of similar pastoral areas in the world.

KEYWORDS

animal husbandry, GDP growth, spatio-temporal differentiation, spatial econometric model, North China

1 Introduction

Animal husbandry, an important component of agriculture, is also a pillar industry that supports the survival and development of farmers and herdsmen (Weindl et al., 2017; Aleshina et al., 2020; Maryunani, 2021; Dai et al., 2022), especially in north China. The animal husbandry industry accounts for about half of the global agricultural economy and

makes important contributions to global food security (Foley et al., 2011; Wang G. et al., 2016; Maryunani, 2021). However, global food demands are expected to continue to increase in the coming decades (Tilman et al., 2002; Tilman et al., 2011; Mueller et al., 2012). This is particularly the case in developing countries, where the consumption of meat, eggs, and milk is expected to increase significantly due to increased population and rising income levels (Godfray et al., 2010; Thornton, 2010; Kastner et al., 2012; Gerber et al., 2013; Ethier et al., 2017; Valenzuela-Lamas and Albarella, 2017; Parlato et al., 2022).

China has 393 million hectares of grasslands, accounting for 42% of the country's total land area. With the continuing economic development in China and the living standards of her residents continue to rise, along with the trend that the animal husbandry industry is shifting from traditional household production (self-consumption and local market allocation) to intensive industrial production (Wang X. et al., 2016; Tan et al., 2017; Cheng et al., 2022), demands for livestock output in China are projected to continue to increase in the near future. This growing demand for animal products, such as meat, eggs, and milk (Shimokawa, 2015; Makkar, 2016; Zhao X et al., 2017), has stimulated further development of the animal husbandry economy. As a result, the share of animal husbandry promoted from 14.98% during the early implementation of the Reform and Opening Up Policy in early 1980s to 28.28% in 2016 (Fu et al., 2012; Qu et al., 2021). However, compared to developed countries, this proportion is still relatively low when considering conditions in other developed countries. For example, the outputs of animal products in the United States, United Kingdom, and France account for 48%, 70%, and 80% of total agricultural output, respectively. Since animal husbandry in China relies mainly on natural and cultivated forage resources (Thornton and Gerber, 2010; Godber and Wall, 2014) and 90% of grasslands has suffered different some degrees of degradation due to overgrazing (Li et al., 2021), it is essential to explore the driving factors that influence the development of animal husbandry and their effects on the animal husbandry economy in order to adapt to and mitigate the impact of global changes in economic development.

Developing the animal husbandry economy to drive up GDP growth without sacrificing the ecological environment has become a focus of international research. Jayaraman and Nyachoti (2016) approached the subject from the perspective of livestock breeding and proposed that the effectiveness in breeding could be the key to a healthy livestock development. Liu et al. (2022a) and Yu et al. (2021) considered that the development of animal husbandry was, to some extent, affected by demographic factors. Influenced by global warming, climate in many regions had changed greatly, which could directly affect vegetation dynamics and biomass. Furthermore, climate changes would also influence the structure and a region's carrying capacity of livestock (Bernués et al., 2011; Middleton et al., 2015; Yao et al., 2017).

Morgan-Davies et al. (2012) studied animal husbandry in the hilly areas of northwestern Europe and found that climate changes and production barriers were the primary factors that hindered the production of animal husbandry and economic development in their study areas. Xie et al. (2022) assessed the vulnerability of animal husbandry toward global climate changes from a macro perspective. Similarly, the Qinghai-Tibet Plateau, an important pastoral area in China, was considered by Wei et al. (2017) and Liu et al. (2014) that global warming and the shortage of forage are the main reasons for the high vulnerability of the local animal husbandry. At the same time, the rapid growth in animal husbandry has led to further increases in the concentration of global greenhouse gases (GHG) in many regions (Hyland et al., 2016; Pardo et al., 2016; Sakadevan and Nguyen, 2017). To that end, Wang et al. (2021) and Zhuang and Li (2017) suggested that GHG emissions were influenced by animal husbandry industry in China. Scholars have also investigated the effects of grazing on the concentration of soil organic carbon (Hewins et al., 2018; Windirsch et al., 2022), phosphorus in grasslands (Sattari et al., 2016), and carbon emissions (Fischer et al., 2022).

In the aforementioned studies, although scholars have made certain achievements in research on the animal husbandry economy, the main regions of focus in those studies have been the United States and European countries, both are developed economies. But studies about China, on the other hand, have tended to adopt the perspective of environmental protection. Since China joined the World Trade Organization (WTO) in 2001, the proportion of animal products in exported agricultural products in its total economy has increased. Animal husbandry has gradually become a primary industry of the nation's economy. There is insufficient research on the spatial spillover effects of factors that could affect the animal husbandry economy and their comprehensive impacts from both anthropogenic and natural environmental factors. In addition, the majority of the studies have approached the subject from a provincial and municipal level. However, studies that targeted larger, more generalized regions are few and limited. Moreover, existing research mostly utilized time-series analyses rather than a geospatial perspective to examine the spatial dependency of animal husbandry development at a regional level. Such approaches tend to assume one model fits all regions in a study area, i.e., spatial stationarity, which of course, is usually not the case in reality. Therefore, in light of the gaps in existing research and limitations of animal husbandry development in China, it is necessary to conduct a comprehensive study to uncover the driving factors of the development of animal husbandry and its contributions to China's GDP. This study selected 13 provinces, including provincial municipalities and autonomous regions in north China, as the focus of research and 2006 to 2017 as the research period in order to

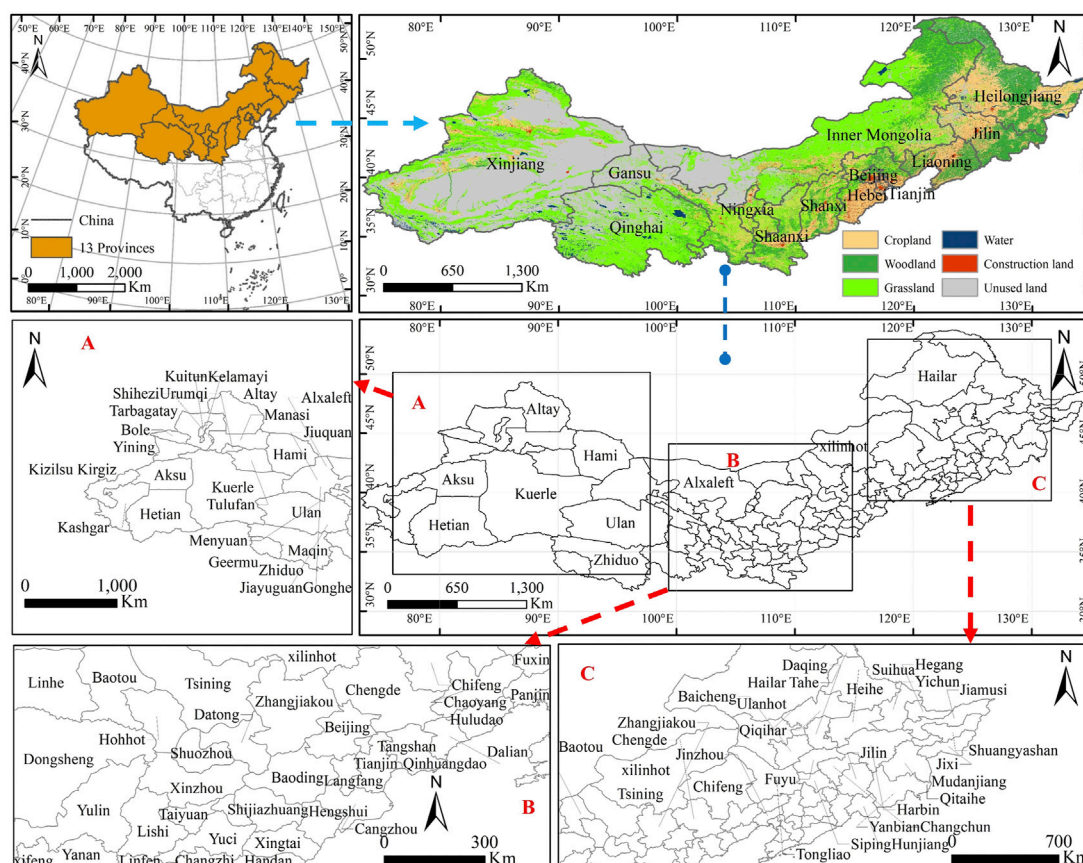


FIGURE 1

Map of study area. Note: A represents the western part of the study area, B represents the central part of the study area, C represents the eastern part of the study area.

comprehensively investigate the impact of regional animal husbandry on GDP. A spatio-temporal evolutionary perspective was adopted and a spatial analytical method was employed to explore influencing factors; an exploratory analysis method was introduced to measure the spatial differentiation of GDP of the 13 investigated provinces; an econometric model was constructed to verify the existence of a spatial spillover effect; and finally, GWR model was used to quantitatively analyze the different levels of influence by factors that affect the spatial distribution of GDP.

The purpose of the study is to provide a theoretical basis as a reference for decision-making and policies by concerned stakeholders, to facilitate the transformation of traditional animal husbandry to modern animal husbandry, to assist in the alleviation of the imbalance in the forage-animal relationship, and to explore new development models for animal husbandry that are in accordance with the characteristics of pasture areas. And in order to maintain a healthy development in animal husbandry and to create a solid foundation for a sustainable development of the agricultural economy in China.

2 Methods and data sources

2.1 Study area

The 13 provinces of north China (31° – 54° N, 73° – 136° E) in this study, consisting of 124 prefecture-level cities that span over three “steps” in China’s topographic “staircase” and four climate zones (wet/semi-wet and arid/semi-arid), accounts for about 57% of the total area of China (see Figure 1). The area has four zones crossing wet, semi-humid, semi-drought and drought. The regional differences and transitionability of the climate are obvious, and the types of vegetation on the surface are diverse and the ecological environment is relatively fragile. The main grasslands, the agro-pastoral zone, and most of China’s desert areas are all located in the study area. With abundant water and forage resources, the region’s animal husbandry was the most widespread in the country. The 13 provinces are a representative area for research on animal husbandry development in China as well as serving as a model region for other developing countries with a similar scale of animal husbandry (Zhen et al., 2020; Yang et al., 2022).

TABLE 1 Data sources.

Type of data	Years	Content	Sources (address)
Vector data	—	The digital boundary of administrative regions	The Data Center for Resources and Environmental Sciences of the Chinese Academy of Sciences (https://www.resdc.cn/)
Socio-economic data	(2003–2018)	GDP, population, output values of animal husbandry, numbers of large livestock, numbers of cattle, numbers of sheep, area sizes of arable land	Beijing Statistical Yearbook, Tianjin Statistical Yearbook, Hebei Economic Yearbook, Shanxi Statistical Yearbook, Inner Mongolia Statistical Yearbook, Jilin Statistical Yearbook, Liaoning Statistical Yearbook, Heilongjiang Statistical Yearbook, Shaanxi Statistical Yearbook, Gansu Statistical Yearbook, Ningxia Statistical Yearbook, Qinghai Statistical Yearbook, Xinjiang Statistical Yearbook, Other Data (http://www.stats.gov.cn/)
Raster data	—	classified images of grassland areas, surface temperature, precipitation	The Data Center for Resources and Environmental Sciences of the Chinese Academy of Sciences (https://www.resdc.cn/)

2.2 Data sources

The data employed in this study were mainly included the following three types, which are shown in Table 1:

- (1) Vector data of administrative regions: The vector data were created with maps at a scale of 1:250,000.
- (2) Socio-economic data: The socioeconomic data used in this study include GDP, population, output values of animal husbandry, numbers of large livestock, numbers of cattle, numbers of sheep, and area sizes of arable land of all geographic units in the study area.
- (3) Raster data: The raster data used in the study include classified images of grassland areas, surface temperature, and precipitation. The spatial resolution of the data was 1 km, which was sufficient to meet the research needs, considering the extent of the study area.

2.3 Methods

2.3.1 ESDA model

Exploratory spatial data analysis (ESDA) examines the spatial dependency (spatial autocorrelation) of attribute values of the 124 cities through data aggregation and spatial interaction to reveal the regional structure of spatial variables, including levels of global and local spatial autocorrelation (Rong et al., 2022; Shi et al., 2022). This study used the Global Moran's *I* to examine if there existed statistically significant spatial autocorrelation among data values of the spatial units.

Global spatial autocorrelation describes only the level of spatial dependency among attribute values of the spatial units being examined. It does not consider any local spatial heterogeneity that may lead to the identification of the locations of the clusters and types of spatial associations. Therefore, this study used local spatial autocorrelation coefficients to describe the levels of spatial dependence and

their different levels among the attribute values of the local area units. A local indicators of spatial association (LISA) map was constructed to identify the patterns of their local spatial differentiation.

2.3.2 Spatial econometric model

Spatial autocorrelation analysis helps to reveal the patterns and the levels of spatial clustering of GDP of the studied provinces from a spatial perspective; however, the method is unable to reveal the factors that influence the corresponding spatial effects. To explore the potential effect of a set of carefully selected indicators on the levels and patterns of spatial agglomeration of GDP under the spatial spillover effect, this study used the Lagrange multiplier (LM) test, which is the most commonly used test in ordinary least square (OLS) models, to construct a spatial lag model (SLM) and a spatial error model (SEM) (Zhao Y et al., 2017).

2.3.2.1 Variable selection

Economic development is the product of human activities and is influenced by factors from various dimensions. Most studies have approached the subject from the perspectives of physical geography, transportation advantages, human activities, and economic policies (Amarasinghe et al., 2005; Liu et al., 2022b). There exists only limited research on the impact of animal husbandry on economic development in China if compared to what had been done in other countries. In recent years, human activities, climate changes, and grassland management policies and management levels have been considered as the main drivers of grasslands in north China (Cheng et al., 2022). Therefore, based on past research and real-life factors in the investigated area, and considering the scientific nature, completeness, and availability of data, this study analyzed the influencing factors of GDP of the 13 provinces using both socio-economic and physical attributes of the cities in 13 provinces (Table 2). With GDP as the dependent variable, husbandry output, population, number of livestock, arable land,

TABLE 2 Index evaluation system.

Variable type	Variable		Indicator
Dependent variable	Y		GDP (1,000 million yuan)
	A	B	
Independent variable	Socio-economic factors	X ₁	Output of animal husbandry (100 billion Yuan)
		X ₂	Population ($\times 10^4$)
		X ₃	Large Livestock ($\times 10^4$)
		X ₄	# Cattle ($\times 10^4$)
		X ₅	# Sheep ($\times 10^4$)
	Natural factors	X ₆	Arable Land (km ²)
		X ₇	Grassland (km ²)
		X ₈	Surface Temperature (°F)
		X ₉	Precipitation (cm)

grassland, temperature and precipitation level were selected as the independent variables to explain the variation in GDP among the cities of the 13 provinces.

2.3.2.2 Econometric model

The SLM model mainly examines whether the spatial dependency between variables leads to spatial autocorrelation and whether adjacent regions have a diffusion (spillover) effect in the study area. The SEM model is mainly used to measure the influence of error in the dependent variable of adjacent regions on local observed values (Zhang et al., 2020a). The models can be presented by the following formula:

$$\text{SLM: } y = \rho W y + X\beta + \varepsilon \quad (1)$$

$$\text{SEM: } y = X\beta + \varepsilon, \text{ where, } \varepsilon = \lambda W\varepsilon + \mu \quad (2)$$

where, y is the dependent variable; ρ is the regression coefficients; W is the weight matrix; β is the correlation coefficients of the independent variables X ; ε is the random error term; λ is the spatial error coefficient; and μ is the random error vector.

2.3.3 Geographically weighted regression (GWR)

The traditional OLS model is a non-spatial model that assumes spatial stationarity of the association between dependent and independent variables. It does not consider the spatial heterogeneity of model parameters and cannot reflect the differences in the impact of animal husbandry development on GDP when the geographic environment is not constant (i.e., spatial non-stationarity). This problem can be addressed by using the GWR model. Extended from the OLS model, GWR model embeds spatial factors and integrates the spatial dependency and spatial heterogeneity in the model (Zhang

et al., 2020b; Chen et al., 2022). For that reason, this study introduced the GWR model as part of the analysis.

The GWR model can be used to quantitatively evaluate spatial instability, or what is often referred to as spatial non-stationarity, of data values. It has been applied widely in different fields (Cohen et al., 2015; Huang et al., 2015). The model can be represented by the following formula:

$$y_i = \beta_0(u_i, v_i) + \sum_k \beta_k(u_i, v_i)x_{ik} + \varepsilon_i \quad (3)$$

where, (u_i, v_i) signifies the spatial position of region i ; $\beta_0(u_i, v_i)$ is a constant term; k indicates the number of independent variables; $\beta_k(u_i, v_i)$ is the value of the continuous function $\beta(u, v)$ at point (u_i, v_i) ; x_{ik} is the value of the k th independent variable of i ; and ε_i is the error term.

3 Results

3.1 Characteristics of the spatio-temporal evolution of animal husbandry

GDP is perhaps the best indicator that can reflect the economic level for a country/region comprehensively. The contribution of animal husbandry to GDP is of particular importance for the analysis in this study. Given that the development of animal husbandry is mainly manifested by its output value, this study used the output values of animal husbandry to support the analysis of the contribution of animal husbandry development on GDP.

Figure 2 shows that between 2006 and 2017, the GDP of the investigated provinces continued to grow with decreasing fluctuations in the growth rates over time. Specifically, GDP

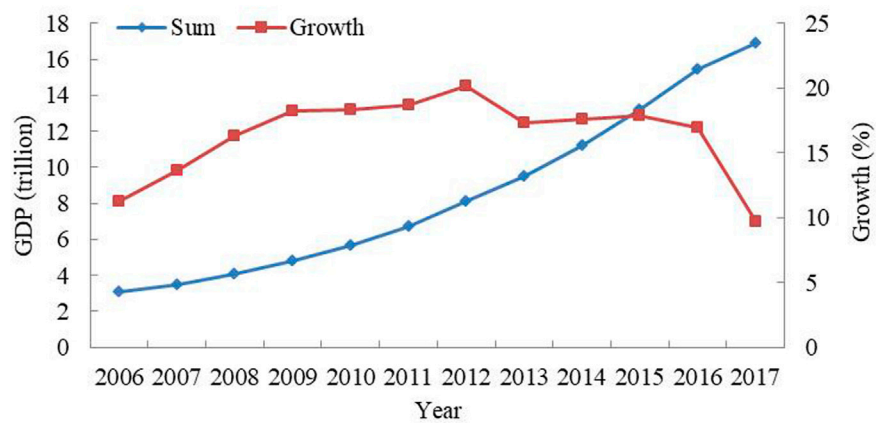


FIGURE 2

Evolutional Trends of GDP and Growth in the 13 Provinces of North China (2006–2017). Note: Sum (Total GDP); Growth (Growth of GDP).

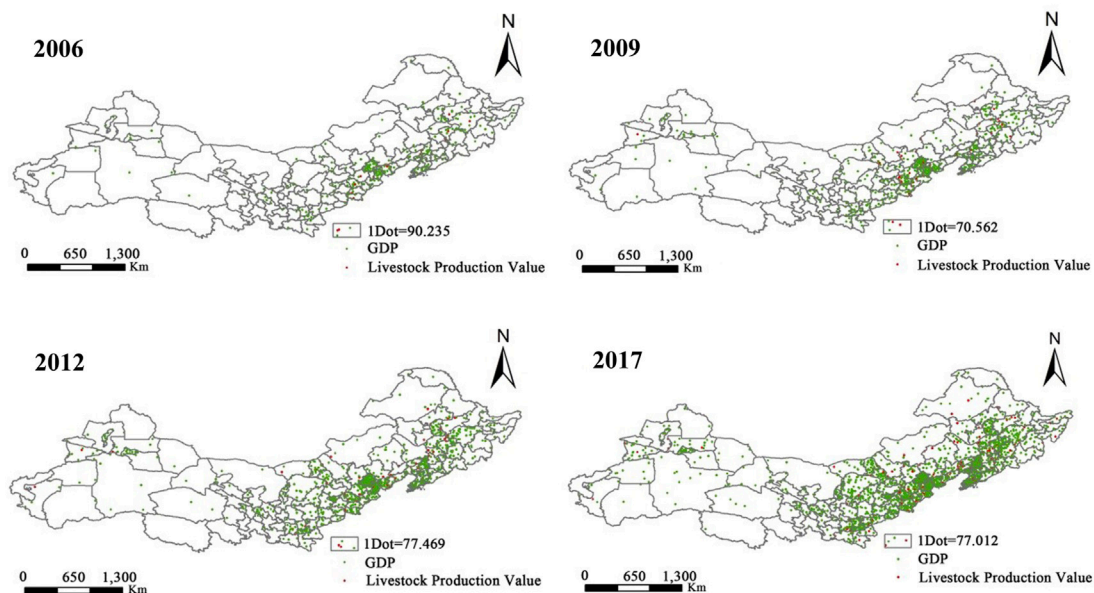


FIGURE 3

Spatial Patterns of GDP and Livestock Production Values in the 13 Provinces of North China (2006, 2009, 2012, and 2017).

increased from 3.073 trillion yuan (RMB) in 2006 to 16.907 trillion yuan in 2017. Animal husbandry has long been the main driving force for economic development in the study area. Owing to the implementation of key region-wide projects, such as animal protection, improvement in the breeding system of livestock and poultry, and restoring grazing lands to grasslands, the increases of GDP reached a peak value in 2004. Thereafter, affected by the global financial crisis and livestock and poultry diseases in 2012 and 2013, the growth

began to slow down. Thus, this study selected 2006 (the first year of the study period), 2009, 2012 (both years with noticeable changes in the growth of GDP), and 2017 (the last year of the study period) to further explore the spatial differences in GDP growth and output values of animal husbandry in the study area (Figure 3). The results showed that GDP were higher in the eastern regions but lower in the western regions of the study area. This agglomerated trend became more apparent as time went on. Moreover, the outputs of animal husbandry were positively

TABLE 3 Spatial autocorrelation index of GDP in the 13 provinces of North China between 2006 and 2017.

Year	Moran's I	E(I)	Variance	Z-score	p-value
2006	0.262	−0.008	0.003	5.398	0.000
2007	0.242	−0.008	0.002	5.188	0.000
2008	0.240	−0.008	0.002	5.192	0.000
2009	0.244	−0.008	0.002	5.270	0.000
2010	0.244	−0.008	0.002	5.279	0.000
2011	0.242	−0.008	0.002	5.234	0.000
2012	0.244	−0.008	0.002	5.211	0.000
2013	0.246	−0.008	0.002	5.195	0.000
2014	0.251	−0.008	0.002	5.235	0.000
2015	0.255	−0.008	0.003	5.260	0.000
2016	0.257	−0.008	0.003	5.272	0.000
2017	0.281	−0.008	0.003	5.421	0.000

Note: E(I) represents the mathematical expectation; "Variance" is the variance of the variables; "Z-score" shows the normalized difference; "p-value" shows the level of significance.

correlated with changes in GDP. These trends could be related to the characteristics of different climate zones and land types of the region. Specifically, western areas of the study areas mostly suffered from desertification and grassland desertification. Owing to environmental factors (e.g., land desertification and reduced biodiversity), GDP and output of animal husbandry in the western areas of the study areas were lower than that of the eastern areas in the study areas.

3.2 Verification of spatial dependency

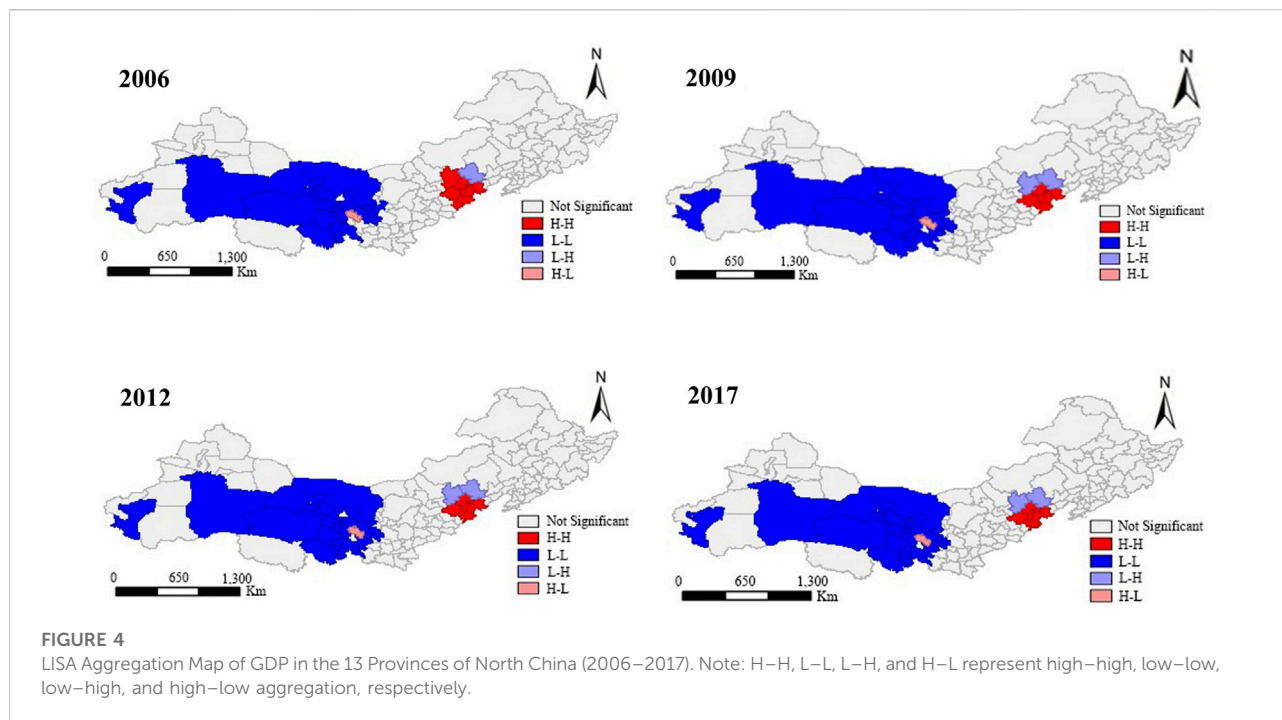
3.2.1 Verification of global spatial autocorrelation of GDP

To explore the spatial relationship of the adjacent areas, this study calculated the Moran's I values of GDP in the 13 Provinces of North China between 2006 and 2017. Table 3 shows, as for GDP, the values of Global Moran's I were calculated (Table 3) based on Eq. 1. The values of Moran's I were all positive and were statistically significant. They indicate a spatially agglomerated distribution of the variable. The Z-scores of the calculated index values were greater than 2.58 ($p < 0.01$), indicating that the GDP of the provinces had significant and positive spatial autocorrelation, which means provinces with high GDP tended to cluster together as did among those with and low GDP. In addition, as shown in Table 2, GDP in 2009 and 2012 showed a trend of recovery following a declining trend before 2004. This trend is consistent with the overall growth trend. These results further verify that 2006, 2009, and 2012 are critical years during the study period.

3.2.2 LISA map of animal husbandry development

The global spatial autocorrelation analysis shows the overall spatial agglomeration pattern of GDP. Results assist the selection of explanatory variables when constructing the research model; however, they do not indicate the trend of aggregation of high and low values between regions in the study area. Thus, a series of LISA maps were created to visualize the spatial patterns of GDP over time to explore the spatial agglomeration of the GDP between neighboring cities in the 13 provinces of north China (Figure 4).

Figure 4 shows, cities with high GDP, such as Beijing, Baoding, Langfang, Tianjin, Zhangzhou, and Tangshan in the eastern area, were found to be aggregated spatially (high–high agglomeration, H–H). Zhangjiakou and Chengde, two cities to the north of the H–H zone, appeared to be agglomerated towards the H–H zone. Cities with low GDP, such as Inner Mongolia, Xinjiang, and Gansu in the western part of the study areas, were also found to be spatially agglomerated (low–low agglomeration). The local spatial agglomerations among other provinces and cities were not significant. Moreover, during the study period, no apparent changes were observed in the statistically spatial agglomeration pattern of GDP among the investigated provinces. The results showed fewer H–H agglomerations in the eastern parts of the study area. A possible explanation is that, although the climate changes and land use types in the eastern areas are more suitable for animal husbandry development, the economic development and livestock and poultry farming techniques of the investigated cities were different. As a result, the overall GDP of cities in the eastern areas were higher than



that in the west; however, local agglomeration was not prominent.

3.3 Verification with spatial econometric model

Moran's I and LISA maps above revealed that the pattern of spatial autocorrelation of the GDP among 13 provinces were statistically significant. To further uncover the quantitative relationship between animal husbandry development and GDP, this study carried out a spatial econometric analysis, using the factors that had significant associations with animal husbandry.

3.3.1 Influencing factors of animal husbandry development

Referring to the determining criteria proposed by [Anselin \(1995\)](#), when the results of the LM tests for the missing spatially lagged dependent variable (LM-lag) and error dependence (LM-err) are both insignificant, the estimation results of the OLS model are considered better to explain the spatial autocorrelation among cities; however, if only one of the test results is significant, the OLS estimation results can be seen as biased and require further analysis with a more appropriate spatial econometric model ([Lin and Long, 2014](#); [Zhu et al., 2017](#)). In other words, the basic principle is that, when the results of the LM-lag test are statistically more significant than those of the LM-err test, and the robust LM-lag is significant while the robust LM-err is

insignificant, an SLM should be adopted; otherwise, the SEM ought to be adopted ([Anselin, 1988](#); [Geng et al., 2022](#)). These results can be seen in [Table 4](#).

[Table 3](#) shows that the LM-err test of GDP in 2006, 2009, 2012, and 2017 were more prominent than those of the LM-lag test, indicating that the SEM is more suitable for analyzing GDP of the investigated years, as the spatial effect of GDP in the region depended on the influence of adjacent cities, rather than solely on itself. For that reason, it was necessary to further verify and analyze the SEM of GDP in the corresponding years.

3.3.2 Testing the spatial econometric model

According to the [Table 4](#), the R^2 values of the SEM of GDP in the years of 2006, 2009, 2012, and 2017 were 0.829, 0.813, 0.796, and 0.792, respectively. These levels were higher than those of the fit of the OLS models. Hence, the SEM was more suitable than OLS estimation. Moreover, population was found to be the most influential factor in promoting GDP growth throughout the 4-year period ($p < 0.01$), followed by the output values of animal husbandry ($p < 0.01$). However, the area of arable land and the number of large livestock units appeared to inhibit GDP growth.

3.4 Results of the GWR model

GWR model was constructed to address the issue of spatial non-stationarity that may exist among attribute data of the cities in the study area. GDP, Y , for each city in 2006, 2009, 2012, and

TABLE 4 OLS Estimates of GDP in the 13 provinces of North China (2006, 2009, 2012, and 2017).

LM text	2006	2009	2012	2017
R^2	0.816	0.799	0.766	0.760
LM-LAG	0.556	0.468	4.950**	2.409
Robust LM-LAG	0.182	0.267	0.209	0.391
LM-ERR	3.818*	3.750*	9.450**	10.557***
Robust LM-ERR	3.444*	3.548*	4.709**	8.539***
LM-SARMA	0.135	4.017	9.659***	10.948***

Notes: 1) ***: $p < 0.01$; **: $p < 0.5$; and *: $p < 0.1$. 2) For analysis purposes, the logarithm of the data was used.

TABLE 5 Descriptive statistics of the regression coefficients in the GWR model (2006, 2009, 2012, and 2017).

	Variable	Average	Maximum	Minimum	Upper quartile	Median	Lower quartile
2006	X_1	0.602	0.628	0.486	0.622	0.615	0.599
	X_2	0.674	0.716	0.651	0.687	0.669	0.658
	X_3	-0.495	-0.481	-0.524	-0.486	-0.493	-0.500
2009	X_2	1.265	1.546	0.914	1.444	1.266	1.118
	X_3	-0.316	-0.258	-0.601	-0.272	-0.286	-0.327
2012	X_1	0.303	0.351	0.041	0.348	0.330	0.292
	X_2	1.062	1.127	0.857	1.103	1.077	1.047
	X_6	-0.313	-0.058	-0.387	-0.289	-0.332	-0.367
2017	X_1	0.270	0.328	0.004	0.324	0.297	0.252
	X_2	0.960	1.008	0.734	0.991	0.980	0.957
	X_6	-0.250	0.051	-0.340	-0.222	-0.273	-0.315

Note: The range of the local standardized residuals of the models in 2006, 2009, 2012, and 2017 were [-3.512, 3.993], [-3.599, 2.811], [-3.100, 3.89], and [-2.715, 3.355], respectively. The residual values of 96.774%, 98.387%, 97.581%, and 98.387%, respectively, were within the range of [-2.58, 2.58].

2017 were introduced as the dependent variable of the model, and X_1 , X_2 , X_3 , X_4 , X_5 , X_6 , X_7 , X_8 , and X_9 in Table 1 were the independent variables. The OLS test was performed several times and the variables with multi-collinearity problem were eliminated according to significance levels and variance inflation factor (VIF). In order to eliminate the dimensional difference between metrics, the logarithm of each indicator was used for the analysis (Table 5). Since the estimated parameters vary with the independent variables, to further explore the spatial differences in the effects of the variables on GDP, the estimated coefficients of the cities were spatially visualized in Figures 5–8.

Table 6 shows that, the impacts of X_1 , X_2 , and X_3 on GDP were spatially different in 2006. Specifically, X_1 and X_2 had a positive effect on GDP, indicating that the output values of animal husbandry remained the primary income of the region. In addition, population, as the main influencing factor of economic development, played an irreplaceable role. The effect of X_3 on GDP was negative, which is consistent with the results

obtained from the spatial econometric models, confirming that the models' goodness of fit was satisfactory.

The distribution of the regression coefficients (Figure 5) reveals that, apart from the coefficients of X_2 of 11 cities (e.g., Kashgar Prefecture, Kizilsu Kirghiz Autonomous Prefecture, and Aksu City region), the coefficients of X_1 , X_2 , and X_3 of the eastern regions were higher than those of the western regions. The reason that the coefficient distribution of the 11 cities did not follow the overall distribution pattern could be that the 11 cities are locations of military bases; hence, the coefficients of population were higher than those of other regions. In 2009, affected by animal diseases, only the influences of X_2 (positive effect) and X_3 (negative effect) on GDP were found to be spatially different. Apart from a few cities that showed spatial fluctuations of the regression coefficients, the pattern of changes was statistically significant (Figures 5, 6, respectively). In 2012 and 2017, the influences of X_1 , X_2 , and X_6 showed spatial differences. In addition, no apparent

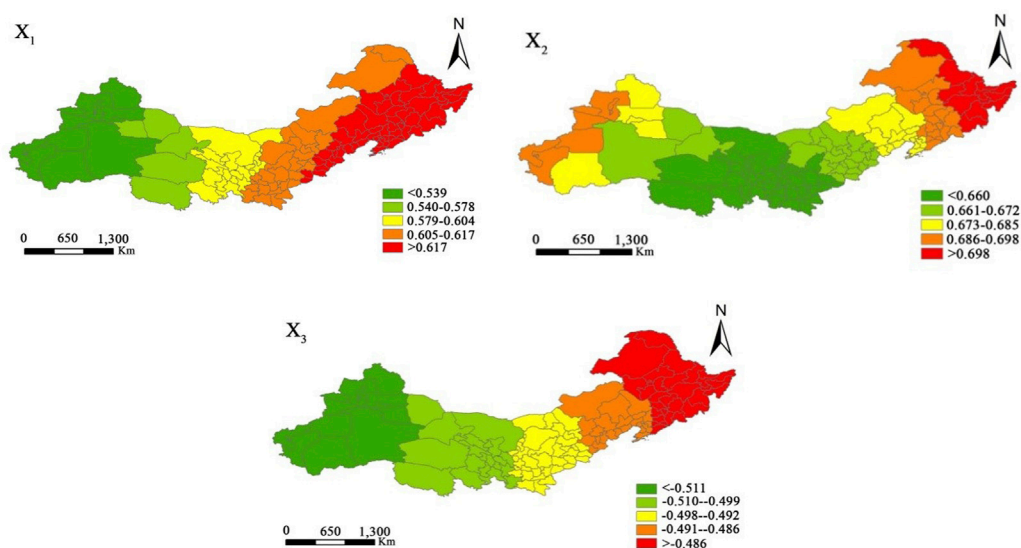


FIGURE 5
Spatial Distribution of Regression Coefficients of the GWR Model (2006).

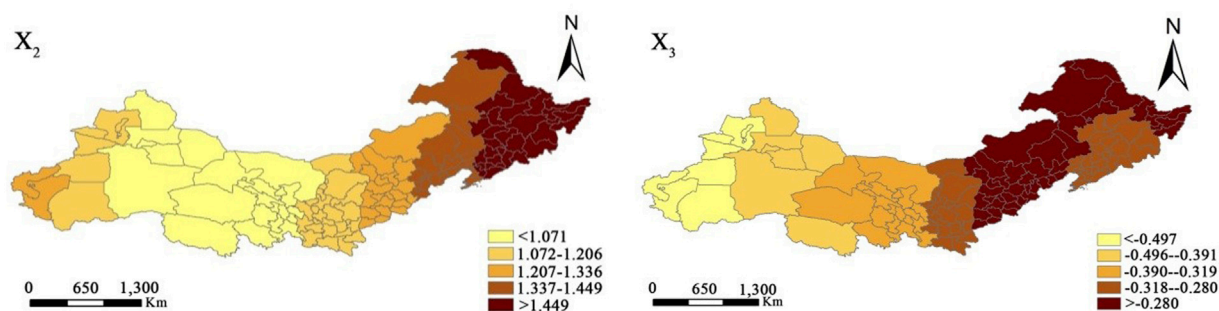


FIGURE 6
Spatial Distribution of Regression Coefficients of the GWR Model (2009).

changes were observed in the spatial distribution of the regression coefficients of the three variables (Figures 5, 7, 8, respectively). The coefficients of X_1 and X_2 were higher in the east than those in the west, while that of X_6 was higher in the west than that in the east. This phenomenon is mainly associated with the physical conditions in the region (distribution of land type and topography), in addition to the influence of human activities. Specifically, forest resources in northeast China accounted for one-third of the country's resources; while the level of influence on husbandry by arable land resources in Xinjiang was the highest in the country. Therefore, the regression coefficients of arable land in the western regions were higher than those in the eastern regions.

In summary, during 2006–2017, the factors that have a significant impact on the GDP of the 13 provinces in north China were the output values of animal husbandry, population, numbers of large livestock units, and areas of arable land. Apart from the areas of arable land, the regression coefficients of the influencing factors were higher in the east and lower in the west. These findings suggest that, in order to promote the economic development in the study area, it is necessary to stimulate the growth of animal husbandry and increase investment in animal husbandry based on the local conditions. In addition, the imbalance in the forage-animal relationship should be addressed and new methods that suit the pasture area should be designed both to promote animal husbandry development and to ensure the protection of local ecology.

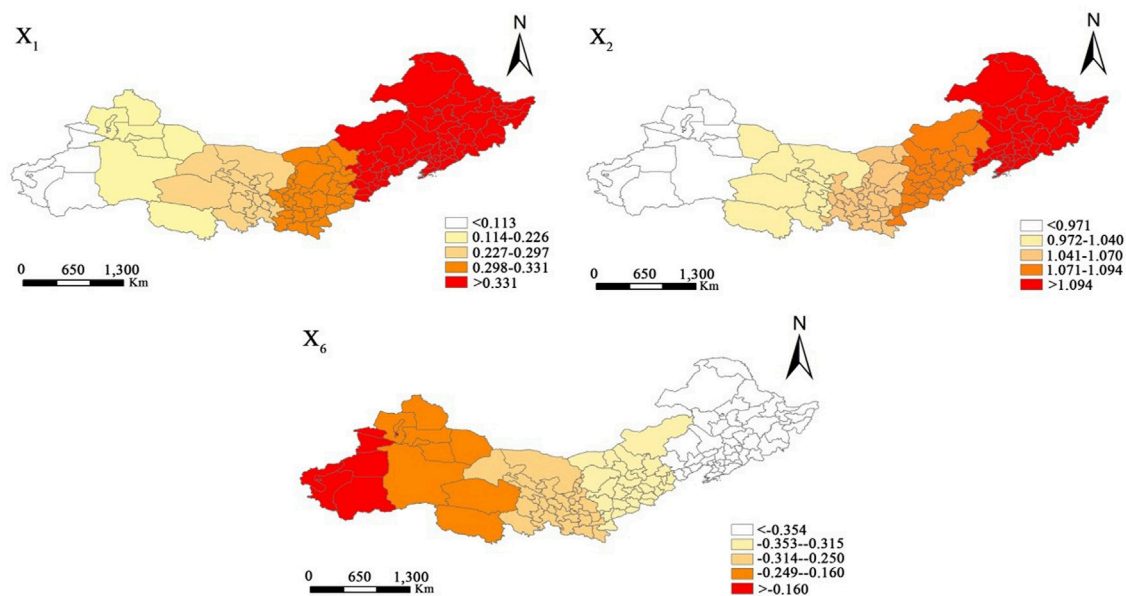


FIGURE 7
Spatial Distribution of Regression Coefficients of the GWR Model (2012).

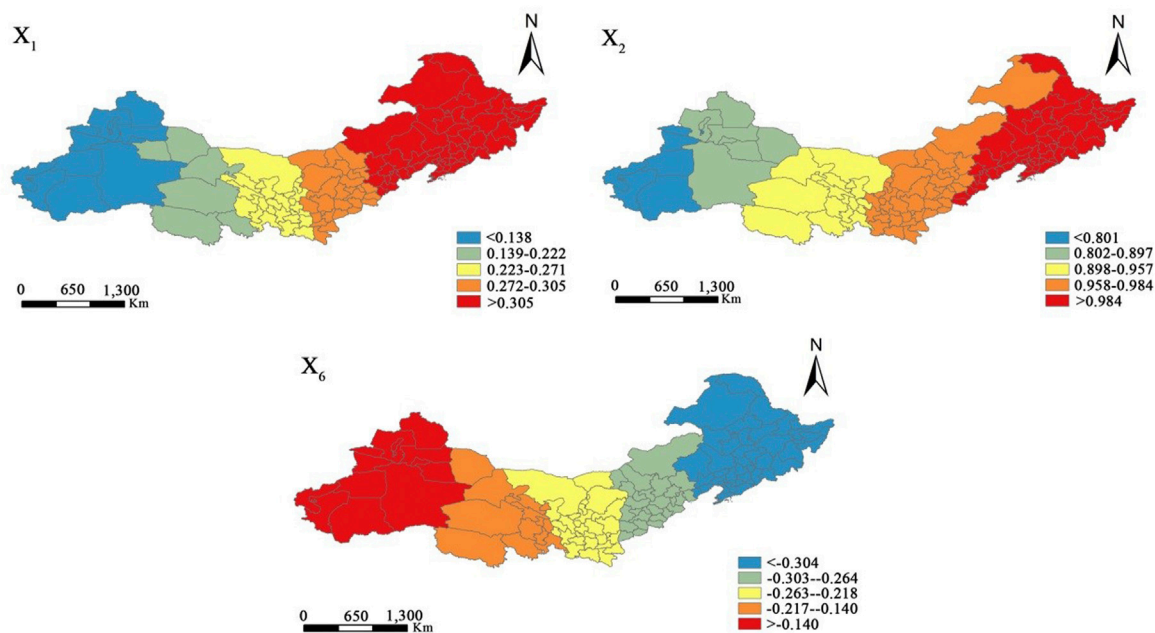


FIGURE 8
Spatial Distribution of Regression Coefficients of the GWR Model (2017).

TABLE 6 Spatial regression results of GDP of the 13 province's in North China (2006, 2009, 2012, and 2017).

Variable	SEM-2006	SEM-2009	SEM-2012	SEM-2017
Dep Var	2.789**	2.888**	2.680*	2.918**
Indep Var				
X ₁	0.587***	0.558***	0.595***	0.524***
X ₂	0.916***	0.935***	0.929***	0.878***
X ₃	-0.392***	-0.464***	-0.308**	-0.127
X ₄	-0.068	-0.013	-0.179	-0.210
X ₅	-0.017	0.013	0.006	-0.021
X ₆	-0.210**	-0.212***	-0.195**	-0.178**
X ₇	-0.063	-0.047	-0.0338	-0.045
X ₈	-0.155	-0.172	-0.066	-0.101
X ₉	-0.031	6.98813e-005	-0.066	0.038
R ²	0.829	0.813	0.796	0.792
AIC	196.223	205.754	220.976	210.965
SC	224.426	233.956	249.179	239.168

Notes: 1) ***: $p < 0.01$; **: $p < 0.05$; and *: $p < 0.1$.

4 Discussion

China has a large animal husbandry industry. Targeting the main region of animal husbandry production, this study investigated the spatial characteristics of GDP of the provinces and applied GWR model to reveal the spatial heterogeneity of the corresponding drivers.

4.1 Spatiotemporal heterogeneity analysis

According to the spatial differences in GDP growth and output values of animal husbandry, the results showed that GDP were higher in the eastern regions but lower in the west of the study area. This agglomerated trend became more apparent as time went on. Moreover, the outputs of animal husbandry were positively correlated with changes in GDP. These trends could be related to the characteristics of different climate zones and land types of the region. Wei et al. (2022) study found that the accelerated expansion of cities in the middle of the study area, and the habitat quality has also declined. Yu et al. (2021) found that regional heterogeneity of water resources severely limits the development of animal husbandry. Specifically, western areas of the study areas mostly suffered from desertification and grassland desertification. Owing to environmental factors (e.g., land desertification and reduced biodiversity), GDP and output of animal husbandry in the western areas of the study areas were lower than that of the eastern areas.

4.2 Exploring localized development

The spatial error model results (Table 4) shows that promotion of agricultural and animal husbandry development should suit

local conditions, such as climate and land use type. Rapid urbanization causes large urban conversions of natural and agricultural land to non-agricultural use (Zhou et al., 2021). This result will inevitably affect the animal husbandry industry. Moreover, the results show that GDP growth was not necessarily linked to the number of livestock and poultry units, but rather, it may be associated with the production, processing, and marketing methods for animal products. Thus, the results suggest that concerned parties should control the total number of livestock in each city based on the local conditions of the cities, accelerate the transition from traditional to modern animal husbandry, increase the industrialization of animal husbandry, and improve the protection of livestock against diseases. These practices would help to promote an animal husbandry industry geared towards standardization, scalability, and industrialization. From 2006 to 2017, the factors that have a significant impact on the GDP of the 13 northern provinces of China are the output value of animal husbandry, population, the number of livestock, and the area of arable land. Except for the area of arable land, the regression coefficients of other factors are all east high in spatial distribution. The low west situation indicates that to improve the regional economic development level, it is necessary to promote the growth of animal husbandry output according to local conditions, increase investment in animal husbandry, alleviate the imbalance of grass-livestock relationship, and explore the new model of ecological protection and animal husbandry development suitable for the characteristics of pastoral areas.

4.3 Limitations and future directions

This study still has uncertainties. This study explores the spatio-temporal differences and the spatial heterogeneity of

factors influencing the varying animal husbandry development of the 13 provinces in the northern China. Animal husbandry is a major component of agriculture. The development of animal husbandry could help alleviate the poverty of farmers and herders significantly and promote effective social supply (Wang and Tan, 2022). The modernization of agriculture through the modernization of animal husbandry would help promote the goal of constructing a strong agricultural sector (Ministry of Agriculture and rural affairs of the people's republic of China, 2018). The influence of human and factors of physical environment on the development of animal husbandry has become increasingly complex. Therefore, concerned parties may want to consider additional influencing factors, make use of relevant favorable policies and government subsidies, and explore new developmental models to facilitate the development of the local economy.

It is noteworthy that, since this study focused on the effect of animal husbandry on GDP, the direct influences of some indicators on GDP were not explored in detail. To further investigate the impact of animal husbandry development on the national economy, we suggest that future studies use the size of the agricultural sector as an independent variable.

5 Conclusion

Exploring the development of animal husbandry is of great significance to stabilizing the people's living standards. This study found, the spatio-temporal differences of GDP were prominent, presenting an increasing trend from west to east. Owing to regional differences in economic development and techniques of livestock and poultry farming, cities with higher GDP tended to concentrate in the east. The impact of the factors (excluding numbers of large livestock units) on GDP, from the largest to the smallest were population, output values of animal husbandry, and areas of arable land. At the early stage of the study period, controlling population (human activities), stimulating the output of animal husbandry, and controlling the numbers of large livestock units (improving techniques for livestock and poultry farming) had a great impact on GDP. At the latter stage of the study period, besides population and animal husbandry output, controlling the areas of arable land gradually became an important driving factor of GDP growth. These results can serve as a scientific reference for accelerating the transformation of animal husbandry in the 13 provinces of north China and for

exploring new ways suitable for promoting local animal husbandry development.

Data availability statement

The original contributions presented in the study are included in the article/Supplementary Material, further inquiries can be directed to the corresponding author.

Author contributions

Conceptualization, CW and WZ; methodology, CW and JZ; software, CW and JZ; formal analysis, CW and WZ; investigation, CW and JZ; resources, CW; data curation, CW and WZ; writing—original draft preparation, CW; writing—review and editing, CW and WZ; project administration, WZ; funding acquisition, WZ. All authors have read and agreed to the published version of the manuscript.

Funding

The GDAS' Project of Science and Technology Development (Grant No. 2022GDASZH-2022010202), and the Science and Technology Program of Guangdong (Grant No. 2021B1212100006).

Conflict of interest

The authors declare that the research was conducted in the absence of any commercial or financial relationships that could be construed as a potential conflict of interest.

Publisher's note

All claims expressed in this article are solely those of the authors and do not necessarily represent those of their affiliated organizations, or those of the publisher, the editors and the reviewers. Any product that may be evaluated in this article, or claim that may be made by its manufacturer, is not guaranteed or endorsed by the publisher.

References

- Aleshina, E. A., Anisimova, E. I., and Serdobintsev, D. V. (2020). Agroindustrial clustering as a driver of the activation of breeding work in animal husbandry. *IOP Conf. Ser. Earth Environ. Sci.* 459 (6), 062018. doi:10.1088/1755-1315/459/6/062018
- Amarasinghe, U., Samad, M., and Anputhas, M. (2005). Spatial clustering of rural poverty and food insecurity in Sri Lanka. *Food Policy* 30 (5-6), 493–509. doi:10.1016/j.foodpol.2005.09.006

- Anselin, L. (1995). Local indicators of spatial association—Lisa. *Geogr. Anal.* 27 (2), 93–115. doi:10.1111/j.1538-4632.1995.tb00338.x
- Anselin, L. (1988). Spatial econometrics: Methods and models. *Econ. Geogr.* 65 (2), 160. doi:10.1007/978-94-015-7799-1
- Bernués, A., Ruiz, R., Olaizola, A., Villalba, D., and Casasús, I. (2011). Sustainability of pasture-based livestock farming systems in the European Mediterranean context: Synergies and trade-offs. *Livest. Sci.* 139 (1–2), 44–57. doi:10.1016/j.livsci.2011.03.018
- Chen, Z., Zhang, S., Geng, W., Ding, Y., and Jiang, X. (2022). Use of geographically weighted regression (GWR) to reveal spatially varying relationships between Cd accumulation and soil properties at field scale. *Land* 11 (5), 635. doi:10.3390/LAND11050635
- Cheng, W., Shen, B., Xin, X., Gu, Q., and Guo, T. (2022). Spatiotemporal variations of grassland ecosystem service value and its influencing factors in inner Mongolia, China. *Agronomy* 12 (9), 2090. doi:10.3390/AGRONOMY12092090
- Cohen, J., Cromley, R., and Banach, K. (2015). Are homes near water bodies and wetlands worth more or less? An analysis of housing prices in one Connecticut town. *Growth Change* 46 (1), 114–132. doi:10.1111/grow.12073
- Dai, Y., Guo, J., Li, Y., Dong, Z., and Li, H. (2022). Soil physical and chemical properties affected by long-term grazing on the desert steppe of Inner Mongolia, China. *Catena* 211, 105996. doi:10.1016/j.CATENA.2021.105996
- Ethier, J., Bánffy, E., Vuković, J., Leshtakov, K., Bacvarov, K., Roffet-Salque, M., et al. (2017). Earliest expansion of animal husbandry beyond the Mediterranean zone in the sixth millennium BC. *Sci. Rep.* 7 (1), 7146. doi:10.1038/s41598-017-07427-x
- Fischer, W., Thomas, C., Zimov, N., and Göckede, M. (2022). Grazing enhances carbon cycling but reduces methane emission during peak growing season in the Siberian Pleistocene Park tundra site. *Biogeosciences* 19 (6), 1611–1633. doi:10.5194/BG-19-1611-2022
- Foley, J. A., Ramankutty, N., Brauman, K. A., Cassidy, E. S., Gerber, J. S., Johnston, M., et al. (2011). Solutions for a cultivated planet. *Nature* 478 (7369), 337–342. doi:10.1038/nature10452
- Fu, Q., Zhu, Y., Kong, Y., and Sun, J. (2012). Spatial analysis and districting of the livestock and poultry breeding in China. *J. Geogr. Sci.* 22 (6), 1079–1100. doi:10.1007/s11442-012-0984-4
- Geng, W., Li, Y., Zhang, P., Yang, D., Jing, W., and Rong, T. (2022). Analyzing spatio-temporal changes and trade-offs/synergies among ecosystem services in the Yellow River Basin, China. *Ecol. Indic.* 138, 108825. doi:10.1016/j.ECOLIND.2022.108825
- Gerber, P. J., Hristov, A. N., Henderson, B., Makkar, H., Oh, J., Lee, C., et al. (2013). Technical options for the mitigation of direct methane and nitrous oxide emissions from livestock: A review. *Animal* 7, 220–234. doi:10.1017/S1751731113000876
- Godber, O. F., and Wall, R. (2014). Livestock and food security: Vulnerability to population growth and climate change. *Glob. Chang. Biol.* 20 (10), 3092–3102. doi:10.1111/gcb.12589
- Godfray, H., Beddington, J. R., Crute, I., Haddad, L., Lawrence, D., Muir, J., et al. (2010). Food security: The challenge of feeding 9 billion people. *Science* 327 (5967), 812–818. doi:10.1126/science.1185383
- Hewins, D., Lyseng, M., Schoderbek, D., Alexander, M., Willms, W., Carlyle, C., et al. (2018). Grazing and climate effects on soil organic carbon concentration and particle-size association in northern grasslands. *Sci. Rep.* 8 (1), 1336–1339. doi:10.1038/s41598-018-19785-1
- Huang, J., Huang, Y., Pontius, R., Jr. and Zhang, Z. (2015). Geographically weighted regression to measure spatial variations in correlations between water pollution versus land use in a coastal watershed. *Ocean. Coast. Manag.* 103, 14–24. doi:10.1016/j.ocecoaman.2014.10.007
- Hyland, J., Styles, D., Jones, D., and Williams, A. (2016). Improving livestock production efficiencies presents a major opportunity to reduce sectoral greenhouse gas emissions. *Agric. Syst.* 147, 123–131. doi:10.1016/j.agry.2016.06.006
- Jayaraman, B., and Nyachoti, C. M. (2016). Husbandry practices and gut health outcomes in weaned piglets: A review. *Anim. Nutr.* 3 (3), 205–211. doi:10.1016/j.aninu.2017.06.002
- Kastner, T., Rivas, M. J., Koch, W., and Nonhebel, S. (2012). Global changes in diets and the consequences for land requirements for food. *Proc. Natl. Acad. Sci. U. S. A.* 109 (18), 6868–6872. doi:10.1073/pnas.1117054109
- Li, M., Liu, S., Sun, Y., and Liu, Y. (2021). Agriculture and animal husbandry increased carbon footprint on the Qinghai-Tibet Plateau during past three decades. *J. Clean. Prod.* 278, 123963. doi:10.1016/j.jclepro.2020.123963
- Lin, G., and Long, Z. (2014). *Spatial economic measurement: Theory and demonstration*. Beijing: Science Press.
- Liu, F., Mao, X., Zhang, Y., Chen, Q., Liu, P., and Zhao, Z. (2014). Risk analysis of snow disaster in the pastoral areas of the Qinghai-Tibet Plateau. *J. Geogr. Sci.* 24 (3), 411–426. doi:10.1007/s11442-014-1097-z
- Liu, Z., Ahmad, M., Li, G., Yang, Y., Liu, Y., Gao, M., et al. (2022a). Decoupling of greenhouse gas emissions from livestock industrial development: Evidence from China agricultural green development modern zone. *Front. Environ. Sci.* 10 (1), 979129. doi:10.3389/FENV.2022.979129
- Liu, Z., Yang, D., Zhang, P., Jiang, L., Li, Y., Rong, T., et al. (2022b). Spatial-temporal characteristics and scenario simulation of carbon emissions from energy consumption based on multiscale in the affected areas of the lower Yellow River. *Int. J. Low-Carbon Tec.* 17, 818–830. doi:10.1093/IJLCT/CTAC027
- Makkar, H. P. (2016). Animal nutrition in a 360-degree view and a framework for future R&D work: Towards sustainable livestock production. *Anim. Prod. Sci.* 56 (10), 1561–1568. doi:10.1071/AN15265
- Maryunani, M. (2021). Establishment of regional-owned food business entities as a means to eradicate poverty and increase economic growth. *SOCIA J. Sosial Ekonomi Pertanian*. 15 (1), 42–54. doi:10.24843/SOCA.2021.v15.i01.p04
- Middleton, N., Rueff, H., Sternberg, T., Batbuyan, B., and Thomas, D. (2015). Explaining spatial variations in climate hazard impacts in Western Mongolia. *Landsc. Ecol.* 30 (1), 91–107. doi:10.1007/s10980-014-0091-2
- Ministry of Agriculture and rural affairs of the people's republic of China (2018). Essentials of animal husbandry. Available at http://www.moa.gov.cn/ztl/negzhy2017/zxd/201802/t20180203_6136401.htm.
- Morgan-Davies, C., Waterhouse, T., and Wilson, R. (2012). Characterisation of farmers' responses to policy reforms in Scottish hill farming areas. *Small Rumin. Res.* 102 (2–3), 96–107. doi:10.1016/j.smallrumres.2011.07.013
- Mueller, N. D., Gerber, J. S., Johnston, M., Ray, D. K., Ramankutty, N., and Foley, J. A. (2012). Closing yield gaps through nutrient and water management. *Nature* 490 (7419), 254–257. doi:10.1038/nature11420
- Pardo, G., Martín-García, I., Arco, A., Yañez-Ruiz, D., Moral, R., and Del Prado, A. (2016). Greenhouse-gas mitigation potential of agro-industrial by-products in the diet of dairy goats in Spain: A life-cycle perspective. *Anim. Prod. Sci.* 56 (3), 646–654. doi:10.1071/AN15620
- Parlato, M., Valenti, F., Midolo, G., and Porto, S. (2022). Livestock wastes sustainable use and management: Assessment of raw sheep wool reuse and valorization. *Energies* 15 (9), 3008. doi:10.3390/EN15093008
- Qu, Y., Zhao, Y., Ding, G., Chi, W., and Gao, G. (2021). Spatiotemporal patterns of the forage-livestock balance in the xilin gol steppe, China: Implications for sustainably utilizing grassland-ecosystem services. *J. Arid. Land* 13 (2), 135–151. doi:10.1007/S40333-021-0053-X
- Rong, T., Zhang, P., Zhu, H., Jiang, L., Li, Y., and Liu, Z. (2022). Spatial correlation evolution and prediction scenario of land use carbon emissions in China. *Ecol. Inf.* 71, 101802. doi:10.1016/j.ECOINF.2022.101802
- Sakadevan, K., and Nguyen, M. (2017). Livestock production and its impact on nutrient pollution and greenhouse gas emissions. *Adv. Agron.* 141, 147–184. doi:10.1016/bs.agron.2016.10.002
- Sattari, S., Bouwman, A., Martinez Rodríguez, R., Beusen, A., and Van Ittersum, M. (2016). Negative global phosphorus budgets challenge sustainable intensification of grasslands. *Nat. Commun.* 7 (1), 10696. doi:10.1038/ncomms10696
- Shi, Y., Han, R., and Guo, L. (2022). Temporal-spatial distribution of ecosystem health and its response to human interference based on different terrain gradients: A case study in gannan, China. *Sustainability* 12 (5), 1773. doi:10.3390/su12051773
- Shimokawa, S. (2015). Sustainable meat consumption in China. *J. Integr. Agric.* 14 (6), 1023–1032. doi:10.1016/S2095-3119(14)60986-2
- Tan, S. H., Liu, B., Zhang, Q. Y., Zhu, Y., Yang, J. H., and Fang, X. J. (2017). Understanding grassland rental markets and their determinants in eastern inner Mongolia, PR China. *Land Use Policy* 67, 733–741. doi:10.1016/j.landusepol.2017.07.006
- Thornton, P. K., and Gerber, P. J. (2010). Climate change and the growth of the livestock sector in developing countries. *Mitig. Adapt. Strateg. Glob. Chang.* 15 (2), 169–184. doi:10.1007/s11027-009-9210-9
- Thornton, P. K. (2010). Livestock production: Recent trends, future prospects. *Phil. Trans. R. Soc. B* 365 (1554), 2853–2867. doi:10.1098/rstb.2010.0134
- Tilman, D., Balzer, C., Hill, J., and Befort, B. L. (2011). Global food demand and the sustainable intensification of agriculture. *Proc. Natl. Acad. Sci. U. S. A.* 108 (50), 20260–20264. doi:10.1073/pnas.1116437108
- Tilman, D., Cassman, K. G., Matson, P. A., Naylor, R., and Polasky, S. (2002). Agricultural sustainability and intensive production practices. *Nature* 418 (6898), 671–677. doi:10.1038/nature01014

- Valenzuela-Lamas, S., and Albarella, U. (2017). Animal husbandry across the western roman empire: Changes and continuities. *Eur. J. Archaeol.* 20 (3), 402–415. doi:10.1017/ea.2017.22
- Wang, F., Chen, Y., Li, T., Wang, C., Wang, D., Fu, B., et al. (2021). Grazing reduces the soil-atmosphere exchange of greenhouse gases during freeze-thaw cycles in meadow steppes in inner Mongolia. *Front. Ecol. Evol.* 9, 795203. doi:10.3389/FEVO.2021.795203
- Wang, G., Wang, M., Wang, J., Yang, C., and Liu, Y. (2016). Characteristics and influencing factors of grass-feeding livestock breeding in China: An economic geographical perspective. *J. Geogr. Sci.* 26 (4), 501–512. doi:10.1007/s11442-016-1282-3
- Wang, L., and Tan, H. (2022). Economic analysis of animal husbandry based on system dynamics. *Comput. Intell. Neurosci.* 2022, 1–13. doi:10.1155/2022/5641384
- Wang X., Wu, X., Yan, P., Gao, W., Chen, Y., and Sui, P. (2016). Integrated analysis on economic and environmental consequences of livestock husbandry on different scale in China. *J. Clean. Prod.* 119, 1–12. doi:10.1016/j.jclepro.2016.01.084
- Wei, L., Zhou, L., Sun, D., Yuan, B., and Hu, F. (2022). Evaluating the impact of urban expansion on the habitat quality and constructing ecological security patterns: A case study of jiziwan in the yellow river basin, China. *Ecol. Indic.* 145, 109544. doi:10.1016/j.ecolind.2022.109544
- Wei, Y., Wang, S., Fang, Y., and Nawaz, Z. (2017). Integrated assessment on the vulnerability of animal husbandry to snow disasters under climate change in the Qinghai-Tibetan Plateau. *Glob. Planet. Change* 157, 139–152. doi:10.1016/j.gloplacha.2017.08.017
- Weindl, I., Bodirsky, B. L., Rolinski, S., Biewald, A., Lotze-Campen, H., Müller, C., et al. (2017). Livestock production and the water challenge of future food supply: Implications of agricultural management and dietary choices. *Glob. Environ. Change* 47, 121–132. doi:10.1016/j.gloenvcha.2017.09.010
- Windirsch, T., Grosse, G., Ulrich, M., Forbes, B., Göckede, M., Wolter, J., et al. (2022). Large herbivores on permafrost— A pilot study of grazing impacts on permafrost soil carbon storage in northeastern siberia. *Front. Environ. Sci.* 1, 893478. doi:10.3389/FENV.2022.893478
- Xie, S., Ding, W., Ye, W., and Deng, Z. (2022). Agro-pastoralists' perception of climate change and adaptation in the Qilian Mountains of northwest China. *Sci. Rep.* 12 (1), 12689. doi:10.1038/S41598-022-17040-2
- Yang, D., Zhang, P., Jiang, L., Jiang, L., Zhang, Y., Liu, Z., et al. (2022). Spatial change and scale dependence of built-up land expansion and landscape pattern evolution—case study of affected area of the lower yellow river. *Ecol. Indic.* 141, 109123. doi:10.1016/j.ecolind.2022.109123
- Yao, Z., Zhang, L., Tang, S., Li, X., and Hao, T. (2017). The basic characteristics and spatial patterns of global cultivated land change since the 1980s. *J. Geogr. Sci.* 27 (7), 771–785. doi:10.1007/s11442-017-1405-5
- Yu, L., Xiong, X., Samim, S., and Hu, Z. (2021). Analysis of water resources and water environmental carrying capacity of animal husbandry in China—based on water footprint theory. *Water* 13 (23), 3386. doi:10.3390/W13233386
- Zhang, P., Yang, D., Qin, M., and Jing, W. (2020a). Spatial heterogeneity analysis and driving forces exploring of built-up land development intensity in Chinese prefecture-level cities and implications for future urban land intensive use. *Land Use Policy* 99, 104958. doi:10.1016/j.landusepol.2020.104958
- Zhang, Y., Geng, W., Zhang, P., Li, E., Rong, T., Liu, Y., et al. (2020b). Dynamic changes, spatiotemporal differences and factors influencing the urban eco-efficiency in the lower reaches of the Yellow River. *Int. J. Environ. Res. Public Health* 17 (20), 7510. doi:10.3390/ijerph17207510
- Zhao, X., Deng, C., Huang, X., and Kwan, M. (2017). Driving forces and the spatial patterns of industrial sulfur dioxide discharge in China. *Sci. Total Environ.* 577, 279–288. doi:10.1016/j.scitotenv.2016.10.183
- Zhao, Y., Xie, K. Y., Wan, J. C., and Zhang, Y. J. (2017). Development and prospects of 'grain-forage supply' in modern animal husbandry. *Pratacultural Sci.* 34 (3), 653–660. doi:10.11829/j.issn.1001-0629.2016-0361
- Zhen, H., Cheng, H., and Chun, Y. (2020). Spatial econometric analysis of environmental total factor productivity of animal husbandry and its influencing factors in China during 2001–2017. *Sci. Total Environ.* 723, 137726. doi:10.1016/j.scitotenv.2020.137726
- Zhou, L., Dang, X., Mu, H., Wang, B., and Wang, S. (2021). Cities are going uphill: Slope gradient analysis of urban expansion and its driving factors in China. *Sci. Total Environ.* 775, 145836. doi:10.1016/j.scitotenv.2021.145836
- Zhu, L., Gan, Q., Liu, Y., and Yan, Z. (2017). The impact of foreign direct investment on SO₂ emissions in the beijing-tianjin-hebei region: A spatial econometric analysis. *J. Clean. Prod.* 166, 189–196. doi:10.1016/j.jclepro.2017.08.032
- Zhuang, M., and Li, W. (2017). Greenhouse gas emission of pastoralism is lower than combined extensive/intensive livestock husbandry: A case study on the Qinghai-Tibet Plateau of China. *J. Clean. Prod.* 147, 514–522. doi:10.1016/j.jclepro.2017.01.126



OPEN ACCESS

EDITED BY

Wenlong Jing,
Guangzhou Institute of Geography,
China

REVIEWED BY

Wei Jiang,
China Institute of Water Resources and
Hydropower Research, China
Zhiyong Wu,
Hohai University, China

*CORRESPONDENCE

Guixia Yan,
✉ guixiayan@nuist.edu.cn

SPECIALTY SECTION

This article was submitted to
Environmental Informatics and Remote
Sensing,
a section of the journal
Frontiers in Environmental Science

RECEIVED 25 October 2022

ACCEPTED 10 March 2023

PUBLISHED 20 March 2023

CITATION

Wang H, Li X, Tong C, Xu Y, Lin D, Wang J,
Yao F, Zhu P and Yan G (2023), Varying
performance of eight evapotranspiration
products with aridity and vegetation
greenness across the globe.
Front. Environ. Sci. 11:1079520.
doi: 10.3389/fenvs.2023.1079520

COPYRIGHT

© 2023 Wang, Li, Tong, Xu, Lin, Wang,
Yao, Zhu and Yan. This is an open-access
article distributed under the terms of the
Creative Commons Attribution License
(CC BY). The use, distribution or
reproduction in other forums is
permitted, provided the original author(s)
and the copyright owner(s) are credited
and that the original publication in this
journal is cited, in accordance with
accepted academic practice. No use,
distribution or reproduction is permitted
which does not comply with these terms.

Varying performance of eight evapotranspiration products with aridity and vegetation greenness across the globe

Hongzhou Wang¹, Xiaodong Li^{2,3}, Cheng Tong⁴, Yongkang Xu⁵,
Dongjun Lin⁶, Jiazhi Wang⁶, Fei Yao¹, Pengxuan Zhu¹ and
Guixia Yan^{1*}

¹School of Hydrology and Water Resources/Key Laboratory of Hydrometeorological Disaster Mechanism and Warning of Ministry of Water Resources, Nanjing University of Information Science and Technology, Nanjing, China, ²School of Civil Engineering, Sun Yat-sen University, Zhuhai, China, ³Water Resources Department, Changjiang River Scientific Research Institution, Wuhan, China, ⁴College of Environmental and Resource Sciences, Zhejiang University, Hangzhou, China, ⁵School of Water Resources, North China University of Water Resources and Electric Power, Zhengzhou, China, ⁶Collaborative Innovation Center on Forecast and Evaluation of Meteorological Disasters/Key Laboratory of Meteorological Disaster, Ministry of Education, Nanjing University of Information Science and Technology, Nanjing, China

The wide application of the evapotranspiration (*ET*) products has deepened our understanding of the water, energy and carbon cycles, driving increased interest in regional and global assessments of their performance. However, evaluating *ET* products at a global scale with varying levels of dryness and vegetation greenness poses challenges due to a relative lack of reference data and potential water imbalance. Here, we evaluated the performance of eight state-of-the-art *ET* products derived from remote sensing, Land Surface Models, and machine learning methods. Specifically, we assessed their ability to capture *ET* magnitude, variability, and trend, using 1,381 global watershed water balance *ET* as a baseline. Furthermore, we created aridity and vegetation categories to investigate performance differences among products under varying environmental conditions. Our results demonstrate that the spatial and temporal performances of the *ET* products were strongly affected by aridity and vegetation greenness. The poorer performances, such as underestimation of interannual variability and misjudged trend, tend to occur in abundant humidity and vegetation. Our findings emphasize the significance of considering aridity and vegetation greenness into *ET* product generation, especially in the context of ongoing global warming and greening. Which hopefully will contribute to the directional optimizations and effective applications of *ET* simulations.

KEYWORDS

evapotranspiration, evapotranspiration products, aridity, vegetation greenness, KGE

1 Introduction

Terrestrial evapotranspiration (*ET*), as a pivotal element of such land-atmosphere interaction processes as what happens to water, carbon, and energy cycle, is constituted of soil evaporation, vegetation transpiration and water surface evaporation (Gao et al., 2016; Tramontana et al., 2016; Zhang et al., 2016; Liu et al., 2021). On the land surface, 60% of precipitation (*Pre*) is returned to the atmosphere through *ET*, consuming half of the solar

energy reaching at the surface (Pan et al., 2020). Consequently, *ET* draws significant interest from hydrology to climate disciplines. Researchers aim to understand the allocation of energy and water at the land and its feedbacks (Zhang et al., 2017), identify dominant control factors of *ET* variation across regions (She et al., 2017; Zhang et al., 2021), and investigate the impact of *ET* on the hydrological cycle under climate change (Gu et al., 2020; Weerasinghe et al., 2020). Hence, accurate estimation of *ET* is crucial for various scientific communities such as hydrology, ecology, climatology, and agriculture.

There is no denying that existing *ET* products have considerable potential to facilitate the estimation of hydrological and energetic components and their inherent hydroclimatic variability. For instance, global *ET* estimates at arbitrary spatial and temporal scales can be compiled by the conventional flux formula (or Land Surface Model (LSM)) and the remote sensing observations about surface temperature, soil moisture and vegetation cover ratio (Wang et al., 2016; Miao and Wang, 2020). Recently, the boom in machine learning methods has also facilitated the acquisition of global *ET* datasets (Jimenez et al., 2011; Alemohammad et al., 2017; Jung et al., 2017), such as model tree, random forest, or artificial neural networks combining observed flux data as inputs. However, these products simultaneously involve some uncertainties derived from the model structural flaws, input-datasets errors (e.g., meteorological forcing, land surface, and parameters related to vegetation), model-parameter errors and scale-scaling issues (Badgley et al., 2015; Michel et al., 2016; Miralles et al., 2016).

However, the existing terrestrial *ET* products widely vary in performance and even oppose long-term trends, indicating the non-negligible uncertainties. For instance, it has been reported that while potential evapotranspiration (*PET*) trends have declined over the last 50 years, *ET* has shown an increasing trend according to the evapotranspiration paradox (Mao et al., 2015; Zhang et al., 2015; Zeng et al., 2018). However, Jung et al. (2010) added that the increase in global terrestrial *ET* has ceased or even reversed from 1998 to 2008. Therefore, a comprehensive evaluation of *ET* products is a prerequisite for model optimizations and global climate-change research, especially, on a regional scale.

ET measurements from the Eddy Current Covariance (EC) site have become typical reference data to validate *ET* products at the point scale. Nevertheless, EC systems generally suffer from energy imbalance, which resulting in *ET* measurement errors. And the mismatch in spatial scale between EC observations and *ET* estimates (points and grid cells) is another limitation. Furthermore, EC sites sparsely spread over spaces, which challenges the evaluation of *ET* products on a regional scale (Pan et al., 2020; Xie et al., 2022). An alternative approach is terrestrial water balance method, i.e., *ET* calculated from the terrestrial water balance (observed *Pre* minus the sum of runoff (*Q*) and total water storage change (TWSC)) is applied as the truth value to validate *ET* products at the basin scale (Liu et al., 2016). Over the last 2 decades, considerable attention has focused on the regional scale (US, African, and Qinghai-Tibetan Plateau), while less on the global scale. For example, Vinukollu et al. (2011) conducted a global evaluation on the *ET* estimates derived from three process-based models (Surface Energy Balance System (Su, 2002), Penman–Monteith–Mu algorithm (Penman, 1948; Mu et al., 2007), and Priestly–Taylor–Fisher of Jet Propulsion Laboratory algorithm (Priestley and Taylor, 1972; Fisher et al., 2008) based on 26 basins worldwide, and suggested a root mean squared difference

(RMSD) of 118–194 mm/yr and a deviation of −132 to 53 mm/yr between the water balance *ET* and the estimated annual *ET*.

However, the total water storage change (TWSC) at the annual scale has often been disregarded in previous studies (*Pre* directly minus *Q*), yet the water budget is unbalanced due to human abstraction, glacial snowmelt, and other activities affecting water storage (Liu et al., 2016; Zhong et al., 2020). For example, Zeng et al. (2012) found that the TWSC cannot be ignored in estimating *ET* at an annual scale, especially in regions with relatively low *ET* values. As a result, the annual reference *ET* must take into account TWSC. Although the Gravity Recovery and Climate Experiment (GRACE) satellite launched in 2002 offers a promising future to the TWSC, the limited GRACE satellite data right now makes it problematic to assess *ET* products with long-time data, especially the pre-2002 data, and subsequently difficult to explore *ET* trends. Recently, the reconstruction of GRACE facilitates the evaluation on long-time series of *ET* products. More importantly, the deficiencies exist in the simultaneous evaluation of *ET* products at the global scale with various levels of dryness and vegetation greenness. The *ET* variation in different regions is closely related to local conditions: *ET* is limited by water in dry conditions and by energy in wet conditions; *ET* is higher in highly-vegetated areas and lower in sparsely-vegetated areas. We postulate that these conditions may affect the performance of *ET* products. For example, Majozi et al. (2017) assessed the accuracy and precision of four *ET* products in two South African ecoregions and showed that no one *ET* product performed best in both zones; Ershadi et al. (2014) found that the performance of European and North American *ET* models varied among zones and the models with relatively high accuracy differed across zones; Kim et al. (2012) concluded that the Moderate Resolution Imaging Spectrometer (MODIS) MOD16 *ET* for Asian woodland cover was more accurate than for other biomes. Consequently, there is a need to fully understand the simulation capacity of *ET* products under heterogeneous conditions (areas with different levels of aridity and vegetation greenness), which will be favorable to developing strategies for adapting to the climate change.

Here, the current study is not to compare the various models, but to investigate how the performances of eight global *ET* products vary with water and energy conditions or vegetation greenness over 1981–2010. In doing so, the globally distributed 1,381 basins were taken into consideration and segmented according to their aridity and vegetation conditions. Then, we illustrated differences in the performance of the products changing with aridity and vegetation based on the terrestrial water balance *ET*. The model performance of the *ET* product was evaluated using newly popular metric–Kling–Gupta efficiency (*KGE*), considering the magnitude, variability of the *ET* and its coefficient to the product. Additionally, the 1981–2010 period was selected, for the knowledge about this period is relatively lacking and the reconstructed the total water storage anomaly (TWSA) products are reliable before 2002. Finally, we discussed the potential reasons for our results.

2 Datasets and methods

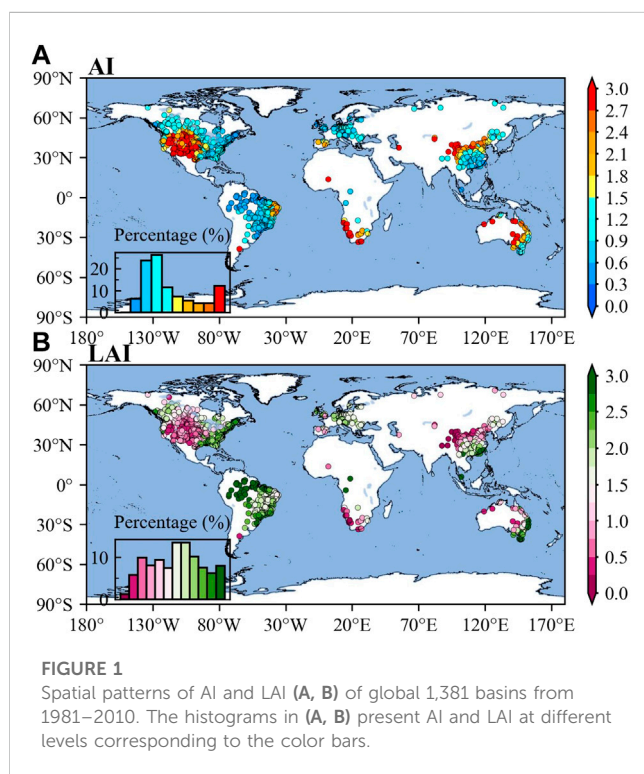
2.1 Datasets

2.1.1 Runoff (*Q*) datasets

To comprehensively assess the *ET* products, the daily *Q* observed at 31,133 hydrological stations across the globe were

TABLE 1 Summary of *Q* observation sources for 11 databases of *Q* observation sources.

Number	Source	Website or reference
222 stations	Australian edition of the catchment attributes and meteorology for large-sample studies (CAMELS-AUS)	https://doi.org/10.1594/PANGAEA.921850
1,529 stations	Australian bureau of meteorology (Bom)	https://portal.wsapi.cloud.bom.gov.au
735 stations	catchments attributes for brazil (CABRA)	https://thecabradataset.shinyapps.io/CABra/
3,679 stations	Brazil edition of the catchment attributes and meteorology for large-sample studies (CAMELS-BR)	https://doi.org/10.5281/
698 stations	Canadian model parameter experiment database (CANOPEX)	http://canopex.etsmtl.net
14,425 stations	Hydrometeorological Sandbox—École de technologie supérieure (HYSETS)	https://doi.org/10.6084/m9.figshare.12600281
859 stations	Large-sample data for hydrology: big data für die hydrologie und umweltwissenschaften (LAMAHA)	https://doi.org/10.5281/
671 stations	Great britain edition of the catchment attributes and meteorology for large-sample studies (CAMELS-GB)	https://catalogue.ceh.ac.uk
140 stations	Ministry of water resources of china and national hydrology almanac of china	http://mwr.gov.cn/
15 stations	Arctic great rivers observatory	https://arcticgreatrivers.org/
8,160 stations	Global runoff data centre	https://www.bafg.de/GRDC/



collected from 11 databases, as listed in Table 1 (Holmes et al., 2013; Arsenault et al., 2016; Awange et al., 2019; Arsenault et al., 2020; Chagas et al., 2020; Coxon et al., 2020; Almagro et al., 2021; Fowler et al., 2021; Klingler et al., 2021).

Considering that the *Q* dataset is derived from different sources; several criteria were implemented to control the dataset quality with reference to some well-established data processing methods (Beck et al., 2015). The details related to the criteria used in this study are as follows:

- 1 The final database retains a hydrological station only once, based on the latitude and longitude information of hydrological station;
- 2 If a station has missing data for more than 15% per day from 1981 to 2010, the station was removed;
- 3 The basin area controlled by the hydrological station must be able to cover two or more 0.5° grids.

Finally, 1,381 stations met these criteria. The global distribution of 1,381 hydrological stations is shown in Figure 1.

2.1.2 Precipitation and GRACE datasets

To reduce the uncertainties in precipitation data, we selected three global gridded precipitation datasets (GPCC, CPC-Unified, and CRU TS4.05) at 0.5° resolution based on precipitation gauges. GPCC precipitation dataset, was selected, for it is widely considered as the precipitation reference dataset (Becker et al., 2013). More importantly, CPC-Unified gauge-based analysis of global daily precipitation at 0.5° resolution (1979–present) was interpolated from the QC station reports, which incorporates the effects of topography (Chen et al., 2008).

Total water storage anomalies (TWSA), monitored by NASA's GRACE satellites *via* satellite gravimetry, are currently used for retrieving the exclusive data of TWSA in hydrological and climatic applications (Landerer and Swenson, 2012; Long et al., 2014; Jing et al., 2020a). Notably, the GRACE TWSA observation data only covers the period 2002–2017 (Jing et al., 2020b). Consequently, the two constructed TWSA datasets (i.e., GRACE-REC and GRID-CSR-GRACE-REC) were chosen, covering the data from 1981–2010 at a spatial resolution of 0.5°. GRACE-REC datasets were generated, using a statistical model trained with GRACE observations, consisting of six reconstructed TWSA datasets derived from two different GRACE observation products and three different meteorological forcing datasets (Humphrey and Gudmundsson, 2019). As for GRID-CSR-GRACE-REC, Li et al. (2021) reconstructed the GRACE observations by developing a methodological framework to compare three methods, including

TABLE 2 Hydrological-component information of used products.

Variables	Products	Methods	Time span/Resolution	Website
<i>Pre</i>	GPCC	Gauge-based interpolation	1901–2010 0.5°/Monthly	https://climatedataguide.ucar.edu/
	CPC-Unified		1979–present 0.5°/Daily	https://climatedataguide.ucar.edu/
	CRU TS4.05		1901–2020 0.5°/Monthly	https://data.ceda.ac.uk/badc/cru/data/
TWSA	GRACE-REC	Machine learning	1901–2019 0.5°/Monthly	https://doi.org/10.6084/m9.figshare.7670849
	GRID-CSR-GRACE-REC		1979–2020 0.5°/Monthly	https://doi.org/10.5061/dryad.z612jm6bt
<i>ET</i>	GLASS	BMA	1982–2018 0.05°/8 Day	http://www.glass.umd.edu/
	ERA5-Land	ECMWF	1979–2021 0.1°/Daily	https://cds.climate.copernicus.eu/
	MERRA-2	GEOS-5 (Penman-Monteith)	1980–2021 0.58° × 0.625°/Hourly	https://disc.gsfc.nasa.gov/
	GLEAM-3.5a	Priestley-Taylor equation	1980–2020 0.25°/Daily	https://www.gleam.eu/
	E2O-En	GHMs (LSMs, WBM)	1979–2012 0.5°/Monthly	http://www.earth2observe.eu/
	PML	Penman-Monteith-Leuning	1981–2012 0.5°/Monthly	https://data.csiro.au/collection
	GLDAS2.0-Noah	Noah (Penman-Monteith)	1948–2014 1.0°/Monthly	https://ldas.gsfc.nasa.gov/gldas/
	MTE	Upscaling	1982–2011 0.5°/Monthly	https://www.bgc-jena.mpg.de/

the multiple linear regression (MLR), autoregressive exogenous (ARX) approaches, and artificial neural network (ANN), using as inputs *Pre*, sea and land surface temperature, surface and subsurface runoff, soil moisture, evaporation, and several climate indices. Please note that the *Pre*-TWSA for each basin was derived from the arithmetic mean value of six datasets-combination: GPCC minus GRACE-REC, CPC-Unified minus GRACE-REC, CRU TS4.05 minus GRACE-REC, GPCC minus GRID-CSR-GRACE-REC, CPC-Unified minus GRID-CSR-GRACE-REC, and CRU TS4.05 minus GRID-CSR-GRACE-REC. The basic information of the *Pre* and TWSA products is shown in Table 2.

2.1.3 ET products

Eight *ET* products using different methods were collected in this study: one remote sensing product (GLASS), two reanalysis products (ERA5-Land and MERRA-2), four LSM-based products (GLEAM-3.5a, E2O-En, PML and GLDAS2.0-Noah), and one machine learning-based product (MTE). The basic information of the *ET* products is shown in Table 2.

To estimate terrestrial *ET*, Global Land Surface Satellite (GLASS) *ET* products used the Bayesian model averaging (BMA) method to ensemble five process-based *ET* algorithms (Yao et al., 2014; Xie et al., 2022), i.e., MODIS *ET* product algorithm (Penman, 1948; Mu et al., 2007; Mu et al., 2011), revised remote-sensing-based Penman-Monteith *ET* algorithm (Yuan et al., 2010), Priestley-Taylor-Fisher of Jet Propulsion Laboratory *ET* algorithm (Fisher et al., 2008), modified Satellite-Based Priestley-Taylor *ET* algorithm (Yao et al., 2013), and semi-empirical Penman *ET* algorithm of the University of Maryland (Wang et al., 2010). It outperforms the five algorithms by using ground-based data of 2000–2009 collected from 240 EC gauges worldwide on all continents except for Antarctica. The ensemble algorithms, integrating multiple algorithms to generate the product, reduces the uncertainties of a single algorithm and ensures the

accuracy of the product. The dataset used in this study is the product with the longest time series and the finest grid, spanning from 1982 to 2018 at a grid of 0.05°.

ERA5-Land (Muñoz-Sabater et al., 2021), an enhanced global dataset for the land component of the fifth generation of European ReAnalysis (ERA5), was published by the European Centre for Medium-Range Weather Forecasts (ECMWF) in 2021. The core of ERA5-Land is the ECMWF surface model: the Carbon Hydrology-Tiled ECMWF Scheme for Surface Exchanges over Land (CHTESSEL). Four meteorological state fields (i.e., temperature, humidity, wind speed, and pressure at the surface) are available in the ERA5, from the lowest level of the model (level 137), which is 10 m above the surface. Surface fluxes involve downward shortwave, longwave radiation and total liquid, and solid precipitation. Compared with latent heat data from 65 EC gauges worldwide, ERA5-Land *ET* performs better than previous versions such as ERA5 and ERA-Interim (Albergel et al., 2018), benefiting from the enhancements on the ECMWF surface model. The dataset used in this study spans the period from 1979 to 2021 and has a grid of 0.1°.

The second Modern Era Retrospective-Analysis for Research and Applications (MERRA-2) reanalysis (Rodell et al., 2011), a widely used atmospheric reanalysis dataset, is provided by Global Modeling and Assimilation Office (GMAO) in NASA. It is produced by the upgraded Goddard Earth Observing System model Version 5 (GEOS-5), along with its associated data assimilation system (DAS) Version 5.12.4, which replaced the original MERRA and MERRA-Land reanalysis. MERRA-2 alleviates some of the deficiencies of the MERRA and MERRA-Land product, such as certain biases and imbalances in the water cycle as well as the false trends and jumps in precipitation associated with changes in the observing system. The dataset used in this study spans from 1980 to 2021 and has a grid of 0.58° × 0.625°.

The Global Land Evaporation Amsterdam Model (GLEAM), a set of algorithms, including a potential evaporation module, stress module, and rainfall interception module, dedicates to estimating the terrestrial evaporation and root-zone soil moisture from the satellite data, which consists of soil evaporation, canopy transpiration, interception loss, snow sublimation, and open-water evaporation (Martens et al., 2017). Among these modules, the potential evaporation module uses the Priestley–Taylor equation, and the stress module is represented by the semi-empirical relationship between vegetation optical depth and root-zone soil moisture. A vital feature of this product is that the Gash analytical model is used to estimate interception loss.

To develop the global water reanalysis on the multi-scale water resource assessment and related research projects, the Earth2Observe (E2O) project also used the reanalysis-based forcing data to drive ten models: five global hydrological models (GHMs), four Land Surface Models (LSMs) with extended hydrological scenarios, and one simple water balance model (WBM) (Schellekens et al., 2017). The forcing dataset is an adjustment of the ERA reanalysis dataset combining the terrestrial meteorological element observations and Climate Research Unit (CRU) datasets. The E2O-En product has proven to be an accurate reanalysis data and been widely used for the multi-scale water resource applications (Schellekens et al., 2017). The generated data from ten models were arithmetically averaged to alleviate the potential errors and uncertainties of the individual model.

The GLDAS is a global assimilation and modeling system developed jointly by NASA, Goddard Space Flight Center (GSFC), and NOAA (Rodell et al., 2004; Rodell et al., 2011). The system provides the near real-time land-surface information from ground and satellite observations, by driving four LSMs. Here, the *ET* product derived from GLDAS2.0-Noah is adopted in our study.

The Model Tree Ensemble (MTE) product, a data-driven estimate (Jung et al., 2009), was compiled using a global monitoring network (the database of the FLUXNET), the meteorological and remote-sensing observations, and a machine-learning algorithm. Its forcing data include a harmonized the Fraction of Absorbed Photosynthetically Active Radiation (FAPAR) product from three sensors (AVHRR (Tucker et al., 2005), SeaWiFS (Gobron et al., 2006), MERIS (Gobron et al., 2008), a remote-sensing-based global land-use, and products of climate variables based on observations. However, the lack of measurements makes it impossible to calculate *ET* in cold and dry deserts; this may result in a slight underestimation of global *ET*.

2.1.4 AI and LAI data

Another monthly *Pre* and potential *ET* dataset (1901–2020) was chosen from CRU TS4.05, to calculate the aridity index (AI): the ratio of *Pre* and potential *ET*. GLASS LAI product was compiled by AVHRR from 1981–2000 and by MODIS from 2001 to 2018 (Xiao et al., 2013). To generate continuous and smooth data, GLASS LAI used a temporal-spatial filtering algorithm to remove cloud contamination from the reflectance data. The vital component of this product is the algorithm to train a general regression neural networks (GRNNs), using fused LAI from MODIS and CYCLOPES products and reprocessed MODIS reflectance for each vegetation type on observation sites (Xu et al., 2018). The dataset spans the

period from 1981 to 2018 and has a grid of 0.05°. Please note that all gridded datasets were aggregated to an annual temporal resolution and a spatial resolution of 0.5°. The spatial patterns of AI and LAI of global 1,381 basins are shown in Figure 1.

2.2 Methods

2.2.1 Water balance *ET*

Eight *ET* products were assessed, using water balance equations. The water-balance-based *ET* is often considered a reference for validating *ET* products on the annual scale. *ET* can be calculated based on precipitation (*Pre*), runoff (*Q*) and total water storage change (TWSC) in the basin, using the following equation:

$$\text{water balance } ET = Pre - Q - TWSC \quad (1)$$

Due to high correlations with static gravity fields, GRACE does not provide the estimates of total continental water content. In this aspect, TWSA is defined as the residual water content at a given time, which is relative to the water content at a reference epoch. The reference storage corresponds to the average water storage during the early phases of the GRACE mission (Han et al., 2005; Yang et al., 2020). Hence, yearly TWSC is the difference between the December anomaly observation of the current year and that of the previous year, i.e., the yearly TWSC equation is as follows:

$$TWSC_i = TWSA_{i,Dec} - TWSA_{i-1,Dec} \quad (2)$$

where *i* and Dec denote the year (ranging from 1981–2010) and the December, respectively.

2.2.2 Evaluation metrics

Kling-Gupta efficiency (*KGE*) and its three components are used to further evaluate the eight *ET* products (Kling et al., 2012). *KGE* is an objective performance metric, which comprehensively combines the components of the key performance statistics (correlation, bias and variability). The *KGE* formulation is defined as follows:

$$KGE = 1 - \sqrt{(R - 1)^2 + (\beta - 1)^2 + (\gamma - 1)^2} \quad (3)$$

where *R* is Pearson's correlation coefficient, β is the bias (the ratio of the estimates and observation means), γ is the variability [the ratio of the coefficients of variation (CV)].

$$\beta = \frac{\mu_e}{\mu_o} \quad (4)$$

$$\gamma = \frac{\sigma_e/\mu_e}{\sigma_o/\mu_o} \quad (5)$$

where μ and σ denote the mean and the standard deviation, respectively; e and o denote the estimate and the observation. Note that the ranges of *KGE*, *R*, β and γ with the optimum value of 1.0 are $-\infty$ –1.0, -1.0 –1.0, $-\infty$ – $+\infty$ and $-\infty$ – $+\infty$, respectively. A comprehensive diagnosis was carried out on the performance of *ET* products in capturing *ET* characteristics at the temporal and spatial scale. Please note that the hit of *ET* trend directions for each product was also evaluated, using the ratio of truly captured *ET* trend directions including positive and negative trends. For example, TPR (FPR, TNR, FNR) denotes the ratio between the number of basins that the *ET* products truly (falsely, truly, falsely) identify the

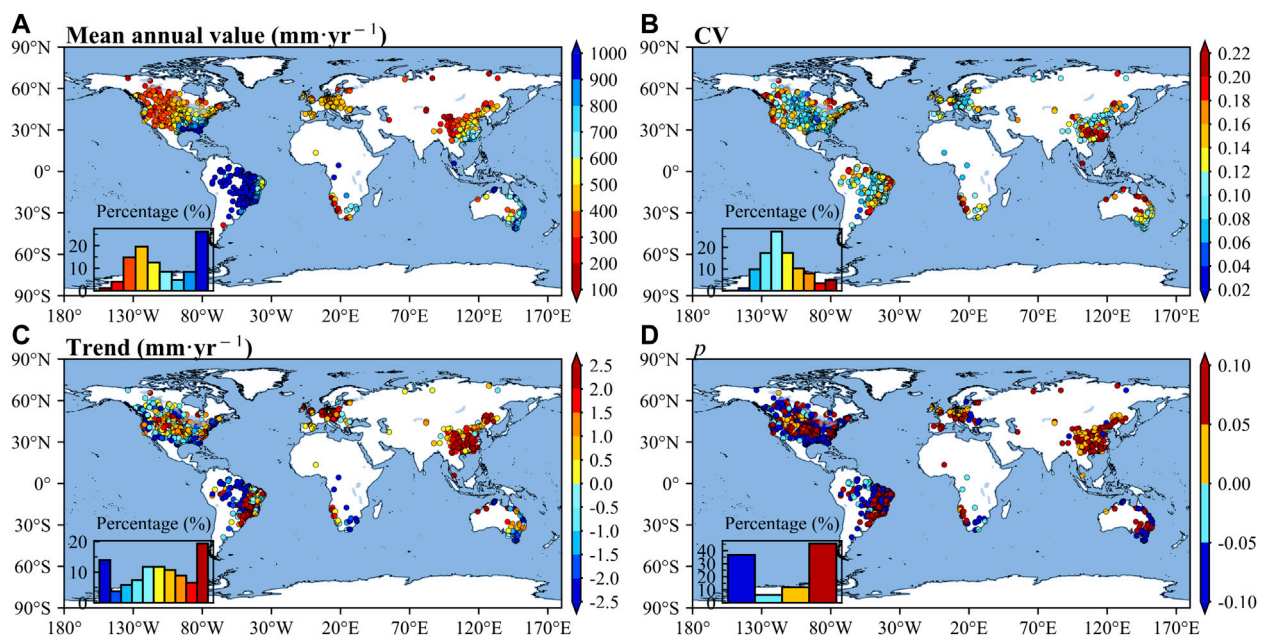


FIGURE 2

Spatial patterns of water balance *ET* at global 1,381 basins during 1981–2010. Small letters (A–D) represent the mean annual value, CV, trend, and significance level ($p < 0.05$) of trend, respectively. The histograms in (A–D) present the *ET* of different levels corresponding to the color bars.

observed positive (positive, negative, negative) *ET* trend as positive (negative, negative, positive) *ET* trend and the number of all basins. The sum of TPR, FPR, TNP, and FNR is equal to 100%. To systematically assess the spatial and temporal capture performance of the *ET* products, we assessed both the spatial dynamic of *ET* climatological value, temporal variability and trends, and the temporal dynamic of *ET* for each basin.

2.2.3 Aridity and vegetation categories

If global basins are diagnosed in overall terms, the information about the performance of *ET* products under given conditions will be lost. Meanwhile, it is important to examine how *ET* products vary with water and energy conditions or vegetation greenness, since the *ET* process is affected by the complex mechanisms of energy, water cycle and vegetation and the strong variability in both space and time. Therefore, the aridity and vegetation categories were created without considering their changes during the evaluation period, for the sake of simplicity. Specifically, the aridity index (AI) is characterized by the long-term climatic aridity condition of a region, for example, the higher AI value indicates the drier condition. The threshold of multiyear-average AI was set at 1.5, based on the conventional definition, i.e., basins with $AI > 1.5$ are classified as the dry basins and those with $AI \leq 1.5$ are classified as the wet basins (Liu et al., 2016). As for vegetation, the LAI is widely applied as the proxy of vegetation greenness, with high values suggesting high greenness. Based on the LAI value for each basin at the evaluation period, the evaluation metrics were re-classified in three categories, i.e., $LAI < 1$, $1 \leq LAI < 2$ and $LAI \geq 2$, which were defined as the LAI-I, LAI-II, and LAI-III, respectively (Jimenez et al., 2011; McCabe et al., 2016), with regard to the intensity of greenness (from brown to green).

3 Results

3.1 Overall assessment of *ET* products

Figure 2A shows the spatial pattern of the mean annual value of *ET* during 1981–2010. The high values ($>1,000$ mm) mainly existed in the Brazilian coast, the Gulf of Mexico and Atlantic coasts in America, the African coast, and the Oceania East coast. Specifically, the *ET* decreased from east (west) to west (east) across the North (South) America, and from southeast to northwest across China. By contrast, the spatial variability of *ET* CV was not line with the *ET* value: the high *ET* occurred in the Amazonian Plain and Brazilian plateau, whereas high *ET* CV occurred in South China (Figure 2B). Additionally, the *ET* tended to increase in the Eurasia and Brazilian plateau, while decreasing in the Amazonian Plain (Figure 2C). Overall, about 20% of basins showed the significant trends, and the significant increases were mainly in the Northwest China, Europe, and the midwest U.S, while the significant decreases were mainly in the Congo Basin and Amazonian Plain (Figure 2D). In conclusion, *ET* regarding magnitude, temporal variability and trend showed the high spatio-temporal heterogeneity.

All *ET* products could reproduce the spatial distribution for climatological values of *ET* with high spatial R values ≥ 0.90 (Table 3). Among these products, the PML performed slightly better than the other products with the highest and R value of 0.96, though not with optimal β and γ . The β values for most *ET* products were consistently around the optimal value of 1.0, except for GLASS (1.27 for β) and MERRA-2 (1.22 for β), suggesting that the magnitudes of climatological values were well captured by most *ET* products. However, the spatial variabilities of *ET* tended to be

TABLE 3 The evaluation results of eight *ET* products against water balance *ET* during 1981–2010 from global 1,381 basins. Bold numbers in the table represent the optimal results corresponding to each metric.

Characteristics	Metrics	GLASS	ERA5-land	MERRA-2	GLEAM-3.5a	E2O-En	PML	GLDAS2.0-Noah	MTE
Mean annual value	β	1.27	1.09	1.22	1.00	1.03	0.94	0.98	0.97
	γ	1.01	0.74	0.95	0.86	0.82	1.08	0.83	0.88
	<i>R</i>	0.89	0.92	0.92	0.92	0.95	0.96	0.92	0.94
	<i>KGE</i>	0.71	0.71	0.76	0.83	0.81	0.89	0.81	0.86
CV	β	0.34	0.57	0.89	0.61	0.62	0.62	0.64	0.26
	γ	1.21	2.13	1.57	2.09	1.77	1.66	1.65	2.39
	<i>R</i>	0.05	0.23	0.23	0.25	0.18	0.01	0.14	0.13
	<i>KGE</i>	−0.17	−0.43	0.04	−0.38	−0.18	−0.24	−0.14	−0.80
Trend	β	21.01	−5.25	−5.14	3.20	5.72	7.03	10.07	4.66
	γ	0.04	−0.13	−0.19	0.18	0.09	0.08	0.06	0.05
	<i>R</i>	0.31	0.25	0.36	0.24	0.19	0.21	0.23	0.09
	<i>KGE</i>	−19.05	−5.04	−5.29	−1.47	−3.87	−5.15	−8.15	−2.88
	TPR (%)	55.11	28.53	36.41	41.27	40.77	41.85	44.46	48.22
	FPR (%)	39.68	13.32	13.47	23.03	27.37	26.29	31.79	29.62
	TNR (%)	3.04	29.40	29.25	19.70	15.35	16.44	10.93	13.11
	FNR (%)	2.17	28.75	22.67	16.00	16.51	15.42	12.82	9.05

underestimated by most *ET* products with $0.7 < \gamma < 1.0$, especially for ERA5-Land with a γ of 0.74. The values of R , β and γ for capturing the *ET* by the products converged to the optimum value of 1.0, resulting in *KGE* values of integrative performances that outweighed 0.71. Notably, the model-based products had higher overall performance ($KGE \geq 0.81$) in reproducing the climatological *ET*, compared to the reanalysis products ($0.71 \leq KGE < 0.81$). Regarding the temporal variability, all *ET* products generally underestimated the CV ($0.34 \leq \beta \leq 0.89$), but evidently overestimated its spatial variability ($1.21 \leq \gamma \leq 2.39$). Moreover, the spatial distribution of *ET* CV were poorly captured by most *ET* products, with GLEAM-3.5a having the maximum R value of 0.25 among the eight *ET* products. Overall, the *KGE* values were mostly negative, ranging from −0.80 (MTE) to 0.04 (MERRA-2), indicating that most *ET* products had limited *KGE*-based ability to simulate *ET* temporal variability. In the view of the *ET* trend, the directions (i.e., upward and downward) could be hit by most products, with 59.29% for $PML \leq TPR + TNR \leq 65.66\%$ for MERRA-2. However, the FPR, near to and even larger than the TNR, suggested that the negative trends would be misidentified as positive trends, especially for GLASS (39.68% versus 3.04%). The R values ranged from 0.09 (MTE) to 0.36 (MERRA-2) indicating that GLASS and MERRA-2 with values above 0.30 could capture the *ET* trends in space. Except for reanalysis products underestimating the *ET* trend, all others overestimated the *ET* trend, with β larger than 1.0. By contrast, all products underestimated the spatial variability of the *ET* trend, with -0.19 (MERRA-2) $\leq \gamma \leq 0.18$ (GLEAM-3.5a). All *KGE* values were negative, indicating that these poor overall performance of these *ET* products in capturing the *ET* trend.

Figure 3 shows the metrics of β , γ , R , and *KGE* for 1,381 basins. The majority of *ET* products overestimated *ET* at more than 50% of basins, especially GLASS and MERRA-2 which overestimated *ET* at above 92% of basins (Figure 3A). However, PML, GLDAS2.0-Noah and MTE underestimated the *ET* at more than 50% of basins. Spatially, the β values displayed evident spatial differences, with most of *ET* products greatly overestimated the *ET* in China, Europe, and North America. Considering the metric of γ (Figure 3B), all *ET* products tended to underestimate the *ET* temporal variabilities at over 70% of basins. When $\gamma < 0.2$, *ET* products, especially MTE and GLASS, underestimated the *ET* temporal variabilities at around 30% of basins worldwide. Additionally, the overestimates of *ET* temporal variabilities tended to be at American Midwest. About the spatial patterns of β and γ , it is worth noting that the higher *ET* magnitude estimates were accompanied by lower *ET* variability estimates, since the ratio of basins having $\beta > 1.0$ outweighed the ratio of basins having $\gamma < 1.0$ for most *ET* products except PML, GLDAS2.0-Noah, and MTE (Figures 3A,B). Regarding temporal fluctuation (Figure 3C), positive R values were observed for 59.30% (MERRA-2) to 84.50% (ERA5-Land) of basins, especially MERRA-2 with $R > 0.6$ at nearly 20% of basins, indicating that *ET* products had a broad R -based ability to simulate *ET* temporal fluctuation. High R values (around 0.8) mainly appeared in the Midwest United States, South Africa, Western Australia. However, the average R values for all *ET* products were slightly low, ranging from 0.06 for GLDAS2.0-Noah–0.24 for ERA5-Land. Based on *KGE* (Figure 3D), negative *KGE* values were found in 47.65% (E2O-En) to 71.76% (MTE) of basins, with general negative basin-averaged *KGE* values (−0.14 (GLASS) to 0.03 (E2O-En)), indicating that all *ET* products had the limited overall performance for temporal scale.

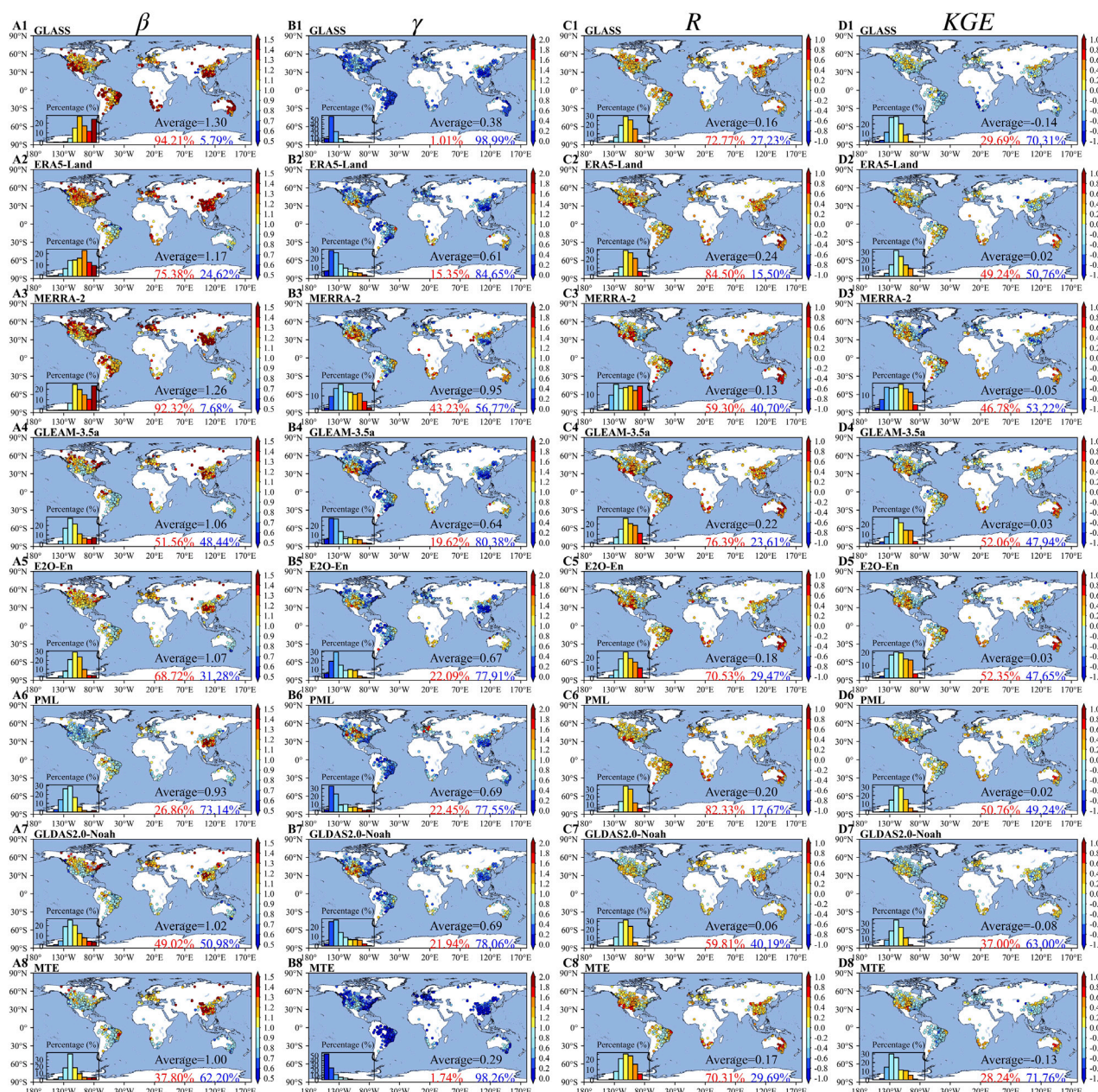


FIGURE 3

Spatial patterns of validation metrics at global 1,381 basins. The histograms in (A–D) present the values of *KGE* and its components *R*, β and γ at different levels corresponding to the color bars.

Relatively, the $KGE > 0.2$ mainly existed at Australia and Midwest America.

3.2 Validation by aridity regimes

In terms of the climatological values of *ET* under dry and wet conditions (Figure 4), except GLASS under all conditions and MERRA-2 under wet condition, the *ET* products could reproduce the magnitudes of *ET* with $0.86 \text{ for } PML \leq \beta \leq 1.17$ for ERA5-Land under dry condition and with $0.96 \text{ for } MTE \leq \beta \leq 1.07$ for ERA5-Land under wet condition, which was consistent with the results

presented in Section 3.1 (Table 3). In particular, most of the *ET* products underestimated the water balance *ET* above 1,200 mm (Figure 4), which mainly occurred in Amazonian Plain and Brazilian Plateau (Figure 2). As for γ , most of the *ET* products could generally detect the spatial variability for the climatological values of *ET* under dry and wet conditions, corresponding to a range of $0.69 \text{ (ERA5-Land)} \leq \gamma \leq 1.32 \text{ (GLASS)}$ and $0.72 \text{ (ERA5-Land)} \leq \gamma \leq 1.07 \text{ (GLASS)}$, respectively. Broadly, the spatial variability estimates of *ET* under dry condition tended to be higher than those under wet condition (represented as $\gamma_{\text{dry}} > \gamma_{\text{wet}}$) except ERA5-Land and MTE. Regarding *R*, the *ET* products had a high *R*-based ability to simulate spatial distribution of *ET* with $R > 0.8$ under dry and

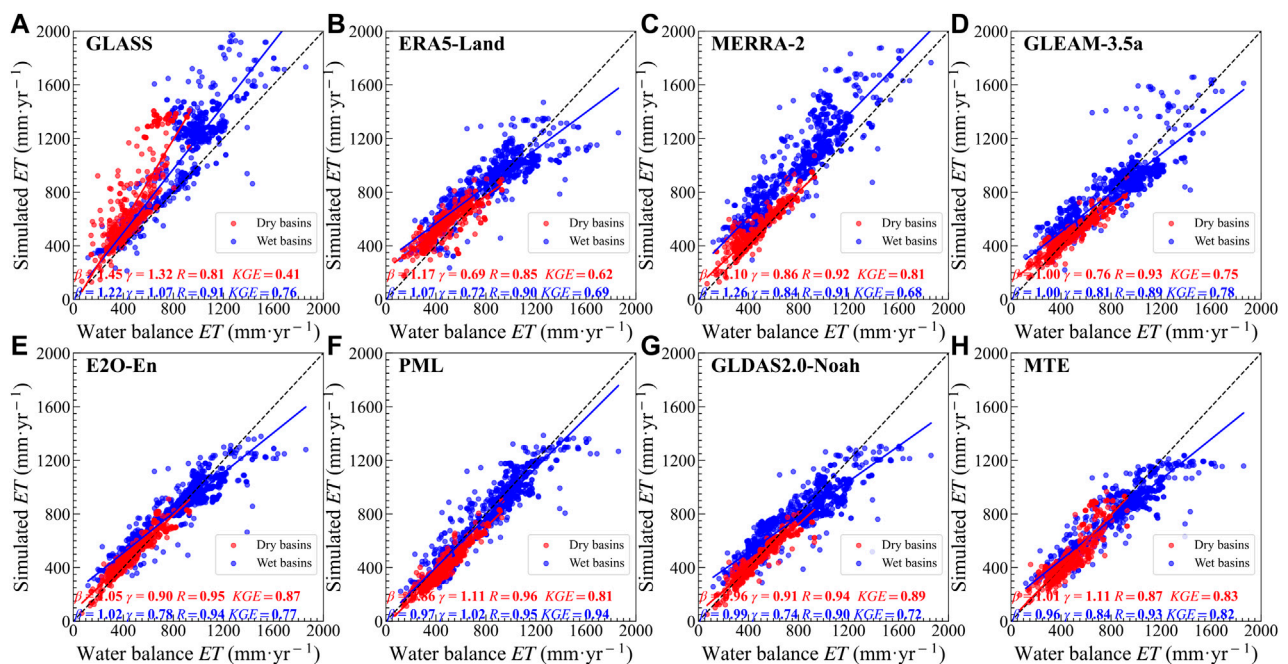


FIGURE 4

Scatterplots of water balance *ET* versus *ET* simulated by *ET* products for wet and dry basins, accompanied by various validation criteria (*KGE* and its components *R*, β and γ) at the bottom of each panel. (A–H) represent the GLASS, ERA5-Land, MERRA-2, GLEAM-3.5a, E2O-En, PML, GLDAS2.0-Noah and MTE, respectively. The blue and red represent wet and dry basins, respectively.

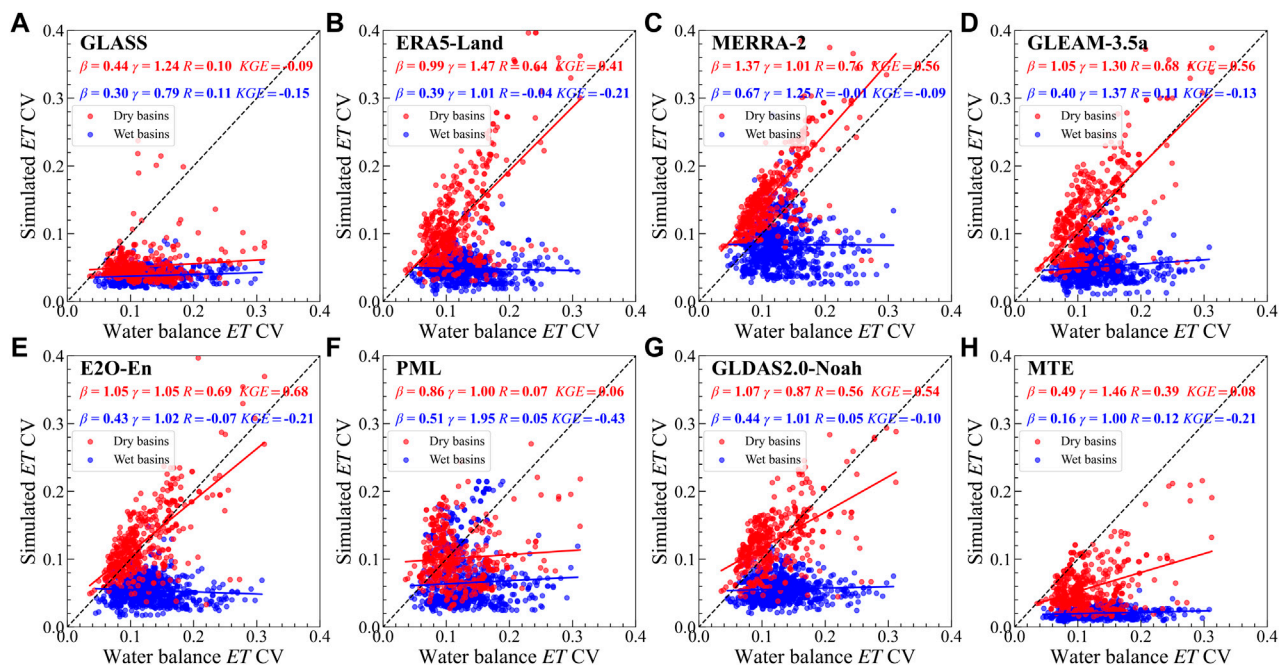


FIGURE 5

Scatterplots of water balance *ET CV* versus *ET CV* simulated by *ET* products for wet and dry basins, accompanied by various validation criteria (*KGE* and its components *R*, β and γ) at the top of each panel. (A–H) represent the GLASS, ERA5-Land, MERRA-2, GLEAM-3.5a, E2O-En, PML, GLDAS2.0-Noah and MTE, respectively. The blue and red represent wet and dry basins, respectively.

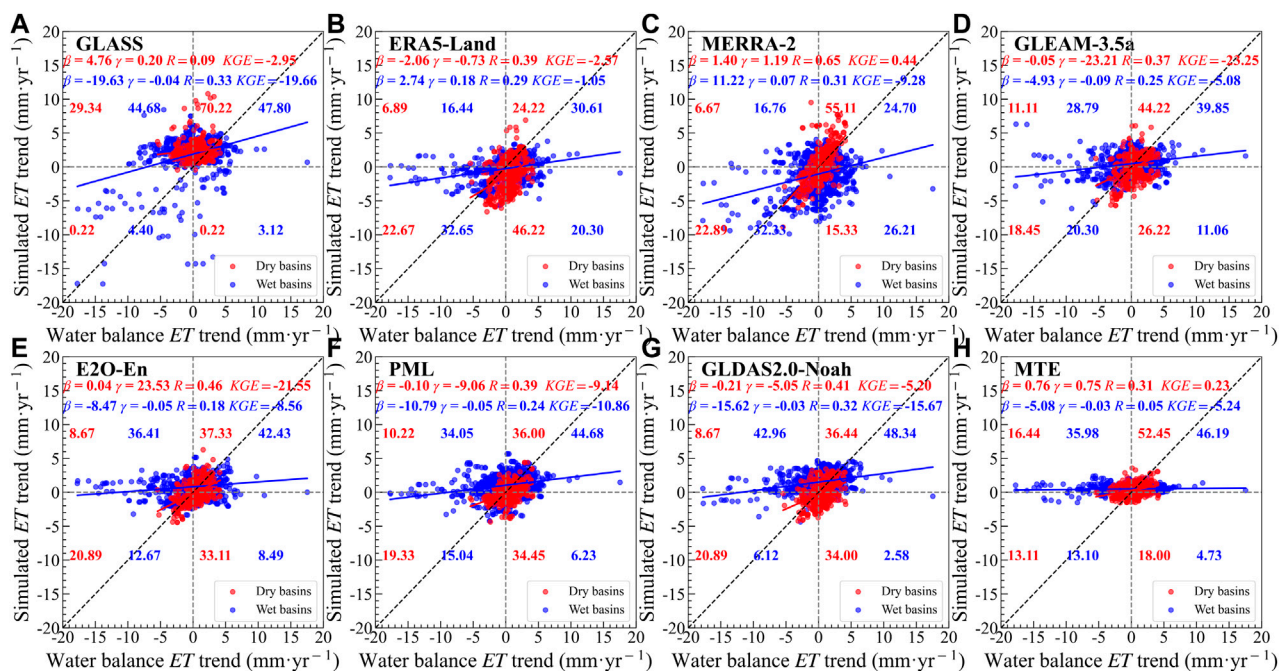


FIGURE 6

Scatterplots of water balance *ET* trend versus *ET* trend simulated by *ET* products for wet and dry basins, accompanied by various validation criteria (*KGE* and its components β , γ and R) at the top of each panel. (A–H) represent the GLASS, ERA5-Land, MERRA-2, GLEAM-3.5a, E2O-En, PML, GLDAS2.0-Noah and MTE, respectively. The blue and red represent wet and dry basins, respectively. The percentages in the first-fourth quadrants represent the TPR, FPR, TNP, and FNR, respectively. The sum of the percentage values in four quadrants is equal to 100 (%).

wet conditions. Meanwhile, the *ET* products could better represent the spatial distribution of climatological *ET* (except for GLASS, ERA5-Land, and MTE) under dry basins than wet basins (represented as $R_{\text{dry}} > R_{\text{wet}}$). As for *KGE*, *ET* products exhibited the high overall performance on climatological *ET* conditioned by aridity, especially generating the highest *KGE* values for GLDAS2.0-Noah (0.89) under dry condition and PML (0.94) under wet condition.

With β at ~ 1.0 , the magnitude of temporal variability of *ET* tended to be more easily simulated under dry condition, compared with wet condition (Figure 5). As for γ , the spatial variability of *ET* temporal variability was generally overestimated by *ET* products under all aridity conditions, with 0.87 for GLDAS2.0-Noah $\leq \gamma \leq 1.47$ for ERA5-Land under dry condition, and 0.79 for GLASS $\leq \gamma \leq 1.95$ for PML under wet condition. As for R , the *ET* products could detect the spatial distribution of *ET* CV under dry basins, of which the highest R value was 0.76 for MERRA-2, followed by 0.69 for E2O-En. However, under wet condition, the *ET* products presented a contrasting performance, compared with dry condition, with R values ranging from -0.07 to 0.12 . Considering *KGE*, similar to R , the *ET* products could not simulate the *ET* CV under wet condition, whereas, under dry condition, ERA5-Land, MERRA-2, GLEAM3.5a, E2O-En and GLDAS2.0-Noah showed better overall performances, generating a *KGE* above 0.40.

Taking the *ET* trend into consideration (Figure 6), more than 50% of the total number of basins were located in the first and third quadrants, with 46.89% for ERA5-Land $\leq \text{TPR} + \text{TNR} \leq 78.00\%$ for MERRA-2 under dry condition and 54.20% for GLASS $\leq \text{TPR} + \text{TNR} \leq 63.26\%$ for ERA5-Land under wet condition. This indicates that

most of the *ET* products can capture the *ET* trend directions. Despite that, it is worth noting that FPRs outweighed the TNRs under wet condition. This suggested that under the wet condition, these products tended to change the negative *ET* trends to the positive *ET* trends. Based on β , under wet condition, most of the *ET* products (except ERA5-Land and MERRA-2) tended to underestimate the magnitude of *ET* trend, with -19.63 for GLASS $\leq \beta \leq -4.93$ for GLEAM-3.5a. By contrast, under dry condition, the underestimations of the *ET* trend got relieved, with -2.06 for ERA5-Land $\leq \beta \leq 4.76$ for GLASS, except that general underestimations still existed in dry condition. In addition, *ET* products underestimated the extreme *ET* trends over the wet basins (< -5 and $> 5 \text{ mm yr}^{-1}$), which mainly occurred in the Amazonian Plain and Brazilian Plateau (Figure 2). As for the spatial variability of *ET* trend, the γ values were around zero for all *ET* products under wet condition, ranging from -23.21 for GLEAM-3.5a to 23.53 for E2O-En. Overall, all *ET* products exhibited limited R -based ability to simulate spatial distribution of the *ET* trend, with 0.09 for GLASS $\leq R \leq 0.65$ for MERRA-2 under dry condition and 0.05 for MTE $\leq R \leq 0.33$ for GLASS under wet condition. Furthermore, the overall performance for each *ET* product under all aridity conditions was poor with -23.25 (GLEAM-3.5a) $\leq KGE \leq 0.44$ (MERRA-2) under dry condition and -19.66 (GLASS) $\leq KGE \leq -1.05$ (ERA5-Land) under wet condition. Notably, the overall performances were generally worse for the latter.

Temporally, as shown in Figure 7A, regarding β , except PML, GLDAS2.0-Noah, and MTE, the magnitudes of *ET* were

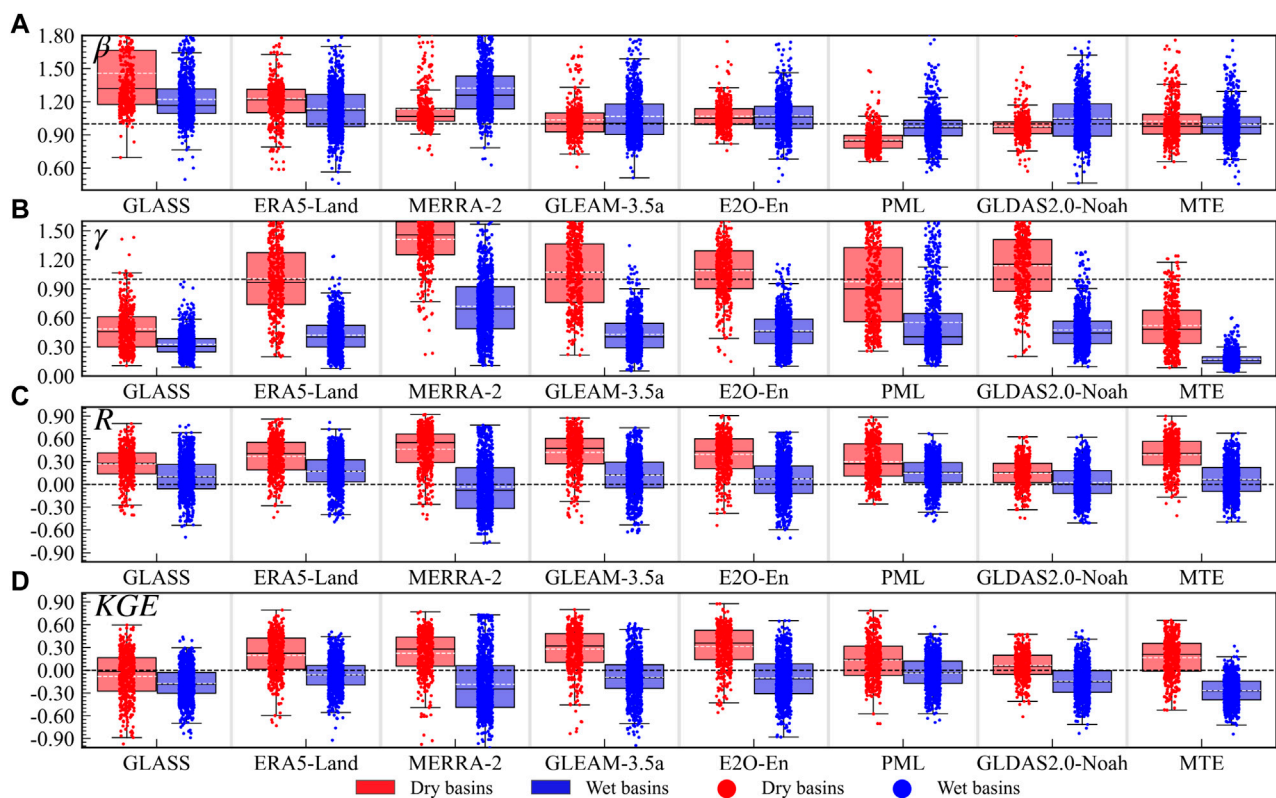


FIGURE 7

Box plots of evaluation metrics for ET products under wet and dry basins. (A–D) represent the KGE and its components R , β and γ , respectively. The blue and red represent wet and dry basins, respectively. The dashed lines represent the average value.

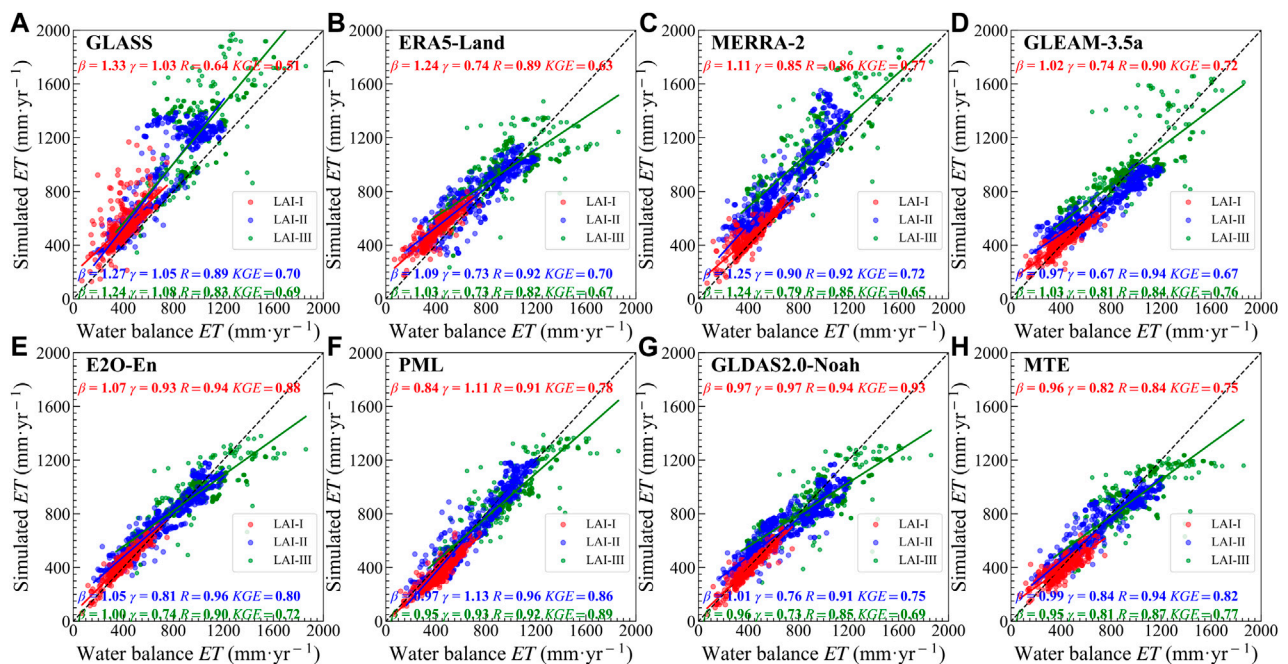


FIGURE 8

Scatterplots of water balance ET CV versus ET CV simulated by ET products under LAI-I, LAI-II, and LAI-III conditions, accompanied by various validation criteria (KGE and its components R , β and γ) at the top of each panel. (A–H) represent the GLASS, ERA5-Land, MERRA-2, GLEAM-3.5a, E2O-En, PML, GLDAS2.0-Noah and MTE, respectively. The red, blue and green represent the vegetation greenness levels of LAI-I ($LAI < 1$), LAI-II ($1 \leq LAI < 2$) and LAI-III ($LAI \geq 2$) respectively.

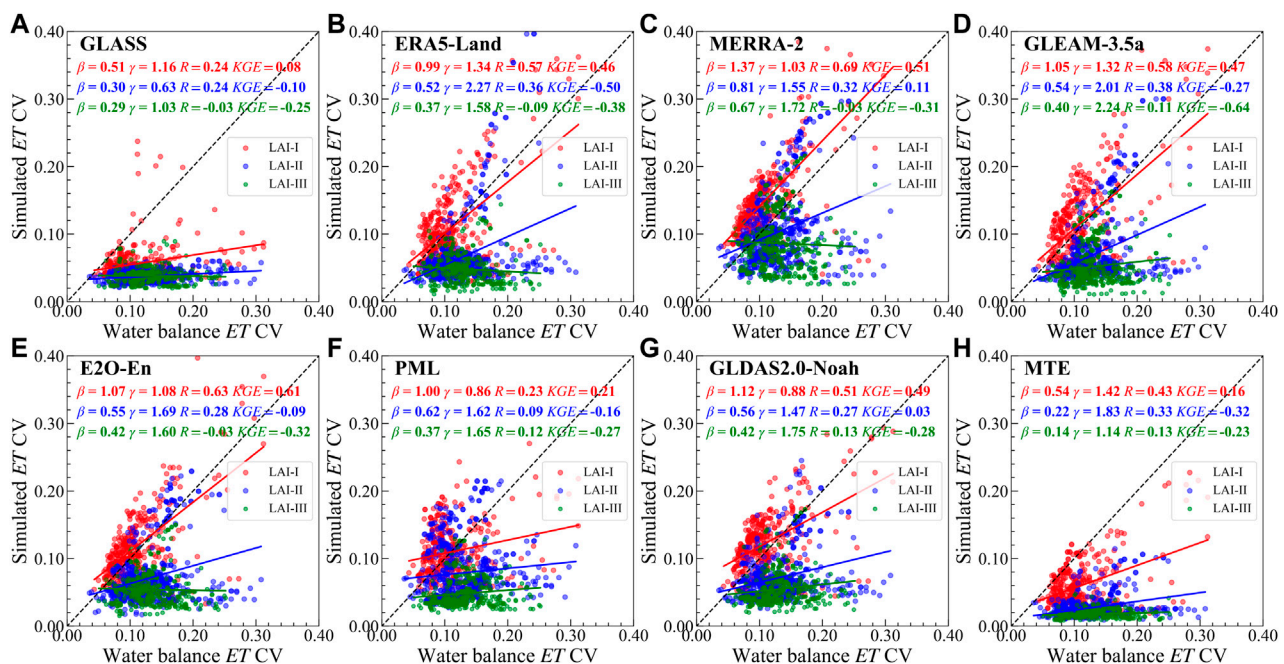


FIGURE 9

Scatterplots of water balance *ET* CV versus *ET* CV simulated by *ET* products under LAI-I, LAI-II, and LAI-III conditions, accompanied by various validation criteria (*KGE* and its components *R*, β and γ) at the top of each panel. (A–H) represent the GLASS, ERA5-Land, MERRA-2, GLEAM-3.5a, E2O-En, PML, GLDAS2.0-Noah and MTE, respectively. The red, blue and green represent the vegetation greenness levels of LAI-I ($LAI < 1$), LAI-II ($1 \leq LAI < 2$) and LAI-III ($LAI \geq 2$), respectively.

overestimated at 51.33% for GLEAM-3.5a to 98.89% for GLASS of dry basins, and at 51.66% for GLEAM-3.5a to 96.46% for MERRA-2 of wet basins. The basin-averaged β values for the *ET* products (except GLASS and MERRA-2) were both near to 1.0 under dry and wet conditions (Figure 7B). The basin-averaged γ values under dry condition were also close to 1.0 for most products, while under wet condition the values were overwhelmingly low, ranging from 0.17 for MTE to 0.72 for MERRA-2. As for *R* (Figure 7C), more than 50% of basins exhibited a value over zero for most products under all conditions. Despite that, each *ET* product showed a higher *R*-based ability to simulate *ET* temporal fluctuation under dry condition than wet condition, with average *R* values ranging from 0.15 for GLDAS2.0-Noah to 0.46 for MERRA-2 under dry condition and -0.03 for MERRA-2 to 0.17 for ERA5-Land under wet condition. As for *KGE* (Figure 7D), compared with the *R*-based ability, the overall performance of *ET* products under wet conditions worsened. For example, 64.12% (ERA5-Land) to 93.88% (MTE) of basins showed negative *KGE* values under wet conditions, whereas 63.11% (GLDAS2.0-Noah) to 87.33% (E2O-En) of basins exhibited positive *KGE* values under dry conditions. Furthermore, all *ET* products showed a negative average *KGE* value under wet conditions, while most products, except for GLASS, showed a positive average *KGE* value under dry conditions.

3.3 Validation by vegetation conditions

From perspective of climatological *ET*, the magnitude and spatial variability of *ET* could be represented by most of the *ET*

products across all vegetation conditions (Figure 8), with both β and γ around 1.0. However, most of the *ET* products (excluding GLASS) also underestimated the *ET* values above 1,200 mm under LAI-III condition, which mainly exist in Amazonian Plain and Brazilian Plateau (Figure 2). Concerning *R*, the capacity to simulate the spatial distribution of climatological *ET* increased first, and then decreased as vegetation became greener for most *ET* products except GLDAS2.0-Noah. In terms of *KGE*, most *ET* products show good *KGE*-based performance. In addition, GLASS, ERA5-Land, MERRA-2, E2O-En, PML, and MTE showed that the *KGE*-based performance was the best under LAI-II condition.

In terms of the *ET* CV (Figure 9), most *ET* products (except GLASS and MTE) reasonably estimated *ET* magnitude under LAI-I condition, with $0.86 \leq \beta \leq 1.34$ for ERA5-Land. However, the β values were limited for other vegetation conditions, with $0.22 \leq \beta \leq 0.62$ for PML under LAI-II condition and $0.14 \leq \beta \leq 0.67$ for MERRA-2 under LAI-III condition. The β values for the *ET* temporal variability decreased as the vegetation turned green for each *ET* product. And the γ values for the spatial variability of *ET* temporal variability tended to be overestimated under all vegetation conditions. For *R*, all the *ET* products (except PML) had the limited *R*-based ability to simulate the spatial distribution of *ET* temporal variability, with vegetation greening. For example, the *R* values under LAI-I, LAI-II, LAI-III conditions ranged from 0.24 to 0.69, 0.24 to 0.38, and -0.09 to 0.13, respectively. Similar trends were occurred to *KGE*, except that the overall performance of *KGE* was even worse than that of *R*-capacity.

In the view of *ET* trend (Figure 10), its condition is similar to the aridity condition. The *ET* products could hit the *ET* trend directions,

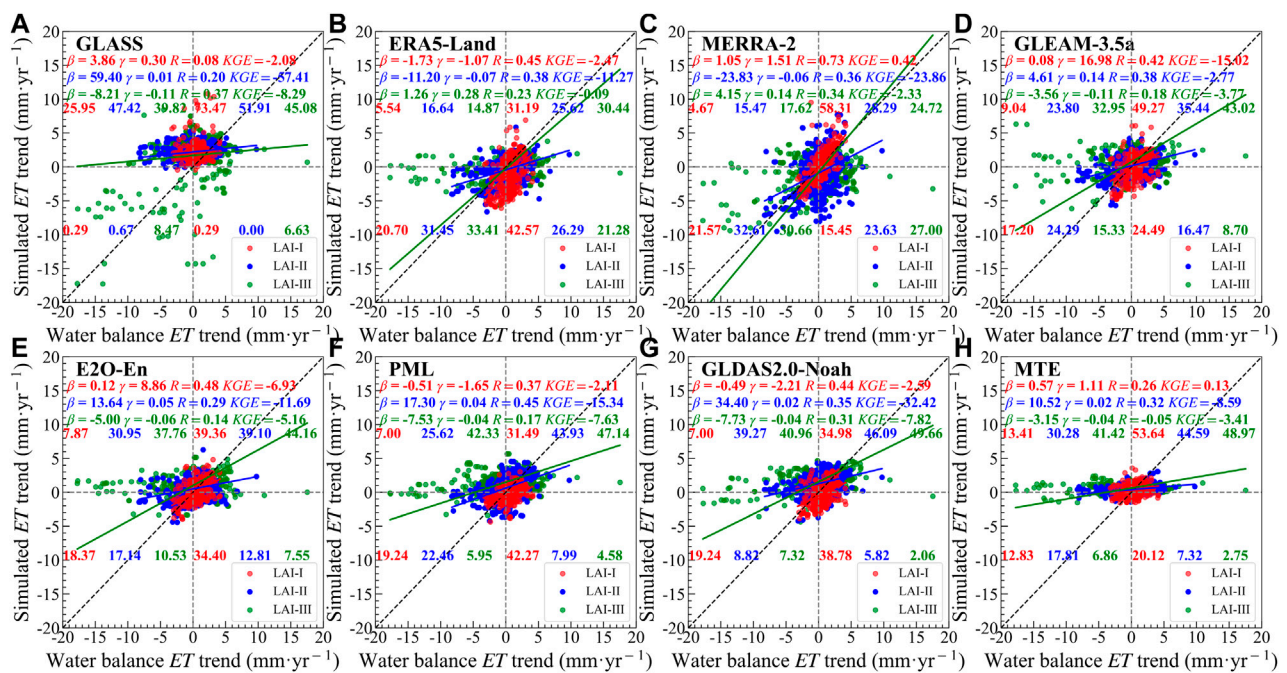


FIGURE 10

Scatterplots of water balance ET trend versus ET trend simulated by ET products under LAI-I, LAI-II, and LAI-III conditions, accompanied by various validation criteria (KGE and its components R , β and γ) at the top of each panel. (A–H) represent the GLASS, ERA5-Land, MERRA-2, GLEAM-3.5a, E2O-En, PML, GLDAS2.0-Noah and MTE, respectively. The red, blue and green represent the vegetation greenness levels of LAI-I ($\text{LAI} < 1$), LAI-II ($1 \leq \text{LAI} < 2$) and LAI-III ($\text{LAI} \geq 2$), respectively. The percentages in the first-fourth quadrants represent the TPR, FPR, TNP, and FNR, respectively. The sum of the percentage values in four quadrants is equal to 100 (%).

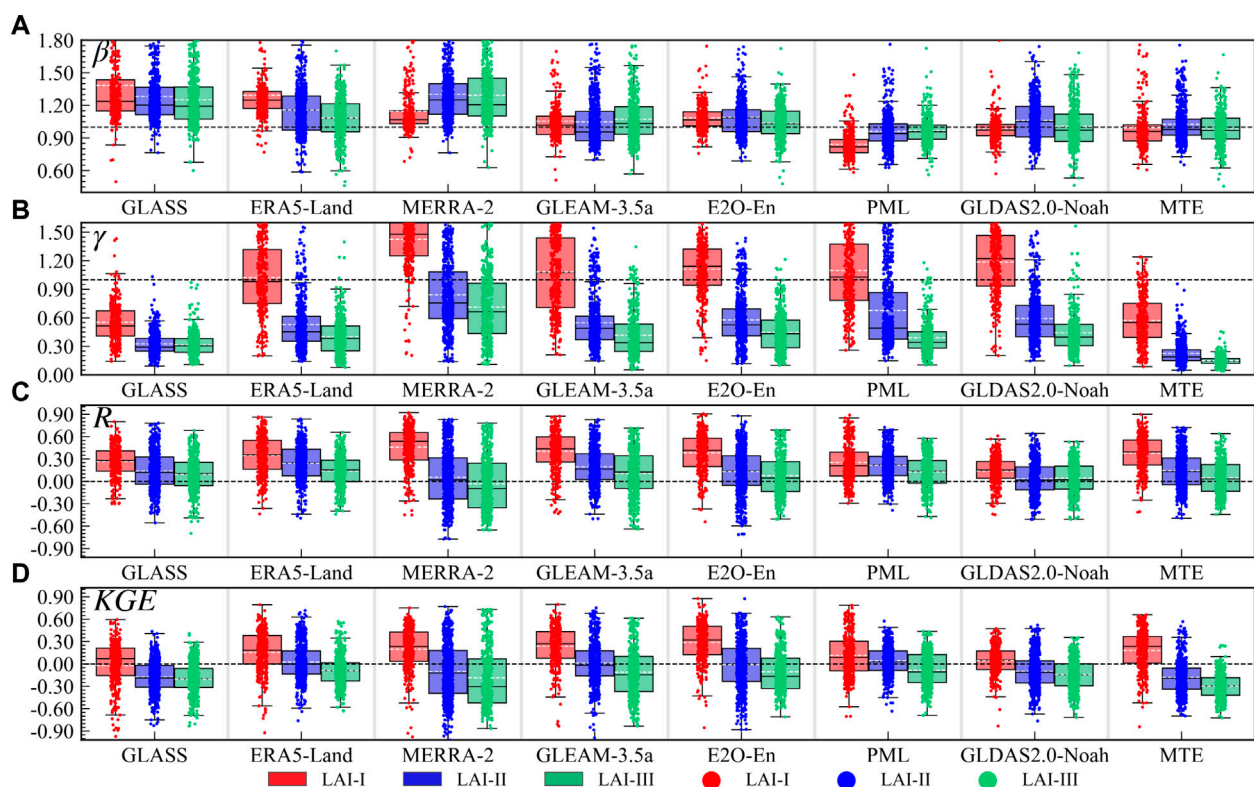


FIGURE 11

Box plots of evaluation metrics for ET products under LAI-I, LAI-II, and LAI-III conditions. (A–D) represent the KGE and its components R , β and γ , respectively. The blue, red and green represent LAI-I, LAI-II, and LAI-III conditions, respectively. The dashed lines represent the basin-averaged value.

with 50.73% for $PML \leq TPR + TNR$ 79.88% for MERRA-2 under LAI-I condition, 52.58% for $GLASS \leq TPR + TNR \leq 66.39\%$ for PML under LAI-II condition, and 52.09% for $PML \leq TPR + TNR \leq 66.85\%$ for ERA5-Land under LAI-III condition. Additionally, FPRs outweighed the TNRs for *ET* products (except ERA5-Land and MERRA-2) under LAI-II and LAI-III conditions, for example, for GLDAS2.0-Noah, FPR *versus* TNR was 39.27% *versus* 8.82% under LAI-II condition, and 40.96% *versus* 7.32% under LAI-III condition, indicating that the *ET* products tended to misidentify the negative *ET* trends as positive *ET* trends. Based on β , except ERA5-Land and MERRA-2, the *ET* products tended to seriously underestimate the magnitudes of *ET* under LAI-III condition, with -8.21 for $GLASS \leq \beta \leq -3.15$ for MTE. And the values of β were much larger than 1.0 under LAI-II condition (excluding ERA5-Land and MERRA-2), suggesting that the overestimation occurred in LAI-II condition. As for γ , all the *ET* products underestimated the spatial variability of the trends (excluding MERRA-2, GLEAM-3.5a, E2O-En and MTE for LAI-I condition). As for *R* values, the *ET* products (except GLASS, MTE and PML) showed lower correlations with the greening of vegetation. Interestingly, the *ET* trends were remarkably overestimated by most products in LAI-II condition, and slightly underestimated under LAI-I and LAI-III conditions. As for *KGE*, most of the *ET* products had bad performance with negative values under all conditions. Especially under LAI-II and LAI-III conditions, they had almost no simulability.

Temporally, the basin-averaged β values were around the 1.0 for all vegetation conditions (Figure 11A), though the temporal magnitudes of *ET* were either overestimated or underestimated by the *ET* products. Considering γ (Figure 11B), the basin-averaged values for all the *ET* products significantly decreased with the vegetation turning green, and were overestimated under LAI-I condition, but underestimated under the other vegetation conditions. It is worth noting that as vegetation was getting greener, the *R*-based ability for all the *ET* products was significantly constrained (Figure 11C). Specifically, all the *ET* products consistently performed, and the average *R* value and the basin percentages of the *R* values over zero decreased with vegetation greening. Figure 11D clearly shows that, like *R*-based ability, the basin-averaged overall performances of all the *ET* products decreased, as the vegetation was getting greener, except that the *KGE* values were lower than *R* values.

4 Discussion

4.1 Validation by dynamic aridity or vegetation conditions

In this study, the simulations of *ET* derived from the eight methods were evaluated by the water balance *ET* of global 1,381 basins under various water, energy, and vegetation conditions. Since water, energy, and vegetation are crucial for accurately simulating *ET*, the lack of sufficient their information, caused by the lack of *ET* algorithm, forcing data and calibration methods, affects the performance of *ET* simulation (Xu et al., 2019; Elnashar et al., 2021; Li et al., 2022; Yu et al., 2022). As is shown, the comprehensive performance of *ET* products (Figures 7, 11) and the capture of *ET* variance (Figures 5, 9) regularly decrease, with the

humidity and vegetation greenness increasing. These phenomena imply that the accuracy of the *ET* simulations may decrease, when the regional climate is wetting and the global vegetation is greening (Mankin et al., 2017; Lian et al., 2021; Zhang et al., 2022). Additionally, the *ET* products tend to misidentify the negative trends as the positive trends, especially under wet and LAI-III conditions, implying that the estimates of *ET* trends may be overestimated across the globe or in wet and LAI-III conditions (Figures 6, 10). These issues will be further discussed in the following.

In terms of the impact of water and energy denoted by AI, *ET* process in dry or wet regions can be conceptualized as a water- or energy-limited process, respectively: *ET* under dry conditions is water-limited, in that it is constrained by the soil moisture available for *ET*, while *ET* under wet conditions is energy limited, since there is sufficient soil moisture available for *ET*. Therefore, the maximum rate and temporal variations of *ET* proceeds are determined by atmospheric water demand (potential evapotranspiration) rather than soil moisture (Draper et al., 2018). All the *ET* products could better capture the mean annual value of all aridity conditions. However, the *ET* CV in wet basins tend to be more remarkably underestimated than in dry basins, by the *ET* products except GLASS and PML (Figures 5, 7). Indeed, wet zones have more active land-atmosphere coupling than dry zones, in that the inevitable *ET* algorithm errors or data forcing errors magnify the uncertainties under wet zones. For instance, Penman-Monteith method (GLDAS2.0-Noah, MERRA-2 and PML) is primarily driven by net radiation (R_n) under wet zones using a linearized approximate solution (Gao, 1988; Grignon, 1992; Leca et al., 2011), which is sensitive to low vapor pressure deficit (VPD) and may induce considerable problems in the extreme conditions (such as the water balance *ET* higher 1,200 mm (Figure 4) and extreme *ET* trends (Figure 6) and the soil evaporative term (Bai and Liu, 2018; Blatchford et al., 2020). More importantly, the presence or absence of *ET* products TWSC components in simulating *ET* under dry and wet areas cannot be ignored. However, most *ET* methods do not have an aquifer storage component, and LSMs lack a good representation of groundwater withdrawal for agricultural depletion, such as irrigation (Liu et al., 2016; Zeng and Cai, 2018). Additionally, the errors in the *ET* estimates and differences among the *ET* products are also mainly dependent on various inputs (Li et al., 2018).

The surface variables also control the *ET* process, especially vegetation (Wang et al., 2022; Zheng et al., 2022). Similarly, the response of *ET* products to vegetation was investigated. Regarding the mean annual value, we found that the simulability of datasets first increased and then decreased, with the increase of vegetation density (Figure 8), in line with the Lu et al. (2021). In addition, we also confirmed that the comprehensive performance (*KGE*) of *ET* products decreases as the vegetation is getting greener (Figures 8, 10). The first reason for this is that whether *ET* algorithms take the LAI or vegetation dynamics into consideration. For example, GLEAM-3.5a model lacks vegetation-related information, though it considers the vegetation optical depth, which may result in lower accuracy in high vegetation regions (Martens et al., 2017; Xu et al., 2019; Qiu et al., 2022). Another reason is that the *ET* algorithm do not comprehensively consider the vegetation process in hydrology or energy cycle. MERRA-2 overestimates the interception loss

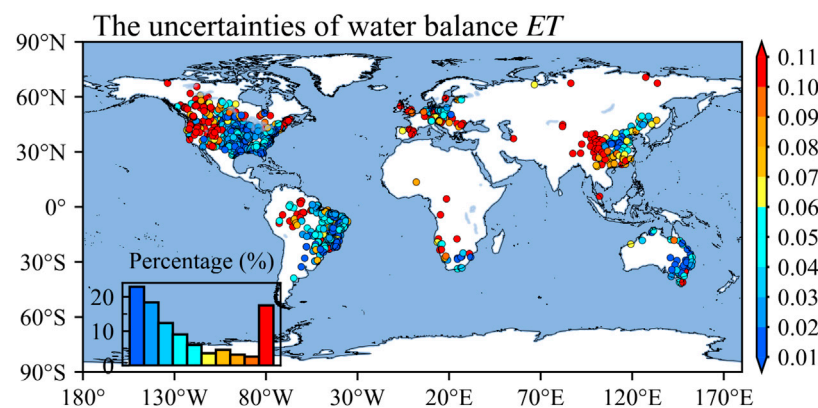


FIGURE 12

Spatial pattern of uncertainties of water balance *ET* at global 1,381 basins. The histogram presents uncertainty values at different levels corresponding to the color bars.

fraction defined as the fraction of rainfall, i.e., rainfall intercepted by the canopy and reevaporating back into the atmosphere without infiltrating into the soil or causing surface runoff (Reichle et al., 2011; Bosilovich et al., 2017; Gelaro et al., 2017; Reichle et al., 2017; Hinkelman, 2019), which could explain why the MERRA-2 generally has the highest β under various LAI conditions among the eight *ET* products (Figures 8, 11, and Lv et al. (2020)). The last easily neglected issue is related to the model forcing data. One aspect of the issue is the forcing data errors. The accuracy of LAI dataset is impacted by the leaf shadowing (Mehrez et al., 1992), especially tall and dense vegetations. Besides, shaded leaves are not light-saturated, leading to diffuse sunlight conditions and then having a higher fraction of FAPAR (the fraction of photosynthetically active radiation absorbed by the canopy) (Jimenez et al., 2011; He et al., 2013; Xu et al., 2019). Another aspect of the issue is the forcing data settings, for instance, MTE *ET* product was generated from machine learning method by compiling the 253 globally distributed flux towers data and remote sensing data, including vegetation information (FAPAR). We speculated that the varying performance of MTE product with various LAI conditions was probably driven by data settings. For example, the vegetation was used to do split not regression, which results in inadequate vegetation information (Jung et al., 2010). Or ERA5-Land was used to generate land elements data including *ET*, by using a static monthly climatology of a fixed land use and leaf area index (LAI) (Muñoz-Sabater et al., 2021). And GLDAS2.0-Noah also uses a static land use, though with high spatial resolution (Rodell et al., 2004). Therefore, they ignored the change of land cover and cities, and lost more frequent LAI anomalies during the reanalysis period (Muñoz-Sabater et al., 2021).

The model calibration methods also have a significant impact on the performance of *ET* simulation. One problem concerning the methods is that the *ET* simulations are often calibrated with the mean annual value not the variance and trend of actual *ET*, though considering multiple calibration metrics. Another problem is that the data used for calibration are often EC site data that are not representative of the regional scale (Bai and Liu, 2018; Xu et al., 2019). In addition, as far as we know, the *ET* products except GLASS and MTE are accompanied by component data such as soil

evaporation, vegetation evapotranspiration and water surface evaporation, but these data are not calibrated with sufficient actual measurements (Swanson, 1994; Brunel et al., 1997; Chen et al., 2014).

4.2 Uncertainties

The uncertainties in *Pre* and TWSA products are the largest source of uncertainties in assessing the *ET* products (Liu et al., 2016). According to the water balance budget, the assessment of global-scale *ET* products needs to rely on grid-scale *Pre* and TWSA products, although the global-scale observatory data is difficult to collect. As for the three *Pre* products selected in this study (GPCC, CPC-Unified, and CRU TS4.05), the uncertainties derive from the number of stations used, the time homogeneity and the quality control procedures (Trenberth et al., 2014; Sun et al., 2018). However, these products are interpolated from an unprecedented number of station data and are the most reliable precipitation products currently available (Sun et al., 2018). Regarding the TWSA data (GRACE-REC and GRID-CSR-GRACE-REC), the uncertainties arise mainly from the models used for the reconstruction (pre-2002) and the driving data (Gyawali et al., 2022). However, the correlation of GRACE-REC with yearly streamflow anomalies have median value of around 0.60 over 1981–2010 (Humphrey and Gudmundsson, 2019); the GRID-CSR-GRACE-REC has high correlation with Global Mean Sea level with R of 0.91 (Li et al., 2021). We further investigated the uncertainties in water balance evapotranspiration defined as the CV of the six *Pre*-TWSC-Q combinations, and found that most of the basins with uncertainties of <0.10 and uncertainties above 0.10 were located mainly in the Midwest USA and Southwest China (rainfall gauges are more sparsely distributed in high mountain areas) and the Arctic (Figure 12). In addition, Q data may be affected by human harvesting of deep groundwater and inter-basin water transfers (Liu et al., 2016). However, TWSC can reasonably take into account the impact of human activities on Q. Moreover, in validating the model, only the terrestrial water balance (not the atmospheric water balance) is considered, and the measured evapotranspiration

values lack the cross-validation to further reduce the error with the true values (Li et al., 2019). The generalizability of our results to other regions of the world may be subject to additional uncertainty, as the basins included in this study do not cover the entire globe. However, it is important to note that the performance of evapotranspiration products varies with dryness and vegetation greenness, and it is necessary to ensure that all types of dryness and vegetation greenness are covered (Figure 1). To minimize errors caused by different spatial resolutions, all *ET* products were re-interpolated linearly to 0.5° before evaluation. Furthermore, our analysis is based on observed *ET* using the water balance method, which represents the average *ET* of watersheds controlled by hydrological stations, reducing the uncertainty caused by a single grid point to some extent. The scale effect on *ET* product performance related to aridity and vegetation greenness response needs further exploration in future research.

5 Conclusion

This study conducted a comprehensive assessment of terrestrial *ET* products to improve *ET* products. In this study, drawing on the data of water balance *ET* from 1981–2010 collected from 1,381 basins, we examined eight *ET* products: one remote sensing product (GLASS), two reanalysis products (ERA5-Land and MERRA-2), four LSM-based products (GLEAM-3.5a, E2O-En, PML and GLDAS2.0-Noah), and one machine learning-based product (MTE). Besides, to gain a deeper insight into the eight *ET* estimates under various conditions, the potential impact of aridity and vegetation greenness were taken in consideration. The evaluation results are summarized below:

- (1) In view of the performance at the global scale, the *ET* products had advantages in capturing the mean annual value of *ET*, with relatively high *KGE* values, among which the PML performed the best with 0.89 for *KGE*. Despite that, the *ET* products had limited *KGE*-ability to simulate the *ET* variability with highest *KGE* of 0.04 for MERRA-2 and the trend with highest *KGE* of −1.47 for GLEAM-3.5a. In addition, the *ET* products tended to underestimate the *ET* temporal variability and overestimate its spatial dynamics, while they tended to overestimate the *ET* trend and underestimate its spatial dynamics. It is worth noting that the *ET* products tended to misidentify the negative *ET* trend as positive trend.
- (2) For each basin, the *ET* products always overestimated the *ET* values and underestimated the *ET* temporal variability at more than 50% of basins. And the *ET* products had a wide *R*-based ability to simulate the *ET* temporal fluctuation, for the *ET* products had positive *R* values at 59.30% (MERRA-2)—84.50% (ERA5-Land) of basins. The high *R* values mainly appeared in the Midwest United States, South Africa, Western Australia. However, all *ET* products showed the limited *KGE*-ability at the temporal scale.
- (3) As for different aridity regimes, the performances of *ET* products were completely opposite in dry and wet areas. Spatially, the *ET* products showed lower ability to capture the temporal variability and the trend of *ET* under wet condition than dry condition. And overall, the *ET* products

tended to misidentify the negative *ET* trend as positive trend, which only existed in wet condition. Temporally, the overall performances of *ET* products were limited under wet condition, for the *ET* products performed the negative *KGE* values under wet condition, and the positive *KGE* values under dry condition at more than 60% of basins.

- (4) Considering the dynamic performances with varying vegetation, the spatial and temporal performances of *ET* products were strongly affected by vegetation greenness, which is similar to the situation with aridity regimes. Spatially, as vegetation became greener, the performance of simulated climatological *ET* increased first and then decreased, and gradually limited the ability to simulate the spatial distribution of *ET* temporal variability. Meanwhile, the *ET* products tended to misidentify the negative *ET* trend as positive trend under lush vegetation condition. Temporally, the basin-averaged overall performances of all the *ET* products decreased, as the vegetation was getting greener.

Overall, the performances of *ET* products were poor in wet or vegetated areas, suggesting that the accuracy of *ET* products may decline in the future when the climate becomes wetter and the vegetation becomes greener. Therefore, this work is hopefully to improve our understanding about the spatio-temporal performance of the *ET* products, and contribute to the directional optimizations and effective applications of *ET* products.

Data availability statement

The raw data supporting the conclusions of this article will be made available by the authors, without undue reservation.

Author contributions

Data curation, HW, CT, YX, and DL; conceptualization, GY, HW, and CT; methodology, HW; visualization, HW, CT, and YX; writing—original draft, HW; writing—review and editing, GY, XL, and CT; investigation, JW, DL, and FY; software, PZ; supervision, GY.

Funding

This study was supported by the National Natural Science Foundation of China (Grant NO. 42075189), the Natural Science Foundation of Jiangsu Province, China (Grant No. BK20200096), Hubei Branch of China National Tobacco Corporation (Grant No. 027Y2021021), and Jiangsu Provincial Bureau of Hydrology and Water Resources Survey (Grant Nos. 2211052001601 and 2211052101801).

Conflict of interest

The authors declare that the research was conducted in the absence of any commercial or financial relationships that could be construed as a potential conflict of interest.

Publisher's note

All claims expressed in this article are solely those of the authors and do not necessarily represent those of their affiliated

References

- Albergel, C., Dutra, E., Munier, S., Calvet, J.-C., Munoz-Sabater, J., De Rosnay, P., et al. (2018). ERA-5 and ERA-interim driven ISBA land surface model simulations: Which one performs better? *Hydrology Earth Syst. Sci.* 22, 3515–3532. doi:10.5194/hess-22-3515-2018
- Alemohammad, S. H., Fang, B., Konings, A. G., Aires, F., Green, J. K., Kolassa, J., et al. (2017). Water, energy, and carbon with artificial neural networks (WECANN): A statistically based estimate of global surface turbulent fluxes and gross primary productivity using solar-induced fluorescence. *Biogeosciences* 14, 4101–4124. doi:10.5194/bg-14-4101-2017
- Almagro, A., Oliveira, P. T. S., Meira Neto, A. A., Roy, T., Troch, P. J. H., and Sciences, E. S. (2021). CABra: A novel large-sample dataset for Brazilian catchments. *Hydrology Earth Syst. Sci.* 25, 3105–3135. doi:10.5194/hess-25-3105-2021
- Arsenault, R., Bazile, R., Ouellet Dallaire, C., and Brissette, F. J. H. P. (2016). Canopex: A Canadian hydrometeorological watershed database. *Hydrol. Process.* 30, 2734–2736. doi:10.1002/hyp.10880
- Arsenault, R., Brissette, F., Martel, J.-L., Troin, M., Lévesque, G., Davidson-Chaput, J., et al. (2020). A comprehensive, multisource database for hydrometeorological modeling of 14,425 North American watersheds. *Sci. Data* 7, 243–312. doi:10.1038/s41597-020-00583-2
- Awange, J., Hu, K., and Khaki, M. (2019). The newly merged satellite remotely sensed, gauge and reanalysis-based Multi-Source Weighted-Ensemble Precipitation: Evaluation over Australia and Africa (1981–2016). *Sci. total Environ.* 670, 448–465. doi:10.1016/j.scitotenv.2019.03.148
- Badgley, G., Fisher, J. B., Jiménez, C., Tu, K. P., and Vinukollu, R. (2015). On uncertainty in global terrestrial evapotranspiration estimates from choice of input forcing datasets. *J. Hydrometeorol.* 16, 1449–1455. doi:10.1175/JHM-D-14-0040.1
- Bai, P., and Liu, X. (2018). Intercomparison and evaluation of three global high-resolution evapotranspiration products across China. *J. hydrology* 566, 743–755. doi:10.1016/j.jhydrol.2018.09.065
- Beck, H. E., De Roo, A., and Van Dijk, A. I. (2015). Global maps of streamflow characteristics based on observations from several thousand catchments. *J. Hydrometeorol.* 16, 1478–1501. doi:10.1175/JHM-D-14-0155.1
- Becker, A., Finger, P., Meyer-Christoffer, A., Rudolf, B., Schamm, K., Schneider, U., et al. (2013). A description of the global land-surface precipitation data products of the Global Precipitation Climatology Centre with sample applications including centennial (trend) analysis from 1901–present. *Earth Syst. Sci. Data* 5, 71–99. doi:10.5194/essd-5-71-2013
- Blatchford, M. L., Mannaerts, C. M., Njuki, S. M., Nouri, H., Zeng, Y., Pelgrum, H., et al. (2020). Evaluation of WaPOR V2 evapotranspiration products across Africa. *Hydrol. Process.* 34, 3200–3221. doi:10.1002/hyp.13791
- Bosilovich, M. G., Robertson, F. R., Takacs, L., Molod, A., and Mocko, D. (2017). Atmospheric water balance and variability in the MERRA-2 reanalysis. *J. Clim.* 30, 1177–1196. doi:10.1175/JCLI-D-16-0338.1
- Brunel, J.-P., Walker, G., Dighton, J., and Monteny, B. (1997). Use of stable isotopes of water to determine the origin of water used by the vegetation and to partition evapotranspiration. A case study from HAPEX-Sahel. *J. hydrology* 188, 466–481. doi:10.1016/S0022-1694(96)03188-5
- Chagas, V. B., Chaffe, P. L., Addor, N., Fan, F. M., Fleischmann, A. S., Paiva, R. C., et al. (2020). CAMELS-BR: Hydrometeorological time series and landscape attributes for 897 catchments in Brazil. *Earth Syst. Sci. Data* 12, 2075–2096. doi:10.5194/essd-12-2075-2020
- Chen, M., Shi, W., Xie, P., Silva, V. B., Kousky, V. E., Wayne Higgins, R., et al. (2008). Assessing objective techniques for gauge-based analyses of global daily precipitation. *J. Geophys. Res. Atmos.* 113, D04110–D04113. doi:10.1029/2007JD009132
- Chen, Y., Xia, J., Liang, S., Feng, J., Fisher, J. B., Li, X., et al. (2014). Comparison of satellite-based evapotranspiration models over terrestrial ecosystems in China. *Remote Sens. Environ.* 140, 279–293. doi:10.1016/j.rse.2013.08.045
- Coxon, G., Addor, N., Bloomfield, J. P., Freer, J., Fry, M., Hannaford, J., et al. (2020). CAMELS-GB: Hydrometeorological time series and landscape attributes for 671 catchments in Great Britain. *Earth Syst. Sci. Data* 12, 2459–2483. doi:10.5194/essd-12-2459-2020
- Draper, C. S., Reichle, R. H., and Koster, R. D. (2018). Assessment of MERRA-2 land surface energy flux estimates. *J. Clim.* 31, 671–691. doi:10.1175/JCLI-D-17-0121.1
- Elmashar, A., Wang, L., Wu, B., Zhu, W., and Zeng, H. (2021). Synthesis of global actual evapotranspiration from 1982 to 2019. *Earth Syst. Sci. Data* 13, 447–480. doi:10.5194/essd-13-447-2021
- Ershadi, A., McCabe, M., Evans, J. P., Chaney, N. W., and Wood, E. F. (2014). Multi-site evaluation of terrestrial evaporation models using FLUXNET data. *Agric. For. Meteorology* 187, 46–61. doi:10.1016/j.agrformet.2013.11.008
- Fisher, J. B., Tu, K. P., and Baldocchi, D. D. (2008). Global estimates of the land-atmosphere water flux based on monthly AVHRR and ISLSCP-II data, validated at 16 FLUXNET sites. *Remote Sens. Environ.* 112, 901–919. doi:10.1016/j.rse.2007.06.025
- Fowler, K. J., Acharya, S. C., Addor, N., Chou, C., and Peel, M. C. J. E. S. S. D. (2021). CAMELS-AUS: Hydrometeorological time series and landscape attributes for 222 catchments in Australia. *Earth Syst. Sci. Data* 13, 3847–3867. doi:10.5194/essd-13-3847-2021
- Gao, G., Fu, B., Wang, S., Liang, W., and Jiang, X. (2016). Determining the hydrological responses to climate variability and land use/cover change in the Loess Plateau with the Budyko framework. *Sci. Total Environ.* 557, 331–342. doi:10.1016/j.scitotenv.2016.03.019
- Gao, W. (1988). Applications of solutions to non-linear energy budget equations. *Agric. For. Meteorology* 43, 121–145. doi:10.1016/0168-1923(88)90087-1
- Gelaro, R., McCabe, W., Suárez, M. J., Todling, R., Molod, A., Takacs, L., et al. (2017). The modern-era retrospective analysis for research and applications, version 2 (MERRA-2). *J. Clim.* 30, 5419–5454. doi:10.1175/JCLI-D-16-0758.1
- Gobron, N., Pinty, B., Aussedat, O., Chen, J. M., Cohen, W. B., Fensholt, R., et al. (2006). Evaluation of fraction of absorbed photosynthetically active radiation products for different canopy radiation transfer regimes: Methodology and results using Joint Research Center products derived from SeaWiFS against ground-based estimations. *J. Geophys. Res. Atmos.* 111, D13110–D13115. doi:10.1029/2005JD006511
- Gobron, N., Pinty, B., Aussedat, O., Taberner, M., Faber, O., Mélin, F., et al. (2008). Uncertainty estimates for the FAPAR operational products derived from MERIS—impact of top-of-atmosphere radiance uncertainties and validation with field data. *Remote Sens. Environ.* 112, 1871–1883. doi:10.1016/j.rse.2007.09.011
- Grignon, F. (1992). A discussion of the Penman form equations and comparisons of some equations to estimate latent energy flux density. *Agric. For. meteorology* 57, 297–304. doi:10.1016/0168-1923(92)90125-N
- Gu, L., Chen, J., Yin, J., Xu, C. Y., and Zhou, J. (2020). Responses of precipitation and runoff to climate warming and implications for future drought changes in China. *Earth's Future* 8, e2020EF001718. doi:10.1029/2020EF001718
- Gyawali, B., Ahmed, M., Murgulet, D., and Wiese, D. N. (2022). Filling temporal gaps within and between GRACE and GRACE-FO terrestrial water storage records: An innovative approach. *Remote Sens.* 14, 1565. doi:10.3390/rs14071565
- Han, S.-C., Shum, C., and Braun, A. (2005). High-resolution continental water storage recovery from low-low satellite-to-satellite tracking. *J. Geodyn.* 39, 11–28. doi:10.1016/j.jog.2004.08.002
- He, M., Ju, W., Zhou, Y., Chen, J., He, H., Wang, S., et al. (2013). Development of a two-leaf light use efficiency model for improving the calculation of terrestrial gross primary productivity. *Agric. For. meteorology* 173, 28–39. doi:10.1016/j.agrformet.2013.01.003
- Hinkelman, L. M. (2019). The global radiative energy budget in MERRA and MERRA-2: Evaluation with respect to CERES EBAF data. *J. Clim.* 32, 1973–1994. doi:10.1175/JCLI-D-18-0445.1
- Holmes, R. M., Coe, M. T., Fiske, G. J., Gurtovaya, T., McClelland, J. W., Shiklomanov, A. I., et al. (2013). "Climate change impacts on the hydrology and biogeochemistry of Arctic rivers," in *Climatic change and global warming of inland waters* (Hoboken, New Jersey, United States: Wiley), 1–26. doi:10.1002/9781118470596.ch1
- Humphrey, V., and Gudmundsson, L. J. E. S. S. D. (2019). GRACE-REC: A reconstruction of climate-driven water storage changes over the last century. *Earth Syst. Sci. Data* 11, 1153–1170. doi:10.5194/essd-11-1153-2019
- Jimenez, C., Prigent, C., Mueller, B., Seneviratne, S. I., McCabe, M., Wood, E. F., et al. (2011). Global intercomparison of 12 land surface heat flux estimates. *J. Geophys. Res. Atmos.* 116, D02102–D02127. doi:10.1029/2010JD014545
- Jing, W., Di, L., Zhao, X., Yao, L., Xia, X., Liu, Y., et al. (2020a). A data-driven approach to generate past GRACE-like terrestrial water storage solution by calibrating the land surface model simulations. *Adv. Water Resour.* 143, 103683. doi:10.1016/j.advwatres.2020.103683

- Jing, W., Zhang, P., Zhao, X., Yang, Y., Jiang, H., Xu, J., et al. (2020b). Extending GRACE terrestrial water storage anomalies by combining the random forest regression and a spatially moving window structure. *J. Hydrology* 590, 125239. doi:10.1016/j.jhydrol.2020.125239
- Jung, H. C., Getirana, A., Policelli, F., McNally, A., Arsenault, K. R., Kumar, S., et al. (2017). Upper Blue Nile basin water budget from a multi-model perspective. *J. hydrology* 555, 535–546. doi:10.1016/j.jhydrol.2017.10.040
- Jung, M., Reichstein, M., and Bondeau, A. J. B. (2009). Towards global empirical upscaling of FLUXNET eddy covariance observations: Validation of a model tree ensemble approach using a biosphere model. *Biogeosciences* 6, 2001–2013. doi:10.5194/bg-6-2001-2009
- Jung, M., Reichstein, M., Ciais, P., Seneviratne, S. I., Sheffield, J., Goulden, M. L., et al. (2010). Recent decline in the global land evapotranspiration trend due to limited moisture supply. *Nature* 467, 951–954. doi:10.1038/nature09396
- Kim, H. W., Hwang, K., Mu, Q., Lee, S. O., and Choi, M. (2012). Validation of MODIS 16 global terrestrial evapotranspiration products in various climates and land cover types in Asia. *KSCE J. Civ. Eng.* 16, 229–238. doi:10.1007/s12205-012-0006-1
- Kling, H., Fuchs, M., and Paulin, M. (2012). Runoff conditions in the upper Danube basin under an ensemble of climate change scenarios. *J. hydrology* 424, 264–277. doi:10.1016/j.jhydrol.2012.01.011
- Klingler, C., Schulz, K., and Herrnegger, M. J. Ö. W.-U. A. (2021). LamaH | Large-Sample Data for Hydrology: Big data für die Hydrologie und Umweltwissenschaften. *Österreichische Wasser- Abfallwirtsch.* 73, 244–269. doi:10.1007/s00506-021-00769-x
- Landerer, F. W., and Swenson, S. (2012). Accuracy of scaled GRACE terrestrial water storage estimates. *Water Resour. Res.* 48, 1–11. doi:10.1029/2011WR011453
- Leca, A., Parisi, L., Lacomte, A., and Saudreau, M. (2011). Comparison of Penman–Monteith and non-linear energy balance approaches for estimating leaf wetness duration and apple scab infection. *Agric. For. meteorology* 151, 1158–1162. doi:10.1016/j.agrformet.2011.04.010
- Li, C., Yang, H., Yang, W., Liu, Z., Jia, Y., Li, S., et al. (2022). Camele: Collocation-analyzed multi-source ensemble land evapotranspiration data. *Earth Syst. Sci. Data Discuss.* 2022, 1–45. doi:10.5194/essd-2021-456
- Li, F., Kusche, J., Chao, N., Wang, Z., and Löcher, A. (2021). Long-Term (1979–Present) total water storage anomalies over the global land derived by reconstructing GRACE data. *Geophys. Res. Lett.* 48, e2021GL093492. doi:10.1029/2021GL093492
- Li, S., Wang, G., Sun, S., Chen, H., Bai, P., Zhou, S., et al. (2018). Assessment of multi-source evapotranspiration products over China using eddy covariance observations. *Remote Sens.* 10, 1692. doi:10.3390/rs10111692
- Li, X., Long, D., Han, Z., Scanlon, B. R., Sun, Z., Han, P., et al. (2019). Evapotranspiration estimation for Tibetan Plateau headwaters using conjoint terrestrial and atmospheric water balances and multisource remote sensing. *Water Resour. Res.* 55, 8608–8630. doi:10.1029/2019WR025196
- Lian, X., Piao, S., Chen, A., Huntingford, C., Fu, B., Li, L. Z., et al. (2021). Multifaceted characteristics of dryland aridity changes in a warming world. *Nat. Rev. Earth Environ.* 2, 232–250. doi:10.1038/s43017-021-00144-0
- Liu, J., You, Y., Zhang, Q., and Gu, X. (2021). Attribution of streamflow changes across the globe based on the Budyko framework. *Sci. Total Environ.* 794, 148662. doi:10.1016/j.scitotenv.2021.148662
- Liu, W., Wang, L., Zhou, J., Li, Y., Sun, F., Fu, G., et al. (2016). A worldwide evaluation of basin-scale evapotranspiration estimates against the water balance method. *J. Hydrology* 538, 82–95. doi:10.1016/j.jhydrol.2016.04.006
- Long, D., Shen, Y., Sun, A., Hong, Y., Longuevergne, L., Yang, Y., et al. (2014). Drought and flood monitoring for a large karst plateau in Southwest China using extended GRACE data. *Remote Sens. Environ.* 155, 145–160. doi:10.1016/j.rse.2014.08.006
- Lu, J., Wang, G., Chen, T., Li, S., Hagan, D. F. T., Kattell, G., et al. (2021). A harmonized global land evaporation dataset from model-based products covering 1980–2017. *Earth Syst. Sci. Data* 13, 5879–5898. doi:10.5194/essd-13-5879-2021
- Lv, M., Xu, Z., and Lv, M. (2020). Evaluating hydrological processes of the atmosphere–vegetation interaction model and MERRA-2 at global scale. *Atmosphere* 12, 16. doi:10.3390/atmos12010016
- Majozi, N. P., Mannaerts, C. M., Ramoelo, A., Mathieu, R., Mudau, A. E., and Verhoef, W. (2017). An intercomparison of satellite-based daily evapotranspiration estimates under different eco-climatic regions in South Africa. *Remote Sens.* 9, 307. doi:10.3390/rs9040307
- Mankin, J. S., Smerdon, J. E., Cook, B. I., Williams, A. P., and Seager, R. (2017). The curious case of projected twenty-first-century drying but greening in the American West. *J. Clim.* 30, 8689–8710. doi:10.1175/JCLI-D-17-0213.1
- Mao, J., Fu, W., Shi, X., Ricciuto, D. M., Fisher, J. B., Dickinson, R. E., et al. (2015). Disentangling climatic and anthropogenic controls on global terrestrial evapotranspiration trends. *Environ. Res. Lett.* 10, 094008. doi:10.1088/1748-9326/10/9/094008
- Martens, B., Miralles, D. G., Lievens, H., Van Der Schalie, R., De Jeu, R. A., Fernández-Prieto, D., et al. (2017). GLEAM v3: Satellite-based land evaporation and root-zone soil moisture. *Geosci. Model Dev.* 10, 1903–1925. doi:10.5194/gmd-10-1903-2017
- Mccabe, M. F., Ershadi, A., Jimenez, C., Miralles, D. G., Michel, D., and Wood, E. F. (2016). The GEWEX LandFlux project: Evaluation of model evaporation using tower-based and globally gridded forcing data. *Geosci. Model Dev.* 9, 283–305. doi:10.5194/gmd-9-283-2016
- Mehrez, M. B., Taconet, O., Vidal-Madjar, D., and Valencogne, C. (1992). Estimation of stomatal resistance and canopy evaporation during the HAPEX-MOBILHY experiment. *Agric. For. Meteorology* 58, 285–313. doi:10.1016/0168-1923(92)90066-D
- Miao, Y., and Wang, A. (2020). A daily 0.25° × 0.25° hydrologically based land surface flux dataset for conterminous China, 1961–2017. *J. Hydrology* 590, 125413. doi:10.1016/j.jhydrol.2020.125413
- Michel, D., Jiménez, C., Miralles, D. G., Jung, M., Hirschi, M., Ershadi, A., et al. (2016). The WACMOS-ET project—Part 1: Tower-scale evaluation of four remote-sensing-based evapotranspiration algorithms. *Hydrology Earth Syst. Sci.* 20, 803–822. doi:10.5194/hess-20-803-2016
- Miralles, D. G., Jiménez, C., Jung, M., Michel, D., Ershadi, A., Mccabe, M., et al. (2016). The WACMOS-ET project—Part 2: Evaluation of global terrestrial evaporation data sets. *Hydrology Earth Syst. Sci.* 20, 823–842. doi:10.5194/hess-20-823-2016
- Mu, Q., Heinsch, F. A., Zhao, M., and Running, S. W. (2007). Development of a global evapotranspiration algorithm based on MODIS and global meteorology data. *Remote Sens. Environ.* 111, 519–536. doi:10.1016/j.rse.2007.04.015
- Mu, Q., Zhao, M., and Running, S. W. (2011). Improvements to a MODIS global terrestrial evapotranspiration algorithm. *Remote Sens. Environ.* 115, 1781–1800. doi:10.1016/j.rse.2011.02.019
- Muñoz-Sabater, J., Dutra, E., Agustí-Panareda, A., Albergel, C., Arduini, G., Balsamo, G., et al. (2021). ERA5-Land: A state-of-the-art global reanalysis dataset for land applications. *Earth Syst. Sci. Data* 13, 4349–4383. doi:10.5194/essd-13-4349-2021
- Pan, S., Pan, N., Tian, H., Friedlingstein, P., Sitch, S., Shi, H., et al. (2020). Evaluation of global terrestrial evapotranspiration using state-of-the-art approaches in remote sensing, machine learning and land surface modeling. *Hydrology Earth Syst. Sci.* 24, 1485–1509. doi:10.5194/hess-24-1485-2020
- Penman, H. L. (1948). Natural evaporation from open water, bare soil and grass. *Math. Phys. Sci.* 193, 120–145. doi:10.1098/rspa.1948.0037
- Priestley, C. H. B., and Taylor, R. J. (1972). On the assessment of surface heat flux and evaporation using large-scale parameters. *Mon. weather Rev.* 100, 81–92. doi:10.1175/1520-0493(1972)100<0081:OTAOSH>2.3.CO;2
- Qiu, J., Crow, W. T., Wang, S., Dong, J., Li, Y., Garcia, M., et al. (2022). Microwave-based soil moisture improves estimates of vegetation response to drought in China. *Sci. Total Environ.* 849, 157535. doi:10.1016/j.scitotenv.2022.157535
- Reichle, R. H., Draper, C. S., Liu, Q., Girotto, M., Mahanama, S. P., Koster, R. D., et al. (2017). Assessment of MERRA-2 land surface hydrology estimates. *J. Clim.* 30, 2937–2960. doi:10.1175/JCLI-D-16-0720.1
- Reichle, R. H., Koster, R. D., De Lannoy, G. J., Forman, B. A., Liu, Q., Mahanama, S. P., et al. (2011). Assessment and enhancement of MERRA land surface hydrology estimates. *J. Clim.* 24, 6322–6338. doi:10.1175/JCLI-D-10-05033.1
- Rodell, M., Houser, P., Jambor, U., Gottschalk, J., Mitchell, K., Meng, C.-J., et al. (2004). The global land data assimilation system. *Bull. Am. Meteorological Soc.* 85, 381–394. doi:10.1175/BAMS-85-3-381
- Rodell, M., McWilliams, E. B., Famiglietti, J. S., Beaudoing, H. K., and Nigro, J. (2011). Estimating evapotranspiration using an observation based terrestrial water budget. *Hydrol. Process.* 25, 4082–4092. doi:10.1002/hyp.8369
- Schellekens, J., Dutra, E., Martínez-De La Torre, A., Balsamo, G., Van Dijk, A., Sperna Weiland, F., et al. (2017). A global water resources ensemble of hydrological models: The earth2Observe tier-1 dataset. *Earth Syst. Sci. Data* 9, 389–413. doi:10.5194/essd-9-389-2017
- She, D., Xia, J., and Zhang, Y. (2017). Changes in reference evapotranspiration and its driving factors in the middle reaches of Yellow River Basin, China. *Sci. Total Environ.* 607, 1151–1162. doi:10.1016/j.scitotenv.2017.07.007
- Su, Z. (2002). The Surface Energy Balance System (SEBS) for estimation of turbulent heat fluxes. *Hydrology earth Syst. Sci.* 6, 85–100. doi:10.5194/hess-6-85-2002
- Sun, Q., Miao, C., Duan, Q., Ashouri, H., Sorooshian, S., and Hsu, K. L. (2018). A review of global precipitation data sets: Data sources, estimation, and intercomparisons. *Rev. Geophys.* 56, 79–107. doi:10.1002/2017RG000574
- Swanson, R. H. (1994). Significant historical developments in thermal methods for measuring sap flow in trees. *Agric. For. meteorology* 72, 113–132. doi:10.1016/0168-1923(94)90094-9
- Tramontana, G., Jung, M., Schwalm, C. R., Ichii, K., Camps-Valls, G., Ráduly, B., et al. (2016). Predicting carbon dioxide and energy fluxes across global FLUXNET sites with regression algorithms. *Biogeosciences* 13, 4291–4313. doi:10.5194/bg-13-4291-2016
- Trenberth, K. E., Dai, A., Van Der Schrier, G., Jones, P. D., Barichivich, J., Briffa, K. R., et al. (2014). Global warming and changes in drought. *Nat. Clim. Change* 4, 17–22. doi:10.1038/nclimate2067

- Tucker, C. J., Pinzon, J. E., Brown, M. E., Slayback, D. A., Pak, E. W., Mahoney, R., et al. (2005). An extended AVHRR 8-km NDVI dataset compatible with MODIS and SPOT vegetation NDVI data. *Int. J. remote Sens.* 26, 4485–4498. doi:10.1080/01431160500168686
- Vinukollu, R. K., Wood, E. F., Ferguson, C. R., and Fisher, J. B. (2011). Global estimates of evapotranspiration for climate studies using multi-sensor remote sensing data: Evaluation of three process-based approaches. *Remote Sens. Environ.* 115, 801–823. doi:10.1016/j.rse.2010.11.006
- Wang, A., Zeng, X., and Guo, D. (2016). Estimates of global surface hydrology and heat fluxes from the Community Land Model (CLM4.5) with four atmospheric forcing datasets. *J. Hydrometeorol.* 17, 2493–2510. doi:10.1175/JHM-D-16-0041.1
- Wang, K., Dickinson, R. E., Wild, M., and Liang, S. (2010). Evidence for decadal variation in global terrestrial evapotranspiration between 1982 and 2002: 1. Model development. *J. Geophys. Res. Atmos.* 115, 20112–D20210. doi:10.1029/2009JD013671
- Wang, T., Wang, P., Wu, Z., Yu, J., Pozdniakov, S. P., Guan, X., et al. (2022). Modeling revealed the effect of root dynamics on the water adaptability of phreatophytes. *Agric. For. Meteorology* 320, 108959. doi:10.1016/j.agrformet.2022.108959
- Weerasinghe, I., Bastiaansen, W., Mul, M., Jia, L., and Van Griensven, A. (2020). Can we trust remote sensing evapotranspiration products over Africa? *Hydrology Earth Syst. Sci.* 24, 1565–1586. doi:10.5194/hess-24-1565-2020
- Xiao, Z., Liang, S., Wang, J., Chen, P., Yin, X., Zhang, L., et al. (2013). Use of general regression neural networks for generating the GLASS leaf area index product from time-series MODIS surface reflectance. *IEEE Trans. Geoscience Remote Sens.* 52, 209–223. doi:10.1109/TGRS.2013.2237780
- Xie, Z., Yao, Y., Zhang, X., Liang, S., Fisher, J. B., Chen, J., et al. (2022). The global LAnd surface satellite (GLASS) evapotranspiration product version 5.0: Algorithm development and preliminary validation. *J. Hydrology* 610, 127990. doi:10.1016/j.jhydrol.2022.127990
- Xu, B., Li, J., Park, T., Liu, Q., Zeng, Y., Yin, G., et al. (2018). An integrated method for validating long-term leaf area index products using global networks of site-based measurements. *Remote Sens. Environ.* 209, 134–151. doi:10.1016/j.rse.2018.02.049
- Xu, T., Guo, Z., Xia, Y., Ferreira, V. G., Liu, S., Wang, K., et al. (2019). Evaluation of twelve evapotranspiration products from machine learning, remote sensing and land surface models over conterminous United States. *J. Hydrology* 578, 124105. doi:10.1016/j.jhydrol.2019.124105
- Yang, P., Zhang, Y., Xia, J., and Sun, S. (2020). Identification of drought events in the major basins of Central Asia based on a combined climatological deviation index from GRACE measurements. *Atmos. Res.* 244, 105105. doi:10.1016/j.atmosres.2020.105105
- Yao, Y., Liang, S., Cheng, J., Liu, S., Fisher, J. B., Zhang, X., et al. (2013). MODIS-driven estimation of terrestrial latent heat flux in China based on a modified Priestley–Taylor algorithm. *Agric. For. Meteorology* 171, 187–202. doi:10.1016/j.agrformet.2012.11.016
- Yao, Y., Liang, S., Li, X., Hong, Y., Fisher, J. B., Zhang, N., et al. (2014). Bayesian multimodel estimation of global terrestrial latent heat flux from eddy covariance, meteorological, and satellite observations. *J. Geophys. Res. Atmos.* 119, 4521–4545. doi:10.1002/2013JD020864
- Yu, L., Qiu, G. Y., Yan, C., Zhao, W., Zou, Z., Ding, J., et al. (2022). A global terrestrial evapotranspiration product based on the three-temperature model with fewer input parameters and no calibration requirement. *Earth Syst. Sci. Data Discuss.* 14, 3673–3693. doi:10.5194/essd-14-3673-2022
- Yuan, W., Liu, S., Yu, G., Bonnefond, J.-M., Chen, J., Davis, K., et al. (2010). Global estimates of evapotranspiration and gross primary production based on MODIS and global meteorology data. *Remote Sens. Environ.* 114, 1416–1431. doi:10.1016/j.rse.2010.01.022
- Zeng, R., and Cai, X. (2018). Hydrologic observation, model, and theory congruence on evapotranspiration variance: Diagnosis of multiple observations and land surface models. *Water Resour. Res.* 54, 9074–9095. doi:10.1029/2018WR022723
- Zeng, Z., Piao, S., Li, L. Z., Wang, T., Ciais, P., Lian, X., et al. (2018). Impact of Earth greening on the terrestrial water cycle. *J. Clim.* 31, 2633–2650. doi:10.1175/JCLI-D-17-0236.1
- Zeng, Z., Piao, S., Lin, X., Yin, G., Peng, S., Ciais, P., et al. (2012). Global evapotranspiration over the past three decades: Estimation based on the water balance equation combined with empirical models. *Environ. Res. Lett.* 7, 014026. doi:10.1088/1748-9326/7/1/014026
- Zhang, K., Kimball, J. S., Nemani, R. R., Running, S. W., Hong, Y., Gourley, J. J., et al. (2015). Vegetation greening and climate change promote multidecadal rises of global land evapotranspiration. *Sci. Rep.* 5, 15956–15959. doi:10.1038/srep15956
- Zhang, X., Zhang, Y., Ma, N., Kong, D., Tian, J., Shao, X., et al. (2021). Greening-induced increase in evapotranspiration over Eurasia offset by CO₂-induced vegetational stomatal closure. *Environ. Res. Lett.* 16, 124008. doi:10.1088/1748-9326/ac3532
- Zhang, Y., Chiew, F. H., Peña-Arancibia, J., Sun, F., Li, H., and Leuning, R. (2017). Global variation of transpiration and soil evaporation and the role of their major climate drivers. *J. Geophys. Res. Atmos.* 122, 6868–6881. doi:10.1002/2017JD027025
- Zhang, Y., Gentile, P., Luo, X., Lian, X., Liu, Y., Zhou, S., et al. (2022). Increasing sensitivity of dryland vegetation greenness to precipitation due to rising atmospheric CO₂. *Nat. Commun.* 13, 4875–4879. doi:10.1038/s41467-022-32631-3
- Zhang, Y., Peña-Arancibia, J. L., McVicar, T. R., Chiew, F. H., Vaze, J., Liu, C., et al. (2016). Multi-decadal trends in global terrestrial evapotranspiration and its components. *Sci. Rep.* 6, 19124–19212. doi:10.1038/srep19124
- Zheng, H., Miao, C., Li, X., Kong, D., Gou, J., Wu, J., et al. (2022). Effects of vegetation changes and multiple environmental factors on evapotranspiration across China over the past 34 years. *Earth's Future* 10, e2021EF002564. doi:10.1029/2021EF002564
- Zhong, Y., Zhong, M., Mao, Y., and Ji, B. (2020). Evaluation of evapotranspiration for exorheic catchments of China during the GRACE era: From a water balance perspective. *Remote Sens.* 12, 511. doi:10.3390/rs12030511



OPEN ACCESS

EDITED BY

Changchun Huang,
Nanjing Normal University, China

REVIEWED BY

Shaohua Lei,
Nanjing Hydraulic Research Institute,
China
Deyong Sun,
Nanjing University of Information Science
and Technology, China

*CORRESPONDENCE

Wenneng Zhou,
✉ zhouwn@gdut.edu.cn
Ji Yang,
✉ yangji@gdas.ac.cn

RECEIVED 02 November 2022

ACCEPTED 02 May 2023

PUBLISHED 18 May 2023

CITATION

Zhang Y, Jing W, Deng Y, Zhou W, Yang J,
Li Y, Cai Y, Hu Y, Peng X, Lan W, Peng M
and Tang Y (2023), Water quality
parameters retrieval of coastal
mariculture ponds based on UAV
multispectral remote sensing.
Front. Environ. Sci. 11:1079397.
doi: 10.3389/fenvs.2023.1079397

COPYRIGHT

© 2023 Zhang, Jing, Deng, Zhou, Yang, Li,
Cai, Hu, Peng, Lan, Peng and Tang. This is
an open-access article distributed under
the terms of the [Creative Commons
Attribution License \(CC BY\)](https://creativecommons.org/licenses/by/4.0/). The use,
distribution or reproduction in other
forums is permitted, provided the original
author(s) and the copyright owner(s) are
credited and that the original publication
in this journal is cited, in accordance with
accepted academic practice. No use,
distribution or reproduction is permitted
which does not comply with these terms.

Water quality parameters retrieval of coastal mariculture ponds based on UAV multispectral remote sensing

Yumeng Zhang^{1,2}, Wenlong Jing^{2,3}, Yingbin Deng^{2,3},
Wenneng Zhou^{1,3*}, Ji Yang^{2,3*}, Yong Li^{2,3}, Yanpeng Cai¹,
Yiqiang Hu², Xiaoyan Peng⁴, Wenlu Lan⁴, Mengwei Peng⁴ and
Yimin Tang^{2,5}

¹Guangdong Provincial Key Laboratory of Water Quality Improvement and Ecological Restoration for Watersheds, School of Ecology, Environment and Resources, Guangdong University of Technology, Guangzhou, China, ²Guangdong Provincial Key Laboratory of Remote Sensing and Geographical Information System, Guangdong Provincial Geospatial Big Data Engineering Laboratory, Guangzhou Institute of Geography, Guangdong Academy of Sciences, Guangzhou, China, ³Southern Marine Science and Engineering Guangdong Laboratory (Guangzhou), Guangzhou, China, ⁴Marine Environmental Monitoring Center of Beihai, Bureau of Environmental Protection of Guangxi, Beihai, China, ⁵School of Geographical Sciences and Remote Sensing, Guangzhou University, Guangzhou, China

The rapid expansion of aquaculture in coastal areas is typically associated with ecological negligence and low water quality owing to the economic exploitation of these areas. However, evaluation of these water bodies tends to be laborious, time-consuming, and costly. Therefore, to overcome the limitations of field surveys, in this study, we evaluated the water quality of the cultured water in the Beibu Gulf of Guangxi, obtained spectral reflectance by unmanned aerial vehicle with multispectral sensors, and constructed inverse models of 11 water quality parameters, namely, ammonia nitrogen ($\text{NH}_3\text{-N}$), chemical oxygen demand (COD), active phosphate (PO_4^{3-}), dissolved oxygen, nitrate nitrogen ($\text{NO}_3\text{-N}$), nitrite nitrogen ($\text{NO}_2\text{-N}$), inorganic nitrogen, total nitrogen, total phosphorus, suspended solids (SS), and chlorophyll a (chl-a), based on the partial least squares method to invert the water quality distribution of regional aquaculture. Furthermore, we compared the retrieval accuracy of different water quality parameters. The following results were obtained: 1) the constructed model's results showed that the retrieval models for COD, $\text{NO}_3\text{-N}$, SS, and chl-a had better accuracy compared with those of other parameters; 2) application of the model to the validation set data yielded a correlation coefficient of 0.93 between the measured and predicted SS values, with a mean absolute error of prediction of 4.65 mg L^{-1} ; this parameter constructed the best prediction model. According to the validation set results, the correlation coefficients of chl-a, COD and $\text{NO}_3\text{-N}$ are all greater than 0.8, which had better performance effects compared with the remaining models, which are 0.87, 0.86, and 0.81 respectively. This study provides a reference for remote sensing monitoring of water quality in mariculture in cloudy and rainy areas.

KEYWORDS

UAV multispectral image, mariculture, water quality retrieval, Qinzhou Bay, partial least squares

1 Introduction

Total global production from fisheries and aquaculture reached a record 214 million tons in 2020, including 178 million tons of aquatic animals and 36 million tons of algae. This increase in production was mostly due to growth in the aquaculture industry, with the greatest increase in Asia, particularly China (FAO, 2022). Since the late 1980s, the rapid expansion of aquaculture in coastal areas has made China the world's largest aquaculture producer (Ren et al., 2019). Economic interests drive the rapid development of mariculture in these areas, often leading to high inputs (e.g., in sea farming, large amounts of bait are input) to achieve high income while neglecting the ecological balance of aquaculture waters and the protection of the aquatic environment, which in turn has impacted the regional ecological environment (Ren et al., 2019). The deterioration of the ecological environment will not only affect the yield of products but also seriously threaten the quality and yield of products and even the income of farmers (Carter et al., 2017; Yuan et al., 2021). Therefore, the monitoring of mariculture water quality is particularly important, not only to ensure the quality of seafood but also to generally protect the environment.

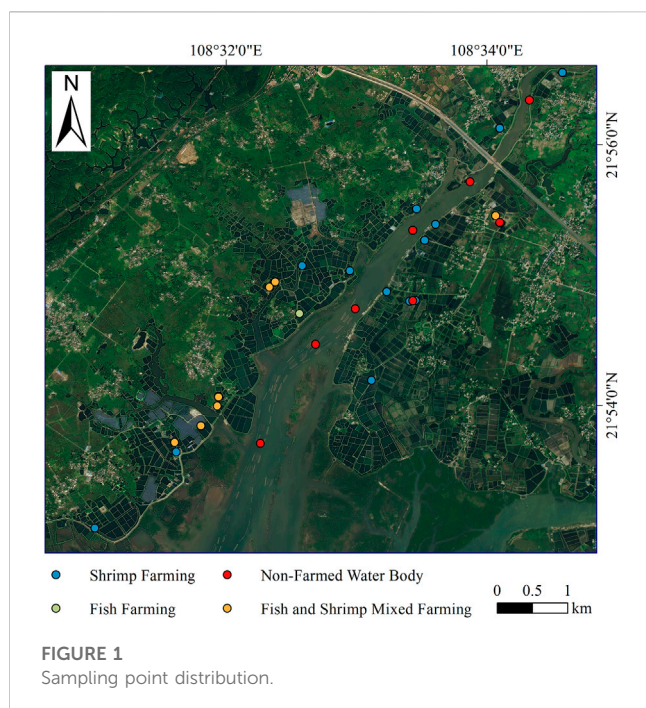
The impact of mariculture on the environment is mainly caused by two aspects, firstly, the bait invested in the mariculture process, and secondly, the metabolites produced during the growth of seafood. In the mariculture process, a large amount of bait is provided, but only a portion of this bait is effectively used, and the rest is discharged into the water column in the form of residual bait and excreta, including feces, forming endogenous pollutants in the water column (Li et al., 2021). Discharging pollutants into the ocean leads to increased nutrient levels in the marine ecosystem, posing a threat to the surrounding ecological environment (Wang et al., 2020; Yuan et al., 2020; Liu et al., 2021).

The traditional water quality monitoring method uses field sampling for laboratory analysis to obtain water quality information or automatic *in-situ* measurements. Although the accuracy is high, the increased labor cost, sampling time consumption, and other multi-factor constraints pose certain limitations (Liang et al., 2021; Liu et al., 2021). In contrast, remote sensing technology offers an effective approach for water quality monitoring owing to advantages such as low cost, high speed, effective synchronization, and large area of observation (Bean et al., 2017; Sagan et al., 2020). Remote water quality monitoring refers to the establishment of water quality retrieval models by studying the relationship between the spectral reflection characteristics of water bodies and each water quality parameter by combining the retrieval models with remote monitoring image data to inverse the water quality condition of the entire region, which is suitable for the regional monitoring of water bodies (Liang et al., 2021). Moreover, with the development of satellite remote sensing technology, water quality remote sensing technology is becoming increasingly advanced, and researchers worldwide have achieved great results regarding the retrieval of water quality parameters. For optically water quality parameters such as CDOM and chl-a, there have been very mature studies, while for non-optically water quality parameters such as TN and TP, machine learning methods have been used for estimate in recent years. (Lobo et al.,

2015; Peterson et al., 2020; Liang et al., 2021; Zhao et al., 2021; Guo et al., 2020; Chen et al., 2021). However, the low spatial resolution of satellite remote sensing imagery has limited the ability to obtain the spatial distribution of water quality in small and micro waters, such as aquaculture ponds. As noted by Liu et al. (2019), high-resolution images are required to overcome this limitation. The novelty of this study lies in its focus on remote sensing of water color in small water bodies, which has received relatively limited attention. Moreover, remote sensing of water color in small water bodies presents challenges, including the low signal level due to limited water volume and the potential influence of bottom reflectance. Thus, our study aims to address these challenges and provide a comprehensive analysis of water quality parameters using remote sensing in small water bodies (Zehra et al., 2019). In addition, optical satellite images are susceptible to different weather conditions (e.g., clouds and rain), and the image acquisition period is long, making it difficult to obtain efficient images over the water bodies (Rui et al., 2021). So that we have to find another safe source to supplement, while, unmanned aerial vehicles (UAVs) are highly mobile, have low operating costs, result in high image resolution, and require short operation cycles (Liu et al., 2021), making them suitable for water quality monitoring through remote sensing.

Recently, UAV remote sensing technology has been widely applied to aerial land surveys, agriculture and forestry plant protection, atmospheric detection, disaster mitigation, and national defense security (Rui et al., 2021; Liu, 2022). Some researchers have studied the application of UAV remote sensing technology in water quality monitoring. Cheng et al. (2020) demonstrated for the first time the use of UAVs to quantitatively map the Chl-a distribution of surface water in coastal waters from low altitude. Liu et al. (2019) constructed an inverse model based on UAV multispectral images for three water quality parameters, namely, total phosphorus (TP), suspended solids (SS), and turbidity. McEliece et al. (2020) used UAV multispectral imagery to inverse chlorophyll-a (chl-a) and turbidity in nearshore water bodies. Moreover, Matsui et al. (2021) used UAV remote sensing imagery combined with neural networks to compensate for the lack of resolution of satellite remote sensing imagery to achieve high-resolution monitoring of suspended sediment concentrations. Chen et al. (2021) have made some achievements in the study of UAV inversion of non-optically active water quality parameters, they found GA_XGBoost inversion model has high accuracy and strong generalization on inverse Chl-a, TP, TN and $\text{NH}_3\text{-N}$. However, research on water quality monitoring by UAV remote sensing is still in the exploratory stage, and thus, further investigation is required to improve our understanding.

In the present study, to evaluate water bodies in the Beibu Gulf, we first obtained the spectral reflectance by UAV with multispectral sensors; then, we constructed retrieval models for 11 water quality parameters, namely, ammonia nitrogen ($\text{NH}_3\text{-N}$), chemical oxygen demand (COD), active phosphate (PO_4^{3-}), dissolved oxygen (DO), nitrate nitrogen ($\text{NO}_3\text{-N}$), nitrite nitrogen ($\text{NO}_2\text{-N}$), inorganic nitrogen (DIN), TN, TP, SS, and chl-a, based on a partial least squares method. Finally, we compared the retrieval accuracy of different water quality parameters. This study will serve as a reference for future studies on monitoring and investigating aquaculture water quality in offshore areas using UAVs.



2 Data and methodology

2.1 Study area and sampling locations

The aquaculture industry in China is widely distributed in coastal areas. Low-lying coastal areas are the most favorable areas for aquaculture (Primavera, 2006). The present study considered the Qinzhou Bay area located in the northern part of the Beibu Gulf of Guangxi, China. Qinzhou Bay consists of inner and outer bays. The inner bay, which lies at the confluence of the Maoling River, Qin River, and Dalan River, is a typical estuarine semi-enclosed tropical bay with a well-developed aquaculture industry and is an essential artificial culture base in China (Lao et al., 2021). The study area is located in an estuary section of the Beibu Gulf, Guangxi and surrounding area, with a total area of approximately 30.3 km². The culture types were mainly South American white shrimp, tilapia, fork-tailed catfish, and fish–shrimp mixed culture. UAV multispectral image acquisition and water quality sampling of the study area were conducted from April 8 to 10, 2021, with a total of 33 sampling points, including 10 sampling points for the fish–shrimp mixed culture, 2 sampling points for fishponds, 13 sampling points for shrimp ponds, and 8 sampling points for non-cultured water bodies, and a density of approximately 1.09 km²; the latitude and longitude were recorded separately during sampling. The collected water samples reflected different types of aquaculture types, and the distribution of sampling points is shown in Figure 1.

A water quality analyzer (AMT-YB101, Shenzhen Yunchuan IOT Technology Co., Shenzhen, China) was used to determine the water temperature and pH on site; moreover, 500 mL water samples were collected and placed in a sealed container to transport back to the laboratory. Eleven parameters, namely, NH₃-N, COD, DO, NO₃-N, NO₂-N, DIN, TN, TP, SS, and chl-a, were evaluated.

Sampling points were located at 0.5 m below the water surface; all samples were collected, pretreated, stored and detection in strict accordance with the Marine Monitoring Code (GB 17378.4-2007, China).

2.2 UAV multispectral data

In this study, a DJI Elf 4 multispectral version UAV (SZ DJI Technology Co., Shenzhen, China) carrying an integrated multispectral camera with one visible light camera and five multispectral cameras (blue light, green light, red light, red edge, and near-infrared), that were responsible for visible light imaging and multispectral imaging, respectively. Each visible and multispectral camera had 2 megapixels and a ground resolution of 5 cm when flying at 100 m. The flight time of the drone was from 9:00 to 16:00 on April 8 to 10, 2021. The flight height was set to 100 m, and a total of 45 sorties were flown; a single flight took approximately 25 min in an area of approximately 0.6 km².

The acquired single images were processed using Pix4D™ (V4.4.12) software for multispectral images taken at nearshore locations. We also completed the mosaicking of each band and the radiometric correction and calibration of them using Pix4Dmapper. To analyze and process these images, we performed four steps using Pix4Dmapper software. First, we preprocessed the original images with this software and generated an interior orientation element file (.cal). This file contained parameters such as focal length, principal point coordinates, radial distortion coefficients and tangential distortion coefficients of the camera. These parameters corrected camera distortion of images in each band. Next, we recorded the attitude angles (pitch angle, roll angle and yaw angle) during flight with the inertial measurement unit (IMU) that came with DJI. We used these angles as one of the parameters in the exterior orientation element file (.ori). These parameters corrected flight attitude of images in each band. Then, we performed feature point matching and three-dimensional reconstruction on the original images with this software and generated a digital elevation model (DEM). This model reflected the elevation distribution of the ground. It corrected terrain relief of images in each band. Finally, we calibrated ground control point (GCP) and set coordinate system on the original images with this software and generated a projection coordinate system file (*.prj). This file contained information such as projection method, ellipsoid parameters and datum parameters used by the image. It transformed images in each band from spatial position to geographic coordinates or projection coordinates. Using image stitching technology based on junction recognition, we corrected the image according to changes in camera angle and distance from the ground and finally read it into ENVI (V5.3) software. The pixel data of each band corresponding to the sampling point was used as the independent variable (Table 1).

2.3 Retrieval method

Water quality remote sensing retrieval methods are generally divided into empirical models based on statistics, machine learning models, and physical semi-analytical models based on the

TABLE 1 Pixel data of each band corresponding to the sampling point.

Band	Band name	Center wavelength/nm	Wavelength/nm
B1	Blue	450	32
B2	Green	560	32
B3	Red	650	32
B4	Red Edge	730	32
B5	NIR	840	52

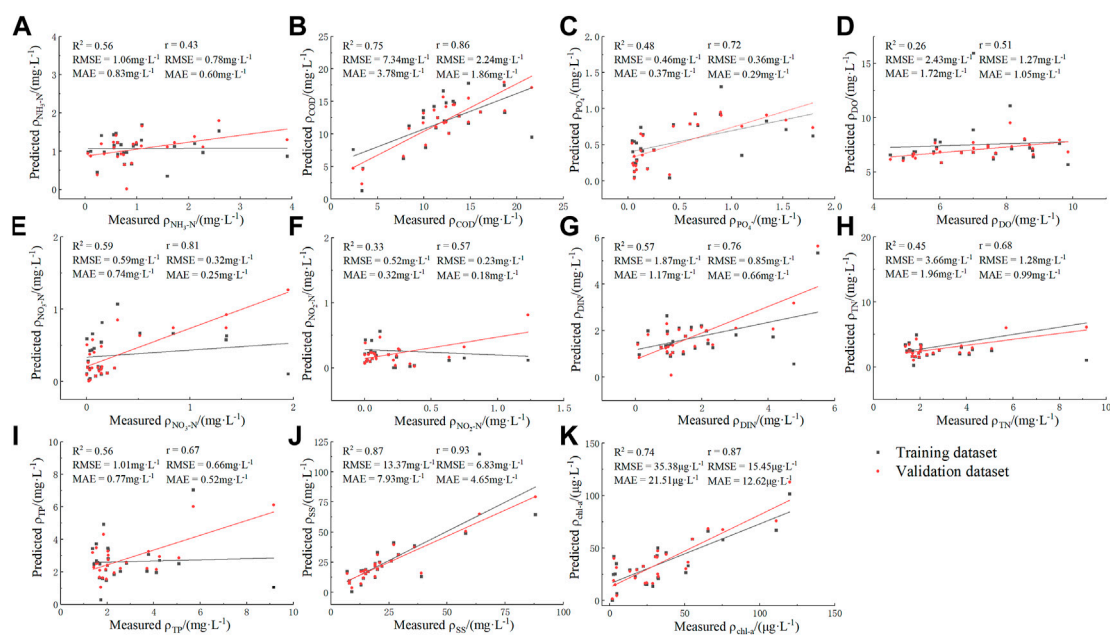


FIGURE 2

Scatterplots of partial least squares inversion model accuracy evaluation: (A) NH₃-N, (B) COD, (C) PO₄³⁻, (D) DO, (E) NO₃-N, (F) NO₂-N, (G) DIN, (H) TN, (I) TP, (J) SS, (K) chl-a.

interaction of light and water bodies. Common water quality retrieval methods include methods such as multiple linear regression, partial least squares regression (PLSR), and support vector machine regression. Among them, PLSR combines multiple linear regression analysis, principal component analysis, and typical correlation analysis to establish a relationship with the dependent variable by extracting several mutually independent principal components from the set of independent variables (Liu et al., 2011), thus minimizing the impact of potential multicollinearity problems.

PLSR requires a strong correlation between the eigenvectors selected from the independent and dependent variables. Theoretically, multiple variables can be used to model the prediction of components, but in practice, the standard prediction model uses only a few variables. The independent and dependent variables are initially subjected to Pearson correlation analysis to screen out the appropriate independent variables for modeling and then further cross checked by the leave-one-out method. Furthermore, the best modeling factors are retained by the

leave-one-out experiment to eliminate unnecessary variables. The details of the modeling process of PLSR were previously described (Wang, 2006). In the present study, the spectral reflectance corresponding to five bands was set as the independent variable, and the feasibility of the water quality retrieval model constructed by UAV multispectral images applied to the monitoring of key water quality parameters in aquaculture ponds was discussed.

After the UAV multispectral images were preprocessed, the reflectance value of each band of the multispectral image data corresponding to the location of the sampling point was extracted using ENVI software, and the spectral reflectance of the single band and band combination pixel was correlated with the measured concentration of each parameter. In summary, analysis was performed; the band with the best correlation was selected as the sensitive band, the measured concentration of each parameter and sensitive band were taken as dependent and independent variables, respectively, and the PLSR model was constructed and verified via the verification dataset. Finally, the accuracy and validity of the model were evaluated according to the verification results.

TABLE 2 Results of the 11 measured parameters per collection site.

Parameter (mg·L ⁻¹)	Fish and shrimp mixed farming				Shrimp farming				Fish farming				Non-farmed water body			
	Max	Min	Mean	Std.	Max	Min	Mean	Std.	Max	Min	Mean	Std.	Max	Min	Mean	Std.
NH ₃ -N	5.09	0.06	1.41	1.59	2.73	0.37	1.29	0.85	1.59	0.32	0.95	0.64	0.93	0.24	0.54	0.23
COD	18.70	9.35	12.84	2.71	18.65	7.81	11.42	3.06	21.60	12.10	16.85	4.75	13.15	1.80	5.11	4.22
PO ₄ ⁻	1.34	0.04	0.45	0.41	1.79	0.06	0.59	0.55	0.08	0.08	0.08	0.03	0.89	0.04	0.18	0.28
DO	8.81	4.90	7.20	1.44	9.85	4.90	6.81	1.34	8.16	7.00	7.58	0.58	9.60	4.51	6.17	1.41
NO ₃ -N	0.27	0.01	0.10	0.08	0.30	0.01	0.09	0.09	1.95	0.52	1.23	0.72	1.36	0.01	0.79	0.50
NO ₂ -N	0.64	0.01	0.18	0.19	0.75	0.01	0.18	0.21	1.23	0.12	0.67	0.56	0.09	0.01	0.06	0.03
DIN	5.49	0.07	1.69	1.66	3.11	0.38	1.55	0.87	4.77	0.95	2.86	1.91	2.14	0.91	1.39	0.45
TN	5.70	1.11	2.52	1.48	4.26	0.98	2.51	1.18	9.15	1.85	5.50	3.65	2.83	1.07	1.92	0.58
TP	3.73	0.18	1.11	1.18	3.07	0.27	1.01	0.82	0.56	0.45	0.51	0.06	1.23	0.07	0.30	0.37
SS	64.00	13.00	25.10	14.78	36.00	7.00	19.00	6.67	88.00	58.00	73.00	15.00	29.00	6.00	12.25	7.07
chl-a (μg·L ⁻¹)	65.50	2.80	26.30	18.46	75.40	2.60	27.00	19.49	120.00	111.00	115.50	4.50	52.30	1.50	17.51	19.53

Note: Standard deviation (Std.).

TABLE 3 Pearson correlation analysis of the 11 determined parameters with the single-band reflectance.

Band	NH ₃ -N	COD	PO ⁴⁻	DO	NO ₃ -N	NO ₂ -N	DIN	TN	TP	SS	Chl-a
B1	0.591**	−0.115	−0.051	−0.027	0.226	0.144	0.638**	0.397*	0.224	0.381	0.099
B2	0.380	−0.330	−0.311	−0.025	0.475*	0.228	0.562**	0.361	−0.053	0.329	0.022
B3	0.598**	0.239	−0.003	0.064	0.225	0.321	0.681**	0.567**	0.287	0.721**	0.479*
B4	0.458*	0.234	−0.069	0.158	0.289	0.360	0.589**	0.519**	0.250	0.761**	0.525**
B5	0.338	−0.391*	−0.261	−0.059	0.445*	0.189	0.505**	0.305	−0.041	0.218	−0.071

**At the 0.01 level (two-tailed), the correlation is significant.

*At the 0.05 level (two-tailed), the correlation is significant.

TABLE 4 Correlation analysis of each single-band reflectance.

Band	B1	B2	B3	B4	B5
B1	1	0.908**	0.878**	0.837**	0.877**
B2	0.908**	1	0.974**	0.778**	0.741**
B3	0.878**	0.974**	1	0.718**	0.666**
B4	0.837**	0.778**	0.718**	1	0.959**
B5	0.877**	0.741**	0.666**	0.959**	1

**At the 0.01 level (two-tailed), the correlation is significant.

*At the 0.05 level (two-tailed), the correlation is significant.

2.4 Model evaluation

The accuracy evaluation indicators of the PLSR model are the root mean square error (RMSE), mean absolute error (MAE), and coefficient of determination (R^2) of the model interpretation evaluation index. The smaller the values of RMSE and MAE, the better the accuracy of the prediction model at describing the experimental data, and the closer the R^2 value is to 1, the better the model fit. Additionally, it is generally considered that when the model fit exceeds 0.8, the superiority of the model is relatively high. The evaluation indicators were calculated as follows:

$$RMSE = \sqrt{\frac{1}{N} \sum_{i=1}^N (y_i - \hat{y}_i)^2}, \quad (1)$$

$$MAE = \frac{1}{N} \sum_{i=1}^N |y_i - \hat{y}_i|, \quad (2)$$

$$R^2 = \frac{\sum_{i=1}^N (\hat{y}_i - \bar{y})^2}{\sum_{i=1}^N (y_i - \bar{y})^2}, \quad (3)$$

where i is the i -th sample, y_i and \hat{y}_i denote the measured and predicted values, respectively, and N is the number of samples.

3 Results

3.1 Model construction

Collected samples were mostly shrimp and fish–shrimp mixed culture water bodies. The results of the 11 determined parameters

(Table 2) indicate that the concentration of each water quality parameter in the water bodies where culture activities were performed was significantly higher than that in the water bodies where non-culture activities were performed, and the water quality of the rivers was significantly better than that of the farming areas on both banks.

Combined with the reflectivity of the five bands of the UAV multispectral images from April 8 to 10, 2021 and the concentration of each parameter, the Pearson correlation analysis was performed (Table 3). In general, we observed a positive correlation between the reflectivity of every single waveband of the UAV and concentration of each parameter, and the correlation coefficient r ranged between −0.391 and 0.761. Among the 11 parameters, the single-band correlation coefficient r value of SS concentration and B4 and B3 bands ranked first and second in the calculation results at 0.761 and 0.721, respectively. A comprehensive analysis comparing the correlation calculation results between other water quality parameters and reflectance of the bands showed that the concentration values of seven parameters, namely, NH₃-N, COD, NO₃-N, DIN, TN, SS, and chl-a, were significantly correlated with some single-band reflectance; in contrast, the concentration values of four parameters, namely, PO⁴⁻, DO, NO₂-N, and TP, were not significantly correlated with all single-band reflectance. Further correlation analysis of each single-band reflectance showed that the correlation coefficients among the five bands were high, ranging from 0.666 to 0.908, and it can be assumed that there is multicollinearity among the five bands (Table 4). Furthermore, we found that compared to the accuracy of sensitive band modeling, that of all-band modeling was better. Therefore, this study proposes the use five bands, B1, B2, B3, B4, and B5, as independent variables and the concentration values of each parameter as dependent variables to establish the PLSR concentration retrieval model.

A total of 33 water quality samples were collected from April 8 to 10, 2021, and because some areas were not covered by the UAV images, 26 sample points were finally used for inverse modeling, which was cross-validated by the leave-one-out method. A standardized partial least squares regression model was finally constructed (Table 5).

3.2 Model validation

3.2.1 Modeling accuracy

The PLSR concentration retrieval models were constructed for each parameter and applied to the spectral reflectance of the

TABLE 5 Established standardized partial least squared regression model.

Parameter	Model
NH ₃ -N	$y = 0.73 \times B1 - 0.71 \times B2 + 0.29 \times B3 - 1.41 \times B4 + 1.76 \times B5$
COD	$y = 2.55 \times B1 - 3.27 \times B2 - 3.96 \times B3 + 7.29 \times B4 - 3.01 \times B5$
PO ₄ ⁻	$y = 0.89 \times B1 - 1.42 \times B2 + 0.46 \times B3 + 0.33 \times B4 - 0.36 \times B5$
DO	$y = 1.60 \times B1 + 0.73 \times B2 - 2.27 \times B3 + 3.59 \times B4 - 3.79 \times B5$
NO ₃ -N	$y = -1.30 \times B1 + 0.92 \times B2 + 0.25 \times B3 - 0.63 \times B4 + 1.00 \times B5$
NO ₂ -N	$y = -0.58 \times B1 + 0.12 \times B2 + 0.21 \times B3 - 0.16 \times B4 + 0.52 \times B5$
DIN	$y = -1.14 \times B1 + 0.31 \times B2 + 0.75 \times B3 - 2.20 \times B4 + 3.29 \times B5$
TN	$y = -2.99 \times B1 + 0.23 \times B2 + 1.48 \times B3 - 2.42 \times B4 + 4.81 \times B5$
TP	$y = 2.45 \times B1 - 2.17 \times B2 - 0.08 \times B3 + 1.71 \times B4 - 1.84 \times B5$
SS	$y = -18.81 \times B1 + 13.97 \times B2 - 13.86 \times B3 + 17.64 \times B4 + 12.31 \times B5$
chl-a	$y = -24.37 \times B1 + 5.08 \times B2 - 19.38 \times B3 + 38.88 \times B4 + 8.17 \times B5$

image elements in each wavelength band; further, the predicted values of each parameter were calculated, and the optimum concentration retrieval model for each parameter was obtained by cross-validation using the leave-one-out method (Figures 2, 3). The RMSE, MAE, and R^2 were calculated to evaluate the model effectiveness. Among the PLSR retrieval models constructed, the best fit model was the SS retrieval model, with $R^2 = 0.87$, followed by the COD retrieval model, with $R^2 = 0.75$; and chl-a retrieval model, with $R^2 = 0.74$. The R^2 values of the four retrieval models, NH₃-N, NO₃-N, DIN, and TP, were all greater than those of other water quality parameters that were modeled with R^2 between 0.26 and 0.48 (Table 6).

3.2.2 Validation accuracy

The constructed PLSR concentration retrieval model was applied to the spectral reflectance of each image pixel in all sampling points to validate the model (Figures 2, 3). The predicted values of each parameter concentration were calculated and compared with the true values. The accuracy of the models was evaluated by calculating the RMSE, MAE, and Pearson's correlation coefficient r between the predicted and true values. The most considerable correlation among the retrieval results of all models was the prediction result of the SS retrieval model, with a correlation coefficient $r = 0.93$, followed by that of chl-a, with a correlation coefficient $r = 0.87$. A comprehensive comparative analysis of R^2 and r for all parameter retrieval models showed that the models for the four parameters COD, NO₃-N, SS, and chl-a had better retrieval results than those for the remaining seven parameters. RMSE and MAE of the inverse model with four parameters, COD, NO₃-N, SS, and chl-a, can

only be used as a reference because the concentration criteria differ between parameters. The RMSE of the four models was 2.24, 0.32, 6.83, and 15.45 $\mu\text{g L}^{-1}$, respectively, and the MAE was 1.86, 0.25, 4.65, and 12.62 $\mu\text{g L}^{-1}$, respectively. In summary, the PLSR retrieval models of COD, NO₃-N, SS, and chl-a constructed in this study can be used to predict the concentrations of these four parameters in culture ponds.

3.3 Multi-optical image retrieval results in water quality parameters

First, the data for water bodies in the study area were extracted from the multispectral images by the normalized difference water index (McFeeters, 1996), and the established PLSR model was applied to the acquired multispectral images to estimate each image element. The concentration of water quality parameters corresponding to each image element in the area was calculated. Finally, the retrieval results were displayed to visualize the spatial distribution pattern of the concentrations of COD, NO₃-N, SS, and chl-a in the study area (Figure 4). This visualization aids in better understanding the spatial distribution of each parameter and provides useful information for water resource management and pollution control.

Inverse results of COD showed that the lowest and highest COD concentrations of water bodies in the study area were 0.69 and 31.76 mg L^{-1} , respectively, with the average value at 10.14 mg L^{-1} , as shown in Figure 4. Generally, culture pond COD concentrations ranged from approximately 2.41–31.76 mg L^{-1} , in contrast to river areas where the concentrations were significantly lower, ranging between 0.69 and 12.48 mg L^{-1} . From the retrieval results of NO₃-N, the average concentration of the entire study area was 0.32 mg L^{-1} , with a few culture ponds with high NO₃-N concentrations reaching approximately 2 mg L^{-1} . The NO₃-N concentration in the river area was higher than that in most of the culture ponds, and that in the upstream water was approximately 1 mg L^{-1} . The retrieval results were the same as those reflected by the sampling results in this study. SS retrieval showed that the average concentration in the study area was 15.93 mg L^{-1} , and the SS concentration in a few ponds was as high as 180 mg L^{-1} . From the retrieval result graph (Figure 4C), most of the blue-greenish areas in the graph were cultured ponds, which implies that the SS concentration in cultured pond water bodies was low. The retrieval results of chl-a concentration showed that the range of chl-a concentration in the water bodies in the study area was wide, ranging from 0 to 289 $\mu\text{g L}^{-1}$ with a mean value of 24.66 $\mu\text{g L}^{-1}$, which is an overall low concentration level, except for a few ponds with unusually high chl-a concentration.

As shown in the retrieval results, the concentrations of COD, SS, and chl-a in the study area were significantly higher than those in the river area, possibly due to the impact of nutrients, organic pollutants, microorganisms, and anthropogenic activities in the surrounding area of the water body during the mariculture process degrading the water quality in the aquaculture area. In contrast, the distribution of NO₃-N concentrations showed that the concentration in the river area was higher than that in the aquaculture water body. However, the concentration in the upstream water was significantly higher than that in the downstream water, which is likely influenced by the upstream domestic sewage discharge; however, further verification is

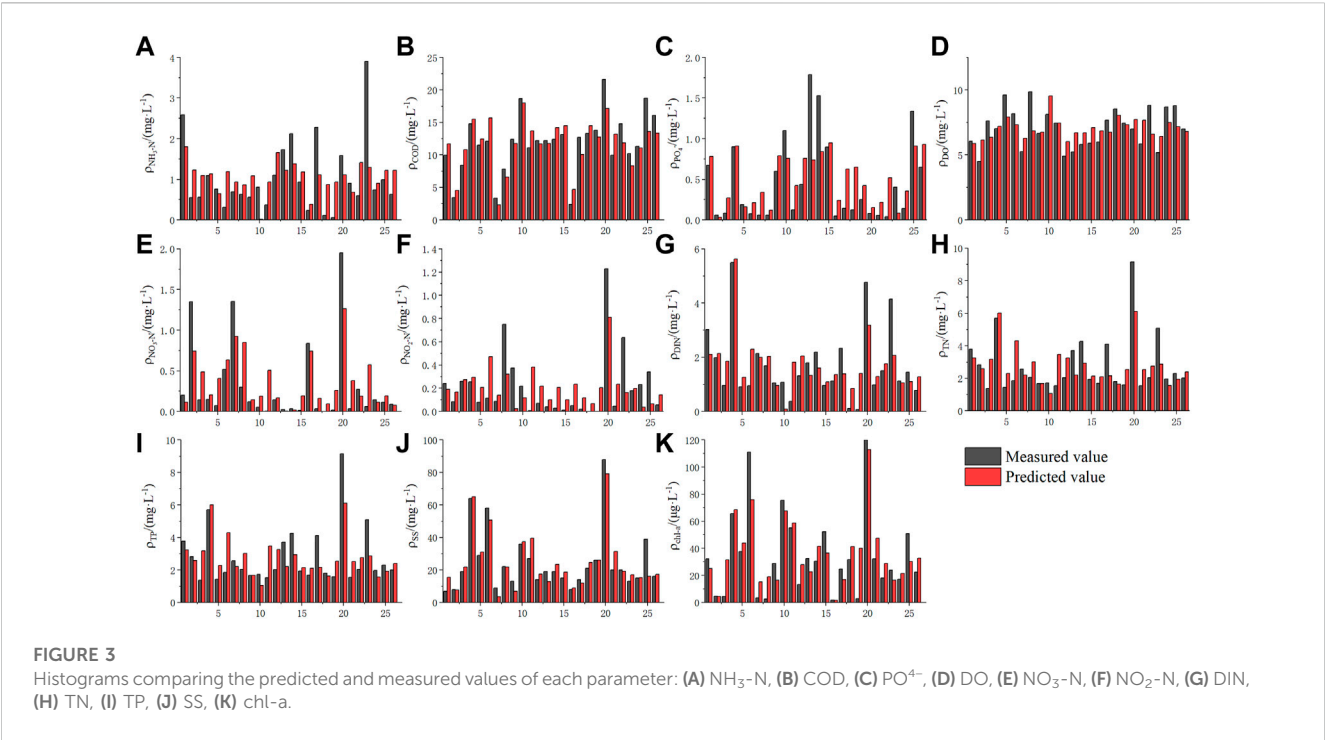


TABLE 6 Statistical determination of the effectiveness of the model.

Parameter	Training dataset			Validation dataset		
	R ²	RMSE	MAE	r	RMSE	MAE
NH ₃ -N	0.56	1.06	0.83	0.43	0.78	0.60
COD	0.75	7.34	3.78	0.86	2.24	1.86
PO ₄ ³⁻	0.48	0.46	0.37	0.72	0.36	0.29
DO	0.26	2.43	1.72	0.51	1.27	1.05
NO ₃ ⁻	0.59	0.74	0.45	0.81	0.32	0.25
NO ₂ ⁻	0.33	0.52	0.32	0.57	0.23	0.18
DIN	0.57	1.87	1.17	0.76	0.85	0.66
TN	0.45	3.66	1.96	0.68	1.28	0.99
TP	0.56	1.01	0.77	0.67	0.66	0.52
SS	0.87	13.37	7.93	0.93	6.83	4.65
chl-a	0.74	35.38	21.51	0.87	15.45	12.62

required. Comparing the graphs of the retrieval results of SS and chl-a, the concentration distributions for the two parameters were found to be similar. Moreover, according to the Pearson correlation analysis, the correlation coefficient *r* of SS and chl-a was 0.84, indicating a high correlation, which is consistent with the final retrieval results of this study. Overall, the concentration levels of all parameters in all culture ponds were relatively uniform, and some ponds showed poor water quality. The inverse results of this study can accurately identify the culture ponds with poor water quality, provide a solid basis for scientific culture, and further provide relevant measures to control water quality.

3.4 Differences in water quality between different types of water bodies

UAV aerial photography covers a large scale, and the study area contains different types of water bodies. To explore the differences in water quality retrieval results between different water bodies, two areas were selected for preliminary quantitative analysis for each of the four types of water bodies: fish and shrimp, fish culture, shrimp culture, and non-culture water bodies. Some of the details are shown in Table 7.

The two ponds with mixed fish and shrimp appeared grayish-green from the UAV red-green-blue (RGB) images on the left pond and darker green on the right pond, with significant differences in COD and NO₃-N concentrations; however, no significant differences were observed between SS and chl-a concentrations. The fish culture from the UAV RGB image of the left pond appeared grayish-green, whereas the right pond appeared dark curry brown, which indicates that the retrieval results of the four water quality parameters of the two ponds were not very different, and the water quality of the two ponds is thus similar. Two ponds for shrimp culture appeared dark blue on the left pond and grayish-curry on the right pond from the RGB images of the UAV. The concentrations of COD, SS, and chl-a in the two ponds were not much different. Moreover, the NO₃-N concentration in the left pond was significantly lower than that in the right pond, and the inverse concentration of each parameter on the north bank of the right pond was higher than that on the south bank from the inverse results of the four parameters. The non-culture water bodies of the two areas are the water bodies around the near-shore mangroves and the river water bodies. The water around the mangroves in the UAV RGB image appeared yellow-green. Results of all four parameters showed that the concentration of the water body in the narrow area of the

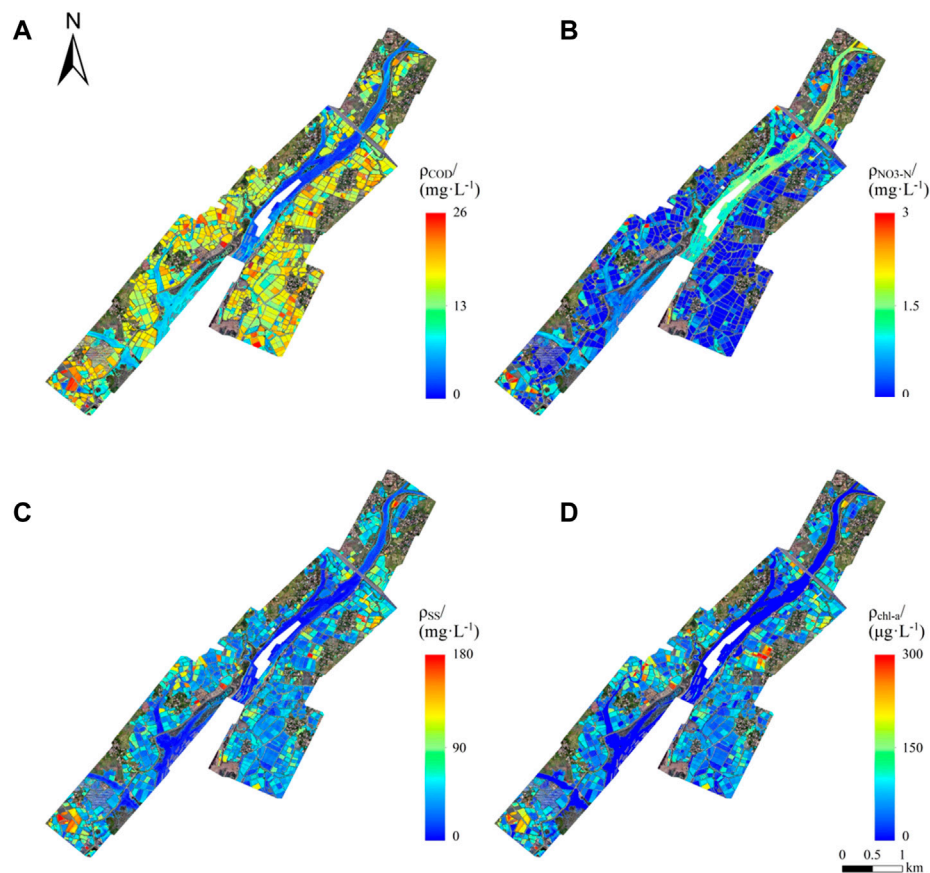


FIGURE 4

Retrieval results visualizing the spatial distribution pattern of the concentrations of COD (A), NO₃-N (B), SS (C), and chl-a (D) in the study area. The legend indicates the heat map scale corresponding to decreasing concentrations. The reddish-yellow-green areas in (A) are generally culture ponds. NH₃-N: ammonia nitrogen, COD: chemical oxygen demand, PO₄³⁻: active phosphate, DO: dissolved oxygen, NO₃-N: nitrate nitrogen, NO₂-N: nitrite nitrogen, DIN: inorganic nitrogen, TN: total nitrogen, TP: total phosphorus, SS: suspended solids, and chl-a: chlorophyll-a.

river was higher than that in the open water, with a higher concentration near the shore. The river water bodies appeared greenish-yellow from the UAV RGB images, and the concentrations of COD, NO₃-N, SS, and chl-a were low.

















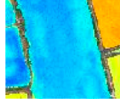
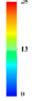


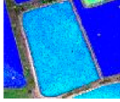




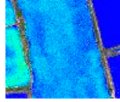








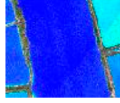
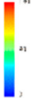







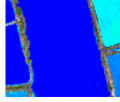

Comprehensive comparison of the different types of water bodies intercepted and removed revealed no direct link between the color of the UAV RGB images of water bodies and their retrieval results. Therefore, the water quality cannot be determined merely by the color of the true color images. In this study, the concentrations of COD, NO₃-N, SS, and chl-a from PLSR retrieval models can indicate the water quality of the ponds more intuitively, as the concentration levels in individual farming ponds did not vary significantly. COD indicates the amount of oxygen required to oxidize 1 L of organic matter in sewage by potassium dichromate under strongly acidic conditions, which can roughly represent the amount of organic matter in the sewage, and NO₃-N and chl-a reflect the nutrient status of the water body; the concentrations of these three parameters are related to the bait fed during aquaculture and metabolites produced during animal growth. SS is a physical indicator of the solids suspended in water, including inorganic and organic matter insoluble in water, such as mud, sand, clay,

and microorganisms. Hence, the concentration of SS is generally high in culture ponds that are less fluid and closed. For the river with better fluidity and unconfined water bodies, the water quality condition is significantly better than that of the aquaculture water bodies, and the concentration of each parameter decreases with the increase in offshore distance; poorer water quality near the shore may be influenced by the effect of poor hydrodynamics and human life.

4 Discussion

In this study, we showed that it is feasible to use UAV multispectral images for retrieval studies of COD and SS in water bodies. After correlation and significance analyses between 11 water quality parameters and spectral reflectance of the cultured water bodies, PLSR was performed by selecting the reflectance of all bands as independent variables. The results obtained from the PLSR models suggest that they hold great potential for accurately estimating water quality parameters from remote sensing data, contributing to our understanding of aquatic ecosystems and their environmental status. We found that among all the obtained models, the accuracy of the

TABLE 7 Unmanned aerial vehicle (UAV) aerial photography of different water bodies in the study area.

	Fish and shrimp mixed farming		Shrimp farming		Fish farming		Non-farmed water body		
RGB Image									
COD									
NO ₃ -N									
SS									
Chl-a									

The first row represents UAV RGB, image, followed by COD, NO₃-N, SS, and chl-a retrieval results. Every two columns represent the same type of water bodies; the rightmost scale bar from blue to red indicates increasing concentration.

retrieval models of COD and SS in the final obtained models were high. The models of other water quality parameters were challenging to meet the estimation requirements.

The inverse results of COD, NO₃-N, SS, and chl-a were obtained by applying the constructed partial least squares regression model to the UAV multispectral images, which showed that the water quality of the farmed water bodies in the study area was poor, which was related to the bait input to the aquaculture process and the animal growth and metabolism. For different types of aquaculture area, only using the inversion results of the four parameters cannot determine the differences in water quality. This is because, on the one hand, the background information collected in this study is limited, so only part of the sampling points can determine the type of aquaculture, and there were too few samples for comparison. On the other hand, using only the four water quality parameters for water quality analysis does not allow the observation of more subtle differences between different water bodies. Although the collected water body samples were analyzed for 11 water quality parameters, the model established could not meet the requirements of prediction. Future research will focus on solving the problem of inverse model accuracy of other water quality parameters.

Our study has certain limitations that should be acknowledged. First, because the background information collected in this study was limited, we could only investigate certain parts of the sampling points to determine the type of aquaculture present. This could lead to biases in the interpretation of the results. Second, the small number of samples available for comparison may limit the generalizability of the results to other small water bodies. Hence, the results of the

experiment should be interpreted with caution. Third, the four water quality parameters used to determine water quality may not be representative enough to capture the subtle differences between different water bodies. To address this limitation, future studies should focus on establishing an inverse model that accurately predicts other water quality parameters. Fourth, due to the power limit of the UAV, each operation time was approximately 25 min, which limits the water quality monitoring capacity for a large area of rivers, such as open water bodies. Additionally, the UAV field sampling is operated in multiple airspaces over water, which can have high tide dynamics that cause spatial and temporal changes in water quality. Because of this, the water flow may not be synchronized with the UAV collection, leading to differences between the quasi-synchronous water body spectral data and the actual river water quality distribution data. As a result, the final retrieval results may exhibit noticeable stripes in some areas. In summary, while our study provides important insights into the use of UAV technology for water quality monitoring, the limitations mentioned above highlight the need for caution in interpreting the results and emphasize the importance of conducting future studies to improve the accuracy and reliability of UAV-based water quality monitoring in small water bodies.

Overall, the retrieval results provided insights into the spatial distribution patterns of water quality parameters in the study area's water bodies. The map generated in Figure 4 can serve as a helpful tool for water resource managers and decision-makers who need to monitor

and manage the water quality of various water bodies in the study area. Additionally, the findings can serve as a baseline for future studies that aim to compare and evaluate changes in water quality over time or after implementation of water pollution mitigation measures.

It is important to note that remote sensing techniques can provide valuable information about water quality parameters over a large area at a low cost, making it a promising technique for water quality monitoring. However, these techniques have limitations, and it is necessary to verify the retrieval results through field measurements and laboratory analysis.

In conclusion, the study demonstrated the potential of remote sensing techniques combined with PLSR models to estimate and map water quality parameters in the study area. The retrieval results for COD, NO₃-N, SS, and chl-a were consistent with the actual water quality conditions in the study area, indicating that this approach can provide reliable information for decision-making to manage water resources and prevent water pollution. Currently, research on low-altitude UAV water quality remote sensing is in the exploration stage, and further study is required for improved rigorous multispectral image acquisition and processing.

5 Conclusion

In this study, we discussed the application of unmanned aerial vehicle (UAV) technology for water quality monitoring in small water bodies, with a focus on aquaculture ponds in the Beibu Gulf of Guangxi. We collected water samples and analyzed them for various water quality parameters, including ammonia nitrogen, chemical oxygen demand, active phosphate, dissolved oxygen, nitrate nitrogen, nitrite nitrogen, inorganic nitrogen, total nitrogen, total phosphorus, suspended solids, and chlorophyll a. We then obtained spectral reflectance data using UAVs equipped with multispectral sensors and constructed inverse models of 11 water quality parameters using the partial least squares method.

Our results showed that the retrieval models for COD, NO₃-N, SS, and chl-a performed better compared to other parameters. The validation set results demonstrated that the correlation coefficients of chl-a, COD, and NO₃-N all exceeded 0.8, with chl-a producing the best prediction model. However, we also acknowledged certain limitations of our study, including the limited background information collected, the small number of samples available for comparison, and the restricted monitoring capacity of UAVs due to power limitations and spatial and temporal changes in water quality.

Overall, our study provides important insights into the potential of UAV technology for water quality monitoring in small water bodies, especially in aquaculture ponds where traditional monitoring methods may be challenging to implement. The results suggest that the use of UAVs with multispectral sensors and the construction of inverse models can offer more efficient and cost-effective methods for monitoring water quality parameters in small water bodies. Despite the study's limitations, future research in this area should continue to address these challenges and further refine the methods for UAV-based water quality monitoring to ensure more accurate and reliable results.

Data availability statement

The original contributions presented in the study are included in the article/[Supplementary Material](#), further inquiries can be directed to the corresponding authors.

Author contributions

YZ: conceptualization, methodology, data curation, writing—original draft, writing—review and editing, visualization, software; WJ: project administration, validation; YD: supervision; WZ: funding acquisition; JY: supervision, funding acquisition YL: funding acquisition; YC: funding acquisition; YH: supervision; XP: investigation, resources; WL: investigation, resources; MP: investigation, resources; YT: software. All authors contributed to the article and approved the submitted version.

Funding

This study was supported in part by grants from National Key R&D Program of China (grant no. 2022YFF0711602); Guangxi Science and Technology Key Research and Development Program (grant no. Gui Ke AB20297037); National Natural Science Foundation of China (grant no. 41976189; grant no. 41976190); Key R&D Program of Guangxi (grant no. Gui Ke AB22035035); the GDAS' Project of Science and Technology Development (grant no. 2022GDASZH-2022020402-01, grant no. 2022GDASZH-2022010111); Guangdong Academy of Sciences and Technology Development funds (grant no. 2022GDASZH-2022010202); Guangdong Provincial Applied Science and Technology Research and Development Program (grant no. 2021B1212100006).

Conflict of interest

The authors declare that the research was conducted in the absence of any commercial or financial relationships that could be construed as a potential conflict of interest.

Publisher's note

All claims expressed in this article are solely those of the authors and do not necessarily represent those of their affiliated organizations, or those of the publisher, the editors and the reviewers. Any product that may be evaluated in this article, or claim that may be made by its manufacturer, is not guaranteed or endorsed by the publisher.

Supplementary material

The Supplementary Material for this article can be found online at: <https://www.frontiersin.org/articles/10.3389/fenvs.2023.1079397/full#supplementary-material>

References

- Bean, T. P., Greenwood, N., Beckett, R., Biermann, L., Bignell, J. P., Brant, J. L., et al. (2017). A review of the tools used for marine monitoring in the UK: Combining historic and contemporary methods with modeling and socioeconomics to fulfill legislative needs and scientific ambitions. *Front. Mar. Sci.* 4, 263. doi:10.3389/fmars.2017.00263
- Carter, C. A., Cui, X. M., Ding, A. J., Ghanem, D., Jiang, F., Yi, F. J., et al. (2017). Stage-specific, nonlinear surface ozone damage to rice production in China. *Sci. Rep.* 7, 44224. doi:10.1038/srep44224
- Chen, B. T., Mu, X., Chen, P., Wang, B., Choi, J., Park, H., et al. (2021). Machine learning-based inversion of water quality parameters in typical reach of the urban river by UAV multispectral data. *Ecol. Indic.* 133, 108434. doi:10.1016/j.ecolind.2021.108434
- Cheng, K. H., Chan, S. N., and Lee, J. H. W. (2020). Remote sensing of coastal algal blooms using unmanned aerial vehicles (UAVs). *Mar. Pollut. Bull.* 152, 110889. doi:10.1016/j.marpolbul.2020.110889
- FAO (2022). *World aquaculture (2022)*. Rome, Italy: FAO Fisheries and Aquaculture Department.
- Guo, H. W., Huang, J. H. J., Chen, B. W., Guo, X. L., and Singh, V. P. (2020). A machine learning-based strategy for estimating nonoptically active water quality parameters using Sentinel-2 Imagery. *Int. J. Remote Sens.* 42 (5), 1841–1866. doi:10.1080/01431161.2020.1846222
- Jang, Y. C., Yin, F., Zhao, Y. F., and Liu, L. (2021). Remote sensing inversion of biochemical oxygen demand in Taihu Lake based on Landsat 8 images. *Ecol. Environ. Sci.* 30 (7), 1492–1502. doi:10.16258/j.cnki.1674-5906.2021.07.018
- Lao, Q. B., Liu, G. Q., Gao, J. S., Shen, Y. L., Guo, Z., Qing, S. M., et al. (2021). Study on the characteristics and eutrophication of nutrients in the mariculture farms of Qinzhou bay, South China. *Mar. Environ. Sci.* 40 (3), 407–416. doi:10.13634/j.cnki.mes.2021.03.011
- Li, M. C., Liu, W. S., and Jiang, J. H. (2021). Analysis of spatial-temporal variation and nutritional status of environmental quality in the mariculture zone at the Yueqing bay. *Mar. Environ. Sci.* 40 (5), 724–731. doi:10.13634/j.cnki.mes.2021.05.010
- Liu, G. H. (2022). Prospects and trends in low-altitude UAV detection technology. *Mod. Radar* 44 (4), 99–100. doi:10.16592/j.cnki.1004-7859.2022.04.018
- Liu, T. S., Yang, B., He, N., Kou, J. F., and Sun, K. F. (2021a). Assessment on the pollutants of mariculture wastewater in Maoming City. *Ecol. Sci.* 40 (4), 195–201. doi:10.14108/j.cnki.1008-8873.2021.04.022
- Liu, X., Zhao, T. Q., Cai, T. Y., Xiao, C. Y., Chen, X. S., and Zhang, W. J. (2021b). Spatiotemporal monitoring of total nitrogen and ammonia nitrogen in Danjiangkou reservoir. *J. Agric. Resour. Environ.* 38 (5), 829–838. doi:10.13254/j.jare.2021.0195
- Liu, Y. J., Xia, K., Feng, H. L., and Fang, Y. M. (2019). Inversion of water quality elements in small and micro-sire water region using multispectral image by UAV. *Acta Sci. Circumstantiae* 39 (4), 1241–1249. doi:10.13671/j.hjkxb.2018.0362
- Liu, Y., Sun, Q., Feng, H. K., and Yang, F. Q. (2021c). Estimation of above ground biomass of potato based on wavelet analysis. *Spectrosc. Spectr. Analysis* 41 (4), 1205–1212. doi:10.3964/j.issn.1000-0593(2021)04-1205-08
- Liu, Z. H., Li, Y. M., Lü, H., Xu, W. F., Xu, X., Huang, J. Z., et al. (2011). Inversion of suspended matter concentration in Lake Chaohu based on partial least squares regression. *J. Lake Sci.* 23 (03), 357–365. doi:10.18307/2011.0307
- Lobo, F. L., Costa, M. P. F., and Novo, E. M. L. M. (2015). Time-series analysis of Landsat-MSS/TM/OLI images over Amazonian waters impacted by gold mining activities. *Remote Sens. Environ.* 157, 170–184. doi:10.1016/j.rse.2014.04.030
- Matsui, K., Shirai, H., Kageyama, Y., and Yokoyama, H. (2021). Improving the resolution of UAV-based remote sensing data of water quality of Lake Hachiroko, Japan by neural networks. *Ecol. Inf.* 62, 101276. doi:10.1016/j.ecoinf.2021.101276
- McEliece, R., Hinz, S., Guarini, J., and Coston-Guarini, J. (2020). Evaluation of nearshore and offshore water quality assessment using UAV multispectral imagery. *Remote Sens.* 12 (14), 2258. doi:10.3390/rs12142258
- McFeeters, S. K. (1996). The use of the normalized difference water index (NDWI) in the delineation of open water features. *Int. J. Remote Sens.* 17 (7), 1425–1432. doi:10.1080/01431169608948714
- Peterson, K. T., Sagan, V., and Sloan, J. J. (2020). Deep learning-based water quality estimation and anomaly detection using Landsat-8/Sentinel-2 virtual constellation and cloud computing. *Giscience Remote Sens.* 57 (4), 510–525. doi:10.1080/15481603.2020.1738061
- Primavera, J. H. (2006). Overcoming the impacts of aquaculture on the coastal zone. *Ocean Coast. Manag.* 49 (9–10), 531–545. doi:10.1016/j.ocecoaman.2006.06.018
- Ren, C. Y., Wang, Z. M., Zhang, Y. Z., Zhang, B., Chen, L., Xi, Y. B., et al. (2019a). Rapid expansion of coastal aquaculture ponds in China from Landsat observations during 1984–2016. *Int. J. Appl. earth Observation Geoinformation* 82, 101902. doi:10.1016/j.jag.2019.101902
- Rui, T. T., Xu, Y. F., Cheng, Q., Yang, B., Feng, Z. J., Zhou, T., et al. (2022). Water content retrieval of winter wheat leaves based on UAV multi-spectral remote sensing. *J. Triticeae Crops* 42 (6), 1–10.
- Sagan, V., Peterson, K. T., Maimaitijiang, M., Sidike, P., Sloan, J., Greeling, B., et al. (2020). Monitoring inland water quality using remote sensing: Potential and limitations of spectral indices, bio-optical simulations, machine learning, and cloud computing. *Earth-Science Rev.* 205, 103187. doi:10.1016/j.earscirev.2020.103187
- Wang, H. W. (2006). *Linear and non-linear methods for partial least squares regression*. Beijing, China: National Defense Industry Press.
- Wang, X. Y., Zhou, T., Ying, Z. M., Wu, J., and Yang, W. (2020). Analyses of water quality and driving forces in Ningde aquaculture area. *Acta Ecol. Sin.* 40 (5), 1766–1778.
- Yuan, B., Yue, F., Wang, X., and Xu, H. (2021). The impact of pollution on China marine fishery culture: An econometric analysis of heterogeneous growth. *Front. Mar. Sci.* 8, 760539. doi:10.3389/fmars.2021.760539
- Yuan, X., Zhang, L., Song, X. X., and Gu, Y. (2020). Remote sensing monitoring and spatial-temporal change analysis of aquaculture ponds in coastal area of Hainan Island. *J. Mar. Sci.* 38 (1), 59–67. doi:10.3969/j.issn.1001-909X.2020.01.007
- Zehra, Y. A., Gordana, K., Serdar, G., and Ugur, A. (2019). Monitoring the water quality of small water bodies using high-resolution remote sensing data. *ISPRS Int. J. Geo-Information* 8 (12), 553. doi:10.3390/ijgi8120553
- Zhao, C., Shen, P., Li, Q., Chen, C., Liu, X. Y., and Liao, F. J. (2021). Retrieval concentration of TN using random forest algorithm based on GF-1 WFV remote sensing data. *Environ. Sci. Technol.* 44 (9), 23–30. doi:10.19672/j.cnki.1003-6504.1080.21.338



OPEN ACCESS

EDITED BY

Junhong Bai,
Beijing Normal University, China

REVIEWED BY

Yanan Guan,
Hebei Normal University, China
Liehui Zhi,
Beijing Normal University, China

*CORRESPONDENCE

Judith Z. Drexler,
✉ jdrexler@usgs.gov

RECEIVED 25 April 2023

ACCEPTED 06 June 2023

PUBLISHED 11 July 2023

CITATION

Drexler JZ, Raine H, Jacobi JD, House S,
Lima P, Haase W, Dibben-Young A and
Wolfe B (2023), A prioritization protocol
for coastal wetland restoration on
Moloka'i, Hawai'i.
Front. Environ. Sci. 11:1212206.
doi: 10.3389/fenvs.2023.1212206

COPYRIGHT

© This work is authored by employees of
the US federal government and is
therefore in the public domain. This is an
open-access article distributed under the
terms of the [Creative Commons
Attribution License \(CC BY\)](https://creativecommons.org/licenses/by/4.0/). The use,
distribution or reproduction in other
forums is permitted, provided the original
author(s) and the copyright owner(s) are
credited and that the original publication
in this journal is cited, in accordance with
accepted academic practice. No use,
distribution or reproduction is permitted
which does not comply with these terms.

A prioritization protocol for coastal wetland restoration on Moloka'i, Hawai'i

Judith Z. Drexler^{1*}, Helen Raine², James D. Jacobi³, Sally House¹,
Pūlama Lima⁴, William Haase⁵, Arleone Dibben-Young⁶ and
Bret Wolfe⁷

¹U.S. Geological Survey, California Water Science Center, Sacramento, CA, United States, ²Pacific Birds Habitat Joint Venture, Kauai, HI, United States, ³U.S. Geological Survey, Pacific Island Ecosystems Research Center, Hawaii National Park, HI, United States, ⁴Ka Ipu Makani, Kaunakakai, HI, United States, ⁵Moloka'i Land Trust, Ho'olehua, HI, United States, ⁶Hawaiian Islands Conservation Collective, Kaunakakai, HI, United States, ⁷U.S. Fish and Wildlife Service, Maui National Wildlife Refuge Complex, Kihei, HI, United States

Hawaiian coastal wetlands provide important habitat for federally endangered waterbirds and socio-cultural resources for Native Hawaiians. Currently, Hawaiian coastal wetlands are degraded by development, sedimentation, and invasive species and, thus, require restoration. Little is known about their original structure and function due to the large-scale alteration of the lowland landscape since European contact. Here, we used 1) rapid field assessments of hydrology, vegetation, soils, and birds, 2) a comprehensive analysis of endangered bird habitat value, 3) site spatial characteristics, 4) sea-level rise projections for 2050 and 2100 and wetland migration potential, and 5) preferences of the Native Hawaiian community in a GIS site suitability analysis to prioritize restoration of coastal wetlands on the island of Moloka'i. The site suitability analysis is the first, to our knowledge, to incorporate community preferences, habitat criteria for endangered waterbirds, and sea-level rise into prioritizing wetland sites for restoration. The rapid assessments showed that groundwater is a ubiquitous water source for coastal wetlands. A groundwater-fed, freshwater herbaceous peatland or "coastal fen" not previously described in Hawai'i was found adjacent to the coastline at a site being used to grow taro, a staple crop for Native Hawaiians. In traditional ecological knowledge, such a groundwater-fed, agro-ecological system is referred to as a lo'ipūnāwai (spring pond). Overall, 39 plant species were found at the 12 sites; 26 of these were wetland species and 11 were native. Soil texture in the wetlands ranged from loamy sands to silt and silty clays and the mean % organic carbon content was $10.93\% \pm 12.24$ (sd). In total, 79 federally endangered waterbirds, 13 Hawaiian coots ('alae ke'oke'o; *Fulica alai*) and 66 Hawaiian stilts (ae'o; *Himantopus mexicanus knudseni*), were counted during the rapid field assessments. The site suitability analysis consistently ranked three sites the highest, Kaupapalo'i o Ka'amola, Kakahai'a National Wildlife Refuge, and 'Ōhi'apilo Pond, under three different weighting approaches. Site prioritization represents both an actionable plan for coastal wetland restoration and an alternative protocol for restoration decision-making in places such as Hawai'i where no pristine "reference" sites exist for comparison.

KEYWORDS

coastal fen, GIS site suitability analysis, Hawaiian islands, indigenous community, sea-level rise, traditional ecological knowledge, wetland restoration, Native Hawaiians

1 Introduction

In many places around the world, there are no pristine wetland “reference” sites to stand as guideposts for restoration targets (Otte et al., 2021). This is the case in the Hawaiian Islands due to the nearly complete alteration of lowland habitats after European contact and before botanical descriptions were documented. To date, 44% of the coastal wetland area in Hawai‘i has been lost to other land uses (Van Rees and Reed, 2013). The remaining coastal wetlands provide crucial habitat for native invertebrates and plants, migratory birds, and federally endangered waterbirds including the Hawaiian stilt (ae‘o; *Himantopus mexicanus knudseni*), Hawaiian coot (‘alae ke‘oke‘o; *Fulica alai*), Hawaiian duck (koloa maoli; *Anas wyvilliana*), and Hawaiian common gallinule (‘alae ‘ula, *Gallinula galeata sandvicensis*; currently extirpated from Moloka‘i) (State of Hawai‘i, 1996; Pacific Coast Joint Venture, 2006; US Fish and Wildlife Service, 2011a; VanderWerf, 2012).

Historically, Hawaiian coastal wetlands were widely used to grow taro, a vital subsistence crop for Native Hawaiians. Taro (*Colocasia esculenta*) patches (lo‘i kalo) were built inland from fish ponds (loko i‘a) along the coast, creating habitat mosaics that expanded the natural wetland habitat for shorebird populations (Burney et al., 2001; Harmon et al., 2021). Hawaiian coastal wetlands continue to have important socio-cultural uses as food sources and producers of native sedges (makaloa, *Cyperus laevigatus*) for weaving (Krauss, 2001; Erickson and Puttock, 2006). In addition, coastal wetlands in Hawai‘i, as well as elsewhere around the world, have long provided essential ecosystem services such as carbon sequestration, trapping of sediments and nutrients, abatement of storm impacts, and protection from flooding (Roman and Burdick, 2012; Craft, 2016; Kroeger et al., 2017).

Land-use change along Hawai‘i’s coastline started with the lo‘i kalo and loko i‘a of the early Polynesians and culminated in rice and sugar plantations in the years following European contact (Athens et al., 1992; Burney et al., 2001; Gon and Winter, 2019). Mauka (toward the mountains, upland) of the lowlands, ranching, invasive ungulates, and pineapple cultivation have caused massive erosion, which has impacted the entire continuum from ridge to reef (Stock et al., 2011; Jacobi and Stock, 2017). The widespread anthropogenic transformation of coastal areas and the introduction of invasive plant species have resulted in the loss of most lowland native flora (Kirch, 1982; Cuddihy and Stone, 1990; Athens et al., 1992; Burney et al., 1997). Currently, most coastal wetlands in Hawai‘i continue to be degraded by sedimentation, non-native ungulates, invasive plants (mainly mangrove (*Rhizophora mangle*), kiawe (*Prosopis pallida*), pickleweed (*Batis maritima*), and Indian fleabane (*Pluchea indica*)), development, and/or hydrologic changes from stream diversion, drought, and/or climate change (US Fish and Wildlife Service, 2011a; Van Rees and Reed, 2013).

Hawaiian coastal wetlands have received scant attention in the scientific literature. The most comprehensive classification of coastal wetlands (Erickson and Puttock, 2006) describes them as saline or brackish in salinity and consisting either of “coastal flats” or “estuarine wetlands.” Coastal flats are defined as groundwater

1. *E u-i aku ana au ia oe* (One question I ask of you:)
2. *Aia i-hea ka Wai a Kane?* (Where flows the water of Kāne?)
3. *Aia i-lalo, i ka homua, i ka Wai Iu,* [The waters of Kāne are] (Deep in the ground, in the gushing spring)
4. *I ka wai kau a Kane me Kanaloa,* (In the ducts of Kane and [Kane] Loa,)
5. *He wai-puna, he wai e inu,* (A well-spring of water, to quaff,)
6. *He wai e mana, he wai e ola* (A water of magic power-)
7. *E ola no, e-a!* (The water of life!)

(Emerson, 1909: pp. 258-260)

FIGURE 1

Sixth and final verse of “He Mele no Kāne,” a traditional Hawaiian mele (chant).

driven, occurring in a floodplain, and containing mineral substrate. This definition differs somewhat from other definitions in the literature in which coastal flats are described as tidal ecosystems dominated by sediments and/or sand and found along coasts with low slope and energy (Jackson, 2013; Murray et al., 2019). Estuarine wetlands are defined by Erickson and Puttock (2006) as surface-water driven, occurring at river mouths or adjacent to tidal rivers, and containing organic or mineral substrates. Due to the complex hydrogeology, varied geomorphology, and novel plant communities on Moloka‘i, we hypothesized that these two main classifications may not encompass the full spectrum of coastal wetlands on the island. In particular, we surmised that there may be freshwater wetlands in areas receiving high rates of groundwater discharge along the coastline of the island (Oki et al., 2019).

Although few data exist in Western science to support this hypothesis, it is well supported by traditional ecological knowledge (TEK) in the Native Hawaiian culture, which speaks not only of the great socio-cultural significance of coastal wetlands but also of their ecohydrological function. The final verse of the mele (chant) “He Mele no Kāne” (The Waters of Kāne) (Figure 1) details various locations and the hydrologic connectivity of the waters of Kāne—the Hawaiian god of life and freshwater (Emerson, 1909). Specifically, the third line of the last verse states that the waters of Kāne can be found deep in the earth and in the gushing springs. This line is a clear reference to coastal aquifers and groundwater discharge at springs. The fourth line alludes to these locales as being coastal wetlands by stating that the waters are in the ducts of Kāne and Kanaloa—the Hawaiian god of salt water. While the translation by Emerson (1909) translates the term “kau” as a duct, “kau” also means to suspend. This line, therefore, references the suspension of Kāne (freshwater) above Kanaloa (saltwater) emphasizing not only the relationship between the two gods but also recognizing that the freshwater lens floats above the denser saltwater lens in coastal aquifers. The fifth to seventh lines of the verse state that these special locales are recognized and reserved for human consumption of their resources, for religious and spiritual functions, and most importantly, for procuring life. The final line of the mele emphasizes the Hawaiian word “ola,” which means livelihood, health, and “to thrive” (Pukui and Elbert, 1986). In short, this mele describes the fundamental importance of coastal wetlands to Native Hawaiians and demonstrates how the understanding of

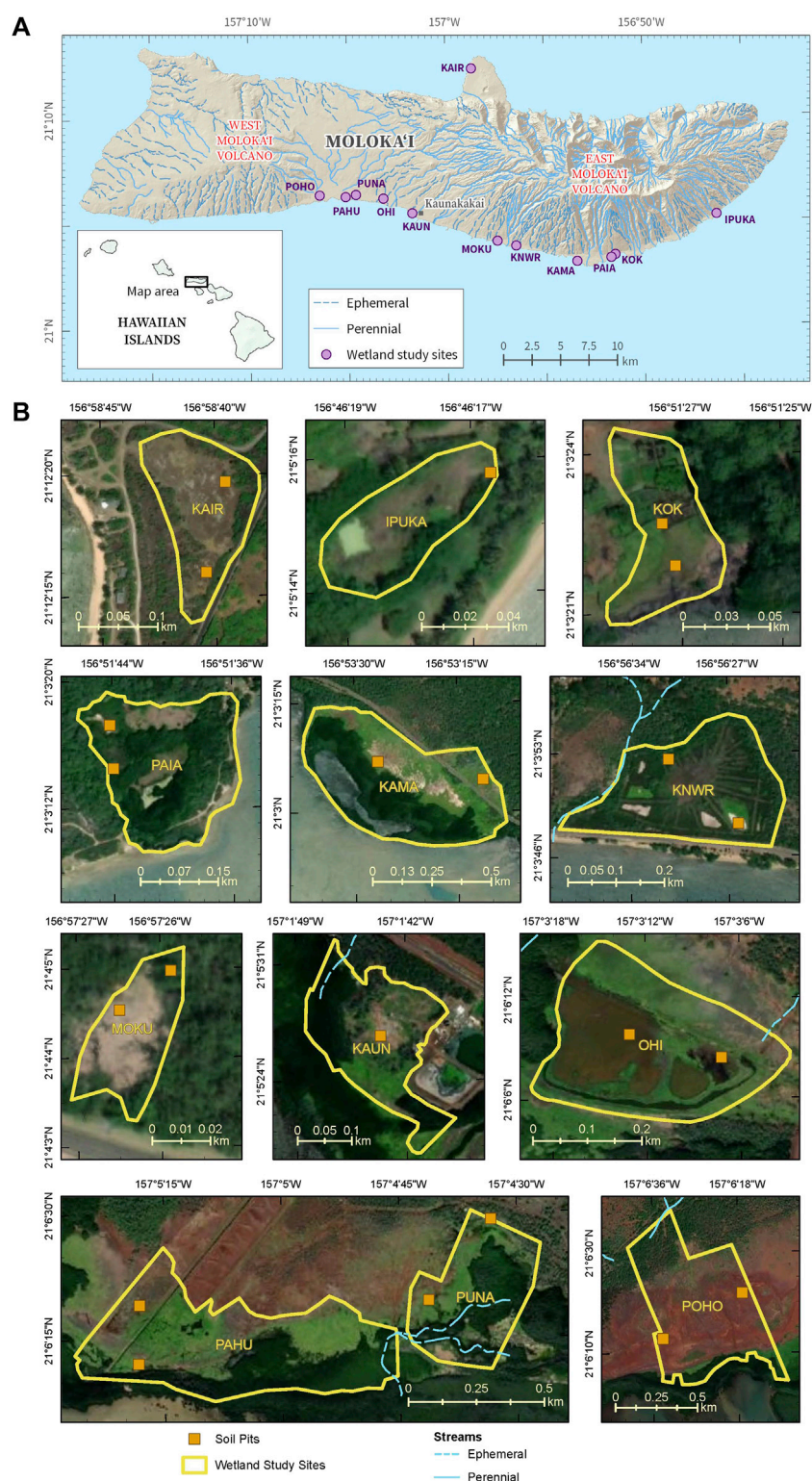


FIGURE 2

(A) Map of the island of Molokai, Hawaii, showing the location of the 12 coastal wetland study sites and (B) imagery showing the site boundaries, soil pits, and streams at each of the study sites. Base imagery modified from the following sources: Esri, Maxar, Earthstar Geographics, and the GIS User Community.

their function is inextricably intertwined with their socio-cultural value, a prime example of the Hawaiian socio-ecological system in which humans are perceived as part of and not separate from nature (Berkes and Folke, 1998; Winter et al., 2018; Gon III et al., 2021).

Because of their current degraded state, much work is needed for Hawaiian coastal wetlands to once again be thriving places for native flora and fauna. Fortunately, a renewed interest in traditional lowland agriculture by the Native Hawaiian community, as well as a need for

TABLE 1 Basic characteristics of the 12 wetland study sites on Moloka'i assessed in April 2022. Abbreviations for land ownership are the Hawai'i Department of Land and Natural Resource, Division of Forestry and Wildlife (DoFAW), Department of Hawaiian Home Lands (DHHL), U.S. Fish and Wildlife Service (FWS), and National Park Service (NPS).

Wetland name (abbreviation)	Date of rapid assessment	Coordinates	Ownership	Size (ha)	Dominant vegetation: native species (N), species introduced by Polynesians (PI), or exotic species introduced since European contact (E)
Ipuka'iole Pond (IPUKA)	4/14/2022	N 21° 05.2714'; W156° 46.2791'	private	0.31	<i>Thespesia populnea</i> (N), <i>Rhizophora mangle</i> (E)
Kakahai'a NWR (KNWR)	4/13/2022	N 21° 03.8760'; W 156° 56.5217'	FWS	5.34	<i>Schoenoplectus californicus</i> (E), <i>Pluchea indica</i> (E)
Kalaupapa airport wetland (KAIR)	4/20/2022	N 21° 12.3284', W 156° 58.660'	NPS	2.10	<i>Bolboschoenus maritimus</i> (E), <i>Cyperus javanicus</i> (N), <i>Prosopis pallida</i> (E)
Kamahu'ehu'e Pond (KAMA)	4/18/2022	N 21° 03.1155'; W 156° 53.4447'	DHHL	33.03	<i>Batis maritima</i> (E), <i>R. mangle</i> (E)
Kaunakakai wastewater treatment plant (KAUN)	4/19/2022	N 21° 05.4446'; W 157° 01.7279'	private	4.99	<i>B. maritima</i> (E), <i>R. mangle</i> (E)
Kaupapalo'i o Ka'amola (KOK)	4/15/2022	N 21° 03.3784'; W 156° 51.4571'	private	0.05	<i>B. maritima</i> (E), <i>R. mangle</i> (E), <i>S. californicus</i> (E), <i>Colocasia esculenta</i> (PI)
Moku Pond (MOKU)	4/13/2022	N21° 04.076'; W156° 57.443'	private	0.13	<i>P. pallida</i> (E)
'Ōhi'apilo Pond Bird Sanctuary (OHI)	4/19/2022	N 21° 06.1406'; W 157° 03.1210'	DHHL	9.76	<i>B. maritima</i> (E)
Pahuauiwai aquaculture site (PAHU)	4/19/2022	N 21° 06.2023'; W 157° 05.3066'	private	36.04	<i>B. maritima</i> (E), <i>R. mangle</i> (E)
Paialoa Pond (PAIA)	4/14/2022	N 21° 03.2877'; W 156° 51.7337'	DoFAW	6.82	<i>R. mangle</i> (E), <i>Pluchea indica</i> (E)
Pohoele Pond (POHO)	4/21/2022	N 21° 04.8789'; W 157° 00.2378'	DoFAW	53.74	<i>B. maritima</i> (E)
Punalau Pond 1	4/15/2021	N 21° 06.4852'; W 157° 04.5558'	private	18.04	<i>B. maritima</i> (E), <i>R. mangle</i> (E)

improved habitat for endangered species, has recently catalyzed a strong interest in wetland restoration. Although opportunities for landscape-scale restoration are limited on the main, highly developed Hawaiian islands, the island of Moloka'i stands apart. This island, with a population of more than half Native Hawaiians (Maui County, 2020), has resisted large-scale development. There are numerous coastal lowland areas that could potentially be restored, including former lo'i kalo, shrimp ponds, an extensive network of loko i'a, and lowland floodplains and wetlands. Of particular interest are a series of relatively isolated coastal wetlands along the south shore, which are strategically proximal to one another (Henry, 2016). Yet, in Hawai'i, just like elsewhere, coastal wetlands are increasingly threatened by sea-level rise (van Rees and Reed, 2013; Kane et al., 2014; Harmon et al., 2021), so any restoration efforts need to incorporate future sea-level rise projections in order to have the best chance for long-term success.

Given the need for coastal wetland restoration in Hawai'i and the rare opportunity on Moloka'i, we conducted a study to prioritize the restoration of 12 coastal wetlands on the island. In particular, we used a GIS site suitability analysis that incorporated 1) rapid field assessments of hydrology, vegetation, soils, and birds, 2) a comprehensive analysis of endangered bird habitat value, 3) spatial characteristics of the sites, 4) sea-level rise projections for 2050 and 2100 and wetland migration potential, and 5) preferences of the Native Hawaiian community. Our main objectives were to develop a protocol to prioritize coastal wetlands

for restoration without the need for reference sites and to use the new protocol to rank each of the 12 sites, thereby creating an actionable blueprint for restoration. Although designed for Moloka'i, our approach could be adapted for use in any place with few or no reference sites and/or strong indigenous community needs. The restoration endpoints we envision for Moloka'i wetlands are driven more by re-establishing functionality and cultural resources rather than by trying to restore their original state, which may not be attainable at this point.

2 Materials and methods

2.1 Study site description

Moloka'i, the fifth largest island in the Hawaiian chain, is situated between 21°00'–21°15' N and 157°20'–156°40' W with an area of 673 km² (Figure 2) (Stearns and Macdonald, 1947). The population in 2020 was 6,253 (County of Maui, 2020). The island is largely composed of the 423 m-high, West Moloka'i volcano and the younger, 1,512 m-high, East Moloka'i volcano (Stearns and Macdonald, 1947). Moloka'i has a mean annual temperature of 23.91°C (1978–2007; Giambelluca et al., 2014). The rainy season typically extends from October through April and the dry summer season extends from May through September (Sanderson, 1994).

The mean rainfall is usually much higher in the northeastern or windward part of Moloka'i, exceeding 406.4 cm, while the West Moloka'i volcano receives less than 63.5 cm (1978–2007; Giambelluca et al., 2013). Most recently (from spring 2019–2022), Moloka'i has experienced a drought throughout the western part of the island and the southcentral coast (NOAA National Integrated Drought Information System NIDIS, 2022a). Along the southcentral coast, drought severity has been extreme (D3) near the main Moloka'i town of Kaunakakai and moderate (D1) along the eastern trajectory to the Kawela Gulch area (NOAA NIDIS, 2022a). The tides in Moloka'i are mixed semidiurnal. The great diurnal tidal range (mean lower low water to mean higher high water) on Moloka'i is 0.651 m (Kaunakakai Harbor, NOAA, 2022b), placing coastal wetlands in the microtidal range. Twelve coastal wetland sites (site abbreviations used hereafter) were chosen for the study based on background data, accessibility, and the ability to gain lawful entry from landowners (Figure 2, Supplementary Figure S1; Table 1).

2.2 GIS database

We created a GIS database of the environmental attributes of Moloka'i, including soil types, hydrology, vegetation, land ownership, and rainfall/moisture zones, to select sites for the study and inform our prioritization process (Supplementary Table S1). The boundaries of each wetland were determined using Pictometry high-resolution aerial imagery (EagleView International, 2021) and Hawai'i State tax map parcels (Hawai'i Statewide GIS Program, 2021). The delineations for each site are approximate and were only created for the purposes of this study.

2.3 Site assessments

Rapid field assessments were conducted in April 2022 of the vegetation, soils, hydrology, and birds at each of the 12 sites. The purpose of the field assessments was to determine the current condition of sites for which little to no data were available.

For the hydrologic component of the rapid assessment, water sources (surface water, precipitation, groundwater, and/or seawater) were determined by examining high-resolution digital imagery (EagleView Technologies, Inc., 2008), site geomorphology, and walking the site periphery to identify springs, seeps, and intermittent streams. In addition, the depth from the wetland surface to the water table was determined in soil pits (see below) and the specific conductance of the groundwater was measured using a Fisherbrand™ Traceable™ expanded range conductivity meter (Fisher Scientific, Waltham, MA) calibrated to the salinity range of each site.

The soil component was focused on determining whether soil textures at the wetland sites followed their mapped classifications (mainly Kealia silt loam; Soil Survey Staff, 2021) and whether there was any within-site variability. Soil pits were dug to the depth of the water table or a maximum of 80 cm in two distinct areas of each site such as mauka (toward the mountains) and makai (toward the sea) in contrasting vegetation types or at different sides of a road or railroad grade that bisected the site. Soil samples at each pit were

collected from 0–2 cm, 24–26 cm, and 48–50 cm depth from the surface, refrigerated, and transported within 5 days to the USGS Coastal and Marine Science Center in Santa Cruz, CA, for soil texture analysis and the USGS California Water Science Center in Sacramento, CA, for the analysis of % organic carbon by weight.

The structure and species composition of the plant communities found within each wetland site were characterized using a rapid field assessment procedure. Vegetation data were collected in survey plots, approximately 5 × 5 m in size, that were located in different plant communities found at each site. In each plot, vegetation cover and bare ground were visually estimated to the nearest 5%, and plant species were recorded in lifeform groups (trees, shrubs, ferns, vines, rushes, sedges, grasses, herbs, and submerged aquatic vegetation). Additional species found outside the plots, within or immediately adjacent to the wetland, were recorded with photographs and added to the site species list. Plant communities were identified both in the field and using the high-resolution digital imagery (EagleView Technologies, Inc., 2008). Taxonomic nomenclature follows the work of Wagner et al. (2005).

The rapid assessment for birds was carried out with a point count. Point counts were carried out for 10 min even if no birds were present. Birds were recorded following the State Waterbird Count methodology (Hawai'i Department of Land and Natural Resources, 2017). The short fieldwork period and extreme drought conditions present on the island at the time resulted in few native birds being present during the rapid assessment. Therefore, to ensure that avian diversity was adequately represented, the rapid assessment was supplemented with an avian dataset for Moloka'i from Arleone Dibben-Young of the non-profit Hawaiian Islands Conservation Collective for the period from 2010 to 2020 (Supplementary Table S2). These data were collected twice per year during the annual State Waterbird Surveys or during bird monitoring trips and *ad hoc* sightings. Only native and migratory birds were included.

2.4 Laboratory analyses

Soil texture was determined using standard USGS methodologies described in Drexler et al. (2021). The percentage of organic carbon by weight (% OC) was determined for the top two samples in the soil pits (0–2 cm and 24–26 cm) using a Costech ECS 4010 CHNS/O elemental analyzer (Costech Analytical Technologies, Inc., Valencia, CA, U.S.A.) according to a modified version of U.S. Environmental Protection Agency Method 440.0 (Zimmerman et al., 2007). Blanks, replicates, and standards were analyzed every 10 samples to assess instrument stability. Replicate samples were reanalyzed if the relative percentage difference between the two replicates was greater than 20%. The detection limit was 0.01%.

2.5 Sea-level rise projections

In this study, we used the SLR projections by Sweet et al. (2022), which incorporate the latest science from the Intergovernmental Panel on the Climate Change Sixth Assessment Report for updated temporal trajectories and exceedance probabilities based on different

TABLE 2 Median values in meters (likely ranges) for observation-based extrapolations and modeled sea-level rise (SLR) scenarios for the Hawaiian Islands for 2050 and modeled SLR scenarios (no range provided) for 2100 from the work of Sweet et al. (2022). The tidal benchmark is mean higher water and the baseline date is 2000 for all extrapolations and scenarios. The intermediate scenario (bold) was chosen for the study due to the high uncertainty of projections (<0.8 probability) along the Moloka'i coastline.

Observation-based extrapolations	Modeled scenarios				
	Low	Intermediate-Low	Intermediate	Intermediate-High	High
2050: 0.24 (0.20–0.28)	0.19 (0.13–0.24)	0.24 (0.18–0.31)	0.29 (0.22–0.39)	0.38 (0.27–0.53)	0.46 (0.31–0.64)
2,100: NA	0.4	0.6	1.1	1.7	2.3

levels of global warming (Fox-Kemper et al., 2021; Garner et al., 2021). Multiple methods of projecting future ice-sheet changes from Antarctica (Levermann et al., 2020; Edwards et al., 2021) and Greenland (Bamber et al., 2019; Edwards et al., 2021) are integrated into the projections. Specifically, we used the relative sea-level rise projections for Moloka'i, which are a part of the 1 x 1-degree grids for the Hawaiian Islands along the coastline relative to the baseline year of 2000. For some parts of Hawai'i, downscaled projections are available near NOAA-tide-gauges, but no such gauges are located on Moloka'i, so the gridded projections were used.

Sweet et al. (2022) provide two kinds of projections: 1) observation-based projections to 2050 and 2) decadal scenario-based (modeled) projections to 2150. The scenario-based projections are combined to generate five sea-level scenarios ranging from low, intermediate-low, intermediate, intermediate-high, and high. On Moloka'i, the observation-based projections to 2050 and the intermediate-low projections for 2050 are almost the same. This would ordinarily point toward using these projections for 2050. However, because the uncertainty of these projections was high at our wetland sites (<0.80 probability across the board), we opted instead to use the intermediate scenarios of SLR for both the 2050 and 2100 timeframes (Table 2).

It is important to note that the SLR projections used here are for passive flooding from SLR only and do not include wave-induced flooding, yearly variability of sea-level from natural processes such as the El Niño–Southern Oscillation, or any additional impacts due to coastal erosion (Anderson et al., 2018; Sweet et al., 2022), which can exacerbate SLR and increase erosive impacts along the coastline (Drexler and Ewel, 2001; Anderson et al., 2018; Goodman et al., 2018).

2.6 GIS site suitability analysis

2.6.1 Sub-models

The site suitability analysis consisted of 1) ranking the coastal wetlands based on specific sub-models or categories consisting of hydrology, resilience to sea-level rise, soils, vegetation, bird habitat value, and community support and 2) carrying out the actual suitability analysis in ArcGISPro based on the sub-models in step 1). Rankings (1 (lowest)–5 (highest)) were based on the best available data from the rapid assessment, the literature, and database sources. Site data were very limited, so we relied on both professional judgement as well as the available data to

develop criteria that best encapsulated the functions and values of the sites. Following are descriptions of the ranking criteria for each of the sub-models and the suitability analysis procedure that was used.

Hydrologic parameters were ranked in three ways and then averaged for an overall score. Depth to groundwater from the land surface was used to assess the availability of water in the rooting zone of common wetland macrophytes (approximately 0–30 cm in depth; Moffett and Gorelick, 2016). The ranking was as follows: <30 cm from land surface to groundwater = 5; 31–50 cm = 3; >50 cm = 1. The second measure was the range of estimated groundwater (gw) discharge at the coastline (Oki et al., 2019) and/or the number of springs mauka of the site (Stearns and Macdonald, 1947). The gw discharge/spring ranking was as follows: >500,000 gallons gw discharge/day and the presence of springs/seeps mauka of site = 5; 100,000–500,000 gallons of gw discharge/day and springs on site = 3 or high gw discharge at the coast but no springs on site = 3; low gw discharge (<500,000 gallons/day) and no springs on site = 1. The third hydrologic category was salinity stress, which was ranked as follows: <35 part per thousand (ppt) in gw = 5, 35–50 ppt in gw = 3, and >50 ppt in gw or extensive salt pan = 1. If groundwater was not accessible at the site, then the condition of the vegetation during the rapid field assessment was used as an indication of the hydrologic status because good condition during drought is indicative of good hydrological status.

The resilience of each wetland to future SLR was ranked in the following way. First, we determined the surface elevation of each site using the Moloka'i digital elevation model provided by Sweet et al. (2022). For 2050, the median elevation of each wetland was then estimated by subtracting 0.29 m (the projected SLR, Table 2) and adding a conservative estimate for vertical accretion over the ensuing years (3 mm/yr * 28 years). The median elevation of each wetland in 2100 was estimated by subtracting 1.1 m (the projected SLR, Table 2) and adding vertical accretion at the same rate but over 78 years. Data were not available for the elevation range of dominant wetland vegetation, which is required to determine the elevation of marsh drowning (Morris et al., 2022). For this reason, we used the elevation capital of each wetland (*sensu* Cahoon et al., 2020) to rank its relative resilience to inundation. Rankings for both 2050 and 2100 were <0 m elevation relative to the mean sea level (MSL) = 1; 0–0.3 m = 2, 0.31–0.6 m = 3, 0.61–0.9 m = 4, and >0.9 m = 5. Wetland migration potential was then determined by the availability of flat land (which was available for all wetlands, so no ranking was needed) and the distance to the nearest mauka road. The rankings for the distance to the nearest

TABLE 3 Criteria used to rank habitat quality for threatened and endangered waterbirds (T&E), migratory shorebirds, and migratory waterfowl at each wetland site.

Criteria	Ranking	Ranking details
1. Area of site	1–5	(1) 0–3.64 ha, (2) 4.04–7.68 ha, (3) 8.09–11.74 ha, (4) 12.14–15.78 ha, and (5) 16.19+ ha
2. Freshwater availability	1, 3, and 5	1- little/none, 3- good, and 5- abundant
3. Proximity to other wetlands (managed and unmanaged)	1–5	(1) 9 km+, (2) 7–8 km, (3) 5–6 km, (4) 3–4 km, and (5) 1–2 km
4. Hazards (unfenced roads, powerlines, and/or contamination from heavy metals and coliform bacteria)	1, 3, and 5 (ranked 3x)	1- multiple, 3- some, and 5- few to none
5. Predator control management activities	1–5	1- none in place
		2- none in place, potential capacity to start
		3- none in place, good capacity to start
		4- predator control in place
		5- constant predator control in place with effectiveness monitoring
6. Botulism control measures	1–5	1- none in place, little capacity to start; no qualified person checks site for dead birds or fish and no response mechanism in place, little/no capacity to start
		2- none in place, potential capacity to start; potential management infrastructure, and/or personnel available to be trained and paid if funds were provided
		3- none in place, good capacity to start, and no qualified person checks the site for dead birds and fish but available infrastructure and personnel
		4- a qualified person checks the site for dead birds and fish and could potentially respond rapidly
		5- a qualified person regularly checks for dead birds, there is regular removal of dead fish, and there is ability to respond rapidly to an outbreak
7. Human disturbance managed	1, 3, and 5	1- site is open access, no on-site management, 3- partially, site either has natural or physical barriers (fence), people are discouraged from entering, and an organization or individual has oversight, and 5- site is closed to disturbance or steps are taken to reduce impacts and active management is in place
8. Restoration status	1, 3, and 5 (ranked 2x)	1- no restoration and none is planned, 3- site is not restored but planning underway, and 5- restoration underway or completed, site is functional
9. Breeding on site for each threatened and endangered (T&E) species	1 and 5	1- no and 5- yes
10. Average T&E bird count in 10-year data set	1–5	(1) 0–14, (2) 15–29, (3) 30–44, (4) 45–59, and (5) 60–75
11. Species richness of all T&E species, migratory shorebirds, and migratory waterfowl	1–5	(1) 0–9, (2) 10–19, (3) 20–29, (4) 30–39, and (5) 40–49
12. Potential suitability for each T&E species, for migratory shorebirds, and for migratory waterfowl after restoration	1–5	Criteria specific for each T&E, migratory shorebirds, and migratory waterfowl (Supplementary Table S11) based on site characteristics including water depth, foraging areas, vegetation, and nesting areas

mauka road were <100 m = 1; 100–250 m = 2, 251–400 m = 3, 401–550 m = 4, and >551 m = 5. Because the coastal lowland zone of Moloka'i is very flat and migration space is limited, we weighted resilience to inundation to be twice as important as migration space in the overall ranking of resilience to SLR. Finally, because the overall resilience to SLR is of critical importance to wetland sustainability, we weighted this sub-model to be three times more important than all the other sub-models except community support, which also received the same weighting.

The soil ranking was based on two parameters, soil texture and % of organic carbon (OC) content. Soil texture is a key measure of water holding capacity and water availability, which are both essential for successful plant colonization ([Sprecher, 2001](#)). The percentage of OC (or organic matter content, which is ~2*OC) is

typically at least 5% in wetland soils and is essential for biogeochemical cycling of nutrients and adequate friability for plant growth ([Mitsch and Gosselink, 2007](#), Ch. 13; [Munkholm, 2011](#)). For soil texture, the ranking criteria were as follows: silty clay loam and silt loam = 5; silty clay and loam = 3; and sandy loam and loamy sand = 1. For % OC, the ranking was simply >2.5% OC (~5% OM) = 5 and <2.5% OC = 1. Both of these ranking criteria were averaged to obtain the final soil rankings for each of the sites.

Vegetation at each of the sites was ranked based on two main criteria: 1) the proportion of native vs. non-native wetland plant species and 2) the species richness of native wetland species. In Hawai'i, the high prevalence of invasive species has largely transformed lowland areas ([Staples and Cowie, 2001](#); [Erickson](#)

and Puttock, 2006), so the presence of native wetland species is a strong indicator of vegetation status and is key to the successful restoration of wetland function. The ranking for native vs. non-native species was as follows: the site contains intact native-dominated wetland plant communities = 5, a small area of the site contains native-dominated wetland plant communities = 4, the site is mostly dominated by non-native alien wetland plant species but with some natives = 3, the site is dominated by non-native wetland plants but no invasive mangroves (*Rhizophora mangle* L.) = 2, and the site has no native wetland plants and high cover of mangrove, pickleweed (*Batis maritima* L.), and other non-native wetland species = 1. For species richness, ranking was as follows: \geq five native wetland species = 5, four native wetlands species = 4, three native wetland species = 3, one or two native wetland species = 2, and no native wetland species = 1. The two criteria were averaged to obtain the overall vegetation ranking for each of the sites.

The current and potential (restored) habitat value of each wetland for threatened and endangered (T&E) wetland birds and migratory birds was ranked using data from the scientific literature, wetland management plans, the rapid assessments, the National Wetland Inventory (NWI), the 10-year database (2010–2020) of bird observations on Moloka'i by the Hawaiian Islands Conservation Collective (Supplementary Table S2), GIS databases, and expert opinions from managers and landowners on Moloka'i (Pacific Coast Joint Venture, 2006; US Fish and Wildlife Service (USFWS), 2011a, 2011b; Chutz, 2014; Malachowski and Dugger, 2018; Malachowski et al., 2018; Sustainable Resource Group International, 2018; Henry and Fredrickson, 2019; Henry and Fredrickson, 2022; USFWS, 2022). Sites were scored using the 12 criteria in Table 3. A multiplier of two was applied to the 'suitability for T&E and migratory birds after restoration' expert scores, as this criterion was evaluated at all sites and provides a more important indication of potential future habitat value than past bird observations, which were not available at all the sites. To ensure that sites with severe hazards for avian species were distinctly noted, a multiplier of three was applied to this category. The rankings used for each criterion and the details on how ranks were determined are provided in Table 3.

The sixth sub-model was community support. This component is of key importance as without broad-scale support from the largely Native Hawaiian community on Moloka'i, wetland restoration is unlikely to come to fruition or be successful in the long term. Community support was carried out in several steps. First, the project community liaison, Pūlama Lima of Ka Ipu Makani, held one-on-one meetings with key Moloka'i community members. This was followed by a larger community meeting during the rapid assessment work in which the project was explained and there was an open discussion about the 12 sites chosen for prioritization. Next, a score sheet for community support regarding the sites was sent out by the community liaison to each member of the Moloka'i Wetland Partnership (MWP), a coalition of local NGOs and state and federal agencies with extensive knowledge of the natural resources and socio-cultural landscape of Moloka'i. A follow-up meeting was then held to discuss any scores, which were in dispute or not well understood. In this way, each site was ranked as follows: likely community opposition (1), possible community opposition (2), community neutral (3), community supportive (4), and community highly supportive (5). Due to the overarching importance of this sub-model, it received a

weight three times that of all the other sub-models except for sea-level rise, which also received the same weight.

2.6.2 Site suitability analysis

All six sub-models were used to carry out the site suitability analysis in ArcGISPro version 3.0.2. Site suitability analyses have been used in a broad range of applications including wind farm placement, refugee camp establishment, and wetland restoration (White and Fennessy, 2005; Darwiche-Criado et al., 2017; Nasery et al., 2021; Younes et al., 2022) to identify locations with desired characteristics by using weighted criteria defined by the analyst to rank and score potential sites based on how closely they match an ideal set of criteria. In order to prepare the data for the analysis, several steps first needed to be followed. Study area boundaries were manually delineated using high-resolution digital imagery (EagleView Technologies, Inc., 2008) and converted to polygons in the GIS using the NAD 1983 UTM Zone 4N projected coordinate system. Feature classes were created in the GIS for each of the datasets collected in the rapid field assessment. For datasets that contained null values, a proxy was assigned to prevent ArcGIS Pro from excluding the site from the analysis. Each dataset was then spatially joined to the wetland site polygons. Each data attribute was then converted to a raster (cell size of 3 m) with the Polygon to Raster tool. Due to the soil data being collected at two pits within each study area boundary, single rankings for each site had to be calculated for use in the final model scenarios to match the study area boundaries of the other sub-models. After the soil sub-model was run at the pit level, the ranks for each site were determined by averaging the soil pit ranks. The new ranks were then assigned to their respective study area boundary polygons and then converted to a raster (cell size of 3 m) with the Polygon to Raster tool. All the raster data were then uploaded to the ArcGIS Pro (version 3.0.2) Site Suitability Modeler tool.

Because some criteria had higher importance than others, the multiplier weighting method was used (White and Fennessy, 2005) in the site suitability analysis to weight the criteria relative to one another within each sub-model and in the overall suitability model. Any weighting within the individual sub-models was already described above. Weighting among the sub-models for the overall site suitability analysis was carried out in three ways: 1) equal weighting for each sub-model, 2) SLR and community support weighted 2x as high as all the other sub-models, and 3) SLR and community support weighted 3x as high as all the other sub-models. All other parts of the suitability analysis remained the same for the three different runs.

3 Results

3.1 Rapid field assessments and sub-model rankings

3.1.1 Hydrology

During rapid assessments, we determined that all the wetland sites receive at least some groundwater inflow. Because many of the springs are located outside of the wetland boundaries of our sites, we relied on the spring

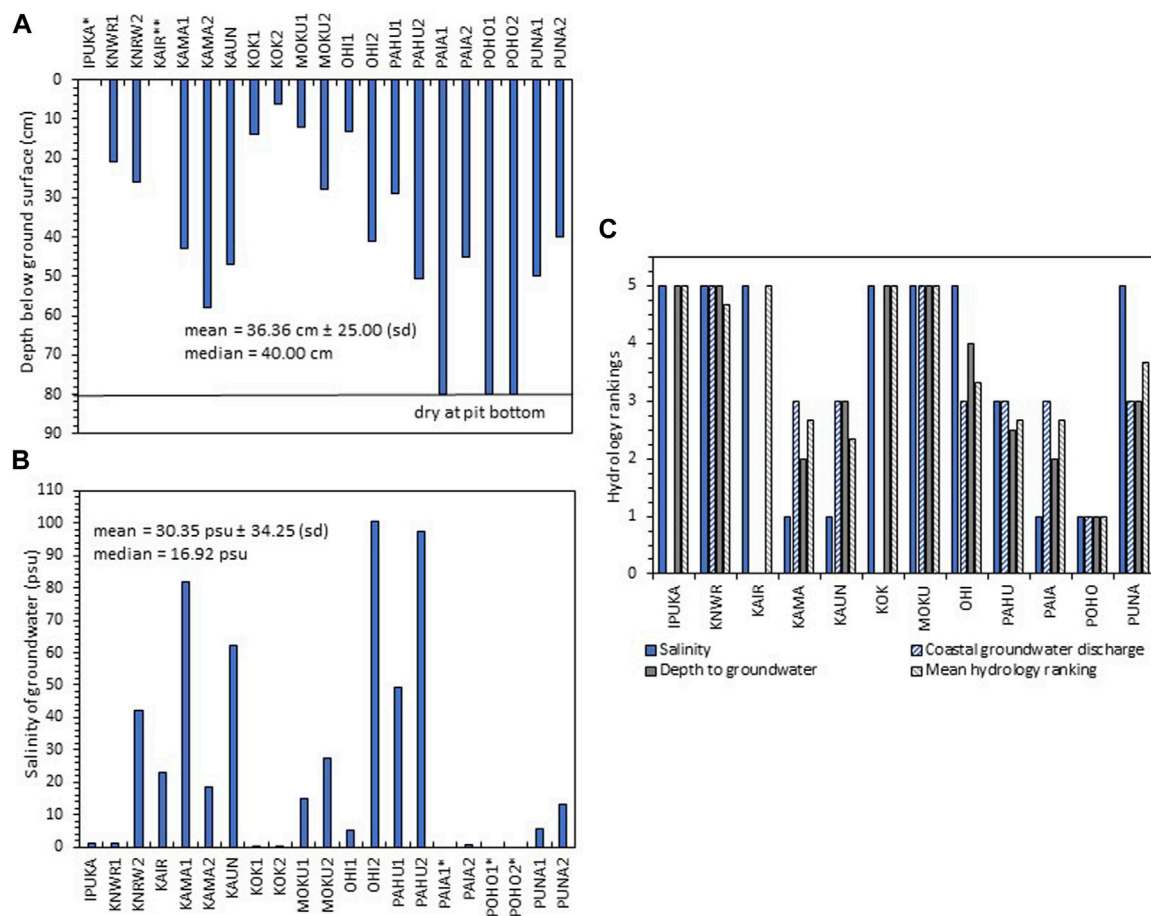


FIGURE 3

(A) Depth to groundwater (the water table) at soil pits at each wetland site during April 2022. Site abbreviations are shown in Table 1. *The water table was at the ground surface at IPUKA. **At KAIR, there was no water table because the site was on lithified sand. For PAIA1, POHO1, and POHO2, the depth to groundwater was below the depth of the pit (80 cm); (B) salinity of groundwater in soil pits in April 2022. Sites without salinity measurements had no water in soil pits; and (C) rankings for salinity, coastal groundwater discharge rate, depth to groundwater, and overall mean hydrology for each of the 12 wetland sites. For sites without available data for one of the three categories, the remaining two categories were averaged instead of all three.

survey by Stearns and MacDonald (1947), which is the most recent to date, to identify springs mauka from our sites. Additional springs/seeps were noted by us at the upland edge of MOKU (Table 1 for site names and their abbreviations). For mauka of KOK, there must be springs or seeps as the groundwater discharge was the strongest of all the sites. However, none were found by Stearns and MacDonald (1947), suggesting either an oversight or a new flow path. Streamflow is intermittent at all sites except PUNA, MOKU, KOK, IPUKA, and KAIR, which have no streams (US Geological Survey, 2019). The measurements of depth to groundwater and salinity illustrate the impact of the ongoing drought on the lowland coastal zone of Moloka'i (Figure 3). Although the water table is usually near the surface in coastal wetlands, the mean depth to groundwater at the sites was 36.36 cm ± 25.00 (sd). At three soil pits, PAIA1, POHO1, and POHO2, the bottom was dry at 80 cm (Supplementary Table S3). The mean groundwater salinity at all the sites was 30.35 psu ± 34.25 (sd) and at soil pits KAMA1, KAUN, OHI2, and PAHUA2 salinities were in the

hypersaline range (>40 psu) (Figure 3B). In contrast, the low salinities and shallow depths to groundwater at KOK1, KOK2, KNWR1, OHI1, and IPUKA demonstrate a high discharge of fresh groundwater at several places along the southern coastline (Supplementary Table S3, Figure 3C). The wetland sites that ranked the highest overall (5) for hydrology were IPUKA, KNWR, KOK, KAIR, and MOKU (Figure 3C, Supplementary Table S3).

3.1.2 Sea-level rise

In the analysis of wetland resilience to future sea-level rise, there were major differences in the migration space and elevation capital among the sites. The mean distance to the nearest upland road (167 m ± 173 (sd)) ranged from 9 m at KOK to almost 600 m at PAHU (Figure 4A). The resilience of the wetland sites to sea-level rise was strong in 2050, as almost all the sites maintained their elevation above MSL except for KAIR (Figure 4B). In 2100, resilience waned with 10 out of 12 sites having projected surface elevations below MSL, which is likely near the lower end of the vegetation elevation range (Figure 4B).

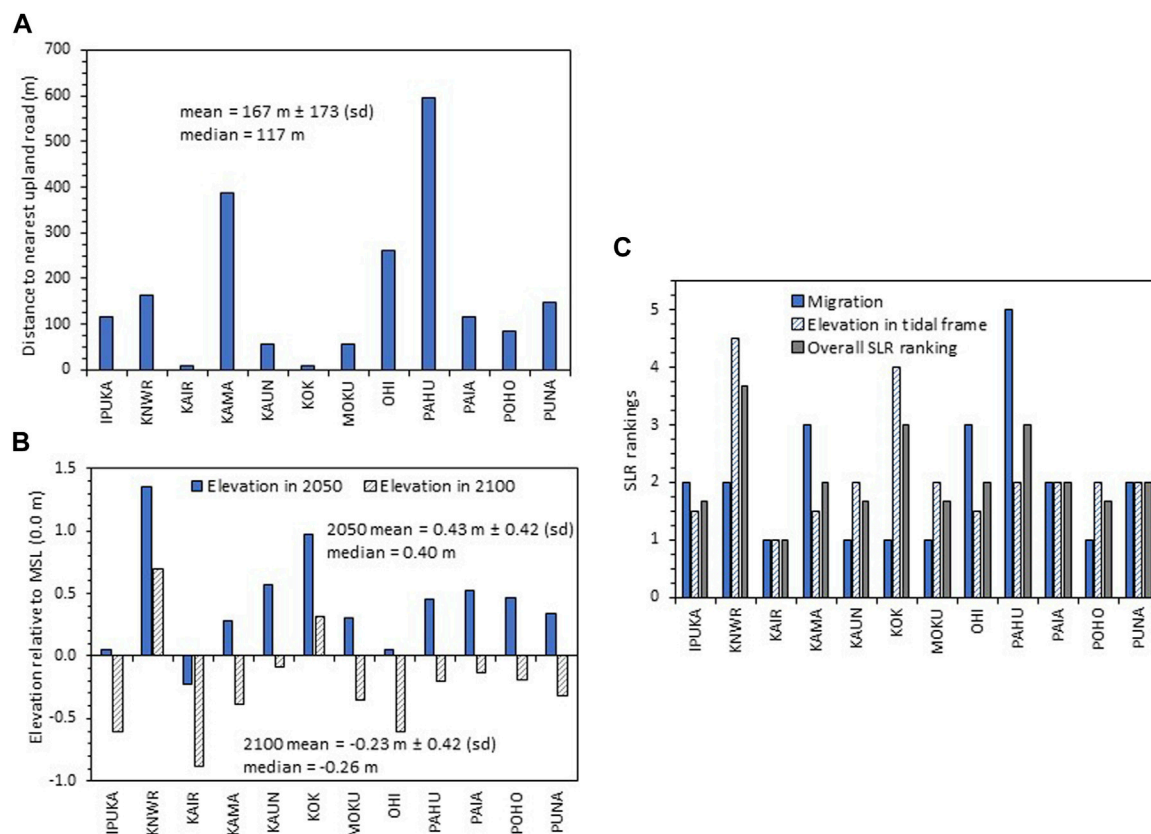


FIGURE 4

(A) Distance to the nearest upland road from the upland border of each of the 12 wetland sites, (B) estimated surface elevation relative to mean sea level (MSL) (0.0 m) for each wetland assuming 3 mm/yr of vertical accretion and incorporating sea-level rise (SLR) projections for 2050 and 2100 from Table 3, and (C) overall mean SLR rankings based on migration potential (weighted 1x) and mean elevation relative to MSL for 2050 and 2100 (weighted 2x).

Overall, the highest overall sea-level rise rankings (3 or higher) were found for KNWR, KOK, and PAHU (Supplementary Table S4; Figure 4C).

3.1.3 Soils

Basic soil characteristics varied broadly across the sites. Soil texture ranged from loamy sands to silt and silty clays (Supplementary Table S5). The mean % OC across the wetland sites was $10.93\% \pm 12.24$ (sd) (Figure 5A). IPUKA, which had no soil *per se*, had a floating mat of vegetation estimated to contain ~44% OC (Byrd et al., 2018). Most sites contained mineral soil except KOK and PUNA, which have organic soils due to their high % OC content (Figure 5A) (USDA-NRCS, 2014). All of the sites except for KOK and IPUKA are situated under reddish brown steep slopes described by gSSURGO as “very stony land-eroded” (Soil Survey Staff, 2021). Reddish brown material was seen in the top layers of many soil pits and the coastal waters, demonstrating chronic erosion and transport of materials from the uplands to the sea. Six sites had overall soil rankings above 4 (Figure 5B).

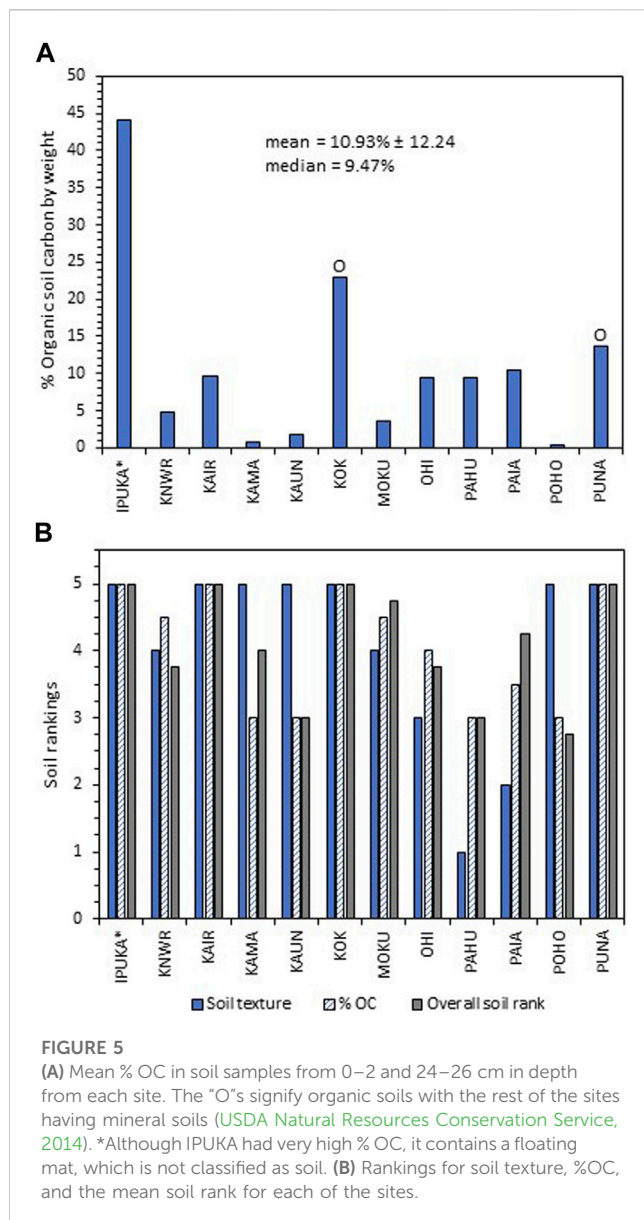
3.1.4 Vegetation

The vegetation survey demonstrated that the coastal flora on Moloka'i contains a high proportion of non-native species dominated by mangroves, pickleweed, and Indian fleabane

(Supplementary Tables S6–S10). There were 39 plant species found overall at the wetland sites. Of this total, 22% or 13 were not wetland species. Of the 26 wetland plant species, 11 were native, one was introduced by Polynesians, and 14 were non-native (Supplementary Table S7). The most diverse plant life form was trees. However, seven of the nine tree species were exotic (non-native) in origin (Supplementary Table S7). Sedges were the next most numerous plant form (seven species), with three native species. Overall, the non-native wetland plant species richness (mean = 3.33 ± 1.92 (sd)) at the wetland sites was slightly greater than the native wetland plant species richness (mean = 2.08 ± 2.02 (sd)) (Figure 6A, Supplementary Table S8), but the difference was not statistically significant (Student's t-test, $p > 0.05$). The number of native species and/or the proportion of native to non-native wetland species resulted in KAIR, KOK, and OHI ranking the highest overall for vegetation (all >4 ; Figure 6B, Supplementary Table S9).

3.1.5 Birds

The assessment of bird habitat value, which consisted of 12 separate criteria (Table 3), ranged from a total score of 55 at POHO to 105 at OHI (Table 4, Supplementary Table S11). It is important to note that PAIA was not included in the rankings due to strong community opposition to restoration of the site (see below).



The criteria with the highest consistent rankings among the sites were potential suitability for T&E birds (mean = 3.5) and managed human disturbance and hazards (means of both = 3.4). The criteria with the lowest scores across the sites were restoration status (mean = 1.9) and adequate predator control (mean = 2.1) (Table 4, Supplementary Table S11). Four sites (KNWR, KAMA, PAHU, and PUNA) ranked above “4” in “potential suitability after restoration for all threatened and endangered waterbirds, migratory shorebirds, and migratory waterfowl” (Table 4). The top ranking sites based on suitability for birds were OHI (5), PUNA (5), KAMA (4), PAHU (4), and KNWR (4) (Table 4).

3.1.6 Community support

The local community expressed support for coastal wetland restoration at eight of the 12 wetland sites (Figure 7). The site rankings were particularly high (rank of 5) for KNWR, KAMA, and KOK. This high level of support was indicative of a broad, shared community vision of restoration at these sites. In contrast,

for PAIA, there was no shared vision for restoration and, thus, no discussion of support due to past trauma from island development efforts, issues around maintaining access for hunting and fishing, and a lack of trust regarding state and federal agencies (Figure 7; Supplementary Table S12). The main concerns raised about wetland restoration included maintaining access for hunting and fishing, protecting sites with iwi kupuna (ancestral bones), the need to include the community in the planning and restoration process, and a desire to see indigenous agro-ecology (lo‘i kalo and loko i‘a) included in wetland restoration planning (Supplementary Table S12).

3.2 Site suitability analysis results

The overall rankings of the 12 wetland sites for restoration suitability were quite similar across the three different weighting approaches (Table 5). The top three sites were KOK, KNWR, and OHI. KOK scored 5’s in hydrology, soils, vegetation, and community support and 3’s in birds and SLR. KNWR scored 5’s in hydrology and community support, 3.75 in soil, 2 in vegetation, 4 in birds, and 3.67 in SLR. OHI scored a 5 in birds, 3.33 in hydrology, 3.75 in soils, 4.5 in vegetation, 2.0 in SLR, and 4 in community support. The bottom three sites, KAUN, PAIA, and POHO, held steady across the three approaches. All three of these sites scored particularly low in SLR and community support and should not be considered further for restoration. The top six sites across all six sub-models, KOK, KNWR, OHI, PUNA, KAMA, and MOKU, constitute an actionable blueprint for restoration actions on Moloka‘i.

4 Discussion

We conducted a comprehensive analysis to prioritize the restoration of 12 coastal wetlands on the island of Moloka‘i using available spatial data, rapid field assessments of site hydrology, soils, birds, and vegetation, a comprehensive bird habitat assessment, sea-level rise projections for 2050 and 2100, and a GIS site suitability analysis using all assembled data (Table 5). In the rapid field assessment, we found a high level of wetland degradation across the 12 sites, which is not surprising as coastal wetlands across Hawai‘i, the Pacific region, and elsewhere have long been altered from their original condition or lost completely due to development, conversion to agriculture, and other forms of land use change (Erickson and Puttock, 2006; McGlone, 2009; Murray et al., 2022). Overall, our study reveals a great potential to restore coastal wetlands into ecosystems “thriving with life” as described long ago in the waters of Kāne mele (Figure 2). The following sections describe what we learned about these understudied systems and how our site suitability analysis provides the first step in actualizing a vision for wetland restoration across the island.

4.1 Classification of Hawaiian coastal wetlands

We found a range of Hawaiian coastal wetlands in our rapid field assessments with diverse hydrology, salinity, geomorphology,

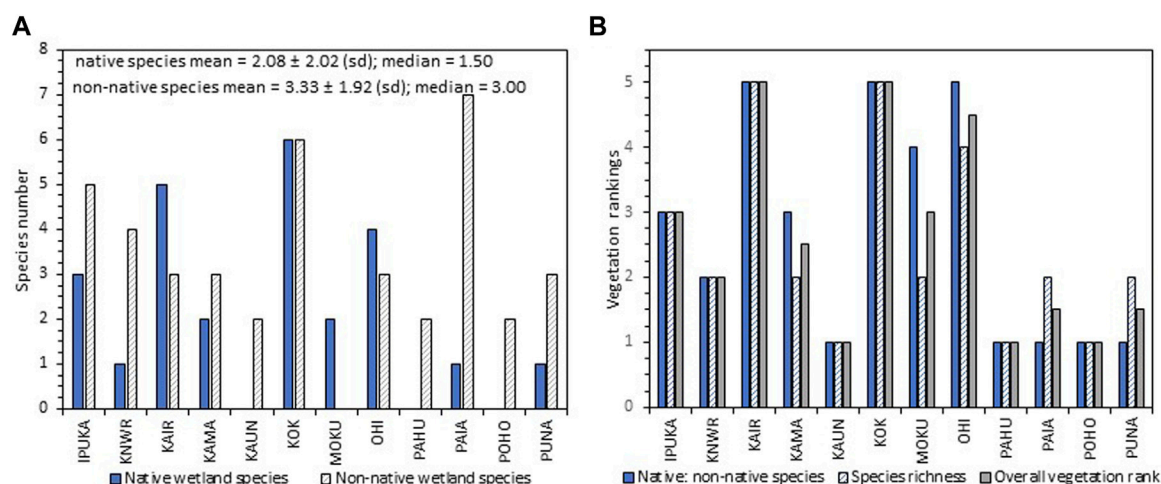


FIGURE 6

(A) Numbers of native and non-native wetland plant species at each site and (B) ranks for the proportion of native: non-native wetland plant species, species richness of native wetland plants, and the overall vegetation rank for each of the sites.

vegetation, and soils (Figures 3–6, Supplementary Table S3, Supplementary Tables S5–S10). Because of this, our results expand upon the previous “tidal flat” classification of coastal wetlands by Erickson and Puttock (2006), which were all described as groundwater driven, saline or brackish, situated in a floodplain, and containing mineral soils (Figure 8). Our study demonstrates that the characteristics of Hawaiian coastal wetlands are much broader: 1) hydrology is typically either groundwater and tidally driven or precipitation and groundwater driven, 2) salinity ranges from fresh to saline, (3) geomorphology includes coastal lowlands (flats) and coastal depressions, and (4) substrate can consist of organic soil, mineral soil, or lithified sand. The most common types of wetlands are mudflats, coastal shrub wetlands, non-native mangrove swamps, and herbaceous marshes (Figure 8).

In addition to these common wetland types, we found two unusual kinds of wetlands. The first is a groundwater-fed, coastal freshwater herbaceous marsh containing organic “peat” soil (KOK), otherwise known as a coastal fen. Peatlands have long been known to occur on summits and relatively flat montane areas in the Hawaiian Islands, but these wetlands are supported by precipitation, causing them to fall into the category of bogs (MacCaughey, 1916; Vogl and Henrickson, 1971). Although groundwater is known to support coastal wetlands in Hawai’i (Hill, 1996), coastal fens, which are common in temperate, boreal, and some tropical climates (Dommain et al., 2014; Toro et al., 2022), have yet to be noted in the Hawaiian Islands. The success of the lo’i kalo (taro patch) at KOK demonstrates that such Hawaiian coastal fens are highly complementary for producing this staple food source. This is no surprise to Native Hawaiians, who have traditionally used such ecosystems to grow taro and refer to them as lo’ipūnāwai (spring ponds; Pukui and Elbert, 1986). Coastal groundwater-fed wetlands, both fens and marshes with mineral soils, were likely numerous across the Hawaiian Islands before conversion to other uses, but now only few remain at reserves such as the James Campbell National Wildlife Refuge on Oahu and the Waihe’e Coastal Dunes and

Wetlands Refuge on Maui (Henry and Frederickson, 2013; Hawaiian Islands Land Trust, 2023).

The second unusual wetland type from our assessment is a novel coastal depressional wetland containing herbaceous vegetation, shrubs, and trees, which lies on a very thin veneer (a few cm) of soil over rock hard, lithified sand. The wetland (KAIR) is supported by precipitation and brackish groundwater. It was thought to have been an ancient fish pond and was rebuilt as one in the 1920s but fell out of operation by 1928 (Wyban, 1993; Fung Associates Inc. and SWCA Environmental Consultants, 2010). It is unclear exactly when the sand hardened into an impenetrable surface, but it could have formed during or after the construction of the newer pond. These days, KAIR floods after major rain storms and stays inundated for many months a time (Wyban, 1993; Supplementary Figure S1).

The presence of two highly unusual wetlands among just 12 sites strongly suggests that more study may be needed to describe the full diversity of coastal wetlands in Hawai’i.

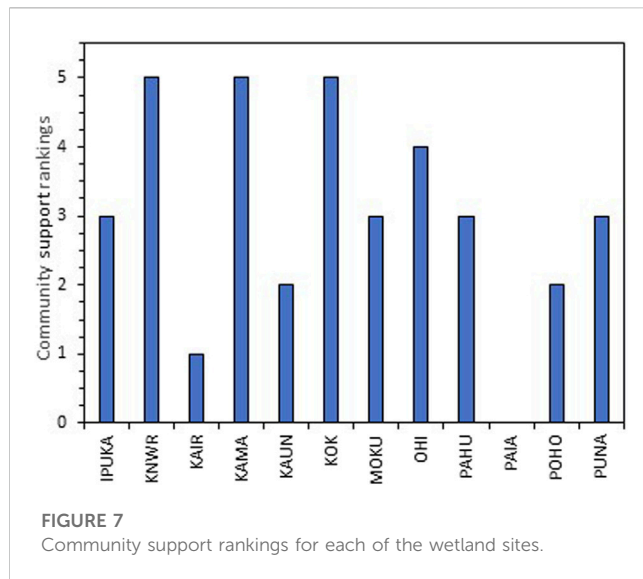
4.2 Site assessments and sub-model rankings

4.2.1 Hydrology and soils

All of the sites receive at least some groundwater inflow. However, erosion from the uplands has resulted in some springs and seeps being at least partially buried under deposited materials (e.g., MOKU and KNWR) and fine silts being carried across the wetlands to nearshore environments (Stock et al., 2011). At some of the sites, the restoration process will need to include the excavation of springs and regrading of the wetland surface so that the site can sit closer to the water table. The degradation of springs from sedimentation and drought has caused salinity levels to climb to the hypersaline range in four of the sites (KAMA, KAUN, OHI, and PAHU; Figure 3B). This situation will need to be remedied in order to create conditions conducive for native plant recruitment (Zedler, 1982; Alexander and Dunton, 2002). Half the sites had % cover of

TABLE 4 Ranks for bird habitat value for threatened and endangered waterbirds (T&E).

Wetland	Site area rank	Current freshwater availability	Proximity to other wetlands	Hazards—(unfenced roads, powerlines, and other unsafe conditions)	Adequate predator control or likely capacity to implement	Botulism control or likely capacity to implement	Human disturbance managed	Restoration status ranking	Breeding recorded on site from 2010 to 2020	Average T&E bird count from 2010 to 2020	Species richness of all T&E, migratory shorebirds, and migratory waterfowl	Mean potential suitability after restoration for T&E, migratory shorebirds, and migratory waterfowl	Final ranking: <64 points (1), 65–74 (2), 75–84 (3), 85–94 (4), and >95 (5)
IPUKA	1	5	1	3	1	1	5	1	No data	No data	No data	2.7	1
KNWR	5	1	4	3	3	3	3	4	0	1	1	4.5	4
KAIR	1	2	1	5	2	3	5	1	No data	No data	No data	2.5	2
KAMA	5	3	4	3	1	2	3	2	5	1	2	4.7	4
KAUN	3	5	4	1	4	4	5	1	15	5	5	2.3	3
KOK	1	5	1	3	4	4	5	5	No data	No data	No data	3.3	3
MOKU	1	1	5	3	2	1	1	1	5	1	1	3.0	2
OHI	3	3	4	3	2	1	3	3	10	3	4	3.0	5
PAHU	5	3	3	3	2	2	5	1	5	2	3	5.0	4
PAIA	--	--	--	--	--	--	--	--	--	--	--	--	1
POHO	5	1	2	5	1	1	1	1	No data	No data	No data	2.3	1
PUNA	5	3	3	5	1	2	1	1	5	1	2	4.8	5
<i>Overall mean of sites</i>	3.2	2.9	2.9	3.4	2.1	2.2	3.4	1.9	--	--	--	3.5	2.8



bare ground greater than 10% (Supplementary Table S7) and in most of these sites, there was precipitated salt on the soil surface (Supplementary Figure S1). Despite these impacts, however, half the sites had soil texture and % OC highly suitable for restoration (a ranking of “4” or above, Figure 5B).

At several sites, the water quality was fresh due to high groundwater discharge along the coastline (Figure 3). Previous work on Moloka'i has shown that a great volume of groundwater travels along flow paths from the ridge to the reef (Oki et al., 2019). As a case in point, groundwater salinity at the KOK soil pits, practically adjacent to the sea, were both 0.5 psu, which is indicative of a *freshwater* ecosystem (Cowardin et al., 1979). The ubiquitous presence of groundwater resulted in half the sites scoring a “4” or higher in their overall hydrologic ranking (Figure 3C).

4.2.2 Sea-level rise

The results of the sea-level rise analysis showed that the elevation capital of the microtidal coastal wetlands on Moloka'i appears to be modest. Most sites are likely resilient to SLR until 2050, but after that, resilience will likely wane dramatically (Figure 4, Supplementary Table S4). It is important to note that these projections for sustainability under sea-level rise have large uncertainties. Due to a major deficit in wetland data such as the vertical accretion rates of sediments and peat, elevation ranges in the tidal frame suitable for dominant vegetation, and primary productivity of coastal wetlands, no marsh sustainability modeling could be performed. Furthermore, the sea-level rise estimates used were for passive flooding only and, thus, did not include wave-induced flooding, yearly variability of sea-level from natural processes including the El Niño–Southern Oscillation, or any additional impacts due to coastal erosion, which can all increase the extent and depth of flooding (Drexler and Ewel, 2001; Anderson et al., 2018; Goodman et al., 2018).

Despite these limitations, the SLR analysis raises some important points about the state of knowledge concerning coastal wetlands on Moloka'i. First, there are some key opportunities (e.g., KAMA and PAHU) for marsh migration (Figure 4) on the island. Second, there is a great need to improve the process-level understanding of coastal wetlands of Hawai'i. In particular, greater knowledge of the two components of vertical accretion, organic matter accumulation and inorganic sedimentation rates, is needed as the first step toward improving projections of coastal wetland resilience.

4.2.3 Vegetation

Non-native, invasive plant species were ubiquitous at the sites, particularly mangroves and pickleweed (Table 1). Mangrove cover was $\geq 36\%$ at KAMA, KAUN, PAHU, PAIA, and PUNA. Monotypic cover of pickleweed was $\geq 26\%$ at KAMA, KAUN, OHI, PAHU, POHO, and PUNA (Supplementary Table S6). Invasive vegetation

TABLE 5 Overall site scores and ranks from the site suitability analysis using three different weighting approaches.

Site names	Equal weighting	Ranks with equal weighting	Site names	SLR and community support weighted 2x	Ranks with SLR and community support weighted 2x	Site names	SLR and community support weighted 3x	Ranks with SLR and community support weighted 3x
KOK	26.00	1	KOK	34.00	1	KOK	42.00	1
KNWR	23.08	2	KNWR	31.75	2	KNWR	40.42	2
OHI	22.58	3	OHI	28.58	3	OHI	34.58	4
PUNA	20.17	4	KAMA	27.17	4	KAMA	34.17	3
KAMA	20.17	5	PUNA	25.17	5	PUNA	30.17	5
MOKU	19.42	6	MOKU	24.08	6	MOKU	28.75	6
KAIR	19.00	7	IPUKA	23.33	7	PAHU	28.67	7
IPUKA	18.67	8	PAHU	22.67	8	IPUKA	28.00	8
PAHU	16.67	9	KAIR	21.00	9	KAIR	23.00	9
KAUN	13.00	10	KAUN	16.67	10	KAUN	20.33	10
PAIA	12.42	11	PAIA	15.42	11	PAIA	18.42	11
POHO	9.42	12	POHO	13.08	12	POHO	16.75	12

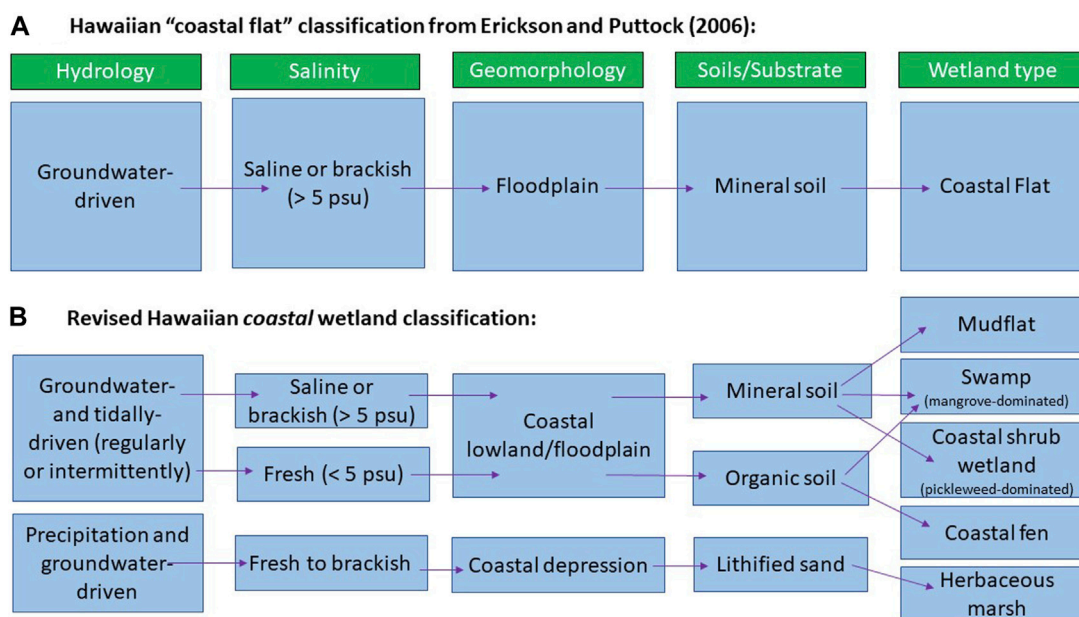


FIGURE 8
(A) Classification of Hawaiian coastal flats by Erickson and Puttock (2006) and (B) revised classification for Hawaiian coastal wetlands based on this study.

will need to be controlled and native species will need to be planted in order to regain some of original plant diversity. Only three sites (OHI, KAIR, and KOK) scored “4” or higher in the vegetation rankings, demonstrating that even having a handful of native wetland species is a high bar (Supplementary Table S7). Overall, plant species richness across all the sites was low (39 species), with only 11 native wetland plants (Figure 6; Supplementary Tables S7–S9). This may be due to competition from invasive plants, or similar to native Hawaiian forests, low plant diversity may have always been the case due to the extreme isolation of the Hawaiian archipelago (Barton et al., 2021).

4.2.4 Bird habitat value

Although proper hydrology, vegetation, soils, and resilience to SLR are critical for restoring tidal wetlands, these basic wetland components are insufficient to adequately support sensitive wildlife. Endangered species, such as the Hawaiian stilt, Hawaiian coot, and Hawaiian duck, are conservation reliant (Harmon et al., 2022), requiring special protections against predators, avian botulism, the encroachment of invasive plant species, and human disturbance (Greer, 2005; US Fish and Wildlife Service, 2011a; Underwood et al., 2014; Malachowski et al., 2022). Predator control, in particular, is of critical importance to protect endangered waterbirds from a suite of non-native species including cats (*Felis catus*), dogs (*Canis familiaris*), pigs (*Sus scrofa*), mongooses (*Herpestes javanicus*), Black, Norwegian, and Polynesian rats (*Rattus rattus*, *Rattus norvegicus*, and *Rattus exulans*), bullfrogs (*Rana catesbeiana*), introduced barn owls (*Tyto alba*), cattle egrets (*Bubulcus ibis*), and the common myna (*Acridotheres tristis*) (Greer, 2005; US Fish and Wildlife Service, 2011a; Underwood et al., 2014). Our analysis showed that breeding and bird counts were low for endangered waterbirds across the sites (Table 4). Furthermore, several of the top

rated sites for bird habitat (OHI, PUNA, KNWR, KAMA, and PAHU) had low ratings for predator and botulism control due to a lack of management (Table 4). Although even simple ponds can provide habitat for endangered waterbirds (including wastewater treatment ponds containing raw sewage (KAUN)), unmanaged sites can act as ‘sinks’ with high mortality, especially for chicks, due to the abovementioned threats (Christensen et al., 2021; Harmon et al., 2021). The recovery of endangered waterbirds in Hawaiian wetlands depends on restoring and expanding high-quality habitat combined with strong protections from predators, hazards, and diseases.

4.2.5 Community support

Public support and local stakeholder involvement have been shown to be critical for conservation efforts, restoration projects, and sustainable resource management (Lee, 2011; Doyle-Capitman et al., 2018; Wilkins et al., 2018). We engaged with the Molokaʻi community at multiple times in our study in order to achieve coproduction of knowledge (Meadow et al., 2015). This process relied strongly on our community liaison and the Molokaʻi Wetland Partnership to effectively engage with residents. This effort allowed us to gain valuable insights about community support regarding our sites. For example, in the beginning of our work, we considered PAIA to be a strong contender for restoration, but as mentioned above, the failed development efforts at this site caused deep trauma for local residents, causing them to omit PAIA from consideration. Ultimately, PAIA received very low scores overall (Table 5). Knowledge of site history and perspectives on “landscape frame,” the environmental vision for the landscape of a person or community, are essential for truly understanding community preferences for restoration (Aggestrom, 2014). Furthermore, there must be strong consideration of local community needs (Doyle-Capitman

et al., 2018), which for Moloka'i include hunting, fishing, and socio-cultural resources.

4.3 Site prioritization

The three different weighting approaches used in the site suitability analysis resulted in KOK, KNWR, OHI, PUNA, KAMA, and MOKU being ranked as the top six sites and KAUN, PAIA, and POHO as the lowest, effectively removing them from further consideration (Table 5). The specific sub-models we used to arrive at this prioritization of sites differ in important ways from most previous studies, which have ranked wetlands for restoration based solely on watershed attributes and specific wetland properties (White and Fennessey, 2005; Ouyang et al., 2011; Horvath et al., 2017; Qu et al., 2018; Medland et al., 2020). In our study, we incorporated community support in addition to wetland attributes and did so before any new restoration activities. The few studies we found that incorporated public opinion did so after wetland restoration was completed, which is useful for improving future actions, but may result in lost opportunities to build trust and community support during the process (Aggestrom, 2014; Sun et al., 2015; Doyle-Capitman et al., 2018). Our approach was the first, to our knowledge, to incorporate projected sea-level rise, which is critical for estimating future coastal wetland resilience. In the future, when more coastal wetland data become available for Moloka'i and neighboring islands, our suitability "tool" could be improved by directly incorporating projections from marsh sustainability models and migration models into the analysis (e.g., Fagherazzi et al., 2020; Morris et al., 2022). Finally, although some studies prioritizing sites for wetland restoration have included bird habitat suitability (Hua et al., 2016; Maleki et al., 2018), our extensive analysis, particularly for endangered waterbirds, outlines specific habitat requirements needed to set the stage for recovery of these endemic Hawaiian species (Table 4; Supplementary Table S11).

The suitability analysis created in this study can be used to rank any additional coastal wetlands on Moloka'i. It can also be applied elsewhere in Hawai'i, but it would need to be adapted to the more developed landscape and the particular needs of the local communities and stakeholders. Beyond application in other places, there is also the option to use this approach for prioritizing the cultural value of sites or various management actions such as increasing carbon sequestration on the landscape or employing nature-based solutions to reduce flooding, nutrient loading, and/or sedimentation. Clearly, one of the main strengths of the suitability analysis approach is that it can be expanded and adapted to accommodate particular uses depending on user needs (Lovette et al., 2018).

4.4 A vision for wetland restoration on Moloka'i

Although wetland restoration has been conducted in Hawai'i since at least the early 1980s (Tummons, 2011), we are not aware of any landscape-scale restoration efforts. The top six sites in this study represent over 66 ha (163 acres) of coastal wetlands along the south

shore, and all of them are within a few kms from at least one other site (Figure 2). Three of the six highly ranked sites are already owned by the state or federal government (Table 1; Figure 2), which could facilitate restoration actions because land purchase would not be needed. There are other potential sites in this area that have yet to be assessed for restoration. The opportunity to restore multiple sites along the south shore of Moloka'i is a rare chance to enact a landscape-scale recovery of wetland habitat in the Hawaiian Islands (Henry, 2016).

The top ranked sites offer an opportunity to restore essential habitat for endangered waterbirds, invertebrates, and native plants as well as reignite the socio-ecological ties of the largely Native Hawaiian community to coastal wetlands. Historically, managed wetlands or lo'i kalo were "keystone" components of the Native Hawaiian socio-ecological system because they constituted the major source of complex carbohydrates in the diet and dominated the lowland landscape in all areas wet enough to sustain them (Gon III et al., 2018; Winter et al., 2018). Recently, there has been renewed interest in traditional agro-ecology as a way to reduce dependence on imported food, regain island sustainability, and reach biodiversity goals (Gon III and Winter, 2019; Harmon et al., 2021). The restoration of coastal wetlands on Moloka'i could be a major component of this renaissance. In particular, the restoration of wetland *mosaics* containing lo'ipūnāwai, lo'ko i'a, and tidal marshes could provide food and cultural resources for local communities and a range of habitat types for flora and fauna.

Much of the lost wetland area across Hawaiian Islands has already been developed (Van Rees and Reed, 2013). Furthermore, sea-level rise threatens urbanized wetland complexes across the state (Henry, 2016). The wetland restoration opportunities available on Moloka'i could reverse some of the degradation and habitat loss resulting from previous land uses and inspire further restoration along the ridge to reef continuum (Stock et al., 2011; Jacobi and Stock, 2017). The restoration of tidal wetlands is preferable sooner than later due to the need to procure migration space and establish wetland functions before the anticipated acceleration in SLR later in the century (Morris et al., 2022; Sweet et al., 2022). Our site rankings are just the first steps in a long process, but hopefully they will serve as a catalyst for revitalization of coastal wetlands on Moloka'i for the benefit of the Native Hawaiian community and a wide range of native wetland species.

Data availability statement

Data on soils, hydrology, vegetation, sea-level rise and migration potential, bird habitat value, and community support are provided in Supplementary Tables S1–S12. The data collected by the U.S. Geological Survey on wetland soils, hydrology, and vegetation are also available in Drexler et al. (2023) at the ScienceBase Repository, <https://doi.org/10.5066/2FP99XSP28>.

Author contributions

All authors except SH participated in the collection of field data. JD wrote the paper with assistance from HR, JJ, PL, and SH. JJ, HR, PL, AD-Y, WH, BW, and JD prepared the rankings and SH carried out the site suitability analysis. All authors contributed to the article and approved the submitted version.

Funding

This work was funded by the USGS Pacific Islands Climate Adaptation Science Center. In-kind support was provided by the affiliations of each of the co-authors.

Acknowledgments

The authors are grateful to Gordon Tribble and Delwyn Oki for their hydrologic expertise, Phil Scoles for his extensive knowledge of wetland soils, and the two journal reviewers and Ken Krauss for improving the manuscript. They thank Nancy McPherson (Department of Hawaiian Home Lands) for helping them understand and incorporate Native Hawaiian perspectives. They acknowledge the importance of the Moloka'i Wetland Partnership in bringing this effort to fruition. Any use of trade, firm, or product names is for descriptive purposes only and does not imply endorsement by the U.S. Government. The authors dedicate this first paper of the Moloka'i Wetland Partnership to the memory of Fern P. Duvall II, a 38-year employee of the Hawai'i DLNR Division of Forestry and Wildlife and a long-time board member of the Pacific Birds Habitat Joint Venture, who had long envisioned the possibilities for wetland restoration on the island of Moloka'i.

References

- Aggestrom, F. (2014). Wetland restoration and the involvement of stakeholders: An analysis based on value-perspectives. *Landsc. Res.* 39, 680–697. doi:10.1080/01426397.2013.819076
- Alexander, H. G., and Dunton, K. H. (2002). Freshwater inundation effects on emergent vegetation of a hypersaline salt marsh. *Estuaries* 25 (6B), 1426–1435. doi:10.1007/bf02692236
- Anderson, T. R., Fletcher, C. H., Barbee, M. M., Romine, B. M., Lemmo, S., and Delevaux, J. M. S. (2018). Modeling multiple sea level rise stresses reveals up to twice the land at risk compared to strictly passive flooding methods. *Sci. Rep.* 8, 14484. doi:10.1038/s41598-018-32658-x
- Athens, J. S., Ward, J. V., and Wickler, S. (1992). Late Holocene lowland vegetation. *O'ahu, Hawai'i*. New Zeal. J. Arch. 14, 9–34.
- Bamber, J. L., Oppenheimer, M., Kopp, R. E., Aspinall, W. P., and Cooke, R. M. (2019). Ice sheet contributions to future sea-level rise from structured expert judgment. *Proc. Natl. Acad. Sci. U.S.A.* 116, 11195–11200. doi:10.1073/pnas.1817205116
- Barton, K. E., Westerband, A., Ostertag, R., Stacy, E., Winter, K., Drake, D. R., et al. (2021). Hawai'i forest review: Synthesizing the ecology, evolution, and conservation of a model system. *Perspect. Plant Ecol. Evol. Syst.* 52, 125631. doi:10.1016/j.ppees.2021.125631
- Berkes, F., and Folke, C. (1998). "Linking social and ecological systems for resilience and sustainability," in *Linking social and ecological systems: Management practices and social mechanisms for building resilience*. Editors F. Berkes and C. Folke (Cambridge, England: Cambridge University Press).
- Burney, D. A., James, H. F., Burney, L. P., Olson, S. L., Kikuchi, W., Wagner, W. L., et al. (2001). Fossil evidence for a diverse biota from Kauai and its transformation since human arrival. *Ecol. Monogr.* 71 (4), 615–641. doi:10.1890/0012-9615(2001)071[0615:fefad]2.0.co;2
- Burney, D. A. (1997). Tropical islands as paleoecological laboratories: Gauging the consequences of human arrival. *Hum. Ecol.* 25, 437–457. doi:10.1023/a:1021823610090
- Byrd, K. B., Ballanti, L., Thomas, N., Nguyen, D., Holmquist, J. R., Simard, M., et al. (2018). A remote sensing-based model of tidal marsh aboveground carbon stocks for the conterminous United States. *ISPRS J. Photogramm. Remote Sens.* 139, 255–271. doi:10.1016/j.isprsjprs.2018.03.019
- Cahoon, D. R., McKee, K. L., and Morris, J. T. (2020). How plants influence resilience of salt marsh and mangrove wetlands to sea-level rise. *Estuaries Coast* 44, 883–898. doi:10.1007/s12237-020-00834-w
- Christensen, D., Harmon, K., Wehr, N., and Price, M. (2021). Mammal-exclusion fencing improves the nesting success of an endangered native Hawaiian waterbird. *PeerJ* 9, e10722. doi:10.7717/peerj.10722
- Chutz, J. (2014). *Kakahai'a national Wildlife refuge - Hawai'i wetland information network. Wetland site description*. California, CA, United States: Pacific Coast Joint Venture.
- County of Maui (2020). County of Maui office of economic development. <https://www.hisbdc.org/business-research-library/maui-county-data-book/>.
- Cowardin, L. M., Carter, V., Golet, F. C., and LaRoe, E. T. (1979). *Classification of wetlands and deepwater habitats of the United States*. FWS/OBS-79/31. Washington, DC, United States: US Fish and Wildlife Service. Available at <http://www.npwrc.usgs.gov/resource/1998/classwet/classwet.htm>.
- Craft, C. B. (2016). "Tidal marshes," in *Creating and restoring wetlands from theory to practice* (Amsterdam, Netherlands: Elsevier).
- Cuddihy, L. W., and Stone, C. P. (1990). *Alteration of native Hawaiian vegetation: Effects of humans, their activities, and introductions*. Honolulu, Hawaii, United States: University of Hawai'i Press.
- Dommain, R., Couwenberg, J., Glasser, P. H., Joosten, H., and Suryadiputra, I. N. N. (2014). Carbon storage and release in Indonesian peatlands since the last deglaciation. *Quat. Sci. Rev.* 97, 1–32. doi:10.1016/j.quascirev.2014.05.002
- Doyle-Capitman, C. E., Decker, D. J., and Jacobson, C. A. (2018). Toward a model for local stakeholder participation in landscape-level wildlife conservation. *Hum. Dimens. Wildl.* 23, 375–390. doi:10.1080/10871209.2018.1444215
- Drexler, J. Z., and Ewel, K. C. (2001). Effect of the 1997–1998 ENSO-related drought on hydrology and salinity in a Micronesian wetland complex. *Estuaries* 24 (3), 347–356. doi:10.2307/1353237
- Drexler, J. Z., Jacobi, J. D., and House, S. F. (2023). *Moloka'i, Hawai'i rapid assessment of hydrology, soils, and vegetation in coastal wetlands 2022*. U.S. Geological Survey data release. doi:10.5066/P99XSP28
- Drexler, J. Z., Khanna, S., and Lacy, J. R. (2021). Carbon storage and sediment trapping by *Egeria densa*, Planch., a globally invasive, freshwater macrophyte. *Sci. Total Environ.* 755, 142602. doi:10.1016/j.scitotenv.2020.142602
- EagleView Technologies Inc. (2008). EagleView Reveal [orthomosaic map]. Retrieved from <https://explorer.pictometry.com/>.
- Edwards, T. L., NowickiMarzeionHock, S. B. R., Goelzer, H., Seroussi, H., et al. (2021). Projected land ice contributions to twenty-first-century sea level rise. *Nature* 593 (7857), 74–82. doi:10.1038/s41586-021-03302-y
- Emerson, N. B. (1909). *Unwritten literature of Hawai'i: The sacred songs of the hula*. Smithsonian institution. Bulletin. Washington, D.C., United States: Bureau of American Ethnology.
- Erickson, T. A., and Puttock, C. F. (2006). *Hawai'i wetland field guide*. Honolulu, Hawaii, United States: Bess Press Books.

Conflict of interest

The authors declare that the research was conducted in the absence of any commercial or financial relationships that could be construed as a potential conflict of interest.

Publisher's note

All claims expressed in this article are solely those of the authors and do not necessarily represent those of their affiliated organizations, or those of the publisher, the editors, and the reviewers. Any product that may be evaluated in this article, or claim that may be made by its manufacturer, is not guaranteed or endorsed by the publisher.

Supplementary material

The Supplementary Material for this article can be found online at: <https://www.frontiersin.org/articles/10.3389/fenvs.2023.1212206/full#supplementary-material>

- Fagherazzi, S., Mariotti, G., Leonardi, N., Canestrelli, A., Nardin, W., and Kearney, W. S. (2020). Salt marsh dynamics in a period of accelerated sea level rise. *JGR. Earth Surf.* 125, e2019JF005200. doi:10.1029/2019JF005200
- Fish, U. S., and Service, Wildlife (2011b). Kakahai'a national wildlife refuge comprehensive conservation plan and environmental assessment. <https://www.fws.gov/pacific/planning/main/docs/HIPI/Maui/Kakahai'a%20NWR%20DCCP-EA.pdf>.
- Fish, U. S., and Service, Wildlife (2021). National wetlands inventory. Available at <https://www.fws.gov/wetlands/Data/State-Downloads.html>.
- Fish, U. S., and Service, Wildlife (2022). *National wetlands inventory*. Washington, D.C., United States: U.S. Department of the Interior, Fish and Wildlife Service.
- Fish, U. S., and Service, Wildlife (2011a). Recovery plan for Hawaiian waterbirds, second revision. Portland: U.S. Fish and wildlife service. https://www.fws.gov/pacificislands/ch_rules/hawaiian%20waterbirds%20rp%202nd%20revision.pdf.
- Fox-Kemper, B., Hewitt, H. T., Xiao, C., Aðalgeirsdóttir, G., Drijfhout, S. S., Edwards, T. L., et al. (2021). "Ocean, cryosphere and sea level change," in *Climate change 2021: The physical science basis. Contribution of working group I to the sixth assessment Report of the intergovernmental Panel on climate change*. (Cambridge, England: Cambridge University Press). doi:10.1017/9781009157896.011
- Fung Associates Inc and Swca Environmental Consultants (2010). *Assessment of natural resources and watershed conditions for kalaupapa national historical Park*. Scotts Valley, California, United States: Natural Resource.
- Garner, G. G., Hermans, T., Kopp, R. E., Slangen, A. B. A., Edwards, T. L., Levermann, A., et al. (2021). IPCC AR6 Sea-Level rise projections. Version 20210809, PO.DAAC. Available at <https://podaac.jpl.nasa.gov/announcements/2021-08-09-Sea-level-projections-from-the-IPCC-6th>.
- Giambelluca, T. W., Chen, Q., Frazier, A. G., Price, J. P., Chen, Y.-L., Chu, P.-S., et al. (2013). Online rainfall atlas of Hawaii. *Bull. Amer. Meteor. Soc.* 94, 313–316. doi:10.1175/BAMS-D-11-00228.1
- Giambelluca, T. W., Shuai, X., Barnes, M. L., Alliss, R. J., Longman, R. J., Miura, T., et al. (2014). Evapotranspiration of Hawai'i. Final report submitted to the U.S. Army corps of engineers—honolulu district, and the commission on water resource management, state of Hawai'i. Available at <http://evapotranspiration.geography.hawaii.edu/assets/files/PDF/ET%20Project%20Final%20Report.pdf>.
- Gon, S. O., III, Tom, S. L., and Woodside, U. (2018). 'Āina momona, honua Au loli—productive lands, changing world: Using the Hawaiian footprint to inform biocultural restoration and future sustainability in Hawai'i. *Sustainability* 10, 3420. doi:10.3390/su10103420
- Gon, S. O., III, and Winter, K. (2019). A Hawaiian renaissance that could save the world. *Amer. Sci.* 107, 232–239. Available at <https://www.americanscientist.org/article/a-hawaiian-renaissance-that-could-save-the-world>.
- Gon, S. O., III, Winter, K. B., and Demotta, M. (2021). Kua-lako-mo'o: A methodology for exploring indigenous conceptualisations of nature and conservation in Hawai'i. *Pac. Conserv. Biol.* 27, 320–326. doi:10.1071/PC20020
- Goodman, A. C., Thorne, K. M., Buffington, K. J., Freeman, C. M., and Janousek, C. N. (2018). El Niño increases high-tide flooding in tidal wetlands along the U.S. Pacific coast. *J. Geophys. Res.-Bioge.* 123, 3162–3177. doi:10.1029/2018JG004677
- Greer, N. M. (2005). *Ethnoecology of taro farmers and their management of Hawaiian wetlands and endangered waterbirds in taro agroecosystems*. Ph.D. thesis. Tacoma, WA, United States: University of Washington.
- Harmon, K. C., Winter, K. B., Kurashima, N., Fletcher, C. H., Kane, H. H., and Price, M. R. (2021). The role of indigenous practices in expanding waterbird habitat in the face of rising seas. *Anthr* 34, 100293. doi:10.1016/j.ancene.2021.100293
- Harmon, K., Opie, E., Miner, A., Paty-Miner, I., Kukea-Shultz, J., Winter, K., et al. (2022). Successful nesting by 2 endangered Hawaiian waterbird species in a restored Indigenous wetland agroecosystem. *Wilson J. Ornithol.* 134, 102–105. doi:10.1676/20-00064
- Hawaii Department of Land and Natural Resources (2008). Surface water hydrologic unit boundaries (watersheds) for the eight major Hawaiian islands. Available at <https://geoportal.hawaii.gov/datasets/HIStateGIS:watersheds/about>.
- Hawaii Statewide Gis Program (2021). TMK Parcels for the State of Hawaii, [ESRI polygon shapefiles]. Available at <https://geoportal.hawaii.gov/datasets/parcels-hawaii-statewide/explore>.
- Hawaiian Islands Land Trust (2023). Waihe'e coastal Dunes and wetlands refuge. Available at https://climatechange.ila.org/case-study/hilt_waihee_restoration/.
- Hawai'i Department of Land and Natural Resources (2017). Hawaii biannual waterbird survey instructions. Available at <https://dlnr.hawaii.gov/files/2019/12/Survey-Instructions.pdf>.
- Henry, A., and Fredrickson, L. (2022). *Managing lowland wetlands in the main Hawaiian islands. Technical guide version 1.0*. Honolulu, Hawaii, United States: U. S. Fish and Wildlife Service.
- Henry, A., and Fredrickson, L. (2019). *Recommendations for wetland enhancement at Kakahai'a national Wildlife refuge*. Honolulu, Hawaii, United States: U. S. Fish and Wildlife Service.
- Henry, A. (2016). *Moloka'i wetlands: Landscape conservation project*. Honolulu, Hawaii, United States: Pacific Birds Joint Venture.
- Henry, A. R., and Fredrickson, L. H. (2013). *Hydrogeomorphic evaluation of ecosystem restoration and management options for James Campbell national Wildlife refuge*. Honolulu, Hawaii, United States: U. S. Fish and Wildlife Service.
- Heron (2023). Conservation design and printing. [/Users/jdrexler/Desktop/HGMReport_JamesCampbell%20\(1\).pdf](https://www.fws.gov/pacific/planning/main/docs/HIPI/Maui/Kakahai'a%20NWR%20DCCP-EA.pdf).
- Hill, B. R. (1996). "Hawaii wetland resources," in *National water summary on wetland resources. United states geological survey water-supply paper*. Editors J. D. Fretwell, J. S. Williams, and P. J. Redman (Washington, D.C., United States: Geological Survey).
- Horvath, E. K., Christensen, J. R., Mehaffey, M. H., and Neale, A. C. (2017). Building a potential wetland restoration indicator for the contiguous United States. *Ecol. Indic.* 83, 463–473. doi:10.1016/j.ecolind.2017.07.026
- Hua, Y., Cui, B., He, W., and Cai, Y. (2016). Identifying potential restoration areas of freshwater wetlands in a river delta. *Ecol. Indic.* 71, 438–448. doi:10.1016/j.ecolind.2016.07.036
- Jackson, N. L. (2013). "Estuaries," in *Treatise on geomorphology*. Editor J. F. Shroder (Cambridge, England: Academic Press). doi:10.1016/B978-0-12-374739-6.00285-2
- Jacobi, J. D., Price, J. P., Fortini, L. B., Gon, S. M., III, and Berkowitz, P. (2017). *Carbon assessment of Hawaii*. Washington, D.C., United States: Geological Survey.
- Jacobi, J. D., and Stock, J. (2017). Vegetation response of a dry shrubland community to feral goat management on the island of Moloka'i, Hawai'i. *Hawai'i U.S. Geol. Surv. Sci. Invest.* doi:10.3133/sir20175136
- Kane, H. H., Fletcher, C. H., Frazer, L. N., and Barbee, M. M. (2014). Critical elevation levels for flooding due to sea-level rise in Hawaii. *Reg. Environ. Change* 15, 1679–1687. doi:10.1007/s10113-014-0725-6
- Kirch, P. V. (1982). The impact of the prehistoric Polynesians on the Hawaiian ecosystem. *Pac. Sci.* 36, 1–14.
- Kirwan, M. L., and Megonigal, J. P. (2013). Tidal wetland stability in the face of human impacts and sea-level rise. *Nature* 504, 53–60. doi:10.1038/nature12856
- Krauss, B. (2001). *Plants in Hawaiian culture*. Honolulu, Hawaii, United States: University of Hawaii Press.
- Kroeger, K. D., Crooks, S., Moseman-Valtierra, S., and Tang, J. (2017). Restoring tides to reduce methane emissions in impounded wetlands: A new and potent blue carbon climate change intervention. *Sci. Rep.* 7, 11914. doi:10.1038/s41598-017-12138-4
- Lee, C. W. (2011). The politics of localness: Scale-bridging ties and legitimacy in regional resource management partnerships. *Soc. Nat. Resour.* 24, 439–454. doi:10.1080/08941920903463820
- Levermann, A., Winkelmann, R., Albrecht, T., Goelzer, H., Gollledge, N. R., Greve, R., et al. (2020). Projecting Antarctica's contribution to future sea level rise from basal ice shelf melt using linear response functions of 16 ice sheet models (LARMIP-2). *Earth Syst. Dyn.* 11 (1), 35–76. doi:10.5194/esd-11-35-2020
- Lovette, J. P., Duncan, J. M., Smart, L. S., Fay, J. P., Olander, L. P., Urban, D. L., et al. (2018). Leveraging big data towards functionally-based, catchment scale restoration prioritization. *Environ. Manage.* 62, 1007–1024. doi:10.1007/s00267-018-1100-z
- MacCaughy, V. (1916). Vegetation of the Hawaiian summit bogs. *Am. Bot.* 22, 45–52.
- Malachowski, C. P., and Dugger, B. D. (2018). Hawaiian duck behavioral patterns in seasonal wetlands and cultivated taro. *J. Wildl. Manag.* 82, 840–849. doi:10.1002/jwmg.21429
- Malachowski, C. P., Dugger, B. D., Ueyhara, K. J., and Reynolds, M. H. (2022). Avian botulism is a primary, year-round threat to adult survival in the endangered Hawaiian Duck on Kaua'i, Hawai'i, USA. *Ornithol. Appl.* 124. doi:10.1093/ornithapp/duac007
- Malachowski, C. P., Dugger, B. D., Ueyhara, K. J., and Reynolds, M. H. (2018). Nesting ecology of the Hawaiian duck, *Anas wyvilliana* on northern Kaua'i, Hawai'i, USA. *Wildfowl* 68, 123–139.
- Maleki, S., Soffianian, A. R., Soltani-Koupaei, S., Pourmanafi, S., and Saatchi, S. (2018). Wetland restoration prioritizing, a tool to reduce negative effects of drought; an application of multicriteria-spatial decision support system (MC-SDSS). *Ecol. Eng.* 112, 132–139. doi:10.1016/j.ecoleng.2017.12.031
- McGlone, M. S. (2009). Postglacial history of New Zealand wetlands and implications for their conservation. *N. Z. J. Ecol.* 33 (1), 1–23.
- Meadow, A. M., Ferguson, D. B., Guido, Z., Horangic, A., Owen, G., and Wall, T. (2015). Moving toward the deliberate coproduction of climate science knowledge. *Weather Clim. Soc.* 7 (2), 179–191. doi:10.1175/WCAS-D-14-00050.1
- Medland, S. J., Shaker, R. R., Forsythe, K. W., Mackay, B. R., and Rybarczyk, G. (2020). A multi-criteria wetland suitability index for restoration across Ontario's mixedwood plains. *Sustainability* 2, 9953. doi:10.3390/su12239953
- Menne, M. J., Durre, I., Korzeniewski, B., McNeill, S., Thomas, K., Yin, X., et al. (2012). *Global historical climatology network - daily (GHCN-Daily)*. Carolina, CA, United States: National Climatic Data Center.

- Mitsch, W. J., and Gosselink, J. G. (2007). "Treatment wetlands," in *Wetlands* (Hoboken, NJ, United States: John Wiley and Sons, Inc.).
- Moffett, K. B., and Gorelick, S. M. (2016). Relating salt marsh pore water geochemistry patterns to vegetation zones and hydrologic influences. *Water Resour. Res.* 52, 1729–1745. doi:10.1002/2015WR017406
- Morris, J. T., Drexler, J. Z., Vaughn, L. J., and Robinson, A. H. (2022). An assessment of future tidal marsh resilience in the San Francisco Estuary through modeling and quantifiable metrics of sustainability. *Front. Environ. Sci.* 10, 1039143. doi:10.3389/fenvs.2022.1039143
- Munkholm, L. J. (2011). Soil friability: A review of the concept, assessment and effects of soil properties and management. *Geoderma* 167–168, 236–246. doi:10.1016/j.geoderma.2011.08.005
- Murray, N. J., Phinn, S. R., DeWitt, M., Ferrari, R., Johnston, R., Lyons, M. B., et al. (2019). The global distribution and trajectory of tidal flats. *Nature* 565, 222–225. doi:10.1038/s41586-018-0805-8
- Murray, N. J., Worthington, T. A., Buntings, P., Duce, S., Hagger, V., Lovelock, C. E., et al. (2022). High-resolution mapping of losses and gains of Earth's tidal wetlands. *Science* 376, 744–749. doi:10.1126/science.abm9583
- Nasery, S., Matci, D. K., and Avdan, U. (2021). GIS-Based wind farm suitability assessment using fuzzy AHP multi-criteria approach: The case of herat, Afghanistan. *Arab. J. Geosci.* 14, 1091. doi:10.1007/s12517-021-07478-5
- National Centers for Coastal Ocean Science (2021). Digital elevation models (DEMs) for the main 8 Hawaiian islands. Available at <https://catalog.data.gov/dataset/digital-elevation-models-dems-for-the-main-8-hawaiian-islands>.
- National Oceanic and Atmospheric Administration (2021). Hawaii sea level rise [data file]. Available at <https://coast.noaa.gov/slrdata/>.
- National Oceanic and Atmospheric Administration (Noaa) (2022a). National integrated drought information system. Available at <https://www.drought.gov/states/hawaii/county/maui>.
- National Oceanic and Atmospheric Administration (Noaa) (2022b). Tides and currents. Available at <https://tidesandcurrents.noaa.gov/datums.html?datum=MHHW&units=1&epoch=0&id=1613198&name=Kaunakakai+Harbor&state=HI>.
- National Park Service (2010). National Park service. Available at <http://www.nature.nps.gov/water/wrdpub.cfm>.
- Oki, D. S., Engott, J. A., and Rotzall, K. (2019). Numerical simulation of groundwater availability in central Molokai, Hawai'i: U.S. *Geol. Surv. Sci. Investig. Rep.* 95. doi:10.3133/sir20191510
- Otte, M., Fang, W.-T., and Jian, M. (2021). A framework for identifying reference wetland conditions in highly altered landscapes. *Wetlands* 41, 40. doi:10.1007/s13157-021-01439-0
- Ouyang, N. L., Lu, S., Wu, B., Zhu, J., and Wang, H. (2011). Wetland restoration suitability evaluation at the watershed scale—a case study in upstream of the Yongdinghe River. *Procedia Environ. Sci.* 10, 1926–1932. doi:10.1016/j.proenv.2011.09.302
- Pacific Coast Joint Venture (2006). Strategic plan for wetland conservation in Hawai'i. Available at <https://www.pacificbirds.org/wp-content/uploads/2014/12/HWJVStrategicPlan-3.pdf>.
- Price, J. P., Jacobi, J. D., Gon, S. M., III, Matsuwaki, D., Mehrhoff, L., Wagner, W., et al. (2012). Mapping plant species ranges in the Hawaiian islands – developing a methodology and associated GIS layers. <http://pubs.usgs.gov/of/2012/1192/>.
- Pukui, M. K., and Elbert, S. H. (1986). *Hawaiian dictionary: Hawaiian-English English Hawaiian revised and enlarge addition*. Honolulu, Hawaii, United States: University of Hawaii Press.
- Qu, U., Luo, C., Zhang, H., Ni, H., and Xu, N. (2018). Modeling the wetland restorability based on natural and anthropogenic impacts in Sanjiang Plain, China. *Ecol. Indic.* 91, 429–438. doi:10.1016/j.ecolind.2018.04.008
- Roman, C. T., and Burdick, D. M. (2012). "A synthesis of research and practice on restoring tides to salt marshes," in *Tidal marsh restoration: A Synthesis of Science and management*. Editors C. T. Roman and D. M. Burdick (Washington, D.C., United States: Island Press).
- Sanderson, M. (1994). *Prevailing trade winds; weather and climate in Hawai'i*. Honolulu, Hawaii, United States: University of Hawai'i Press.
- Soil Survey Staff (2021). Natural resources conservation service, United States department of agriculture. Available at <https://websoilsurvey.nrcs.usda.gov/>.
- Sprecher, S. W. (2001). "Basics concepts of soil science," in *Wetland soils: Genesis, hydrology, landscapes, and classification*. Editors J. L. Richardson and M. J. Vepraskas (Boca Raton, FL, United States: CRC Press).
- Staples, G. W., and Cowie, R. H. (2001). *Hawaii's invasive species: A guide to invasive plants and animals in the Hawaiian islands*. Honolulu, Hawaii, United States: Bishop Museum Press.
- State of Hawaii (1996). *Hawai'i's coastal nonpoint pollution control Program management plan*. Hawaii office of state planning, pursuant to national oceanic and atmospheric administration award nos. NA47OZ0264 and NA57OZ0270. Available at https://files.hawaii.gov/dbedt/op/czm/initiative/nonpoint/cnppc_mgmt_plan_sections/III_7-Wetlands.pdf.
- Stearns, H. T., and Macdonald, G. A. (1947). *Geology and ground-water resources of the island of Molokai*. Honolulu, Hawaii, United States: U.S. Geological Survey.
- Stock, J. D., Cochran, S. A., Field, M. E., Jacobi, J. D., and Tribble, G. (2011). From Ridge to reef—linking erosion and changing watersheds to impacts on the coral reef ecosystems of Hawai'i and the pacific ocean. <http://pubs.usgs.gov/fs/2011/3049/>.
- Sun, X., Xiong, S., Zhu, J., Zhu, X., Li, Y., and Li, B. L. (2015). A new indices system for evaluating ecological-economic-social performances of wetland restorations and its application to Taihu Lake Basin, China. *Ecol. Modell.* 295, 216–226. doi:10.1016/j.ecolmodel.2014.10.008
- Sustainable Resources Group International (2018). Comprehensive management plan for 'Ohī'apilo ponds enhancement site, kalamaula, Moloka'i. <https://srgii.com/resource-management>.
- Sweet, W. V., Hamlington, B. D., Kopp, R. E., Weaver, C. P., Barnard, P. I., Bekaert, D., et al. (2022). Global and regional sea level rise scenarios for the United States: Updated mean projections and extreme water level probabilities along U.S. Coastlines. NOAA technical report NOS 01. <https://oceanservice.noaa.gov/hazards/sealevelrise/noaa-nos-techrpt01-global-regional-SLR-scenarios-US.pdf>.
- Toro, M., Ptak, T., Massmann, G., Sültenfuß, J., and Janssen, M. (2022). Groundwater flow patterns in a coastal fen exposed to drainage, rewetting and interaction with the Baltic Sea. *J. Hydrol.* 615, 128726. doi:10.1016/j.jhydrol.2022.128726
- Tummons, P. (2011). Hawai'i, mangrove's drawbacks outweigh benefits. Environmental Hawai'i. Available at <https://www.environment-hawaii.org/?p=7092>.
- Underwood, J. G., Silbernagel, M., Nishimoto, M., and Uyehara, K. J. (2014). Non-native mammalian predator control to benefit endangered Hawaiian waterbirds. *Proc. Vertebrate Pest Conf.* 26. doi:10.5070/V426110653
- U.S. Census Bureau (2021). Topologically integrated geographic encoding and referencing system (TIGER), TIGER/line and TIGER-related products electronic resource: Map. Available at <https://www.census.gov/cgi-bin/geo/shapfiles/index.php>.
- Usda (2014). Keys to soil taxonomy. <https://www.nrcs.usda.gov/sites/default/files/2022-09/Keys-to-Soil-Taxonomy.pdf>.
- U.S. Geological Survey (2019). National hydrography dataset (ver. USGS national hydrography dataset plus high resolution (published 20191209)). Available at <https://services.arcgis.com/P3ePLMYs2RVChkxj/arcgis/rest/services/NHDPlusV21/FeatureServer>.
- U.S. Geological Survey (2018a). USGS NED 1/3 arc-second contours for Maui NE, Hawaii 20180211 1 X 1 degree shapefile. Retrieved from <https://data.usgs.gov/catalog/data/USGS:3a81321b-c153-416f-98b7-cc8e5f0e17c3#idp1908403156>.
- U.S. Geological Survey (2018b). USGS NED 1/3 arc-second contours for Oahu E, Hawaii 20180211 1 X 1 degree shapefile. Retrieved from <https://data.usgs.gov/catalog/data/USGS:3a81321b-c153-416f-98b7-cc8e5f0e17c3#idp1908403156>.
- Van Rees, C. B., and Reed, M. J. (2013). Wetland loss in Hawai'i since human settlement. *Wetlands* 34, 335–350. doi:10.1007/s13157-013-0501-2
- VanderWerf, E. A. (2012). Hawaiian bird conservation action plan. Honolulu: Pacific rim conservation. <https://pacificrimconservation.org/wp-content/uploads/2013/10/Introduction%202.pdf>.
- Vogl, R. J., and Hendrickson, J. (1971). Vegetation of an alpine bog on East Maui, Hawai'i. *Pac. Sci.* 25, 475–483.
- Wagner, W. L., Herbst, D. R., and Lorence, D. H. (2005). Flora of the Hawaiian islands website. Available at <http://botany.si.edu/pacificislandbiodiversity/hawaiianflora/index.htm>.
- White, D., and Fennessy, S. (2005). Modeling the suitability of wetland restoration potential at the watershed scale. *Ecol. Eng.* 24, 359–377. doi:10.1016/j.ecoleng.2005.01.012
- Wilkins, E. J., Sinclair, W., Miller, H. M., and Schusters, R. M. (2018). Does proximity to wetlands matter? A landscape-level analysis of the influence of local wetlands on the public's concern for ecosystem services and conservation involvement. *Wetlands* 39, 1271–1280. doi:10.1007/s13157-018-1076-8
- Winter, K. B., Lincoln, N. K., and Berkes, F. (2018). The social-ecological keystone concept: A quantifiable metaphor for understanding the structure, function, and resilience of a biocultural system. *Sustainability* 10, 3294. doi:10.3390/su10093294
- World Climate Research Program (2020). CMIP6 - coupled model intercomparison project phase 6. Available at <https://pcmdi.llnl.gov/CMIP6/>.
- Wyban, C. A. (1993). *Report on the kalaupapa fishpond. On file with the national Park service*. Washington, D.C., United States: U.S. Department of the Interior.
- Younes, A., Koth, K. M., Ghazala, M. O. A., and Elkadeem, M. R. (2022). Spatial suitability analysis for site selection of refugee camps using hybrid GIS and fuzzy AHP approach: The case of Kenya. *Int. J. Disaster Risk Reduct.* 77, 103062. doi:10.1016/j.jidrr.2022.103062
- Zedler, J. B. (1982). *The ecology of southern California coastal salt marshes: A community profile*. Washington, D.C., United States: U.S. Fish and Wildlife Service.
- Zimmerman, C. F., Keefe, C. W., and Bashe, J. (2007). Determination of carbon and nitrogen in sediments and particulates of estuarine/coastal waters using elemental analysis. <http://www.caslab.com/EPAMethods/PDF/EPAMethod-440.pdf>.



OPEN ACCESS

EDITED BY

Yiping Wu,
Xi'an Jiaotong University, China

REVIEWED BY

Xiang Zhang,
Wuhan University, China
Dénes Lóczy,
University of Pécs, Hungary

*CORRESPONDENCE

Gabriel Stecher,
✉ gabriel.stecher@boku.ac.at

RECEIVED 10 May 2023

ACCEPTED 05 July 2023

PUBLISHED 28 July 2023

CITATION

Stecher G, Hohensinner S and
Herrnegger M (2023), Changes in the
water retention of mountainous
landscapes since the 1820s in the
Austrian Alps.
Front. Environ. Sci. 11:1219030.
doi: 10.3389/fenvs.2023.1219030

COPYRIGHT

© 2023 Stecher, Hohensinner and
Herrnegger. This is an open-access
article distributed under the terms of the
[Creative Commons Attribution License](#)
(CC BY). The use, distribution or
reproduction in other forums is
permitted, provided the original author(s)
and the copyright owner(s) are credited
and that the original publication in this
journal is cited, in accordance with
accepted academic practice. No use,
distribution or reproduction is permitted
which does not comply with these terms.

Changes in the water retention of mountainous landscapes since the 1820s in the Austrian Alps

Gabriel Stecher ^{1*}, Severin Hohensinner ² and
Mathew Herrnegger ¹

¹Institute of Hydrology and Water Management, University of Natural Resources and Life Sciences, Vienna, Austria, ²Institute of Hydrobiology and Aquatic Ecosystem Management, University of Natural Resources and Life Sciences, Vienna, Austria

Interactions of humans with the environment are strongly related to land use and land cover changes (LULCCs). In the last decades, these changes have led to a degradation of ecosystem services, including water regulation and flood control. In the Alpine areas of Austria, land cover changes have increased flood risk since the middle of the 19th century. In this paper, we assess the influence of these long-term land use changes on the landscape's ability to retain water using the qualitative Water Retention Index (WRI). The changes are thereby evaluated on the basis of the historical (1826–1859) and present (2016) land cover situation, which is to our knowledge the first high-resolution and regional application of the WRI. The results show that the water retention potential mimics the mountainous characteristic and features. Except for areas strongly dominated by settlement areas, the highest retention potentials are found in valley floors and the lowest values are depicted along the main Alpine complex. In low-lying areas, the retention decreased by over 10%. It was found that this decrease can be mostly attributed to settlement expansion. Above 1,250 m, land use transformations led to slightly increasing water retention values owing to the transformation of wasteland or glaciers to stagnant waters and to the expansion of forest and grassland in high elevations. This examination allows for a holistic and spatially distributed LULCC impact assessment on the landscape's water regulation capacities and offers valuable high-resolution information for future land use planning and sustainable land development.

KEYWORDS

water retention, land use, land cover change, flood control, ecosystem service, Alpine regions

1 Introduction

Anthropogenic interactions with the environment through land use and land cover change (LULCC) are strongly connected to ecosystem functions and the provision of ecosystem services (ESS) (Hasan et al., 2020). Ecosystem services benefit society and are obtained either directly or indirectly from ecosystems (e.g., Gómez-Baggethun & Barton, 2013; Silvestri et al., 2013). These benefits comprise a variety of services and can be categorized into four types including, (i) supporting services (e.g., soil formation, nutrient supply), (ii) provisioning services (e.g., raw materials, water, food), (iii) regulating services (e.g., climate regulation, water purification), and (iv) cultural services (e.g., ecotourism, recreational uses) (MEA, 2005; Hasan et al., 2020). Multiple authors reported a decline of ESSs due to LULCC (e.g., Haines-Young et al., 2012; Kindu et al., 2016;

Rai et al., 2018), while long-term LULCC (1960–2019) are four times greater than estimated before and affect almost one-third of the global land area (Winkler et al., 2021). LULCC negatively affect hydrological provisioning and regulating ecosystem services as well as the supporting services of natural flows to sustain ecosystems (Jin et al., 2015) and also leads to the alterations of hydrological processes and their functions (Maitima et al., 2009; Guzha et al., 2018). The dependence of hydrological ecosystem services on specific land uses subsequently leads to effects on regulating services such as water conservation, water availability, and flood control due to LULCC (Hasan et al., 2020).

Land use changes, such as deforestation, urbanization, and wetland drainage, as well as agricultural utilization of land, affect various hydrological processes including evapotranspiration, infiltration, and surface and subsurface water storage (e.g., Andréassian, 2004; Oudin et al., 2008; Hall et al., 2014; Wesemann et al., 2018). LULCC and associated agriculturally modified hillslopes can influence flow paths, flow velocity, water storage, and concentration times. Vertical soil infiltration and water retention can also be reduced due to the intensification of agricultural practices (Rogger et al., 2017). Similarly, numerical simulations showed that flood peaks in small headwater catchments can increase by up to 75% due to the construction of forest roads (Wesemann, 2021; Herrnegger et al., 2022). These examples show that human landscape interventions and intensification in land use can adversely affect regulating ecosystem services such as water retention. LULCCs also influence flood generation processes by altering the infiltration capacity of the landscape (Hall et al., 2014). Among climate change and river channelization, land use change is therefore another potential main driver of flood regime changes (Merz et al., 2012). However, the impact on flood regimes is stronger in smaller headwater catchments (e.g., Wesemann, 2021). In larger catchments, other factors such as river straightening, loss of floodplains, and changes in atmospheric conditions, such as changes in regional precipitation based on different atmospheric circulation patterns, are more dominant (Viglione et al., 2016). If managed properly, LULCC can be beneficial for water regulation in urban areas but also in upstream runoff-generating areas (Vandecasteele et al., 2017). Thus, flood risk management plans might also include the encouragement of sustainable land use as well as the improvement of water retention and the controlled flooding of certain areas in case of a flood event as defined in the EU Floods Directive 2007/60/EC (EU, 2007). The integrated flood risk management (IFRM) approach thus aims to reduce the severity and vulnerability to flooding based on a portfolio of approaches that include structural and non-structural measures (Van Herk et al., 2015).

In the Alpine areas of Austria, LULCC has increased flood risk since the mid-19th century, especially in valley corridors as shown by Hohensinner et al. (2021). In their study, digitalized historical maps from 1826 to 1859 were compiled and compared with a detailed land cover dataset approximating the land cover of 2016. During this period, arable land was reduced by 69%, forests increased by 23%, and various agricultural areas declined by 27%. At the same time, settlement areas have expanded by over 6 times (Hohensinner et al., 2021). The expansion of settlements in flood-prone areas by 28% has resulted in increased flood damage potential

(Junger et al., 2022). Although agricultural areas have declined since the mid-19th century, over 12% of highly valuable agricultural areas are currently located in flood-prone areas (Junger et al., 2022). In mountainous areas, where areas for agriculture are topographically limited, over 30% of agricultural land important for food security is located in flood-risk areas (Grüneis et al., 2021). At the same time, the construction of hydropower reservoirs in Alpine valleys since the middle of the 20th century led to large flood retention potentials and to a strong decrease of flood peaks and flood risk (Stecher & Herrnegger, 2022).

Currently, 41 km² of productive soils are commanded for land development in Austria annually. Thereof 15–21 km² are permanently sealed and their associated ESS, including water retention, are eternally lost (UBA, 2022). The Austrian government, therefore, aims to reduce land consumption to 9 km² annually by 2030 (Gov., 2020). Future land use changes (2030) might increase flood-affected residential areas by 159% in an Austrian Alpine valley (Cammerer et al., 2013). At the same time, flood risk could be reduced by the introduction of non-structural flood protection measures. The enhancement of private precaution and stricter land use regulations reduces flood risk by approximately 30%. Regardless of future changes in flood risk due to climate and land use change, non-structural measures always reduce flood risk (Thieken et al., 2016). In Austria, flood policies should prefer non-structural measures, flood retention, and natural retention over structural measures (linear structures, technical/controlled retention) (BMLFUW, 2015; Nordbeck et al., 2019; Nordbeck et al., 2023). Therefore, land use and land development management are crucial tools for maintaining hydrological ecosystem services including water retention and flood control.

Grüneis et al. (2021), Hohensinner et al. (2021), and Junger et al. (2022) investigated flood risk changes due to LULCC, thereby analyzing flood exposure focusing on Alpine valley corridors. In contrast, the present contribution examines how LULCCs since the mid-19th century (Hohensinner et al., 2021) have affected the hydrological ecosystem services of water regulation and flood control based on the Water Retention Index (WRI). The qualitative Water Retention Index was developed by Vandecasteele et al. (2017) to assess the water regulation of landscapes on a European scale. Here, we apply the index on a regional scale to assess the impact of LULCC on the ecosystem services of water retention and flood control. The objectives of this study are i) the application of the WRI for a spatially high-resolution regional evaluation of the landscape's water retention potential, ii) to derive spatially distributed water retention index (WRI) maps for the present and past land cover situation and iii) to quantify the water retention changes for individual land use transformations but also elevation bands.

The findings complement the studies on flood risk in the Alpine regions and additionally quantify the effect of LULCC on water retention. These results might assist policymakers responsible for land management and spatial planning who are also concerned with integrated flood risk management.

2 Materials and methods

The study area is 19,307 km² large and covers the Austrian catchments of the rivers Rhine (provincial state Vorarlberg), Salzach (Salzburg), and Drava (Carinthia and Eastern Tyrol). The extent of

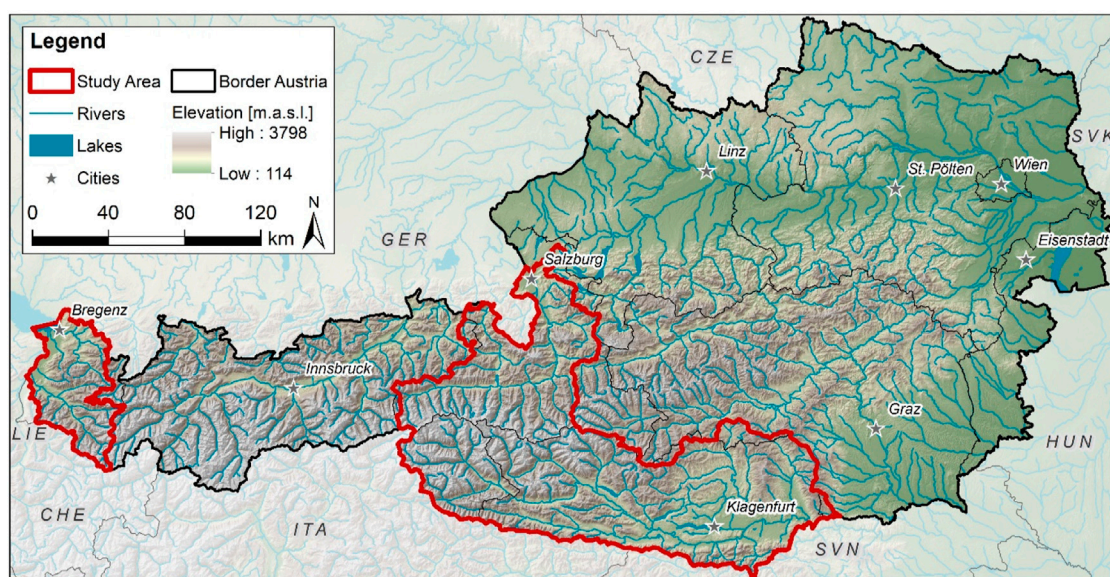


FIGURE 1

Location of the study area covering the provincial states of Vorarlberg (Rhine catchment), Salzburg (Salzach) and Eastern Tyrol/Carinthia (Drava) in the context of Austria.

the study area is determined by the data availability of the land cover dataset provided by Hohensinner et al. (2021). The land cover datasets of the past (1826–1859) and present (2016) are shown in the Supplementary Appendix Figure SA1. The altitude ranges from 338 to 3,798 m.a.s.l. and the topography is largely dominated by the Alpine main ridge. The study area is strongly characterized by high mountain ranges, steep slopes, and glacially formed valleys. Towards the southeast, it also includes parts of the Alpine forelands (Figure 1). Thus, space for land development is restricted by these natural features and only approximately 21% of the area of the Austrian Alps is suitable for permanent settlements (Alpine Convention, 2015; Löschner et al., 2017).

To determine how LULCC from the mid-19th century to the present affected the natural water retention of the alpine landscape of Austria, the Water Retention Index (WRI) is calculated based on the historical and current land use and land cover. The WRI is a qualitative composite indicator showing the relative water retention potential on a scale from 0 to 10 (Vandecasteele et al., 2017). The index can be used to represent the landscape's ability to regulate water, thereby reducing the risk of floods and also droughts. The WRI aims to represent the physical processes of interception, infiltration, and retention in soil, percolation to groundwater and water storage in surface water bodies by using proxy datasets. Water retention is also influenced by the slope angle and sealed surface areas of the landscape. Therefore, these parameters are also considered in the calculation of the WRI (Vandecasteele et al., 2017).

In the current study, the WRI was derived at a resolution of 100*100 m to capture the heterogeneity of the Alpine topography and was calculated as a weighted average (with the weights w_i) of 6 input parameters (Eq. 1):

$$WRI = (R_{gw} * w_{gw} + R_s * w_s + R_v * w_v + R_{sl} * w_{sl} + R_{wb} * w_{wb}) * \left(1 - \frac{R_{ss}}{100}\right) \quad (1)$$

Figure 2 shows the schematic workflow of the computation and analysis of the WRI for the present study. The input parameters represented by proxy datasets used to characterize the factors influencing the water retention capacity are given at the top of Figure 2. Compared to the study of Vandecasteele et al. (2017), the input parameters were derived from different data sources, because they were either released only recently or are available only on the regional Austrian level. The input layers represent similar proxy data, mostly at a higher spatial resolution.

The input parameter R_{gw} represents groundwater storage and was derived from the GLHYMPS 2.0 dataset (Huscroft et al., 2018). This dataset represents global permeability data of the unconsolidated and consolidated Earth in a vector format. Permeability represents the ability of porous media to transmit fluids and is therefore a suitable parameter to derive the potential of infiltration and percolation to groundwater. The soil storage component (R_s) represents the infiltration and retention capacity in the soil matrix. This parameter is derived from a soil water storage dataset, which was estimated using a spatial predicting XGBoost model for Austria at a 1*1 km² grid (Zeitfogel et al., 2022). The potential retention in vegetation is represented by the input parameter R_v . Following Vandecasteele et al. (2017), it is assumed that the capacity of vegetation to intercept water is linearly related to the Leaf Area Index (LAI). Therefore, the globally available Copernicus Global Land Service LAI dataset (VITO, 2018) was used to calculate the average LAI per land cover class and catchments of the LamaH dataset (Klingler et al., 2021) for the period 2014 to 2020. The input parameter R_{sl} describes the slope of the landscape and is derived from an Austrian digital elevation model, which is available at a 10*10 m resolution at <https://www.data.gv.at/> (BMF, 2022). R_{sl} is assumed to have a negative linear relationship with water retention (Vandecasteele et al., 2017). The input parameter R_{wb} represents the retention in water bodies and is calculated as the areal share of water bodies within each spatial unit of 100*100 m. In contrast to Vandecasteele et al. (2017), we did not only

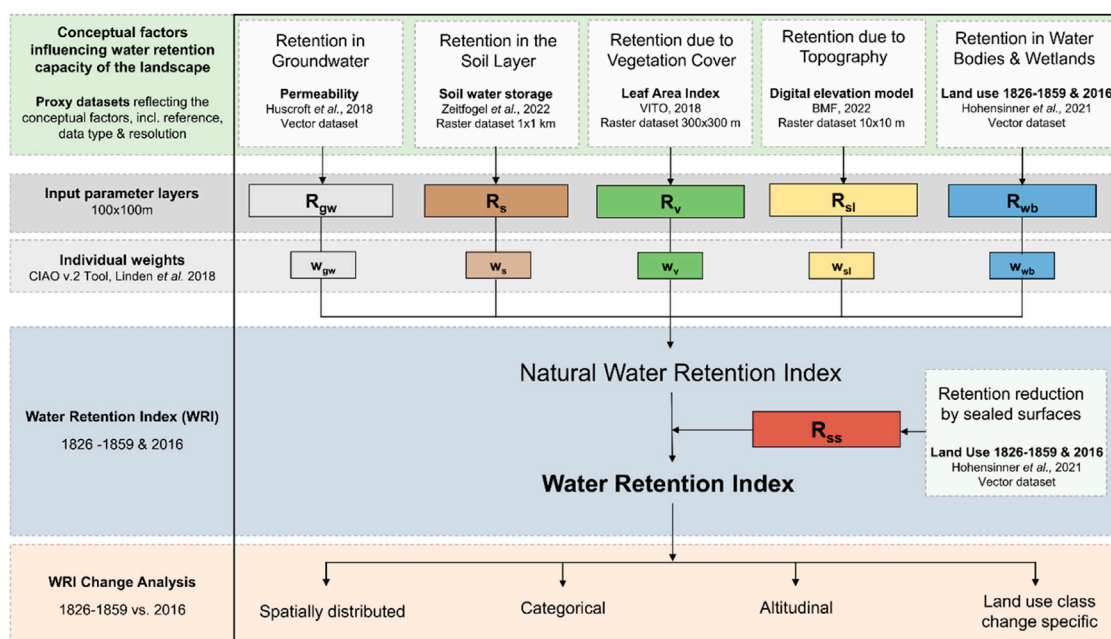


FIGURE 2

Schematic workflow diagram of the calculation and analysis of the Water Retention Index adjusted from Vandecasteele et al. (2017) and extended for the present study.

consider surface water bodies but also wetlands in this input parameter, assuming a similar retention behavior of wetlands and surface water bodies on the water retention capacity. The input parameter R_{ss} represents the share of settlement area per spatial unit (100×100 m). R_{wb} and R_{ss} are derived from the high-resolution land use and land cover dataset provided by Hohensinner et al. (2021). A summary of all original data obtained to derive the 6 input parameters is given in the Supplementary Appendix Table SA1. All input parameter datasets were rescaled or converted to a consistent raster with a resolution of 100×100 m. Except for the parameter of sealed surface (R_{ss}), all parameters were rescaled from 0 to 10 using a linear function. The minimum and maximum values for the linear function are represented by the minimum and maximum values of each original input layer. This assures a uniform scale for all input parameters. In order to assign steep slopes with low and flat areas with high values, the slope parameter R_{sl} was inversely rescaled.

For the calculation of the historical Water Retention Index (WRI_{his}) the input parameters R_v , R_{wb} , and R_{ss} had to be adjusted with respect to the historical land cover dataset. The input parameters R_{ss} and R_{wb} were derived from the historical land cover dataset. The vegetation parameter R_v representing the historical land cover state was estimated by transferring the average R_v values per land cover class and catchment of the current state onto the historical land cover classes in each catchment. This approach considers the spatial characteristics, dependencies, and shifts of land use and land cover (LULC) transformation within each catchment. The parameters R_{gw} , R_s , and R_{sl} and their impact on water retention were assumed to be constant over time.

The next step consists of the aggregation of the composite indicator by assigning individual weights to each input parameter, except for R_{ss} (see Eq. 1). The soil sealing parameter

is considered a multiplying factor, which linearly affects the WRI. The applied weights reflect the importance of each input parameter with regard to the composite indicator. The importance of each parameter is often a source of contention and can significantly influence the composite indicator (OECD, 2008). Therefore, we used the same methodological approach as Vandecasteele et al. (2017). This method uses a weight optimization approach which is based on the calculation of the first-order sensitivity index S_i (Sobol, 1993) for each input parameter with respect to the overall indicator (WRI). It incorporates penalized splines as a method of nonlinear regression (Paruolo et al., 2013) and an adopted optimization scheme developed by Becker et al. (2017). The general objective of the optimization is that each input parameter contributes equally to the (spatial) variance of the composite indicator.

The optimization of the individual weights was carried out using the Composite Indicator Analysis and Optimization (CIAO) Tool v.2 (Lindén et al., 2021), which incorporates the optimization procedure as described above. Due to the computationally intensive approach, all input parameters were aggregated to the LamaH catchment level (Klingler et al., 2021) and are listed in the (Supplementary Appendix Table SA2). This decreased the input data drastically from 1.9 million pixels to 201 catchment values. The optimization process was started by assigning equal weights to all input parameters and with the condition that the sum of all weights must be one. Using these weights, the associated normalized S_i values were unsatisfying and showed large differences between the input parameters. The parameters R_v and R_{gw} exhibited strong nonlinearities (Supplementary Appendix Figure SA2). After running the optimization routine, the normalized sensitivity indices of all input parameters showed equal values. The algorithm searched for the individual weights of each parameter to diminish the differences between the S_i values between all parameters.

TABLE 1 Weights and sensitivity indices (S_i) before and after the optimization for the individual layer of the WRI R_{gw} (groundwater storage), R_s (soil water storage), R_v (Interception), R_{wb} (share of water bodies), R_{sl} (slope), R_{ss} (share of sealed surface).

	before optimization		after optimization	
	weights	S_i norm	weights	S_i norm
R_{gw}	0.20	0.15	0.24	0.2
R_s	0.20	0.28	0.01	0.2
R_{sl}	0.20	0.20	0.38	0.2
R_v	0.20	0.26	0.16	0.2
R_{wb}	0.20	0.12	0.21	0.2

This means that the individual contribution to the (spatial) variance of the overall composite indicator was equally distributed between all input parameters. The optimized S_i values and the associated weights are listed in Table 1. These weights were subsequently used for the calculation of the WRI of both periods.

3 Results

3.1 Input parameter layers

The resulting input parameter layers for the calculation of the current Water Retention Index (WRI_{cur}) are plotted in Figure 3. The high resolution of all input parameters revealed a spatial pattern following the topographic features. Large valleys and high mountain ranges can be strongly recognized in several parameters, including R_{gw} , R_s , and R_v . The parameter R_s revealed that areas with sealed surfaces occur mostly on valley floors. All input parameters for the calculation of the WRI_{his} are represented in the Supplementary Appendix Figure SA1.

3.2 Spatial distributed WRI characteristics

In Figure 4, the current WRI (2016) and the historical WRI (1826–1859) are plotted in the top and middle panels, respectively. The difference in WRI between the current and historical state is shown in the bottom panels. The numbers on each map indicate different regions of the study area. Vorarlberg (1) includes the area

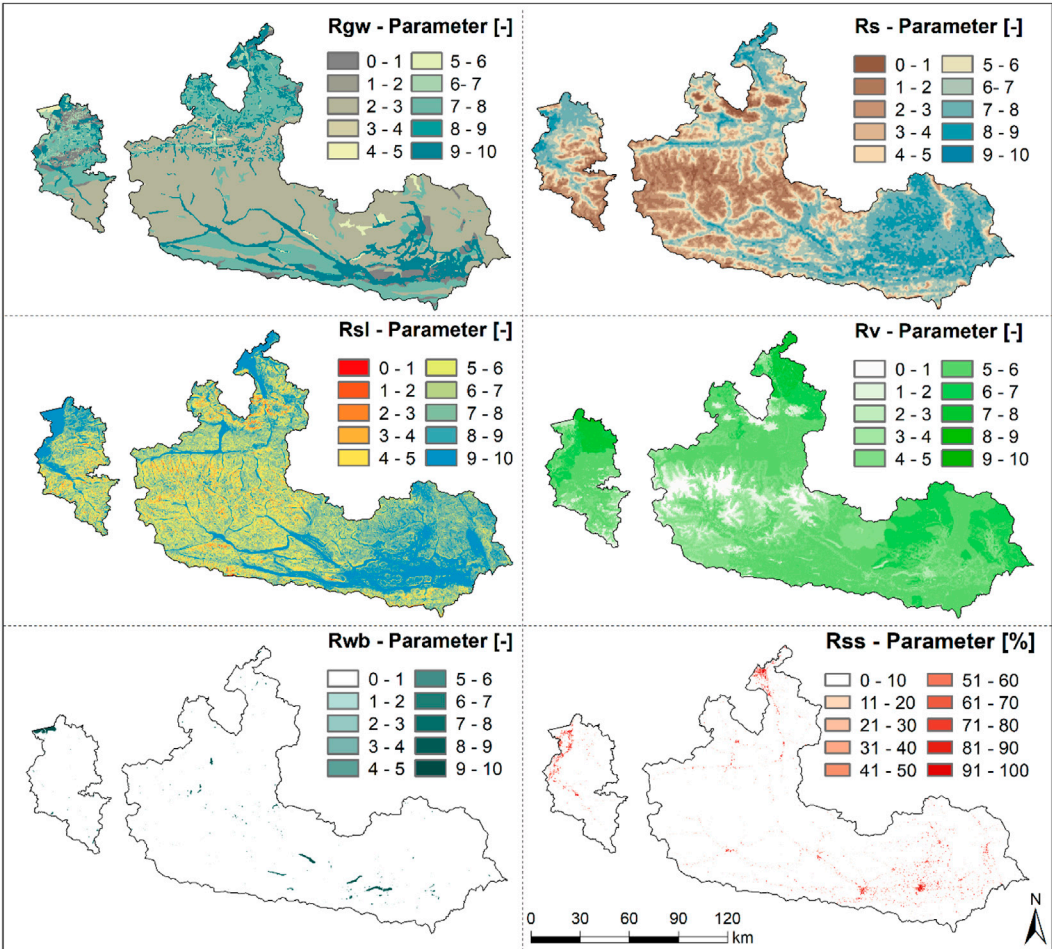


FIGURE 3 Overview WRI input parameters layers for 2016; R_{gw} (groundwater storage), R_s (soil water storage), R_v (Interception), R_{wb} (share of water bodies), R_{sl} (slope), R_{ss} (share of sealed surface).

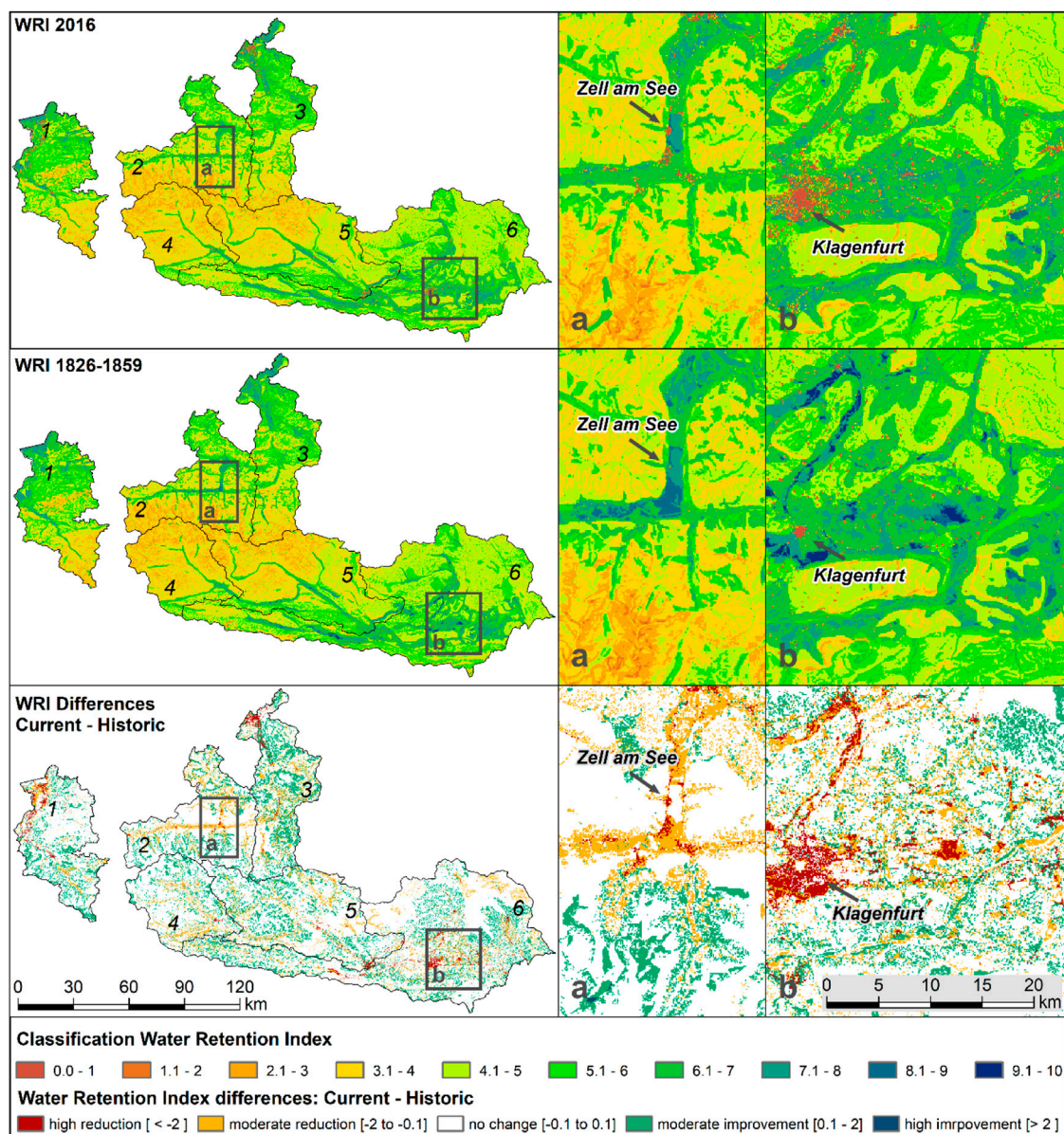


FIGURE 4

On the left side the resulting current WRI (top), historical WRI (middle), and the differences between the current and historical WRI (bottom) are shown. On the right-hand side, panels a) show the Salzach Valley with Zell am See and panels b) show the area around the city of Klagenfurt in detail for all three representations.

of the Austrian Rhine catchment. Two and three represent the Upper and Lower Salzach catchments, respectively, and thus compose the Austrian Salzach catchment. Eastern Tyrol (4) is in the upper part of the Drava catchment and together with the Upper (5) and Lower Drava (6) regions defines the Drava catchment.

The WRI shows a comparable and distinct spatial pattern for both calculated time periods. In general, values are higher in valley floors and rather flat areas, such as in the Rhine Valley, along the Drava River, or in the eastern part of the analyzed area, compared to areas characterized by steep topography and Alpine features. This is the result of the combination of low vegetation cover, shallow soil water storage, and low permeability in mountainous areas, e.g.,

along the main Alpine complex. This shows that water retention is more pronounced in valley areas than in steep headwater catchments. The results also indicate that the general spatial WRI patterns did not change significantly due to LULCC but are strongly influenced by the topographic features.

The WRI difference plot, shown in the bottom panel of Figure 4, however, depicts a moderate (-0.1 to -2) to high (< -2) reduction of the retention potential, especially in the Alpine valleys at low elevations and along watercourses. This can largely be explained by the expansion and development of settlement areas. In addition, the loss of river landscapes, the draining of wetlands, and the clearing of forested areas at lower elevations reduced water

retention. River channelization, which can significantly limit the retention effect of rivers and their formerly available fluvial corridors also adversely affected the regulation potential. In contrast, there are large areas that showed a moderate increase (0.1–2) in the WRI. These are attributed to the increase in forest and to the transformation of wasteland to grassland in these areas. In addition, new artificial water areas have been added due to the construction of Alpine storage reservoirs, which positively affect the retention potential.

The areas of the Salzach Valley (panel a) and Klagenfurt area (panel b) illustrate the current and historical WRI values exemplary for a more rural (a) and urban (b) land development setting. The bottom panel a) shows that water retention has decreased in large parts of the Salzach Valley. Moderate reduction rates (−0.1 to −2) were observed in most parts, but some areas also showed strong WRI reductions (≤ -2), due to increased settlement density. At the same time, it can be seen that the retention potential moderately improved ($>0.1-2$) along the valley flanks at higher altitudes. In panel b) a strong reduction of the retention potential was detected due to the expansion of built-up surfaces in the Klagenfurt area. Areas with very high WRI values in the north of Klagenfurt transformed into areas with significantly less retention potential. Similar developments can also be seen in the east of Klagenfurt. The WRI change characteristics between the historical and current state for these two examples are somewhat representative of other regions in the study area. High WRI reductions due to intense settlement development are also visible in the Rhine Valley in Vorarlberg or around the city of Salzburg in the North. Moderate reductions are depicted in almost all valley floors due to river channelization, loss of wetlands, or the reduction of forest cover.

3.3 Aggregated WRI results

For further analysis, the continuous WRI values were aggregated into 5 categories, namely, very low (0–2), low (2–4), moderate (4–6), high (6–8), and very high (8–10). This allows for categorical analysis of the WRI changes. In Table 2, the relative changes between 1826–1859 and 2016 are shown for each region of the study area. The table reveals that large areas of each region did not show any class changes (highlighted in grey). The sum of the constant areas per region (highlighted in blue) ranged from 97.2% in Eastern Tyrol to 92.5% in the Lower Salzach region, respectively. This indicates that regions with lower changes in WRI exhibited lower land development compared to other regions. Overall, these results suggest that only minor areas show class changes. The total relative sum of negative and positive areas, in which class shifts occurred are highlighted with orange (−) and green (+) colors, respectively. Generally, the negative effects on the WRI based on LULCC exceed the positive impacts in all regions.

Figure 5 shows the WRI class shifts for the overall study area in a Sankey diagram. Sankey diagrams illustrating Table 2 and the results for each region are shown in the Supplementary Appendix Figure SA3. Large areas (94.9%) of the study area (19,307 km²) did not exhibit any categorical shifts. Accordingly, Figure 5 only represents 5.1% of the study area, which experienced class changes between the historical and current WRI situation. In addition, the absolute areas

and the relative proportions of the total area are shown. The results suggest that there has been an over 9-fold increase in areas with very low WRI (0–2; red). The largest contribution to the very low WRI class can be assigned to historically high WRI values (6–8). In contrast, large areas with historically low WRI values (2–4; yellow) have improved and shifted to moderate WRI values (4–6; green). Areas with moderate WRI values have increased by approximately 50%. LULCCs have also led to a large reduction in areas with high and very high WRI (6–10; light and dark blue). A comparison of historical and current conditions shows a 13-fold decrease in very high WRI values (8–10; dark blue).

The individual WRI classes can be related to different land cover classes. The lowest class (WRI 0–2) is strongly dominated by settlements and wasteland. Low WRI values (2–4) relate mostly to a combination of forest, wasteland, and grasslands. Forest and grassland define moderate WRI ranges (4–6). High WRI values are frequently attributed to grassland and forest, but also arable land is dominant in this class. The highest WRI class (8–10) is represented by stagnant and running water in the current WRI. Interestingly, the historic very high WRI (8–10) class is related to various land cover types, including grassland, arable land, stagnant water, or forest. The relative contributions to each WRI class described here only focus on the major land cover class contributions. The detailed relative contributions of each land cover class to the WRI classes (1826–1859 and 2016) are given in the Supplementary Appendix Table SA4 and Supplementary Appendix Figure SA5.

3.4 Altitudinal gradients of the historical and present WRI

The study area is dominated by strong topographic gradients. These are also present in the resulting WRI values in both time periods and are shown in the spatially distributed difference plot (Figure 4; bottom panel). Figure 6 shows the relative WRI differences for elevation bands of 250 m. Additionally, the natural Water Retention Index (WRI_{nat}) is plotted. WRI_{nat} is calculated as the WRI but does not consider the soil sealing parameter R_{ss} (see Eq. 1) which is the linear scaling factor considering artificially introduced surfaces. The comparison of these two indicators allows us to distinguish between the WRI with and without the soil sealing factor (Vandecasteele et al., 2017). Based on this differentiation, the impact of soil sealing due to the construction of infrastructure and settlement areas is illustrated. At the bottom of the plot, the area per elevation band is given in km² and % as additional information.

Generally, Figure 6 confirms the similar WRI-change pattern as shown in the spatially distributed WRI plots (Figure 4). WRI values strongly decreased in lower elevations. In areas with an elevation lower than 500 m (i.e., valley floors), the water retention capabilities of the landscape decreased by over −10% on average due to LULCC. WRI values in slightly higher areas up to 1,000 m, also show decreasing values, however only with a mean of around −3%. The WRI_{nat} shows comparable changes to the WRI for areas above 1,000–1,250 m. In contrast, especially in elevations covering valley floors, a strong difference can be detected. In these regions (<500 m), the WRI_{nat} exhibits an over 5-fold smaller decrease in the water retention potential. At altitudes

TABLE 2 Change matrix WRI_{his} (1826–1859) and WRI_{cur} (2016) for each region and river catchment [%]. The values are calculated based on the WRI categories very low (0–2), low (2–4), moderate (4–6), high (6–8), and very high (8–10); orange cells show the relative sum of areas, where the WRI deteriorated; green cells show the relative sum of areas, where the WRI improved; blue cells show the sum of area, where no change occurred.

	Water Retention Index 2016						
	Rhine (Vorarlberg)	very low	low	moderate	high	very high	Σ positive Δ
Water Retention Index 1826–1859	very low	0.1	0.0	0.0	0.0	0.0	0.0
	low	0.1	27.6	1.2	0.0	0.0	1.2
	moderate	0.4	0.7	46.4	0.7	0.0	0.7
	high	1.0	0.9	0.8	19.8	0.1	0.1
	very high	0.0	0.0	0.0	0.1	0.0	2.1
	Σ negative Δ	1.5	1.6	0.8	0.1	4.1	93.8
	Drava (Eastern Tyrol)	very low	low	moderate	high	very high	Σ positive Δ
	very low	0.6	0.1	0.0	0.0	0.0	0.1
	low	0.0	71.3	1.0	0.0	0.0	1.0
	moderate	0.0	1.0	21.1	0.1	0.0	0.1
	high	0.1	0.1	0.3	4.2	0.0	0.0
	very high	0.0	0.0	0.0	0.0	0.0	1.2
	Σ negative Δ	0.2	1.1	0.3	0.0	1.6	97.2
	Upper Salzach (Salzburg)	very low	low	moderate	high	very high	Σ positive Δ
	very low	0.4	0.2	0.0	0.0	0.0	0.2
	low	0.0	43.6	1.5	0.0	0.0	1.5
	moderate	0.0	0.8	39.9	0.6	0.0	0.6
	high	0.2	0.2	0.7	11.1	0.0	0.0
	very high	0.0	0.0	0.0	0.6	0.0	2.3
	Σ negative Δ	0.2	1.1	0.8	0.6	2.7	95.0
	Lower Salzach (Salzburg)	very low	low	moderate	high	very high	Σ positive Δ
	very low	0.1	0.0	0.0	0.0	0.0	0.0
	low	0.1	22.4	2.3	0.0	0.0	2.3
	moderate	0.1	0.8	48.4	1.1	0.0	1.1
	high	1.1	0.8	1.0	21.5	0.0	0.0
	very high	0.0	0.0	0.0	0.2	0.0	3.5
	Σ negative Δ	1.3	1.6	1.0	0.2	4.1	92.5
	Upper Drava (Carinthia)	very low	low	moderate	high	very high	Σ positive Δ
	very low	0.3	0.1	0.0	0.0	0.0	0.1
	low	0.0	47.1	1.5	0.0	0.0	1.5
	moderate	0.1	1.3	39.7	0.3	0.0	0.3
	high	0.3	0.3	0.5	8.3	0.0	0.0
	very high	0.0	0.0	0.0	0.3	0.1	1.9
	Σ negative Δ	0.4	1.5	0.5	0.3	2.7	95.4
	Lower Drava (Carinthia)	very low	low	moderate	high	very high	Σ positive Δ
	very low	0.6	0.0	0.0	0.0	0.0	0.0
	low	0.1	9.3	1.1	0.0	0.0	1.1
	moderate	0.1	0.6	66.9	0.3	0.0	0.3
	high	0.3	0.4	0.9	18.4	0.1	0.1
	very high	0.0	0.0	0.0	0.9	0.1	1.4
	Σ negative Δ	0.6	1.0	0.9	0.9	3.3	95.2

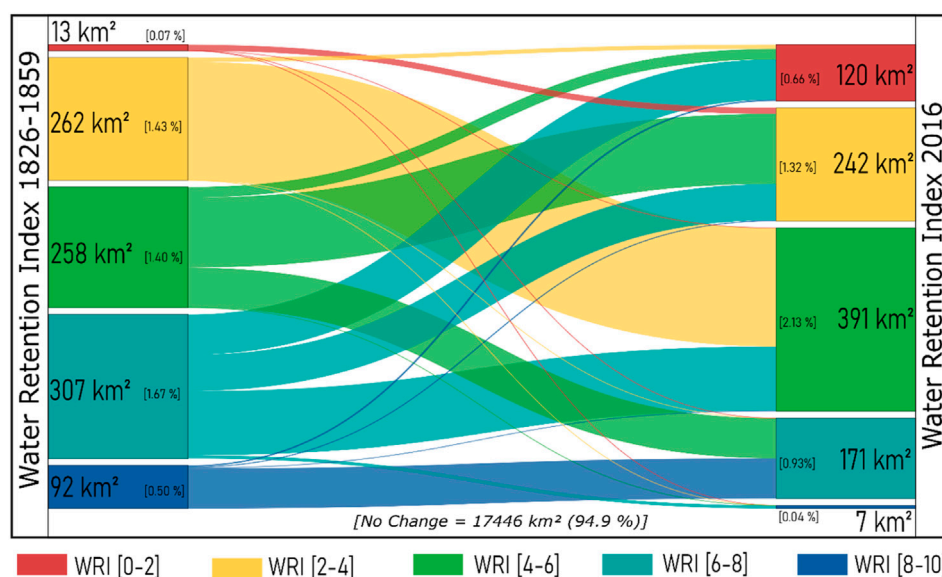


FIGURE 5

Shifts in water retention index between historical (1826–1859; left) and current (2016; right) conditions. For this purpose, the WRI was divided into 5 classes with the categories very low (0–2), low (2–4), moderate (4–6), high (6–8), and very high (8–10). The changes shown are for 5.1% (1,861 km²) of the total area, where class shifts have occurred.

below 1,250 m, a smaller decrease of the WRI_{nat} can be detected compared to the WRI. Interestingly, almost no difference between the two indices can be seen at higher altitudes. In comparison to lower elevations, WRI values show an increase above 1,250 m. The settlement area development (R_{ss}) since the mid-19th century reveals likewise altitudinal features. In areas lower than 500 m, these areas have increased by 107%. In areas between 500–750 m and 750–1,000 m, settlement areas and associated soil sealing have expanded by 54% and 16% respectively. This reveals that large areas of degrading water retention values are associated mostly with settlement expansion but also loss of wetlands and deforestation, especially in low-lying regions (e.g., valley floors) as reported by Hohensinner et al. (2021). On the other hand, an increase in water retention capabilities is detected in higher altitudes, due to the LULCCs since the mid-19th century. A similar altitudinal signal can also be observed for the development of the input parameter R_v . R_v values have generally increased at all elevations, except in areas lower than 500 m. At altitudes between 2000 and 2,750 m, the highest increases of R_v by approximately 2.3%–3.1% can be detected. This shows that the increase in vegetation at higher elevations is also related to increasing WRI values to some degree.

3.5 Impact of LULC changes on the water retention

As a further step, the relative WRI changes associated with the specific LULCC are investigated. Here we relate the past and present LULC classification to the changes in the WRI since land development and certain land cover changes can be related to changes in water retention. Table 3 gives the relative change of

the WRI for each possible land cover transformation. The numbers given in the table represent the relative spatial mean changes between the historical and current LULC situations. Additionally, the 5th and 95th quantiles are given to represent the spatial variability of WRI value changes per land cover transformation.

The vector-based land cover datasets were spatially aggregated to a 100*100 m raster based on the major LULC class within the resulting grid consistently with the WRI maps. Some land use and land cover class might therefore be under or over-estimated by the aggregation from a vector to a raster dataset and might be afflicted with some degree of inaccuracy. Table 3 shows that settlement areas have not been transformed into any other land use and land cover class in the current LULC situation. Interestingly, results indicate that current settlement areas reduced the WRI by –17% on average, compared to historical settlement areas. According to the results, wetlands also show a slight decrease of –4% in the water retention capability compared to the historical land cover situation. These inaccuracies might result from the spatial aggregation to a raster dataset by using the major LULC class per raster pixel. Both input parameters (R_v , R_{ss}) are derived based on the areal coverage per pixel (100*100 m). Therefore, the change of the areal share per pixel linearly influences the resulting input parameters. So, the results indicate that settlement areas have increased by 17% at pixels classified as such in the past and present. Likewise, wetlands have decreased by 4% at pixels constantly classified as wetlands on average.

Transformations from historical wetland areas to any other land cover class result in decreasing WRI values. On average former wetland areas experienced a drop of 22% in their water regulation abilities. Similar results can be obtained for areas classified as stagnant water in the historical land cover dataset. These areas show a mean reduction of 20% considering all land cover class

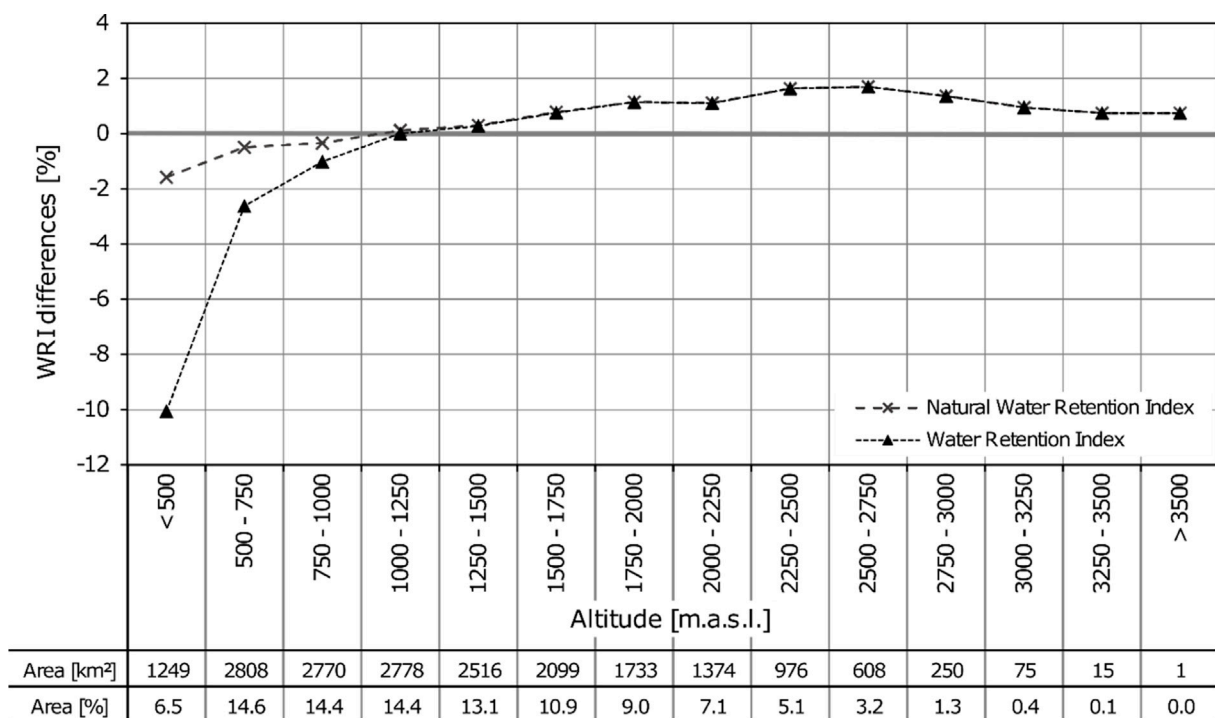


FIGURE 6

Mean WRI changes for different elevation bands, including the absolute areas and relative share compared to the overall study area (19,307 km²). The natural WRI does not consider soil sealing and is thus an indicator of the water retention without settlement or infrastructure development.

transformations. The strongest reduction can be detected for areas, which were transformed from wetlands to settlement areas. These areas show a spatial mean drop in water retention of 66%. On average, areas transformed into settlement areas experienced the largest reduction rates of 44%. Former glacier and wasteland areas increased their water retention ability by 20% and 9%, on average. On the other hand, most areas that were transformed into wetlands and stagnant water from any LULC increased the water retention potential by 10% and 22%, respectively. The transformations from glacier to forest and from grassland to stagnant water resulted in increases of 26% and 27%, respectively. The largest increase in WRI values was detected for areas that have changed from wasteland or glaciers to stagnant water. These LULCCs resulted in over 40% increases in water retention.

4 Discussion

4.1 Input data and weight estimation

Although the concept of the Water Retention Index was developed and proposed to assess the landscape's water regulation potential on a macroscale (Vandecasteele et al., 2017) our results show that the methodological framework of the WRI is also suitable for a regional high-resolution analysis of the landscape's potential of water retention and regulation. Compared to the methodology and input data of Vandecasteele et al. (2017) slight changes have been applied in our study due to the

availability of more recent and more regionally differentiating datasets. The input parameters representing the infiltration and retention in soil (R_s) and the retention in groundwater (R_{gw}) were derived differently. R_s was retrieved from a recently released dataset representing the soil water storage for Austria (Zeitfogel et al., 2022). Additionally, no temporal change of the input parameter R_s depending on the changes in organic carbon content and soil bulk density over time was incorporated. The parameter representing groundwater retention was derived from the GLHMPs 2.0 dataset (Huscroft et al., 2018) already incorporating the permeability of the consolidated and unconsolidated Earth. Therefore we did not consider a reduction of the bedrock permeability factor based on hydrological categories of the overlying soil as Vandecasteele et al. (2017). Compared to the original WRI approach, in the presented study the input layer R_{wb} not only considers stagnant water but also wetland areas, suggesting that these land cover classes have similar water retention abilities. The high-resolution LULC datasets used to derive R_{ss} and R_{wb} for the historical and current state are additionally subject to some degree of uncertainty due to potential inaccuracies and misinterpretations. Especially, settlement areas might be underestimated in the historical dataset (Hohensinner et al., 2021).

The applied weighting scheme yielded large differences between the individual input layers. The slope input parameter (R_{sl}) was assigned the highest weight (0.38), which could be explained by the strong topographic gradients of the study area and emphasizes the importance of the slope factor for water retention. On the other

TABLE 3 Spatial mean relative WRI change matrix [%] for land cover class changes, also including 5% (q5) and 95% (q95) quantile values. For example, the transformation category of all wetlands (1826–1859) to the current sparsely wooded land cover (2016) led to a spatial mean reduction of the WRI by 23% in this transformation category. There were, however, single cases where the reduction was stronger (q5 of –29%) or less pronounced (q95 of –12%).

		Land cover 2016																																
		Sparsely wooded			Arable land			Wetlands			Running water			Glacier			Grassland			Wasteland			Settlement area			Stagnant water			Forest			Vineyards		
		q5	mean	q95	q5	Mean	q95	q5	mean	q95	q5	mean	q95	q5	mean	q95	q5	mean	q95	q5	mean	q95	q5	mean	q95	q5	mean	q95	q5	mean	q95	q5	mean	q95
Land cover 1826 – 1859	Sparsely wooded	0	0	0	−5	−2	3	5	15	24	−5	−1	3	—	—	—	−2	1	4	−10	−9	−7	−110	−52	−3	6	27	36	0	3	5	−2	−2	0
	Arable land	−6	0	5	0	0	0	13	19	26	−5	−4	0	—	—	—	−6	−1	4	−14	−9	−2	−106	−59	−5	6	20	30	−3	2	6	−2	1	2
	Wetlands	−29	−23	−12	−26	−21	−12	−16	−4	4	−28	−19	−5	—	—	—	−27	−20	−7	−40	−30	−21	−105	−66	−21	−18	−6	5	−27	−19	−7	−25	−14	−1
	Running water	−5	−1	5	−3	0	3	5	20	32	0	0	0	—	—	—	−4	0	5	−13	−10	−1	−102	−47	−1	7	25	35	−1	2	7	—	-	-
	Glacier	17	22	27	—	—	—	—	—	—	24	24	24	0	0	0	11	17	21	1	3	7	−13	3	18	25	44	58	22	27	28	—	-	-
	Grassland	−5	0	3	−3	−1	2	4	18	28	−6	−2	4	—	—	—	0	0	0	−11	−9	−7	−104	−51	−4	7	26	37	−2	2	5	−2	0	2
	Wasteland	9	12	16	3	5	10	—	—	—	1	12	16	—	—	—	8	13	21	0	0	0	−116	−29	12	20	42	57	7	14	22	—	-	-
	Settlement area	—	—	—	—	—	—	—	—	—	—	—	—	—	—	—	—	—	—	—	—	—	−96	−17	0	—	—	—	—	—	—	-	-	
	Stagnant water	−29	−17	−8	−27	−18	−3	−17	−6	2	−27	−26	−18	—	—	—	−27	−18	−1	−40	−26	−14	−98	−56	−22	−4	0	0	−27	−14	4	—	-	-
	Forest	−5	−3	−1	−5	−3	0	6	8	11	−7	−3	1	—	—	—	−4	−2	1	−11	−10	−9	−109	−51	−4	4	21	30	0	0	0	−6	−4	−3
	Vineyards	—	—	—	4	4	4	—	—	—	—	—	—	—	—	—	−2	1	3	—	—	—	−103	−58	−19	—	—	—	0	4	5	0	0	0

hand, the optimization yielded the lowest weight of 0.01 for the soil retention parameter. The correlation matrix between all input parameters ($n = 201$) for the weight optimization showed strong correlations of 0.77 ($p < 0.001$) and 0.84 ($p < 0.001$) between R_s and both R_{sl} and R_v , respectively (Supplementary Appendix Table SA3). The strong correlations might explain the very low weight of R_s and it suggests that the importance of soil retention might already be captured in R_{sl} and R_v to some degree. The optimized weights of 0.21 (R_{wb}) and 0.24 (R_{gw}) suggest that the retention in surface water bodies and wetlands is comparably important as groundwater retention for the resulting WRI. These weights are close to those applied by Vandecasteele et al. (2017). Additionally, the relative contribution of each input parameter (except R_{ss}) and the associated weights with regard to the resulting WRI_{cur} have been calculated and ranked from 1st to 5th and are presented in the (Supplementary Appendix Figure SA4). The spatially distributed contribution of each input parameter and their respective weights yield additional information on the importance of each retention process represented by the proxy input datasets. The results suggest that R_{sl} is the most important input parameter for large areas of the study region. R_v and R_{gw} are the second and third most important input parameters. Thus, it is clear that the weights, which define the importance of the input parameters, have a strong impact on the results. The weights in this work were estimated based on a frequently applied method from the literature (Becker et al., 2017; Vandecasteele et al., 2017; Lindén et al., 2021) and the applied optimization framework guarantees objectivity, transparency, and reproducibility, and some degree of comparability between different estimations of the WRI. Advances in the estimation of spatially distributed parameters in hydrological models, also using Machine Learning (e.g., Klotz et al., 2017; Feigl et al., 2020; Feigl et al., 2022) may be used in the future for calculating the weights of the WRI. For example, runoff data could be used for weight optimization.

4.2 Spatial and altitudinal patterns between LULCC and the WRI

The resulting WRI changes per region echoes the spatially different LULCC in these regions. Since the mid-19th century, Eastern Tyrol (region 4) experienced the lowest settlement area development of all six regions (Kofler, 2021) and accordingly showed the lowest negative WRI changes. Here settlements have increased slightly over two times, while, to put this into context, Hohensinner et al. (2021) reported a 6-fold increase for the whole study area. On the contrary, the Vorarlberg region and the Lower Salzach region showed the highest reductions in water retention (Table 2) due to LULCC. In Vorarlberg and the Lower Salzach, settlement areas have increased by over 9 and 6 times, respectively. At the same time, wetlands have decreased dramatically by 7 times in Vorarlberg. In the Lower Salzach region, wetlands have almost vanished completely (Rapottnig, 2021; Bozzetta, 2022).

The spatial distribution of the WRI changes suggests that large decreases did occur in the Alpine valley corridors and at locations where major settlement developments took place (Figure 4). At the same time, slight retention capacity increases along the valley slopes can be depicted. The decrease of WRI in the valley floors is strongly associated with the development of settlement areas and the reduction of wetland areas by 95%. The strong settlement development led to an increase in

settlement areas located within flood-prone areas. This also increased flood exposure and therefore flood risk (Junger et al., 2022). Accordingly, large-scale losses of fluvial corridors led to decreasing flood retention capacity (Hohensinner et al., 2021), somehow a lose-lose situation. The LULCC-induced vertical separation of Alpine landscape features reported by Hohensinner et al. (2021) also transitioned into a comparable separation of increasing and decreasing WRI areas. Strong decreasing WRI values are obtained for low-elevation areas. The natural water retention index (WRI_{nat}), which does not consider sealed surface areas, shows a significantly lower decrease in the water retention capacities of low-elevation areas. The changes in WRI_{nat} in low-lying areas can therefore be attributed to the loss and transformation of wetlands to agricultural land and forests. The altitudinal investigation shows that the WRI and WRI_{nat} values increased accordingly in areas above 1,250 m. The general increase of the water retention potential in higher altitudes suggests that the water regulation potential has increased. This reflects the increase of forest areas and the large areal transformation from wasteland and glaciated areas to Alpine grassland, by 16% and 4.2%, respectively (Hohensinner et al., 2021).

4.3 WRI changes due to specific land use class changes

The specific WRI changes with regard to certain LULC transformations (Table 3) represent spatial mean values over the whole study area. To address the variability of the WRI change per LULCC the 5th and the 95th quantile were additionally presented. The results indicate, e.g., that current settlement areas reduced the WRI by 17% on average, for areas already classified as settlement areas in the past. The 5th quantile suggests even a reduction of 98%. This might be due to the introduced uncertainty in the aggregation but could also suggest that today's settlement areas are constructed with a higher building and soil sealing density. In addition, the input land cover dataset might already be subject to some degree of uncertainty due to inaccuracies and potential misinterpretations during the digitalization of the historical datasets. Therefore, settlement areas might be underrepresented (Hohensinner et al., 2021). The transformation from a glacier to a settlement area would indicate a slight positive change in the water retention potential. This explicit result is highly uncertain and might represent another limiting factor of the spatial aggregation and the representation of spatial mean values. Generally, transformations from any LULC class to wetlands resulted mostly in an increase in the WRI. At the same time, areas that are constantly classified as wetlands over time show a minor reduction of -4% ($q_5 = -16\%$, $Q_{95} = 4\%$). This slight reduction might have also been introduced due to the reclassification based on the majority and is therefore afflicted with some degree of uncertainty. In addition, wetlands and stagnant water land cover classes are both presented within the input parameter R_{gw} , assuming a similar retention behavior. This might also lead to an overestimation of the retention potential of wetlands, which strongly depends on the saturation status and therefore on the maximum available retention potential. Especially during extreme events, such as floods, wetlands can either contribute to amplification or mitigation (Bullock & Acreman, 2003; Acreman & Holden, 2013). Accordingly, the results presented for each specific land use change category might show some inaccuracies and are certainly subject to some degree of

uncertainty. However, the given relative WRI values assist in the qualitative interpretation and allow for comparison between certain land use transformations. Additionally, other accompanying LULCC effects on the water retention potential processes such as soil storage reduction due to soil compaction with heavy machinery on arable land were not considered (Rogger et al., 2017) in our investigation. Therefore, it can be assumed that the presented impacts of land use transformations with regard to water regulation might be somewhat underestimated.

5 Summary and conclusion

Regulating ecosystem services, such as water purification, flood control, and water regulation are strongly affected by LULCC (Hasan et al., 2020). Various studies have linked LULCCs to declining ecosystem services (e.g., Haines-Young et al., 2012; Kindu et al., 2016; Rai et al., 2018). Human-induced land use change not only affects hydrological ecosystem services but also affects hydrological processes (e.g., Rogger et al., 2017; Wesemann, 2021) and can therefore also affect flood-generating processes and consequently flood risk (Hall et al., 2014). Alpine areas of Austria have experienced strong LULCC since the mid-19th century. Recent studies showed that these LULCCs have resulted in increased flood exposure and flood risk, especially in Alpine valley corridors (Hohensinner et al., 2021; Junger et al., 2022). However, sustainable land use and properly managed LULCC can be beneficial for water regulation (Vandecasteele et al., 2017). Accordingly, the present study aimed to investigate the effects of these LULCCs on the water retention of the landscape in the Alpine areas of Austria. We calculated the Water Retention Index (WRI) developed by Vandecasteele et al. (2017) for the past (1826–1859) and present (2016) land cover situation for the Austrian catchment of the Rhine, Salzach, and Drava rivers.

The resulting WRI maps show a clear spatial pattern mimicking the characteristic Alpine topography, the difference between the historical and present WRI maps reveals that LULCC negatively affected the water retention potential primarily in valley floors. This links the significant settlement expansion in Alpine valleys, leading to increased flood exposure (Hohensinner et al., 2021; Junger et al., 2022), with a decreasing capacity for water regulation. The altitudinal comparison of the WRI with the natural WRI, which does not consider the settlement area parameter in the calculation, shows that the reduction of the water retention capacity is significantly lower without settlements. Without settlement areas, the water retention reduction would be 77% lower in areas lower than 1,000 m.a.s.l. At elevations higher than 1,250 m.a.s.l., almost equally increasing values of the WRI and the natural WRI are present. The strongest WRI reduction of 66% is attributed to the land use changes from wetlands to settlement areas. The highest intensifications of the landscape's potential to regulate water could be observed by the transformation from wasteland or glacier to stagnant water. In these areas, WRI values increased by over 40%. The results indicate a large variability of WRI changes depending on the specific LULC transformation within the investigated time period.

The results presented in this study showed that a high-resolution utilization of the Water Retention Index can be very supportive to investigate the impacts of LULCC on water regulation on a regional scale. The land cover changes are very well reflected in the calculated WRI maps and the spatial distributed WRI value maps yielded new insights

about the impact of LULCC on flood control and water regulation. The results also highlight that soil sealing through settlement developments shows the strongest adverse effects and leads to a decline in regulating ecosystem services including flood control. In an already very limited area for permanent settlements, such as the Austrian Alps, these adverse impacts might lead to further pressures on ecosystem services and conflicts between different land uses. Therefore, sustainable land use and land cover change management would enhance the landscape's ability to retain water and support flood risk mitigation measures.

Data availability statement

The datasets presented in this article are not readily available because underlying data are partly subject to third party restrictions. Selected data and data supporting the conclusion of the paper are available on request. Requests to access the datasets should be directed to gabriel.stecher@boku.ac.at.

Author contributions

GS: conceptualization, methodology, investigation, validation, writing; SH: validation, writing, reviewing; MH: conceptualization, methodology, investigation, validation, writing, reviewing, funding. All authors contributed to the article and approved the submitted version.

Funding

This work was funded by the Earth System Sciences (ESS) research programme of the Austrian Academy of Sciences (ÖAW) within the project “Integrated Flood Risk Management in Mountain Areas: Assessing Sectoral Interdependencies, Conflicts and Options for Policy Coordination” (PoCo-FLOOD).

Conflict of interest

The authors declare that the research was conducted in the absence of any commercial or financial relationships that could be construed as a potential conflict of interest.

Publisher's note

All claims expressed in this article are solely those of the authors and do not necessarily represent those of their affiliated organizations, or those of the publisher, the editors and the reviewers. Any product that may be evaluated in this article, or claim that may be made by its manufacturer, is not guaranteed or endorsed by the publisher.

Supplementary material

The Supplementary Material for this article can be found online at: <https://www.frontiersin.org/articles/10.3389/fenvs.2023.1219030/full#supplementary-material>

References

- Acreman, M., and Holden, J. (2013). How wetlands affect floods. *Wetlands* 33, 773–786. doi:10.1007/s13157-013-0473-2
- Alpine Convention (2015). *Demographic changes in the alps. Report on the state of the Alps*. Austria: Innsbruck.
- Andréassian, V. (2004). Waters and forests: From historical controversy to scientific debate. *J. Hydrology* 27, 1. doi:10.1016/j.jhydrol.2003.12.015
- Becker, W., Saisana, M., Paruolo, P., and Vandecasteele, I. (2017). Weights and importance in composite indicators: Closing the gap. *Ecol. Indic.* 80, 12–22. doi:10.1016/j.ecolind.2017.03.056
- BMF (2022). *Digital elevation model Austria*. Wien: Bundesministerium für Finanzen.
- BMLFUW (2015). Richtlinien für die Bundes- Wasserbauverwaltung (RIWA-T) Bundesministerium für Land-und Forstwirtschaft, Umwelt und Wasserwirtschaft, Wien.
- Bozzetta, T. (2022). *Land cover change in the catchment of the rhine river (Vorarlberg)*. Vienna: University of Natural Resources and Life Sciences Vienna.
- Bullock, A., and Acreman, M. (2003). The role of wetlands in the hydrological cycle. *Hydrology Earth Syst. Sci.* 7, 358–389. doi:10.5194/hess-7-358-2003
- Cammerer, H., Thieken, A. H., and Verbürg, P. H. (2013). Spatio-temporal dynamics in the flood exposure due to land use changes in the Alpine Lech Valley in Tyrol (Austria). *Nat. Hazards* 68, 1243–1270. doi:10.1007/s11069-012-0280-8
- EU (2007). Directive 2007/60/EC of the European Council and European Parliament of 23 October 2007 on the assessment and management of flood risks. *Official J. Eur. Union*, 27–34.
- Feigl, M., Herrnegger, M., Klotz, D., and Schulz, K. (2020). Function space optimization: A symbolic regression method for estimating parameter transfer functions for hydrological models. *Water Resour. Res.* 56, e2020WR027385–24. doi:10.1029/2020WR027385
- Feigl, M., Thober, S., Schweppe, R., Herrnegger, M., Samaniego, L. E., and Schulz, K. (2022). Automatic regionalization of model parameters for hydrological models. *Water Resour. Res.* 58, e2022WR031966. doi:10.1029/2022WR031966
- Gómez-Baggethun, E., and Barton, D. N. (2013). Classifying and valuing ecosystem services for urban planning. *Ecol. Econ.* 86, 235–245. doi:10.1016/j.ecolecon.2012.08.019
- Gov (2020). *Federal Government Austria: Aus Verantwortung für Österreich: Zusammenfassung des Regierungsprogrammes 2020-2024. Report*. Vienna.
- Grüneis, H., Schroll, K., and Wagner, K. (2021). The role of agriculture in flood risk management in Austria FÖBE conflicts and challenges. *J. Environ. Sci. Eng. B* 10, 112–127. doi:10.17265/2162-5263/2021.03.004
- Guzha, A. C., Rufino, M. C., Okoth, S., Jacobs, S., and Nóbrega, R. L. B. (2018). Impacts of land use and land cover change on surface runoff, discharge and low flows: Evidence from East Africa. *J. Hydrology Regional Stud.* 67, 49. doi:10.1016/j.ejrh.2017.11.005
- Haines-Young, R., Potschin, M., and Kienast, F. (2012). Indicators of ecosystem service potential at European scales: Mapping marginal changes and trade-offs. *Ecol. Indic.* 21, 39–53. doi:10.1016/j.ecolind.2011.09.004
- Hall, J., Arheimer, B., Borga, M., Brázdil, R., Claps, P., Kiss, A., et al. (2014). Understanding flood regime changes in Europe: A state-of-the-art assessment. *Hydrology Earth Syst. Sci.* 18, 2735–2772. doi:10.5194/hess-18-2735-2014
- Hasan, S. S., Zhen, L., Miah, M. G., Ahamed, T., and Samie, A. (2020). Impact of land use change on ecosystem services: A review. *Environ. Dev.* 34, 100527. doi:10.1016/j.envdev.2020.100527
- Herrnegger, M., Wesemann, J., Fürst, J., and Schulz, K. (2022). “Event-based runoff simulations show forest roads enhancing floods,” 18th biennial conference of the euromediterranean network of experimental and representative basins ERB 2022, Portoferraio, Italy.
- Hohensinner, S., Atzler, U., Berger, M., Bozzetta, T., Höberth, C., Kofler, M., et al. (2021). Land use and cover change in the industrial era: A spatial analysis of alpine river catchments and fluvial corridors. *Front. Environ. Sci.* 9, 1–17. doi:10.3389/fenvs.2021.647247
- Huscroft, J., Gleeson, T., Hartmann, J., and Börker, J. (2018). Compiling and mapping global permeability of the unconsolidated and consolidated earth: GLobal HYdrogeology MaPS 2.0 (GLHYMPS 2.0). *Geophys. Res. Lett.* 45, 1897–1904. doi:10.1002/2017GL075860
- Jin, G., Li, Z., Lin, Q., Shi, C., Liu, B., and Yao, L. (2015). Land use suitability assessment in low-slope hilly regions under the impact of urbanization in yunnan, China. *Adv. Meteorology* 2015, 1, 9. doi:10.1155/2015/848795
- Junger, L., Hohensinner, S., Schroll, K., Wagner, K., and Seher, W. (2022). Land use in flood-prone areas and its significance for flood risk management—a case study of alpine regions in Austria. *Land* 11, 392. doi:10.3390/land11030392
- Kindu, M., Schneider, T., Teketay, D., and Knoke, T. (2016). Changes of ecosystem service values in response to land use/land cover dynamics in Munessa-Shashemene landscape of the Ethiopian highlands. *Sci. Total Environ.* 547, 137–147. doi:10.1016/j.scitotenv.2015.12.127
- Klingler, C., Schulz, K., and Herrnegger, M. (2021). LamaH-CE: LARge-SaMple DATA for Hydrology and environmental Sciences for central Europe. *Earth Syst. Sci. Data* 13, 4529–4565. doi:10.5194/essd-13-4529-2021
- Klotz, D., Herrnegger, M., and Schulz, K. (2017). Symbolic regression for the estimation of transfer functions of hydrological models. *Water Resour. Res.* 53, 9402–9423. doi:10.1002/2017WR021253
- Kofler, M. (2021). *Land cover change in the catchment of the Drava River (eastern Tyrol)*. (Master thesis). University of Natural Resources and Life Sciences Vienna/Vienna.
- Lindén, D., Cinelli, M., Spada, M., Becker, W., and Burgherr, P. (2021). *Composite indicator analysis and optimization (CIAO) tool, v.2*. doi:10.13140/RG.2.2.14408.75520
- Löschner, L., Herrnegger, M., Apperl, B., Senoner, T., Seher, W., and Nachtnebel, H. P. (2017). Flood risk, climate change and settlement development: A micro-scale assessment of Austrian municipalities. *Reg. Environ. Change* 17, 311–322. doi:10.1007/s10113-016-1009-0
- Maitima, J. M., Mugatha, S. M., Reid, R. S., Gachimb, L. N., Majule, A., Lyaruu, H., et al. (2009). The linkages between land use change, land degradation and biodiversity across East Africa. *Afr. J. Agric. Res.* 3, 310–325. doi:10.5897/AJEST08.173
- MEA (2005). *Millennium ecosystem assessment - ecosystems and human well-being: Synthesis*. Washington, D.C: Island Press. doi:10.1016/B978-0-12-809665-9.09206-5
- Merz, B., Vorogushyn, S., Uhlemann, S., Delgado, J., and Hündecha, Y. (2012). HESS opinions: More efforts and scientific rigour are needed to attribute trends in flood time series. *Hydrology Earth Syst. Sci.* 16, 1379–1387. doi:10.5194/hess-16-1379-2012
- Nordbeck, R., Seher, W., Grüneis, H., Herrnegger, M., and Junger, L. (2023). Conflicting and complementary policy goals as sectoral integration challenge: An analysis of sectoral interplay in flood risk management. *Policy Sci.* doi:10.1007/s11077-023-09503-8
- Nordbeck, R., Steurer, R., and Löschner, L. (2019). The future orientation of Austria's flood policies: From flood control to anticipatory flood risk management. *J. Environ. Plan. Manag.* 62, 1864–1885. doi:10.1080/09640568.2018.1515731
- OECD (2008). *Handbook on constructing composite indicators. Methodology and user guide, 2*. Berlin: OECD PUBLICATIONS. rue André-Pascal.
- Oudin, L., Andréassian, V., Lerat, J., and Michel, C. (2008). Has land cover a significant impact on mean annual streamflow? An international assessment using 1508 catchments. *J. Hydrology* 357, 303–316. doi:10.1016/j.jhydrol.2008.05.021
- Paruolo, P., Saisana, M., and Saltelli, A. (2013). Ratings and rankings: Voodoo or science? *J. R. Stat. Soc. Ser. A Statistics Soc.* 176, 609–634. doi:10.1111/j.1467-985X.2012.01059.x
- Rai, R., Zhang, Y., Paudel, B., Acharya, B. K., and Basnet, L. (2018). Land use and land cover dynamics and assessing the ecosystem service values in the trans-boundary Gandaki River Basin, Central Himalayas. *Sustain. Switz.* 10, 3052–3122. doi:10.3390/su10093052
- Rapottnig, L. (2021). *Land cover change in the catchment of the middle Salzach river (Salzburg)*. Vienna: University of Natural Resources and Life Sciences Vienna.
- Rogger, M., Agnoletti, M., Alaoui, A., Bathurst, J. C., Bodner, G., Borga, M., et al. 2017. Land use change impacts on floods at the catchment scale: Challenges and opportunities for future research. *Water Resour. Res.* 53: 5209–5219. doi:10.1002/2017WR020723
- Silvestri, S., Zaibet, L., Said, M. Y., and Kifugo, S. C. (2013). Valuing ecosystem services for conservation and development purposes: A case study from Kenya. *Environ. Sci. Policy* 31, 23–33. doi:10.1016/j.envsci.2013.03.008
- Sobol, I. M. (1993). Sensitivity estimates for nonlinear mathematical models. *Math. Model. Comput. Exp.*, 407–414.
- Stecher, G., and Herrnegger, M. (2022). Impact of hydropower reservoirs on floods: Evidence from large river basins in Austria. *Hydrological Sci. J. Accept.* 67, 2082–2099. doi:10.1080/02626667.2022.2130332
- Thieken, A. H., Cammerer, H., Dobler, C., Lammel, J., Sch, ?, and berl, F. (2016). Estimating changes in flood risks and benefits of non-structural adaptation strategies - a case study from Tyrol, Austria. *Mitig. Adapt. Strategies Glob. Change* 21, 343–376. doi:10.1007/s11027-014-9602-3

- UBA (2022). Vienna: Umweltbundesamt - Environmental Agency Austria.
- Van Herk, S., Rijke, J., Zevenbergen, C., and Ashley, R. (2015). Understanding the transition to integrated flood risk management in The Netherlands. *Environ. Innovation Soc. Transitions* 15, 84–100. doi:10.1016/j.eist.2013.11.001
- Vandecasteele, I., Mari i Rivero, I., Baranzelli, C., Becker, W., Dreoni, I., Lavalle, C., et al. (2017). The Water Retention Index: Using land use planning to manage water resources in Europe. *Sustain. Dev.* 26, 122–131. doi:10.1002/sd.1723
- Viglione, A., Merz, B., Dung, N. V., Parajka, J., Nester, T., and Blöschl, G. (2016). Attribution of regional flood changes based on scaling fingerprints. *J. Hydrology* 52, 5322–5340. doi:10.1002/2016wr019036
- VITO. (2018). *Gio global land component - lot I; operation of the global land component - product user manual*.
- Wesemann, J., Herrnegger, M., and Schulz, K. (2018). Hydrological modelling in the anthroposphere: Predicting local runoff in a heavily modified high-alpine catchment. *J. Mt. Sci.* 15, 921–938. doi:10.1007/s11629-017-4587-5
- Wesemann, J. (2021). *Hydrologische Modellierung des natürlichen Abflussverhaltens und dessen Veränderung durch anthropogene Einflüsse*. PhD thesis. Vienna: University of Natural Resources and Life Sciences.
- Winkler, K., Fuchs, R., Rounsevell, M., and Herold, M. (2021). Global land use changes are four times greater than previously estimated. *Nat. Commun.* 12, 2501. doi:10.1038/s41467-021-22702-2
- Zeitfogel, H., Herrnegger, M., Feigl, M., and Schulz, K. (2022). “Groundwater recharge modeling – the importance of distributed soil information in hydrological models,” in EGU General Assembly 2022, Vienna, Austria, 23–27 May 2022, EGU22–8526. doi:10.5194/egusphere-egu22-8526

Frontiers in Environmental Science

Explores the anthropogenic impact on our natural world

An innovative journal that advances knowledge of the natural world and its intersections with human society. It supports the formulation of policies that lead to a more inhabitable and sustainable world.

Discover the latest Research Topics

[See more →](#)

Frontiers

Avenue du Tribunal-Fédéral 34
1005 Lausanne, Switzerland
frontiersin.org

Contact us

+41 (0)21 510 17 00
frontiersin.org/about/contact

